Part I: Kinetic Mechanisms and Thermodynamics in Diblock Copolymer Micelles
&
Part II: Inhomogeneous Thermodynamics of Polar Fluids and Ionic Liquids

Thesis by
Samuel Varner

In Partial Fulfillment of the Requirements for the
Degree of
Doctor of Philosophy in Chemical Engineering

CALIFORNIA INSTITUTE OF TECHNOLOGY
Pasadena, California

2026
Defended October 31, 2025

Samuel Varner
ORCID: 0000-0002-1365-1027

ACKNOWLEDGEMENTS

I am deeply indebted to my wife, family, friends, and mentors for their unwavering support during my time at Caltech. I have been privileged to have the resources, opportunities, and encouragement to pursue my passion for science through learning, discovery, and teaching. Graduate school has been the most incredible period of my life, and I owe a profound debt of gratitude to all who helped make it so meaningful. I extend special thanks to my advisor, Prof. Zhen-Gang Wang, and to the Department of Energy Computational Science Graduate Fellowship for supporting my research and granting me the freedom to explore throughout my Ph.D.

I will forever be grateful to my wonderful advisor, Prof. Zhen-Gang Wang, who has been nothing short of the perfect mentor for me. His unwavering support and advocacy have inspired me to doubt myself less and to be more confident in my abilities and self-worth. Through his guidance, I have learned and accomplished more than I ever thought possible. I would also like to thank Dr. Christopher Balzer for being the first to welcome me to Caltech and for continuing to serve as my primary mentor throughout my Ph.D. research. It is impossible to fully express the impact Chris has had on me, both personally and professionally.

I would like to thank Prof. John Brady, Prof. Kim See, Prof. Garnet Chan, and Prof. Zhen-Gang Wang for serving on my candidacy and thesis committees. I am also grateful to Prof. Juan de Pablo for serving as my advisor during the completion of my research practicum at Argonne National Laboratory. He welcomed me into his group without hesitation and treated me as one of his own. I would further like to thank Prof. Marcus Müller for his generosity with his time and for providing invaluable guidance as I ventured into uncharted territory and learned new computational methods.

The administration and faculty of the Department of Chemistry and Chemical Engineering have always been incredibly supportive. In particular, Allison Kinard and Dr. Michael Vicic have shown extraordinary warmth, kindness, and selflessness, which I know have made a profound impact on all CCE graduate students. Their dedication to improving the lives of both graduate and undergraduate students is truly admirable and deeply appreciated.

I would like to thank all past and present members of the Wang group. In particular, I am grateful to Dr. Christopher Balzer for his selflessness, generosity, and friendship.

My office mates, Pierre Walker and Dr. Alec Glisman, inspired me in many ways and made me laugh more times than I can count. I am also thankful to Dr. Benjamin Ye and Dr. Dorian Bruch for helping me stay grounded through lighthearted lunches and late nights playing games. Although the first year of graduate school was especially challenging due to the COVID-19 stay-at-home policies, I will always cherish living with Vignesh Bhethanabotla and Alex Ye during that time. I am especially thankful for Vignesh, whom I am lucky to call a friend; our dinners, ice cream runs, and intense board game nights made Pasadena feel more like home.

My undergraduate mentors, Prof. Jeffrey Richards, Prof. Linda Broadbelt, and Prof. Muzhou Wang, originally inspired me to pursue research and an academic career. Had I not been fortunate enough to meet them at Northwestern University when I did, I most likely would not have attended graduate school. I owe them immense gratitude for their continued support in everything I do, even to this day. They always believed in me, even when I did not believe in myself.

The Caltech Center for Teaching, Learning, and Outreach provided me with the opportunity to pursue my teaching interests during my time at Caltech. Co-teaching a graduate chemical engineering course was a truly unique and valuable experience. I am also very grateful to Prof. Bilin Zhuang at Harvey Mudd College for allowing me to teach computational chemistry to undergraduate students. These opportunities were invaluable in giving me practical teaching experience and in reaffirming my desire to pursue a career in academia and education.

My family has always provided me with unconditional love and support in everything I do. My parents have made incredible sacrifices without hesitation, all to enable me to pursue my dreams. I am eternally grateful and truly blessed to have them. My sister, Sydney, has been an amazing supporter throughout my life, and I can never thank her enough for the love she has shown me.

Most of all, I am thankful for my wife, Gina, who has been with me and supported me through everything. She consoles me during the hard times and lifts me up during the good ones. Getting married in 2023 was not only the highlight of my time at Caltech but the highlight of my life. Adopting our first puppy in 2025 was another beautiful milestone that further cemented Pasadena as the place where our little family began. Over the course of our lives, I can only hope that my love and support will ease the burden she has carried on my behalf.

ABSTRACT

Part I: Block copolymers can undergo microphase separation to form a range of ordered nanostructures, including lamellae, lattice-ordered spheres and cylinders, and even network phases. In selective solvents, they self-assemble into micelles, similar to surfactant molecules. However, unlike surfactants, block copolymers often contain hundreds or thousands of repeat units, which significantly slows their dynamics and equilibration. As a result, solutions of diblock copolymer micelles are frequently kinetically trapped far from equilibrium due to large free energy barriers associated with equilibration mechanisms such as chain exchange, micelle fusion, and micelle fission. For applications ranging from viscosity modification and drug delivery to nanoreactors, understanding these kinetic processes is essential. Moreover, developing strategies to achieve consistent and stable micelle size distributions remains a key challenge, particularly in systems far from equilibrium.

This work analyzes the single-chain exchange mechanism in highly segregated copolymer micelles, with particular attention to its chain length dependence, a topic that has been actively debated since the introduction of the Halperin and Alexander theory in 1989. The kinetics of chain exchange are examined under two representative regimes: one involving polymeric solvents, where the micelle core gradually shrinks, and the other involving small-molecule solvents, where the core fully collapses. A combination of simulation and sampling techniques is employed to compare the thermodynamics of the underlying free energy landscape with the actual kinetic pathways of chain escape.

This work also analyzes the kinetic pathways involved in a widely used copolymer micelle preparation technique known as thin film dissolution, or direct dissolution. Mesoscale molecular dynamics simulations are performed to provide a molecular-level picture of micelle formation, starting from both ordered and disordered initial states. In parallel, a mean-field theory is developed to assess how closely the intermediate structures and the final micelles resemble equilibrium configurations.

Part II: Electrolytes are ubiquitous in our world and play essential roles in biology, consumer products, and energy storage. Fundamentally, an electrolyte consists of charged species and a solvent, both of which significantly influence its behavior in the bulk and near interfaces. While it is relatively straightforward to predict charge interactions in a vacuum, the presence of a liquid solvent mediates these interactions

in complex and nontrivial ways. Moreover, the interaction of ions with surfaces is highly nuanced and can be strongly affected by the specific chemistry of the ions, solvent, and interface. This is especially relevant in the context of the electric double layer, a subject of scientific inquiry since 1853. Gaining a deeper understanding of these intricate effects and how they govern electrolyte behavior is critical not only for explaining biologically relevant phenomena such as macromolecular complexation, but also for designing batteries and supercapacitors with optimized energy storage performance.

This work presents an analysis of three distinct systems in which the behavior of charged and polar fluids were poorly understood. One area of focus is the effect of introducing non-polar solvents on the charging behavior and energy storage performance of room-temperature ionic liquid supercapacitors, with particular attention to specific surface effects and complex tricritical surface phase behavior. Another topic explored is the entropic origin of ionic interactions in polar solvents, highlighting how entropy is the dominant force driving ion association. Separately, we also investigate the unique surface polarization that arises in asymmetric polar fluids at liquid–vapor interfaces, revealing subtle interfacial phenomena driven solely by molecular asymmetry.

PUBLISHED CONTENT AND CONTRIBUTIONS

(1) Varner, S.; Lodge, T.; Wang, Z.-G. In, APS March Meeting Abstracts, 2025.

(2) Varner, S.; Müller, M.; Gallegos, A., et al. Mechanisms of Chain Exchange in Diblock Copolymer Micelles, 2025, DOI: 10.48550/arXiv.2509.06528.

(3) Varner, S.; Walker, P. J.; Venkatachalam, A.; Zhuang, B.; Wang, Z.-G. Stockmayer Fluid with a Shifted Dipole: Interfacial Behavior, 2025, DOI: 10.48550/arXiv.2509.05523.

(4) Varner, S.; Balzer, C.; Wang, Z.-G. A Jacobian-free pseudo-arclength continuation method for phase transitions in inhomogeneous thermodynamic systems. *The Journal of Chemical Physics* **2024**, *161*, 064107, DOI: 10.1063/5.0220849.

(5) Varner, S.; Balzer, C.; Wang, Z.-G. Entropic Origin of Ionic Interactions in Polar Solvents. *The Journal of Physical Chemistry B* **2023**, *127*, 4328–4337, DOI: 10.1021/acs.jpcb.3c00588.

(6) Varner, S.; Wang, Z.-G. Effects of dilution in ionic liquid supercapacitors. *Physical Chemistry Chemical Physics* **2022**, *24*, 27362–27374, DOI: 10.1039/D2CP03398D.

In each of the publications above, I contributed to the conception of the project, develope code, conducted calculations, analyzed data, and participated in the writing of the manuscript.

TABLE OF CONTENTS

LIST OF ILLUSTRATIONS

LIST OF TABLES

Part I

Kinetic Mechanisms and Thermodynamics in Diblock Copolymer Micelles

Chapter 1

INTRODUCTION

1.1 Copolymer Micelles

Block copolymers (BCPs) are amphiphilic molecules that can self-assemble into nanostructured materials in both melts and solutions. In solution, BCPs can spontaneously self-assemble into micellar structures of various morphologies, such as spheres, cylinders, and vesicles depending on the relative volume fraction of the two blocks and their degrees of incompatibility with the solvent and with each other [1].

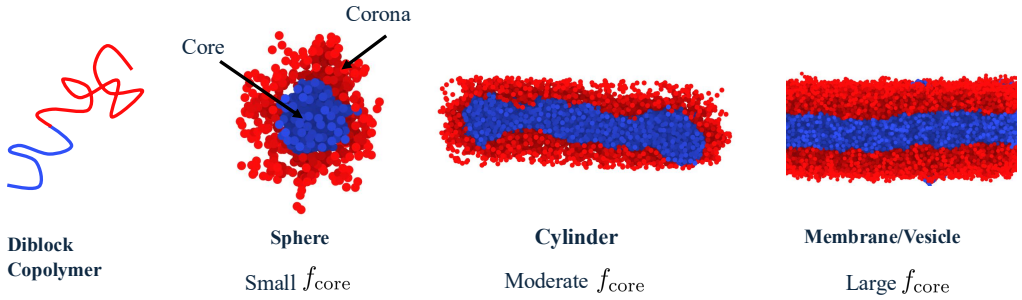

Figure 1.1: Schematic of common block copolymer micelle morphologies including (a) spherical micelles, (b) cylindrical micelles, and (c) vesicles where f_{core} is the volume fraction of the core-forming block.

The thermodynamic and kinetic properties of copolymer micelles including their size and stability under environmental changes naturally inform their use in applications such as nanoreactors [2–5], drug delivery and encapsulation [6–10], and nanolithography [11, 12]. Copolymer micelles are a versatile platform for applications requiring spontaneous self-assembly into nanoscale structures due to the wide variety of monomer chemistries and polymer architectures that can be synthesized. Figure 1.2 shows examples of different use cases of block copolymer micelles. In the case of diblock copolymer membranes, copolymer micelles are casted into a thin film, where they serve as a template for the formation of nanopores [13–18]. In drug delivery applications, hydrophobic therapeutics can be embedded in the micelle core, while signaling ligands can be attached to the corona [6, 8–10, 19]. Copolymer micelles can also serve as nanoreactors where solvophobic reactants are sequestered within the micelle core. Althernatively, the core monomers themeselves can serve as reactants for the formation of nanoparticles [20, 21].

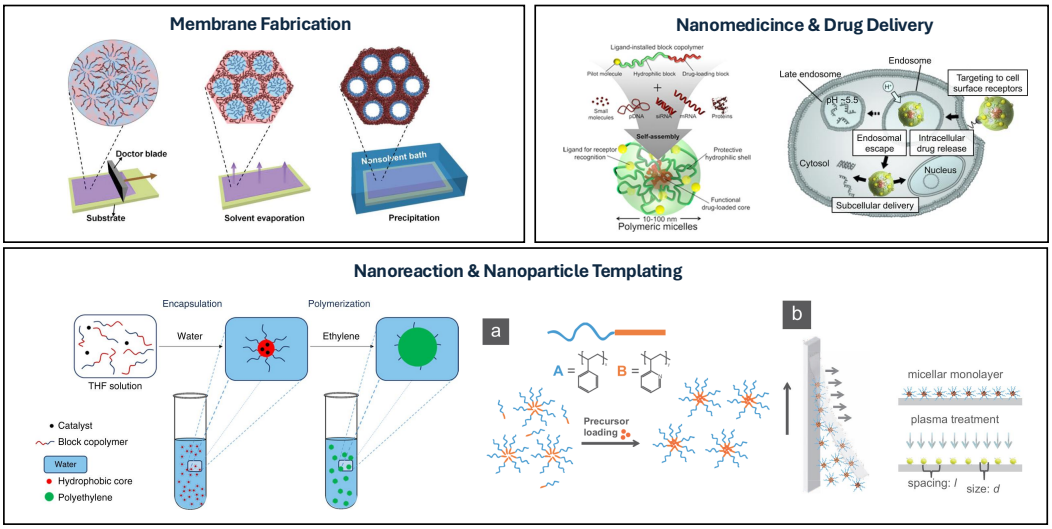

Figure 1.2: Examples of different use cases of block copolymer micelles. Schematic of membrane fabrication reproduced from [14]. Schematic of drug delivery reproduced from [19]. Schematic of nanoreaction reproduced from [20]. Schematic of nanoparticle templating reproduced from [12].

At the most fundamental level, the formation of copolymer micelles is governed by a comptentition between three factors: (1) the unfavorable surface interaction between the core-forming block and the solvent, (2) the stretching of the core-forming block to fill out the micelle core, and (3) the stretching of the corona-forming block similar to a polymer brush [22]. The balance of these three factors determines the morphology, micelle size, and aggregation number. Theories based on scaling arguments have been developed to predict the equilibrium sizes of spherical copolymer micelles by estimating the free energy from each contribution [23–25]. Later, Zhulina et al. developed a comprehensive theory that accurately predicted the relative stability and equilibrium sizes of spherical, cylindrical, and vesicular micelles [1].

While simple scaling theories can give accurate predictions of of the free energy under certain limiting conditions and for simple geometries, self-consistent field theory (SCFT) is a versatile tool that can be applied to a wide variety of copolymer architectures, chemistries, and micelle morphologies [26–28]. Most importantly, SCFT allows for the calculation of component density profiles, which sheds additional insight into the structure of the micelle core and corona. In the last few decades, SCFT has been employed to study many different micellar systems including copolymer micelles dissolved in a homopolymer melt [29–33], copolymer micelles in selective solvents [34–37], copolymers with complex architectures such

as coil-comb copolymers [38], and even copolymers with charged blocks [39–46].

While SCFT provides the framework for computing the internal free energy of an isolated micelle, it does not account for the translational entropy of micelles of varying sizes and concentrations in a solution. To account for this, a common approach is to obtain the internal free energy though SCFT or a scaling theory, and then combine it with the translational entropy of an ideal gas of micelles subject to conservation of mass. This approach has been successfully applied to predict the critical micelle concentration (CMC) and equilibrium micelle size distribution for a variety of copolymer micelle systems [32, 38, 39, 47–50].

1.2 Dynamics and Equilibration

At concentrations exceeding the critical micelle concentration (CMC), micelles form through a multi-stage mechanism, starting with rapid formation of small aggregates, and ending with slow equilibration of the micelle size distribution and micelle concentration [51–55]. Aggregate formation is fast in concentrated solutions due to a low aggregation free energy barrier, which has been thoroughly discussed in many studies of BCP micelle kinetics [47, 50]. In contrast, equilibration is slow due to the large free energy barriers associated with available mechanisms, including single-chain (or unimer) exchange, and fission/fusion [56]. In single-chain exchange, a chain escapes from one micelle, diffuses through solution, and enters another. Fusion occurs when two aggregates or micelles (possibly of different sizes) combine to form a larger micelle, while fission/fragmentation is its reverse. A schematic of these mechanisms is shown in Figure 1.3.

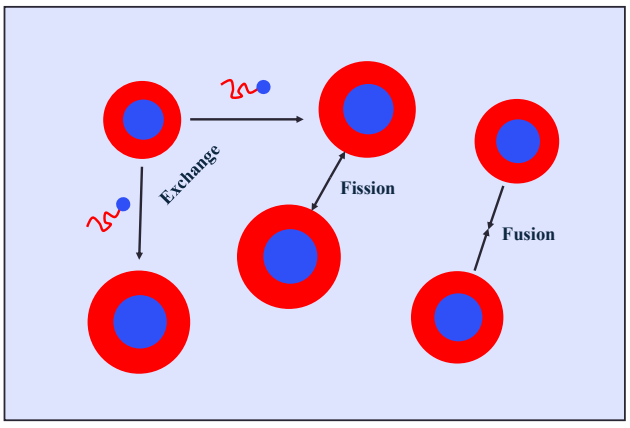

Figure 1.3: Schematic of different equilibration mechanisms in diblock copolymer micelles including single-chain exchange, fusion, and fission.

It was originally argued that single chain exchange would be the dominate mechanism for equilibration throughout the entire micellization process [57] due to insurmountable fusion barriers. However, it has been shown both experimentally and theoretically that the fusion of aggregates of strongly asymmetric sizes can become dominant in the intermediate stages of micelle formation [58, 59], while unimer, dimer, and trimer exchange tend to dominate near equilibrium [47, 60]. Equilibration via these mechanisms is expected to occur in the case of relatively short chains and low to moderate interfacial tensions, where the free energy barriers are not prohibitively high. However, in many experimental systems, the equilibration timescale is effectively infinite due to high degrees of polymerization and strong solvent selectivity [56, 61, 62]. It is well know that for a huge variety of copolymer-solvent systems that the hydrophobicity of the core is high enough to prevent exchange on practical timescales, leading to an inherent nonergodicity in the micellization process [56, 63, 64].

In this regime, the final micelles are often kinetically trapped metastable structures with sizes that are linked to the specific experimental conditions and procedures [56]. Johnson and coworkers demonstrated when the solvent quality is dropped rapidly, the resulting micelles were kinetically trapped, whereas gradual solvent quality changes allowed for exchange and fusion events to occur [65]. Similarly, Mattice and coworkers conducted Monte Carlo simulations where they found that increasing the segregation strength during micellization leads to the freezing of micelles in metastable states [66]. Wang and coworkers found similar results in their lattice Monte Carlo simulations, where the concentration of unimers rapidly decreased to a constant level while the average aggregation number slowly continued to increase until eventually plateauing [67]. They also found that high degrees of incompatibility between the core and solvent could lead to frozen micelles.

It was further demonstrated by Meli and Lodge in two seminal studies that copolymer micelles formed through decreasing the solvent quality (e.g., by evaporating a cosolvent) lead to small, kinetically trapped micelles [68, 69]. They compared these micelles to those formed through direct dissolution of a copolymer in a selective solvent, and found that the direct dissolution method lead to significantly larger micelles. Despite converging to two very different distributions, the micelles from both methods were stable to extended thermal annealing, further demonstrating the non-equilibrium nature of copolymer micelles under high segregation. The fact that the micelle size distributions were insensitive to extended thermal annealing at high

temperatures suggests that the equilibration barriers are exceedingly high, which poses significant challenges for connecting theoretical predictions of equilibrium micelles to experimental observations.

As it stands, work is still needed to fully understand the mechanisms of micelle equilibration under experimentally relevant conditions where equilibrium is elusive. This requires appealing to simulation techniques beyond conventional brute force molecular dynamics due to the exceedingly long timescales involved. Seeger and coworkers were the first to attempt to study chain exchange in copolymer micelles under strong seggregation through the use of umbrella sampling simulation [70, 71]. Their work is a great first step to understading the dynamics of copolymer micelles far away from equilibrium. This area is still ripe for further exploration, particularly in understanding the non-equilibrium pathways of micelle formation and how they connect to the final micelle structures.

1.3 Outline

In the following two chapters, we investigate two specific questions in the kinetics of diblock copolymer micelles. First, we study the mechanism of single-chain exchange using enhanced sampling molecular dynamics simulations as well as forward flux sampling coupled to single-chain Monte Carlo simulations. We outline the methods in detail and provide results for the free energy barriers, minimum free energy pathways, and kinetic pathways for chain exchange in different regimes. In the subsequent chapter, we use DPD simulations and SCFT calculations to investigate the pathway-dependent micelle formation discovered by Meli and Lodge [68]. We outline the simulation methods and develop a novel field theory based on DPD to connect observations from particle-based simulations to theoretical free energy calculations without the need to map between two different models. We present results on the morphological phase behavior and how it connects to the two different pathways observed experimentally.

References

(1) Zhulina, E. B.; Adam, M.; LaRue, I.; Sheiko, S. S.; Rubinstein, M. Diblock Copolymer Micelles in a Dilute Solution. *Macromolecules* **2005**, *38*, 5330–5351, DOI: 10.1021/ma048102n.

(2) Cotanda, P.; Lu, A.; Patterson, J. P.; Petzetakis, N.; O'Reilly, R. K. Functionalized Organocatalytic Nanoreactors: Hydrophobic Pockets for Acylation

Reactions in Water. *Macromolecules* **2012**, *45*, 2377–2384, DOI: 10.1021/ma2027462.

(3) Khullar, P.; Singh, V.; Mahal, A., et al. Block Copolymer Micelles as Nanoreactors for Self-Assembled Morphologies of Gold Nanoparticles. *The Journal of Physical Chemistry B* **2013**, *117*, 3028–3039, DOI: 10.1021/jp310507m.

(4) Boontongkong, Y.; Cohen, R. E. Cavitated Block Copolymer Micellar Thin Films: Lateral Arrays of Open Nanoreactors. *Macromolecules* **2002**, *35*, 3647–3652, DOI: 10.1021/ma0117357.

(5) Bakshi, M. S. Colloidal micelles of block copolymers as nanoreactors, templates for gold nanoparticles, and vehicles for biomedical applications. *Advances in Colloid and Interface Science* **2014**, *213*, 1–20, DOI: 10.1016/j.cis.2014.08.001.

(6) Kazunori, K.; Glenn S., K.; Masayuki, Y.; Teruo, O.; Yasuhisa, S. Block copolymer micelles as vehicles for drug delivery. *Journal of Controlled Release* **1993**, *24*, 119–132, DOI: 10.1016/0168-3659(93)90172-2.

(7) Luo, L.; Tam, J.; Maysinger, D.; Eisenberg, A. Cellular Internalization of Poly(ethylene oxide)-b-poly(ϵ-caprolactone) Diblock Copolymer Micelles. *Bioconjugate Chemistry* **2002**, *13*, 1259–1265, DOI: 10.1021/bc025524y.

(8) Kataoka, K.; Harada, A.; Nagasaki, Y. Block copolymer micelles for drug delivery: Design, characterization and biological significance. *Advanced Drug Delivery Reviews* **2012**, *64*, 37–48, DOI: 10.1016/j.addr.2012.09.013.

(9) Gaucher, G.; Dufresne, M.-H.; Sant, V. P., et al. Block copolymer micelles: preparation, characterization and application in drug delivery. *Journal of Controlled Release* **2005**, *109*, 169–188, DOI: 10.1016/j.jconrel.2005.09.034.

(10) Chiappetta, D. A.; Sosnik, A. Poly(ethylene oxide)–poly(propylene oxide) block copolymer micelles as drug delivery agents: Improved hydrosolubility, stability and bioavailability of drugs. *European Journal of Pharmaceutics and Biopharmaceutics* **2007**, *66*, 303–317, DOI: 10.1016/j.ejpb.2007.03.022.

(11) Förster, S.; Antonietti, M. Amphiphilic Block Copolymers in Structure-Controlled Nanomaterial Hybrids. *Advanced Materials* **1998**, *10*, 195–217, DOI: 10.1002/(SICI)1521-4095(199802)10:3<195::AID-ADMA195>3.0.CO;2-V.

(12) Lohmüller, T.; Aydin, D.; Schwieder, M., et al. Nanopatterning by block copolymer micelle nanolithography and bioinspired applications. *Biointerphases* **2011**, *6*, MR1–MR12, DOI: 10.1116/1.3536839.

(13) Müller, M.; Abetz, V. Nonequilibrium Processes in Polymer Membrane Formation: Theory and Experiment. *Chemical Reviews* **2021**, *121*, 14189–14231, DOI: 10.1021/acs.chemrev.1c00029.

(14) Blagojevic, N.; Das, S.; Xie, J., et al. Toward Predicting the Formation of Integral-Asymmetric, Isoporous Diblock Copolymer Membranes. *Advanced Materials (Deerfield Beach, Fla.)* **2024**, *36*, e2404560, DOI: 10.1002/adma.202404560.

(15) Hub, L.; Koll, J.; Buhr, K.; Radjabian, M.; Abetz, V. pH-responsive size- and charge-selective block copolymer membrane for the separation of small proteins. *Journal of Membrane Science* **2024**, *708*, 123021, DOI: 10.1016/j.memsci.2024.123021.

(16) Cooper, A. J.; Grzetic, D. J.; Delaney, K. T.; Fredrickson, G. H. Investigating microstructure evolution in block copolymer membranes. *The Journal of Chemical Physics* **2024**, *160*, 074903, DOI: 10.1063/5.0188196.

(17) Zhang, Z.; Rahman, M. M.; Bajer, B.; Scharnagl, N.; Abetz, V. Highly selective isoporous block copolymer membranes with tunable polyelectrolyte brushes in soft nanochannels. *Journal of Membrane Science* **2022**, *646*, 120266, DOI: 10.1016/j.memsci.2022.120266.

(18) Hamta, A.; Ashtiani, F. Z.; Karimi, M.; Moayedfard, S. Asymmetric block copolymer membrane fabrication mechanism through self-assembly and non-solvent induced phase separation (SNIPS) process. *Scientific Reports* **2022**, *12*, 771, DOI: 10.1038/s41598-021-04759-7.

(19) Cabral, H.; Miyata, K.; Osada, K.; Kataoka, K. Block Copolymer Micelles in Nanomedicine Applications. *Chemical Reviews* **2018**, *118*, 6844–6892, DOI: 10.1021/acs.chemrev.8b00199.

(20) Boucher-Jacobs, C.; Rabnawaz, M.; Katz, J. S.; Even, R.; Guironnet, D. Encapsulation of catalyst in block copolymer micelles for the polymerization of ethylene in aqueous medium. *Nature Communications* **2018**, *9*, 841, DOI: 10.1038/s41467-018-03253-5.

(21) Piradashvili, K.; Alexandrino, E. M.; Wurm, F. R.; Landfester, K. Reactions and Polymerizations at the Liquid–Liquid Interface. *Chemical Reviews* **2016**, *116*, 2141–2169, DOI: 10.1021/acs.chemrev.5b00567.

(22) Zhulina, E. B.; Borisov, O. V. Theory of Block Polymer Micelles: Recent Advances and Current Challenges. *Macromolecules* **2012**, *45*, 4429–4440, DOI: 10.1021/ma300195n.

(23) Halperin, A. Polymeric micelles: a star model. *Macromolecules* **1987**, *20*, 2943–2946, DOI: 10.1021/ma00177a051.

(24) Izzo, D.; Marques, C. M. Formation of micelles of diblock and triblock copolymers in a selective solvent. *Macromolecules* **1993**, *26*, 7189–7194, DOI: 10.1021/ma00078a012.

(25) Izzo, D.; Marques, C. M. Selectively Swollen Phases of Diblock Copolymers. *Macromolecules* **1997**, *30*, 6544–6549, DOI: 10.1021/ma970264e.

(26) Fredrickson, G. H., *The equilibrium theory of inhomogeneous polymers*; International series of monographs on physics 134; Clarendon Press ; Oxford University Press: Oxford : New York, 2006; 437 pp.

(27) Matsen, M. W. Self-Consistent Field Theory for Melts of Low-Molecular-Weight Diblock Copolymer. *Macromolecules* **2012**, *45*, 8502–8509, DOI: 10.1021/ma301788q.

(28) Matsen, M. W. The standard Gaussian model for block copolymer melts. *Journal of Physics: Condensed Matter* **2001**, *14*, R21, DOI: 10.1088/0953-8984/14/2/201.

(29) Greenall, M. J.; Buzza, D. M. A.; McLeish, T. C. B. Micelle Formation in Block Copolymer/Homopolymer Blends: Comparison of Self-Consistent Field Theory with Experiment and Scaling Theory. *Macromolecules* **2009**, *42*, 5873–5880, DOI: 10.1021/ma9000594.

(30) Zhou, J.; Shi, A.-C. Critical Micelle Concentration of Micelles with Different Geometries in Diblock Copolymer/Homopolymer Blends. *Macromolecular Theory and Simulations* **2011**, *20*, 690–699, DOI: 10.1002/mats.201100042.

(31) Cavallo, A.; Müller, M.; Binder, K. Formation of Micelles in Homopolymer-Copolymer Mixtures: Quantitative Comparison between Simulations of Long Chains and Self-Consistent Field Calculations. *Macromolecules* **2006**, *39*, 9539–9550, DOI: 10.1021/ma061493g.

(32) Wang, J.; Müller, M.; Wang, Z.-G. Nucleation in A/B/AB blends: Interplay between microphase assembly and macrophase separation. *The Journal of Chemical Physics* **2009**, *130*, 154902, DOI: 10.1063/1.3105340.

(33) Thiagarajan, R.; Morse, D. C. Micellization kinetics of diblock copolymers in a homopolymer matrix: a self-consistent field study. *Journal of Physics: Condensed Matter* **2011**, *23*, 284109, DOI: 10.1088/0953-8984/23/28/284109.

(34) Yuan, X. F.; Masters, A. J.; Price, C. Self-consistent field theory of micelle formation by block copolymers. *Macromolecules* **1992**, *25*, 6876–6884, DOI: 10.1021/ma00051a024.

(35) Leermakers, F. A. M.; Wijmans, C. M.; Fleer, G. J. On the Structure of Polymeric Micelles: Self-Consistent-Field Theory and Universal Properties for Volume Fraction Profiles. *Macromolecules* **1995**, *28*, 3434–3443, DOI: 10.1021/ma00113a050.

(36) Leibler, L.; Orland, H.; Wheeler, J. C. Theory of critical micelle concentration for solutions of block copolymers. *The Journal of Chemical Physics* **1983**, *79*, 3550–3557, DOI: 10.1063/1.446209.

(37) Noolandi, J.; Hong, K. M. Theory of block copolymer micelles in solution, ACS Publications https://pubs.acs.org/doi/abs/10.1021/ma00243a007 (accessed 10/22/2025).

(38) Wang, J.; Guo, K.; An, L.; Müller, M.; Wang, Z.-G. Micelles of Coil-Comb Block Copolymers in Selective Solvents: Competition of Length Scales. *Macromolecules* **2010**, *43*, 2037–2041, DOI: 10.1021/ma901977h.

(39) Duan, C.; Wang, M.; Ghobadi, A.; Eike, D. M.; Wang, R. Quantifying the Critical Micelle Concentration of Nonionic and Ionic Surfactants by Self-Consistent Field Theory, 2024, DOI: 10.48550/arXiv.2412.03549.

(40) Ting, C. L.; Wang, Z.-G. Interactions of a Charged Nanoparticle with a Lipid Membrane: Implications for Gene Delivery. *Biophysical Journal* **2011**, *100*, 1288–1297, DOI: 10.1016/j.bpj.2010.11.042.

(41) Ting, C. L.; Appelö, D.; Wang, Z.-G. Minimum Energy Path to Membrane Pore Formation and Rupture. *Physical Review Letters* **2011**, *106*, 168101, DOI: 10.1103/PhysRevLett.106.168101.

(42) Ting, C. L.; Wang, Z.-G. Nucleated Pathways Involving Nanoparticles and Lipid Membranes. *Biophysical Journal* **2012**, *102*, 297a, DOI: 10.1016/j.bpj.2011.11.1646.

(43) Kik, R. A. Molecular modeling of proteinlike inclusions in lipid bilayers: Lipid-mediated interactions. *Physical Review E* **2010**, *81*, DOI: 10.1103/PhysRevE.81.021915.

(44) Leermakers, F. A. M.; Scheutjens, J. M. H. M. Statistical thermodynamics of association colloids. I. Lipid bilayer membranes. *The Journal of Chemical Physics* **1988**, *89*, 3264–3274, DOI: 10.1063/1.454931.

(45) Lauw, Y.; Leermakers, F. A. M.; Stuart, M. A. C.; Borisov, O. V.; Zhulina, E. B. Coexistence of Crew-Cut and Starlike Spherical Micelles Composed of Copolymers with an Annealed Polyelectrolyte Block. *Macromolecules* **2006**, *39*, 3628–3641, DOI: 0.1021/ma060163t.

(46) Borisov, O. V.; Zhulina, E. B.; Leermakers, F. A. M.; Müller, A. H. E. In *Self Organized Nanostructures of Amphiphilic Block Copolymers I*, Müller, A. H. E., Borisov, O., Eds.; Springer: Berlin, Heidelberg, 2011, pp 57–129.

(47) Dormidontova, E. E. Micellization Kinetics in Block Copolymer Solutions: Scaling Model. *Macromolecules* **1999**, *32*, 7630–7644, DOI: 10.1021/ma9809029.

(48) Duan, C.; Wang, R. A Unified Description of Salt Effects on the Liquid–Liquid Phase Separation of Proteins. *ACS Central Science* **2024**, *10*, 460–468, DOI: 10.1021/acscentsci.3c01372.

(49) Duan, C.; Wang, R. Electrostatics-Induced Nucleated Conformational Transition of Protein Aggregation. *Physical Review Letters* **2023**, *130*, 158401, DOI: 10.1103/PhysRevLett.130.158401.

(50) Nyrkova, I. A.; Semenov, A. N. On the Theory of Micellization Kinetics. *Macromolecular Theory and Simulations* **2005**, *14*, 569–585, DOI: 10.1002/mats.200500010.

(51) Aniansson, E. A. G.; Wall, S. N. Kinetics of step-wise micelle association. *The Journal of Physical Chemistry* **1974**, *78*, 1024–1030, DOI: 10.1021/j100603a016.

(52) Aniansson, E. A. G.; Wall, S. N. Kinetics of step-wise micelle association. Correction and improvement. *The Journal of Physical Chemistry* **1975**, *79*, 857–858, DOI: 10.1021/j100575a019.

(53) Aniansson, E. A. G.; Wall, S. N.; Almgren, M., et al. Theory of the kinetics of micellar equilibria and quantitative interpretation of chemical relaxation studies of micellar solutions of ionic surfactants. *The Journal of Physical Chemistry* **1976**, *80*, 905–922, DOI: 10.1021/j100550a001.

(54) *Dynamics of Surfactant Self-Assemblies: Micelles, Microemulsions, Vesicles and Lyotropic Phases*; Zana, R., Ed.; CRC Press: Boca Raton, 2005, 536 pp.

(55) Goldmints, I.; Holzwarth, J. F.; Smith, K. A.; Hatton, T. A. Micellar Dynamics in Aqueous Solutions of PEO-PPO-PEO Block Copolymers. *Langmuir* **1997**, *13*, 6130–6134, DOI: 10.1021/la970534m.

(56) Lodge, T. P.; Seitzinger, C. L.; Seeger, S. C., et al. Dynamics and Equilibration Mechanisms in Block Copolymer Particles. *ACS Polymers Au* **2022**, *2*, 397–416, DOI: 10.1021/acspolymersau.2c00033.

(57) Halperin, A.; Alexander, S. Polymeric micelles: their relaxation kinetics. *Macromolecules* **1989**, *22*, 2403–2412, DOI: 10.1021/ma00195a069.

(58) Rao, J.; Zhang, J.; Xu, J.; Liu, S. Cononsolvency-induced micellization kinetics of pyrene end-labeled diblock copolymer of N-isopropylacrylamide and oligo(ethylene glycol) methyl ether methacrylate studied by stopped-flow light-scattering and fluorescence. *Journal of Colloid and Interface Science* **2008**, *328*, 196–202, DOI: 10.1016/j.jcis.2008.09.001.

(59) Zhang, J.; Xu, J.; Liu, S. Chain-Length Dependence of Diblock Copolymer Micellization Kinetics Studied by Stopped-Flow pH-Jump. *The Journal of Physical Chemistry B* **2008**, *112*, 11284–11291, DOI: 10.1021/jp803700n.

(60) Li, Z.; Dormidontova, E. E. Kinetics of Diblock Copolymer Micellization by Dissipative Particle Dynamics. *Macromolecules* **2010**, *43*, 3521–3531, DOI: 10.1021/ma902860j.

(61) Creutz, S.; van Stam, J.; Antoun, S.; De Schryver, F. C.; Jérôme, R. Exchange of Polymer Molecules between Block Copolymer Micelles Studied by Emission Spectroscopy. A Method for the Quantification of Unimer Exchange Rates. *Macromolecules* **1997**, *30*, 4078–4083, DOI: 10.1021/ma961922i.

(62) Creutz, S.; van Stam, J.; De Schryver, F. C.; Jérôme, R. Dynamics of Poly((dimethylamino)alkyl methacrylate-block-sodium methacrylate) Micelles. Influence of Hydrophobicity and Molecular Architecture on the Exchange Rate of Copolymer Molecules. *Macromolecules* **1998**, *31*, 681–689, DOI: 10.1021/ma970987y.

(63) Jain, S.; Bates, F. S. Consequences of Nonergodicity in Aqueous Binary PEO-PB Micellar Dispersions. *Macromolecules* **2004**, *37*, 1511–1523, DOI: 10.1021/ma035467j.

(64) Patterson, J. P.; Robin, M. P.; Chassenieux, C.; Colombani, O.; O'Reilly, R. K. The analysis of solution self-assembled polymeric nanomaterials. *Chemical Society Reviews* **2014**, *43*, 2412–2425, DOI: 10.1039/C3CS60454C.

(65) Johnson, B. K. Mechanism for Rapid Self-Assembly of Block Copolymer Nanoparticles. *Physical Review Letters* **2003**, *91*, DOI: 10.1103/PhysRevLett.91.118302.

(66) Rodrigues, K.; Mattice, W. L. Simulation of the steric stabilization of polymer colloids by diblock copolymers. *The Journal of Chemical Physics* **1991**, *94*, 761–766, DOI: 10.1063/1.460344.

(67) Wang, Y.; Mattice, W. L.; Napper, D. H. Simulation of the formation of micelles by diblock copolymers under weak segregation, ACS Publications https://pubs.acs.org/doi/abs/10.1021/la00025a017 (accessed 10/22/2025).

(68) Meli, L.; Santiago, J. M.; Lodge, T. P. Path-Dependent Morphology and Relaxation Kinetics of Highly Amphiphilic Diblock Copolymer Micelles in Ionic Liquids. *Macromolecules* **2010**, *43*, 2018–2027, DOI: 10.1021/ma902366c.

(69) Meli, L.; Lodge, T. P. Equilibrium vs Metastability: High-Temperature Annealing of Spherical Block Copolymer Micelles in an Ionic Liquid. *Macromolecules* **2009**, *42*, 580–583, DOI: 10.1021/ma802020a.

(70) Seeger, S. C.; Dorfman, K. D.; Lodge, T. P. Free Energy Trajectory for Escape of a Single Chain from a Diblock Copolymer Micelle. *ACS Macro Letters* **2021**, *10*, 1570–1575, DOI: 10.1021/acsmacrolett.1c00508.

(71) Seeger, S. C.; Lodge, T. P.; Dorfman, K. D. Mechanism of Escape of a Single Chain from a Diblock Copolymer Micelle. *Macromolecules* **2022**, *55*, 10220–10228, DOI: 10.1021/acs.macromol.2c01742.

Chapter 2

MECHANISMS OF CHAIN EXCHANGE IN DIBLOCK COPOLYMER MICELLES

In this chapter we investigate the mechanism of chain exchange in diblock copolymer micelles using two distinct yet complementary simulation techniques. First, the spectral adaptive biasing force enhanced sampling method is combined with coarse-grained molecular dynamics to compute a two-dimensional free energy surface for the chain expulsion process in the strong segregation regime. To facilitate chain expulsion, a distance-based collective variable is biased, and the end-to-end distance of the core block is additionally biased to ensure sufficient sampling of chain conformations. The resulting free energy surface reveals a bimodal distribution of chain conformations along the effective reaction coordinate. The minimum free energy pathway, computed via the string method, qualitatively aligns with the Halperin–Alexander budding-like mechanism. The free energy barrier along this pathway is calculated for core block lengths ranging from $N_{\mathrm{core}} = 4$–100, and the barrier is shown to scale as $\beta\Delta F_{\mathrm{barr}} \sim N_{\mathrm{core}}^{2/3}$, consistent with the Halperin–Alexander prediction for a globular transition state. Notably, the free energy surface also reveals a nearly degenerate alternative pathway in which the chain escapes by extending out "bead-by-bead," in agreement with previous simulations. We also study the case of a dense copolymer melt, where the core-block shrinks but does not collapse into a dry compact globule in the opposite phase. To examine the kinetic pathway, a simplified model is introduced in which a single chain escapes from a planar interface within a mean-field background. Using Monte Carlo moves to drive forward flux sampling simulations, the unbiased exchange rate and corresponding free energy barrier are computed. These calculations yield a linear scaling of the barrier, $\beta\Delta F_{\mathrm{barr}} \sim N_{\mathrm{core}}$, in agreement with experimental observations and prior simulations. Moreover, analysis of successful escape trajectories highlights an extended chain conformation at the transition state, providing further evidence that experimental conditions favor the hyperstretching escape mechanism over the Halperin–Alexander mechanism.

This chapter includes content from our previously published article:

Varner, S.; Müller, M.; Gallegos, A., et al. Mechanisms of Chain Exchange in Diblock Copolymer Micelles, 2025, DOI: 10.48550/arXiv.2509.06528

I am very thankful for an immense number of discussions with Professor Marcus Müller, who taught me forward flux sampling and provided me a base for single-chain Monte Carlo simulations. I also would like to thank Professor Kevin Dorfman and Professor Lodge for sharing their challenging and exciting problems with me and mentoring me through them as well. Without these amazing collaborations, my PhD experience would have been very different and I would not have been able to learn the wide variety of subjects and techniques that I had the fortune to study.

2.1 Introduction

The importance of exchange in micelle equilibration has motivated extensive theoretical and experimental studies of its mechanism and free energy barrier. The earliest and most widely cited theory was derived by Halperin and Alexander in 1989, who proposed a free energy barrier for single-chain exchange [2, 3]. They also considered fusion and fragmentation but concluded that these processes are much slower near equilibrium [4]. Exchange is rate-limited by the barrier for a chain to escape from the soluble micelle core into the less favorable solvent [5]. For BCPs with much longer hydrophobic blocks than conventional nonionic surfactants, this barrier can reach hundreds of k_BT, effectively prohibiting equilibration on experimental timescales [6, 7]. Halperin and Alexander postulated that the chain escapes from the micelle with the core block in a collapsed state to minimize unfavorable contacts with the solvent and corona. Their mechanism applied with Kramers' rate theory led to an escape time of $\tau_{\mathrm{esc}} \sim \exp(\gamma\rho^{-2/3}N_{\mathrm{core}}^{2/3}/k_BT)$, where γ is the interfacial tension, ρ is the segment density, and N_{core} is the degree of polymerization of the core-forming block. The scaling of $N_{\mathrm{core}}^{2/3}$ follows directly from their assumption of a compact spherical globule. The prefactor to the exponential includes the dependence on the corona-forming block, scaling as $N_{\mathrm{corona}}^{9/5}$ for star-like micelles and $N_{\mathrm{corona}}^{7/3}$ for crew-cut.

In the limit of melts with a large invariant degree of polymerization, $\bar{N}$, however, a single core block embedded in a matrix does not collapse; its relative size change only scales as $\Delta R/R \sim \chi N/\sqrt{\bar{N}}$ [8]. For a fully solvated core block, the associated free-energy barrier is given by $\Delta F_{\mathrm{melt}}/k_BT \sim \chi N f_{\mathrm{core}}$. In contrast, the Halperin–Alexander scenario [2] predicts $\Delta F_{\mathrm{HA}} \sim \gamma(N_{\mathrm{core}}/\rho)^{2/3} \sim k_BT\bar{N}^{1/6}f_{\mathrm{core}}^{2/3}\sqrt{\chi N}$, where ρ is the segment density, and we have used the strong-segregation estimate for the interfacial tension γ. [9] Consequently, for long-chain melts, the ratio of the two barrier estimates is $\Delta F_{\mathrm{melt}}/\Delta F_{\mathrm{HA}} \sim \sqrt{\chi N}/\bar{N}^{1/6} < 1$, implying that the free-energy barrier scales linearly with N_{core} [10].

For decades, fluorescence and non-radiative energy transfer experiments were analyzed according to the Halperin–Alexander theory [5–7, 11–16], until the development of time-resolved small-angle neutron scattering (TR-SANS) enabled more direct measurements of the exchange rate, and therefore the exchange free energy barrier [17, 18]. TR-SANS elucidates the exchange rate by tracking the decay of scattering intensity as chains hop between micelles in a solution containing two distinct micelle populations (normal versus perdeuterated cores). By selecting a solvent with a scattering length density intermediate between the two core types, the exchange rate is directly related to the decay of the scattering intensity, $R(t)$, as the chains mix over time. Measurements at several temperatures can be combined into a master curve using time–temperature superposition, extending the dynamic range of TR-SANS over 12 decades [19]. Exchange has been shown to follow rate-limited kinetics with an activation barrier, which should yield a single-exponential decay of scattering intensity with time [2, 20, 21]. TR-SANS measurements, however, consistently revealed a broad relaxation much closer to a logarithmic decay. The explanation for this anomalous behavior is both simple and elegant: because the exchange rate is essentially the escape rate, which depends exponentially on the core-block length, a broad relaxation arises naturally from the polydispersity of the core block. Lund and co-workers were the first to address the role of polydispersity [22–24], and Choi and co-workers subsequently connected it directly to the logarithmic decay [25]. Zinn et al. later confirmed this interpretation by demonstrating that monodisperse polymers exhibit single-exponential relaxation [26]. Lu et al. further showed that a logarithmic decay is recovered in solutions with a bimodal chain length distribution [27].

Analyzing exchange kinetics from the decay of scattering intensity requires both a functional form of the escape rate constant, $k_{\mathrm{esc}}(N_{\mathrm{core}})$, and the chain length distribution, $f(N_{\mathrm{core}})$. The dynamic scattering intensity is then expressed as a convolution,

$$R(t) = \int_1^\infty dN_{\mathrm{core}} f(N_{\mathrm{core}}) \exp\left[-k_{\mathrm{esc}}(N_{\mathrm{core}})t\right] \tag{2.1}$$

The functional form of the rate constant proposed by Halperin and Alexander can be generalized to include two free parameters, α and β:[23, 25, 28]

$$k_{\mathrm{esc}} \sim \frac{1}{\tau_0} \exp\left(-\alpha \chi N_{\mathrm{core}}^{\beta}\right) \tag{2.2}$$

where α and β depend on the chain conformation and escape mechanism. The exponent β ranges from $2/3$ for the Halperin–Alexander collapsed mechanism to

1 for a core fully exposed to solvent. The prefactor τ_0 sets the timescale and is taken to be the Rouse time, $\tau_0 = \tau_R = \xi N_{\text{core}}^2 l_B^2/(6\pi^2 k_B T)$ [25, 28]. The parameter χ is the monomer-level Flory–Huggins interaction parameter, replacing the macroscopic interfacial tension. The chain length distribution originally used by Lund and coworkers was a Poisson distribution, characteristic of an ideal living anionic polymerization [23]. Choi et al. later opted for the more flexible Schulz–Zimm distribution that describes imperfect polymerization and can match any experimentally obtained chain length distribution [25]. With this framework, several TR-SANS studies on different polymers and solvents have been used to extract the unimer exchange rate and its dependence on polymer and solvent properties [25, 26, 28, 29]. In all cases, the free energy barrier scaled linearly with core block length, in direct disagreement with the Halperin–Alexander prediction of $N_{\text{core}}^{2/3}$ but consistent with theoretical predictions for self-diffusion of BCPs in melts [30–32].

This discrepancy between the Halperin–Alexander theory and experimental observations prompted extensive discussion and several simulation studies aimed at verifying the linear scaling and elucidating the true escape mechanism. Some studies attempted to replicate the experimental procedure *in silico* by constructing micellar solutions, artificially labeling cores, and monitoring exchange over the course of long unbiased simulations [33–37]. While these simulations supported linear scaling with N_{core}, they did not provide a detailed mechanism for chain escape under experimentally relevant conditions. Namely, *in silico* exchange experiments are required to operate at low enough segregation strength (χ) where a significant number of exchange events can feasibly be observed within the simulation timescale. This is in contrast to experiments where the segregation strength is generally high enough to halt exchange at room temperature on timescales of seconds to hours. In addition, these simulations were limited to core blocks containing only a very small number of coarse-grained beads where the Halperin–Alexander theory would not apply due to the lack of a coil–globule transition.

To resolve these issues, Seeger and coworkers used a different approach relying on enhanced sampling molecular dynamics [38, 39]. Specifically, they utilized umbrella sampling with the weighted histogram analysis method (WHAM) to compute the free energy profile, or potential of mean force (PMF), of a single chain to escape from an isolated micelle. A similar approach has been used to study the escape free energy of short surfactant molecules [40, 41]. With BCPs, this approach allowed them to resolve large free energy barriers for high χ values and for larger N_{core}

within a feasible simulation time. They computed a linear scaling of the free energy barrier with N_{core} and explained its origin through a simple scaling theory where they assumed the chain escapes "bead-by-bead". Their calculations shed light on a hyperstretching (or "bead-by-bead") escape mechanism as an explanation for the failure of the Halperin–Alexander mechanism to match experimental observations. The term hyperstretching refers to the chain extending far beyond its ideal end-to-end distance. However, these simulations were limited by the use of a single collective variable and still relatively short chain lengths, with N_{core} ranging from 4 to 12. Due to the use of a single distance collective variable, they observe a discontinuous jump in the polymer conformation along their effective reaction coordinate. This indicates that there is an additional barrier in the polymer conformation that can lead to incomplete sampling for each value of the chosen distance CV, especially near the transition state [42].

In this work, we address some of the challenges encountered in previous simulation studies by taking two different but complementary approaches. In doing so, we provide a complete picture of the exchange mechanism in the high segregation regime where exchange is rare, both in the case of core collapse and only partial shrinking. First, we utilize coarse-grained molecular dynamics (CGMD) simulations with force-bias enhanced sampling to compute the 2-dimensional free energy surface (FES) of the chain exchange process, where one dimension corresponds to the distance of the chain from the micelle, and the other to the degree of chain extension. Through the use of two collective variables, we can achieve more complete sampling of the chain conformation during the escape process. In agreement with the previous work by Seeger and coworkers, we identify distinct collapsed and extended conformations. As expected, we observe a barrier between the collapsed and extended conformation at the transition state, which highlights the need for external biasing in two collective variables over just one. With the 2d FES, we compute the minimum free energy pathway (MFEP) using the string method and show that it corresponds to the Halperin–Alexander mechanism. We also identify a low free energy region of the FES corresponding to a possible extended escape mechanism that may be kinetically favored under some circumstances in the presence of fluctuations. It is still unclear if there is a regime where the chain is collapsed in the solution and follows a hyperstretching mechanism that would lead to a linear scaling as observed in many experiments.

Additionally, we study the escape mechanism in the high density (polymer melt)

limit where the core block does not fully collapse, leaving most or all of the core beads exposed to the unfavorable surroundings. In this regime we employ forward flux sampling (FFS) on a simplified single-chain model that mimics a polymer immersed in a dense melt. In our case, specifically a phase separated copolymer melt. FFS is a transition path sampling technique that introduces no external force biases, and therefore preserves dynamics [43–45]. We compute both the rate of chain escape and the free energy barrier as a function of core block length, and show that the free energy scales linearly with N_{core}. Additionally, we analyze different ensembles of chain properties during the escape process by extracting full escape trajectories. These ensembles reveal that the chains prefer to escape by first extending ("bead-by-bead") into the solution, and then shrinking.

In the following sections, we start by describing the MD simulation model, enhanced sampling methods, and analysis of the free energy surface for escape within the Halperin–Alexander regime. We then discuss the single-chain model, forward flux sampling, and the escape mechanism within the melt regime.

2.2 Enhanced Sampling Molecular Dynamics

Simulation Model

We model diblock copolymers in an explicit solvent using highly coarse-grained molecular dynamics simulations. For simplicity, we assume that all particles have the same effective diameter (σ). In line with previous works, we borrow the conservative force from the DPD potential to describe the non-bonded repulsion between beads [33, 34, 38, 39, 46, 47],

$$\beta U_{nb}(r_{ij}) = \frac{1}{2}\beta\epsilon_{ij}\left(1 - \frac{r_{ij}}{\sigma}\right)^2, \qquad r_{ij} < \sigma \tag{2.3}$$

where $\beta = 1/k_BT$, and ϵ_{ij} is the repulsion strength between particles i and j. We choose the base repulsion between all species to be $\epsilon = 25\,k_BT$. Incompatible pairs of species such as the core-forming polymer block and monomeric solvent have an $\epsilon_{ij} = 48\,k_BT$. Polymeric beads are bonded together using a harmonic spring potential given by,

$$\beta U_b(r_{ij}) = \frac{1}{2}\kappa(r_{ij} - \sigma)^2 \tag{2.4}$$

where κ is the spring constant, and we use σ as the bond length. We use a value of $\kappa = 100\,k_BT/\sigma^2$ which is in line with previous studies of block-copolymer micelles [38, 39]. In the system there are n polymers each having N monomers, which are divided into two blocks of length N_A and $N_B = N - N_A$. A is the

core-forming block, and B is the corona-forming block. The system also contains N_S monomeric solvent molecules, for a total of $nN + N_S$ monomers in the system. In line with previous studies, we utilize a reduced density of $\rho = 3.0\sigma^{-3}$. The maximum chain-length that we study is $N = 124$, which has an ideal end-to-end distance of $R_{\mathrm{e2e}} = \sigma\sqrt{N-1} \approx 11.1\sigma$. We utilize a box size of $L = 55\sigma$ which corresponds to $L \approx 5R_{\mathrm{e2e}}$ to ensure that there are no finite size effects. For the smallest polymer we study, $N_A = 4$ yielding an invariant degree of polymerization of $\sqrt{\bar{N}} = \rho\sigma^3\sqrt{N_A} \approx 6$. The largest polymer we study has $N_A = 100$, yielding $\sqrt{\bar{N}} \approx 30$.

In all simulations, we use $n = 36$ chains to form the isolated micelle such that our results are directly comparable to previous works [38, 39]. Note that the equilibrium micelle size distribution is very wide, and thus there are a large number of reasonable choices for n. One has to ensure that n is not so far above the optimal aggregation number such that the micelle undergoes spontaneous fission during the course of a long simulation. The choice of a relatively small n results in a diffuse corona to avoid any enhancement of the exchange rate due to corona crowding across all values of N_A used [48]. Also note that in the strongly segregated regime, the exchange rate is exceedingly low, such that we do not observe any exchange events that are not a direct result of our biasing methods described below.

We run our simulations in OpenMM[49] by making use of the open-source MD-Craft[50] python package that contains helper functions and additional custom non-bonded potentials. We use the *middle* Langevin integrator with a time-step of $\Delta t = 0.01\tau$ and a friction coefficient of $\eta = 1/\tau$, where $\tau = \sqrt{m\sigma^2/(k_BT)}$. See Figure 2.1 below for a visual example of a stable micelle.

Enhanced Sampling

In order to compute the free energy barrier for chain expulsion, we employ enhanced sampling to bias collective variables (CVs) between low and high free energy regions of the phase space. To define our CVs, we separate the type A atoms into two groups: (1) $N_A(n-1)$ atoms forming the core of the micelle, which includes all chains minus one, and (2) the N_A atoms of a selected chain which will undergo expulsion. We define the coordinates of the atoms in group 1 as $\mathbf{R}$, and the atoms of group 2 as $\mathbf{r}$. We define Basin1 as the stable basin in which the selected chain is within the micelle, and Basin2 as the metastable plateau region in which the selected chain has escaped and no longer *sees* the micelle. We define two different distance-based

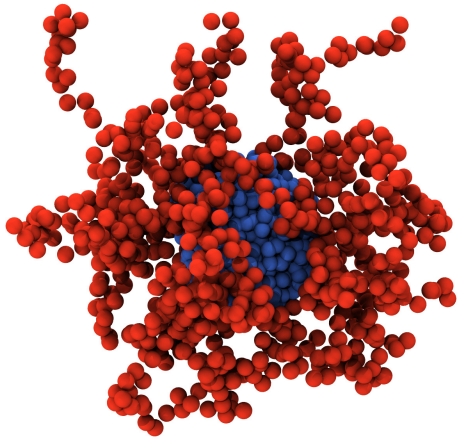

Figure 2.1: Example of a stable micelle with $n = 36$, $N_A = 21$, $N_B = 24$, $\epsilon = \epsilon_{ii} = \epsilon_{BS} = 25\, k_B T$, and $\Delta\epsilon = \epsilon_{AS} - \epsilon = \epsilon_{AB} - \epsilon = 23\, k_B T$. Solvent particles are omitted for visual clarity.

CVs to track the progress of the system between Basin1 and Basin2. The first is the distance between the center of mass of the micelle (excluding the selected chain) and the junction point of the selected chain, where the junction refers to the point of connection between the A and B blocks.

$$\text{CV1} = R_{\text{cm-jp}} = ||\mathbf{R}_{\text{cm}} - \mathbf{r}_{\text{jp}}||_2 \tag{2.5}$$

The second is the distance between the center of mass of the micelle (excluding the selected chain) and the center of mass of the core block of the selected chain.

$$\text{CV1}' = R_{\text{cm-cm}} = ||\mathbf{R}_{\text{cm}} - \mathbf{r}_{\text{cm}}||_2 \tag{2.6}$$

Previous studies have utilized $R_{\text{cm-jp}}$ to conduct umbrella sampling simulations [38, 39], where free energy profiles are constructed using the weighted histogram analysis method (WHAM). However, we expect that a single CV is not sufficient to obtain an accurate free energy estimate due to the possible presence of barriers in other collective variables. The presence of barriers in orthogonal CVs causes insufficient sampling in configurational space [42]. Namely, in this case, the polymer conformation can range from fully extended to fully collapsed, however, this full spectrum cannot be readily explored at each value of $R_{\text{cm-jp}}$ due to significant barriers in changing the polymer conformation. To remedy this, we propose running simulations with two collective variables simultaneously, which has become much more feasible in recent years due to advancements in enhanced sampling methods and accessibility of high performance graphical processing units (GPUs). We

define a third collective variable, r_{e2e} to be used in conjunction with either of the two distance based CVs defined above. r_{e2e} is the end-to-end distance of the core block (A block) of the selected chain.

$$\text{CV2} = r_{\text{e2e}} = ||\mathbf{r}_{N_A} - \mathbf{r}_1||_2 \tag{2.7}$$

This collective variable allows us to bias the conformation of the escaping chain to sample the full range from fully collapsed to fully extended. To clarify, we denote the overall end-to-end distance of the chain as R_{e2e} and the end-to-end distance of the core block only as r_{e2e}.

We compute the 2d FES for the combinations $\{R_{\text{cm-jp}}, r_{\text{e2e}}\}$ and $\{R_{\text{cm-cm}}, r_{\text{e2e}}\}$ for various different values of N_A and $\Delta\epsilon$ to elucidate the preferred escape mechanism and the scaling relationships of the free energy barrier (exchange rate). We study both combinations of CVs to ensure that the results are independent of the choice of CV. We utilize the recently developed Spectral Adaptive Biasing Force (SABF) method available in the PySAGES enhanced sampling package [51, 52]. SABF is an improved version of the ABF method, that has improved efficiency and stability. ABF-type methods also have an advantage over metadynamics-type methods for our particular system because our CVs all have hard boundaries at 0, which poses a problem for metadynamics but not for ABF-type methods [53].

Results and Discussion

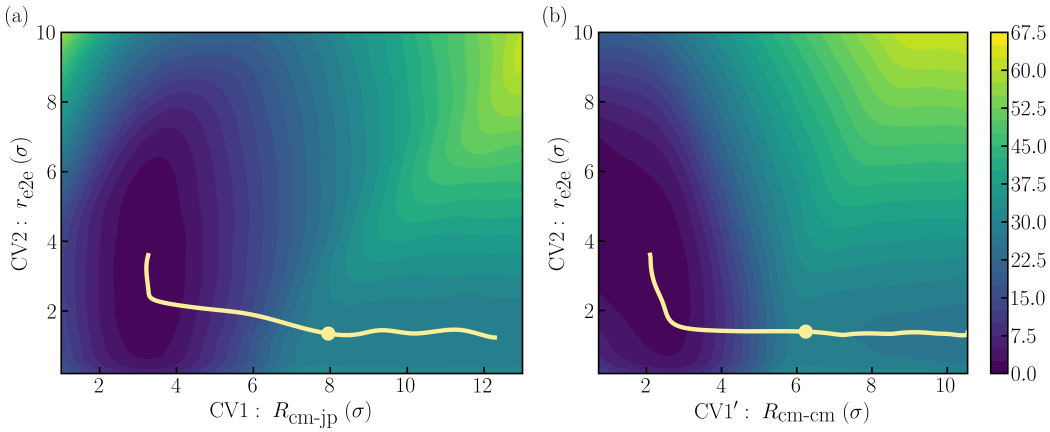

Figure 2.2: 2-dimensional FES for CV pairs $R_{\text{cm-jp}}$,r_{e2e} (a) and $R_{\text{cm-cm}}$,r_{e2e} (b) with $N_A = 15$, $N_B = 24$, $\beta\Delta\epsilon = 23$. Each surface is shifted such that the minimum free energy is 0. The red lines trace the MFEPs as computed by the string method, with the yellow circles indicating the transition states.

First, we compute the 2-dimensional FES for both pairs of CVs, $\{R_{\text{cm-jp}}$,$r_{\text{e2e}}\}$ and $\{R_{\text{cm-cm}}$,$r_{\text{e2e}}\}$ for the particular case of $N_A = 15, N_B = 24$ and $\beta\Delta\epsilon = 23$. Both

surfaces are presented in Figure 2.2. In the following discussion, we refer to the surfaces in Figures 2.2a and 2.2b as FES1 and FES2, respectively. Both FES1 and FES2 have a significant free energy basin at low values of all CVs, which corresponds to the selected chain being located within the micelle. Note that when the chain is within the micelle, r_{e2e} can take on a wide range of values at low free energy cost. Large fluctuations in r_{e2e} are expected since the micelle core presents a *theta* solvent environment. The average value of the core block end-to-end distance in the basin is $\langle r_{\text{e2e}} \rangle = 3.3$ which is reasonably close to the ideal value of $\sqrt{N_A - 1} = 3.7$ for a freely-jointed chain. FES1 displays a near-vertical basin, indicating that the chain may extend and collapse while the junction point is consistently localized to the surface of the micelle. From FES1, we compute the average value of the relative position of the junction point in the basin to be $\langle R_{\text{cm-jp}} \rangle \approx 3.4$. This agrees with the radius of the micelle, as shown in Figure S1 in the ESI[†].

FES1 (FES2) is characterized by the presence of a large basin for low $R_{\text{cm-jp}}$ ($R_{\text{cm-cm}}$) and a plateau for high values of $R_{\text{cm-jp}}$ ($R_{\text{cm-cm}}$). The plateau at high $R_{\text{cm-jp}}$ ($R_{\text{cm-cm}}$) and low r_{e2e} corresponds to an escaped chain that is collapsed in solution. It is clear from both FES1 and FES2 that there exists a pathway where the chain exits the micelle in a collapsed state. This is indicated by the entrance to the plateau (tube) being centered around $r_{\text{e2e}} \approx 1$. This pathway is qualitatively consistent with the collapsed Halperin–Alexander mechanism [2, 3].

While the basin and plateau are the two main features of FES2, FES1 has additional interesting behavior at intermediate values of $R_{\text{cm-jp}}$ and r_{e2e}. In this region the chain has partially escaped, but is able to take on an extended conformation with some monomers still located within the micelle core. For $R_{\text{cm-jp}}$ in the range of (5,8), the extended conformation has a lower free energy than the collapsed conformation. This becomes more obvious when we plot the conditional probability distribution, $P(r_{\text{e2e}}|R_{\text{cm-jp}})$, which is calculated directly from the FES using Equations (2.8) and (2.9).

$$P(r_{\text{e2e}}, R_{\text{cm-jp}}) = \exp\left[-\beta \Delta F(R_{\text{cm-jp}}, r_{\text{e2e}})\right] \tag{2.8}$$

$$P(r_{\text{e2e}}|R_{\text{cm-jp}}) = \frac{P(r_{\text{e2e}}, R_{\text{cm-jp}})}{\int \mathrm{d}r_{\text{e2e}} P(r_{\text{e2e}}, R_{\text{cm-jp}})} \tag{2.9}$$

The resulting distribution shown in Figure 2.3 indicates that an extended conformation is actually more probable prior to complete escape. At the saddle point position of CV1 (red dot), we find that the extended conformation (large CV2) has a lower free energy, indicated by the higher conditional probability density. This

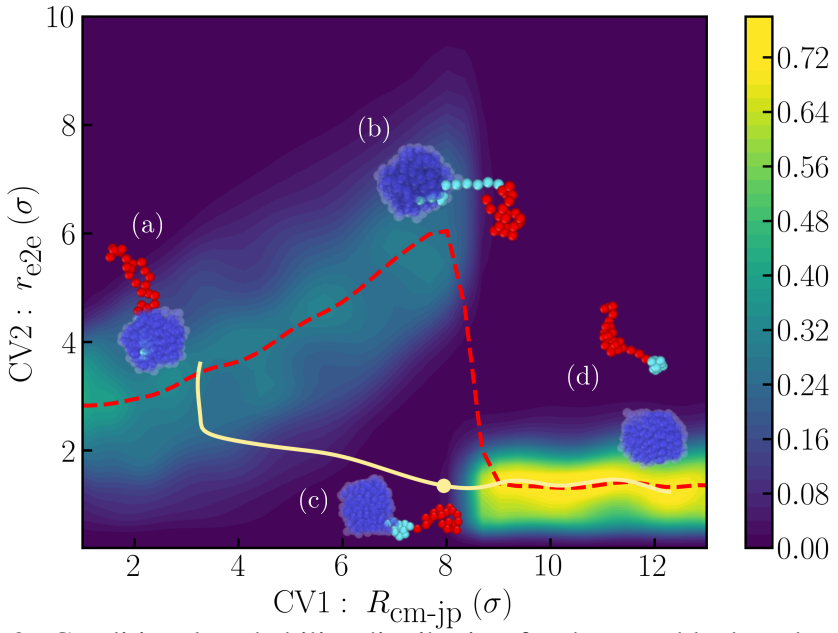

Figure 2.3: Conditional probability distribution for the core block end-to-end distance as a function of the location of the junction point for $N_A = 15$, $N_B = 24$, $\beta\Delta\epsilon = 23$. The distribution is computed using FES1 from Figure 2.2a. The red-dashed line traces the mean of r_{e2e} from the conditional distribution, and the yellow line traces the MFEP from FES1. Visualizations are (a) the chain in the micelle, (b) the chain extended into solution, (c) the chain collapsed at the micelle interface and (d) the chain fully expelled.

suggests that the chain may escape first by extending into solution until the contact with solvent is too unfavorable, at which point the chain collapses, expelling the remaining beads and forming a compact globule. This analysis assumes that the chain has enough time to fully relax at each value of $R_{\mathrm{cm\text{-}jp}}$ during the expulsion process. These results agree with and further support previous findings by Seeger et al. who used umbrella sampling simulations to compute 1-dimensional potentials of mean force (PMFs) for chain expulsion [38, 39]. They found that R_g gradually increased with $R_{\mathrm{cm\text{-}jp}}$ up to a certain point, where the chain then collapsed. Similarly, we also observe a bimodal distribution in $P(r_{\mathrm{e2e}}|R_{\mathrm{cm\text{-}jp}})$ near the transition state.

In addition to the FES and conditional distribution, it is of interest to compute the 1-dimensional free energy profile along an effective reaction coordinate. For this we consider both the minimum free energy path (MFEP) and free energy projection. First, we compute the MFEP via the string method (see the ESI† for method details) [54–56]. We conduct the string method optimization on the already computed 2d FES; we do not employ the string method during the MD simulations themselves.

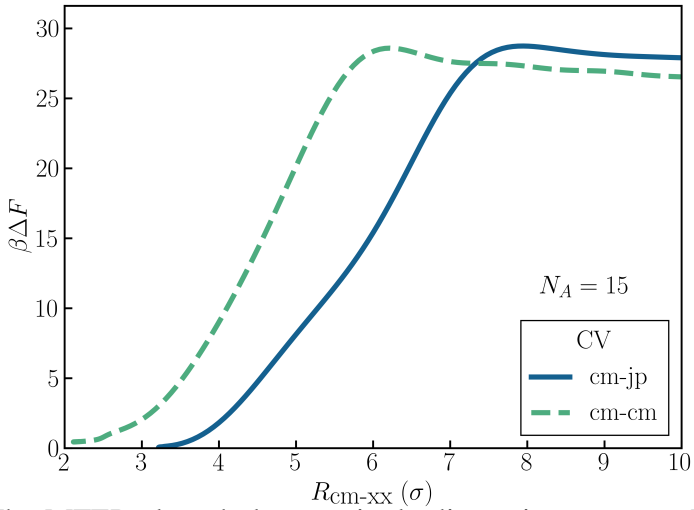

Figure 2.4: The MFEP plotted along a single dimension, $R_{\text{cm-xx}}$. The MFEP are extracted from the 2d FES in Figure 2.2.

In Figure 2.2, we plot the MFEP on top of both FES1 and FES2. We also plot the MFEP in one dimension as a function of only the $R_{\text{cm-xx}}$ collective variables in Figure 2.4. Note that the two MFEP are nearly identical barring a horizontal shift.

The computed MFEP qualitatively follows the Halperin-Alexander (HA) picture of micelle chain exchange. In the HA mechanism, the chain escapes the micelle in a collapsed state, resulting in a free energy barrier that scales with $N_A^{2/3}$. In order to confirm that the MFEP computed from our simulations yields the same scaling as the HA theory, we computed the MFEP for a range of core block lengths and computed the scaling relationship. The free energy curves and resulting regression analysis are given in Figure 2.5. In Figure 2.5b we find that the scaling is very near $2/3$, providing further support that the MFEP follows the HA mechanism, and that a $2/3$ scaling does exist under conditions where core collapse is expected. In the inset of Figure 2.5b we plot the free energy barrier as a function of the core block length on a linear–linear scale. Interestingly, we find that a linear fit is reasonable at small N_A, consistent with the results of previous simulations [34, 39], and with the expectation that very short core blocks cannot collapse to effectively shield monomers from the solvent.

In addition to the MFEP, we project the 2-dimensional free energy surface into 1 dimension corresponding to the $R_{\text{cm-cm}}$ pseudo-reaction coordinate. This analysis allows us to draw a more direct comparison with the simulations of Seeger et al. where only a single collective variable was biased [38, 39]. In principle,

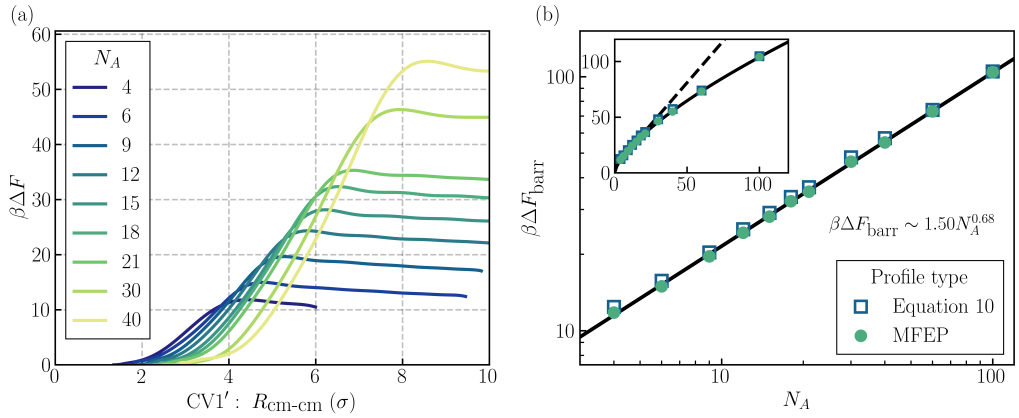

Figure 2.5: (a) 1-dimensional free energy profile of the MFEP for various core block lengths, N_A. Note that all MFEP are computed on a 2d FES similar to FES2 from Figure 2.2. (b) Free energy barriers from MFEP and free energy projection plotted against core block length, N_A, on a log-log scale. The solid line regression was conducted for the expression, $\ln(\beta\Delta F_{\text{barr}}) = a\ln(N_A) + b$, where a and b were fitting parameters, and the MFEP was used. The inset is the same as (b) on a linear–linear scale, and the dotted line is a linear regression, $\beta\Delta F\text{barr} = aN_A + b$, of the first five points corresponding to the small N_A region.

the projection should be more reliable than the direct single collective variable calculation as the dual collective variable simulation enables much more complete sampling of the polymer conformation (r_{e2e}). The projection is done using the normalization constant in Equation (2.9) which accumulates the weight of the free energy surface at each $R_{\text{cm-cm}}$.

$$\beta F(R_{\text{cm-cm}}) = -\ln\left[\int dr_{\text{e2e}} P(R_{\text{cm-cm}}, r_{\text{e2e}})\right] \tag{2.10}$$

We plot the barriers of the 1-dimensional free energy profiles as blue squares in Figure 2.5b. We find that the free energy barriers computed from the projected free energy are only slightly higher than those computed from the MFEP, and therefore still yield the same $N_A^{2/3}$ scaling of the free energy barrier, in contrast to the linear scaling obtained in previous simulations [39]. We provide a direct comparison of the barriers obtained from the two different methods in the ESI†.

We can foresee two potential reasons for the discrepancy, with the first being simple and the latter being rather complicated. The simple explanation is that a linear scaling should be observed at short chain lengths due to incomplete collapse of the core block, as shown in the inset of Figure 2.5b. While this is true for very short chain lengths, we still found a significant deviation from a linear scaling beyond

$N_A = 8$, while Seeger et al. studied chains up to $N_A = 12$ and still found linear scaling. The other, more probable reason, is the presence of the ridge between the collapsed and extended conformations on FES1 of Figure 2.5a. This ridge is consistent with the observations made by Seeger et al. that the R_g of the core block becomes bimodal as $R_{\text{cm-jp}}$ approaches the transition state. In simulations with a single CV, one could encounter hysteresis that can affect the computed barrier. If the chain starts in the micelle and is progressively pulled out, then the upper valley on FES1 will be preferred since the free energy gradient there is initially lower. The chain can remain in the extended conformation beyond the saddle point value of CV1 in FES1 (yellow dot) due to the significant barrier between the two conformations which would lead to a delayed transition state and an enhanced free energy barrier. The ridge between the two conformations increases in height for larger values of N_A which can impact the scaling of the barrier with N_A. If the chain is instead pushed into the micelle (reverse direction), then we expect that the MFEP will be followed and the observed barrier will be lower. This serves as a reasonable explanation for why the 1d umbrella sampling simulations yielded an apparent linear scaling, whereas our simulations yielded the Halperin–Alexander 2/3 scaling that is expected for large χ and large N_A.

With these results we have qualitatively and quantitatively identified the Halperin–Alexander collapsed mechanism as the MFEP for chain escape under strong segregation at sufficiently long core-block lengths, and have provided further context for the linear scaling observed in DPD simulations of shorter chains [34, 39]. Additionally, we have shown that the extended conformation observed by Seeger et al [38, 39]. is a valley on the free energy landscape that is actually slightly more favorable than the collapsed chain prior to the transition state. Thus, the chain may attempt to escape more frequently by fluctuating out of the micelle "bead-by-bead", at which point it is met with an additional barrier to collapse and fully escape. Physically, this additional free energy cost is associated with exposing the remaining monomers to the solvent while keeping the junction point fixed. On the other hand, the chain may attempt to escape less frequently by first collapsing within the micelle core, but when it does, it is met by a lower free energy barrier due to having a minimal number of contacts with the solvent.

The question still remains as to why the MFEP from these simulations is at odds with experimental observations in terms of the scaling of the free energy barrier. As mentioned previously, one can expect a crossover from linear scaling of the

barrier for a chain fully exposed to the solvent, to the Halperin–Alexander 2/3 scaling for a collapsed chain. The free energy barrier for a solvated chain in DPD is $\beta F_{\text{solv}} \sim \beta\Delta\epsilon N_A/(\rho\sigma^3)$, while the barrier for a collapsed chain is approximately $\beta F_{\text{HA}} \sim \beta\Delta\epsilon N_A^{2/3}(\rho\sigma^3)^{-2/3}$, ignoring constant prefactors. Thus, the ratio of the two barriers is expected to scale as $F_{\text{solv}}/F_{\text{HA}} \sim (N_A/\rho\sigma^3)^{1/3}$. In other words, the scaling should be linear with N_A when the effective coordination number of a monomer with the solvent is much higher than N_A. The scaling should go as $N_A^{2/3}$ when the coordination number is much lower than N_A, since a large portion of the monomers can replace solvent contacts with other monomer contacts upon collapse. Therefore, at low densities and long chain lengths, the chain should be collapsed and follow the Halperin–Alexander mechanism. In our DPD simulations with $\rho\sigma^3 = 3$ and N_A up to 100, we are comfortably within the Halperin–Alexander regime. This is further validated in the ESI† where we plot the average end-to-end distance of the core block and find that it is fully collapsed within the solvent for most of the studied chain lengths.

In experiments, it is unclear and highly situational whether the system corresponds more to the polymer melt case with only a partially shrunken core block upon escape, or the Halperin–Alexander case with a dry collapsed core block. For hairy micelles with very dilute coronas (as in our simulations), it is expected that the core block should escape in a collapsed state and produce $N_A^{2/3}$ scaling. Indeed, Lund et al. measured chain exchange in micelles formed from highly asymmetric PEP1-PEO20 and found that the exchange barrier could be fit well with a 2/3 power law [23]. For crew cut micelles that have a dense corona, the escape of the core could be viewed as escaping into the corona domain, rather than directly into the solvent. If the corona is sufficiently dense, Lund et al. argued that the increased pressure could prevent the core from collapsing, and lead to a barrier scaling linearly with N_A [28]. This was corroborated by exchange measurements they conducted on symmetric PEP1-PEO1 where they computed a linear exchange barrier. They use a simple blob scaling argument to determine when the density of the corona is high enough to prevent collapse of the core block upon escape and verified that their prediction was consistent with their PEP1-PEO20 and PEP1-PEO1 systems as well as the PS-PEP/squalene system of Choi, Lodge, and Bates [25]. In summary, whether the free energy barrier will scale as N_A or $N_A^{2/3}$ depends directly on the ability of the core block to collapse in the unfavorable domain. Our simulation results clearly show that the DPD model and chain/micelle parameters used here correspond to the Halperin–Alexander case.

We can also call into question the underlying assumptions of the zero-temperature string method and the nature of the MFEP. Namely, the computed MFEP only considers the structure of the underlying FES, and ignores any effects of thermal fluctuations or chain dynamics. As a result, the MFEP is most reliable when it corresponds to a deep valley or saddle on the free energy landscape. In addition, the kinetic pathway will only mimic the MFEP if the duration of an escape trajectory is significantly longer than the chain relaxation time. Our computed 2d FES does not feature a deep transition *tube*, but rather two possible competing free-energy valleys connected by a continuous distribution of pathways with nearly degenerate free energies.

In the following section, we study the other dominant regime corresponding to a very dense polymer melt, where the core block shrinks upon escaping, rather than collapsing into a compact globule. As discussed, this could be representative of a micelle with a dense corona, as in the crew cut case. To study the chain escape at high density, we employ a single-chain model that is appropriate for high $\bar{N}$ systems wherein the interaction of the tagged chain with other chains can be accurately represented instead by interactions with a mean-field background [10]. To avoid the assumptions of the MFEP, we turned to an alternative method that would allow us to determine the kinetic pathway traversed by escaping chains. This is preferable to the MFEP in our case since we expect that fluctuations could play a significant role in how the chain explores the free energy landscape. We utilize a transition path sampling method known as Forward Flux Sampling that can resolve the ensemble of escape trajectories, including one or both of the mechanisms implied from the FES obtained from our MD simulations.

2.3 Single-Chain Monte Carlo Forward Flux Sampling

In this section we investigate the expulsion mechanism of a copolymer from an interface using a single-chain (implicit background) model. Here we employ forward flux sampling (FFS) to elucidate the transition pathway for chain escape from a lamellar interface where the background is a dense polymer. Under this regime, the polymer does not collapse when in the opposing domain. In addition, we use 2d umbrella sampling to compute the free energy surface in order to better understand the FFS results. We apply these same methods to the case of a monomeric solvent where there is a coil-to-globule transition of the core block through the use of a many-body framework similar to that of many-body DPD (M-DPD).

Simulation Model for Polymer Melt

We utilize a soft particle simulation model that is similar to that used previously to study dynamic single-chain processes in dense polymer systems [10, 57–59]. We consider a single polymer chain with bead coordinates $\mathbf{r}_i$ for $i \in 0, 1, \cdots, N-1$. The polymer beads are connected by harmonic springs with the following potential,

$$\frac{H_b}{k_B T} = \sum_{i=1}^{N-1} \frac{3}{2\sigma^2} |r_i - r_{i-1}|^2 = \sum_{i=1}^{N-1} \frac{3(N-1)}{2R_{\mathrm{e2e}}^2} |r_i - r_{i-1}|^2 \tag{2.11}$$

where R_{e2e} denotes the ideal root-mean-square end-to-end distance, $R_{\mathrm{e2e}}^2 = (N-1)\sigma^2$, and σ is the statistical segment length. We divide the chain into two blocks, with the first N_A beads belonging to block A and the final $N_B = N - N_A$ beads belonging to block B. The non-bonded interactions consist of two contributions, $H_{\mathrm{nb}} = H_{\mathrm{ext}} + H_{\mathrm{pair}}$. The first term represents the interactions between the polymer beads and the surrounding background fluid, which is a melt of diblock copolymers of the same nature. The background is static and gives rise to effective fields, such that the Hamiltonian can be written as

$$\frac{H_{\mathrm{ext}}}{k_B T} = \sum_{i=0}^{N_A-1} w_A(\mathbf{r}_i) + \sum_{i=N_A}^{N-1} w_B(\mathbf{r}_i) = \sum_{i=0}^{N-1} w_{t(i)}(\mathbf{r}_i) \tag{2.12}$$

where $t(i)$ is the type of bead i, either A or B. The fields, $w_A(\mathbf{r})$ and $w_B(\mathbf{r})$ are parameters of the model and are not impacted by the presence of the tagged polymer. Conceptually, these interactions represent the interactions of a given polymer bead with the beads in the surrounding environment, where unfavorable AB contacts increase the energy by $\epsilon k_B T$, while AA and BB contacts decrease the energy by the same amount. Let z_c denote the average number of contacts of a single polymer bead (including inter- and intramolecular contacts). If the composition of the background medium is denoted as ϕ_A and $\phi_B = 1 - \phi_A$, then the interaction strength between the chain and the background can be approximated as $w_A = -z_c\epsilon(\phi_A - \phi_B)$. Similarly, we have $w_B = -z_c\epsilon(\phi_B - \phi_A)$. Note that in an A-rich domain, the energy of an A segment is $-z_c\epsilon$, while the energy of a B segment is $z_c\epsilon$. This energy can be mapped to the Flory-Huggins model with $\chi \approx 2\epsilon z_c$, since that is the difference in energy for an A segment to go from an A-rich domain to a B-rich domain.

Some non-bonded interactions come from intramolecular contacts, and these can be accounted for explicitly in the single-chain Hamiltonian,

$$\frac{H_{\mathrm{pair}}}{k_B T} = \sum_{i<j} v(\mathbf{r}_i - \mathbf{r}_j) \left\{ -\epsilon[2\delta(t(i), t(j)) - 1] - \frac{w_{t(i)}(\mathbf{r}_i) + w_{t(j)}(\mathbf{r}_j)}{2z_c} \right\} \tag{2.13}$$

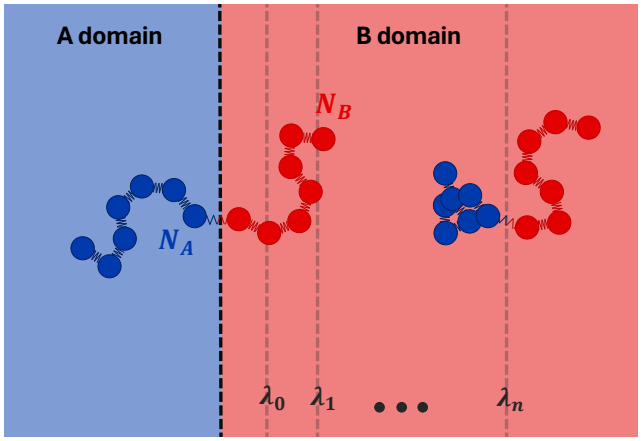

Figure 2.6: A visual representation of the MC simulation setup. The two bead-spring chains represent the same chain at different points in the expulsion process. The left chain is localized to the interface, and the right chain has escaped and collapsed. The dashed lines represent virtual interfaces used for FFS, and they are placed at chosen values of the reaction coordinate (order parameter) λ.

where pairwise contacts are defined by $v(\Delta\mathbf{r}) = 1$ for $|\Delta\mathbf{r}| < b = R_e/\sqrt{N-1}$, and otherwise 0. For simplicity, we set the two microscopic length scales – statistical segment length and interaction range – equal. δ is the Kronecker delta function, which is 1 when the segments are of the same type (i.e. $t(i) = t(j)$), and 0 otherwise. The first term quantifies the energy of an intramolecular contact. The second term corrects for double counting, since Equation (2.12) already includes interactions with z_c contacts. We need to subtract any assumed contacts that can be replaced with true intramolecular contacts from beads within the same chain. The number of intramolecular contacts depends largely on the chain conformation, and therefore also on the surrounding environment. A chain of A beads will be extended in an A-rich domain, yielding a low number of intramolecular contacts. Conversely, the chain will be more collapsed in a B-rich domain, yielding a high number of intramolecular contacts. Thus, this model includes the essential physics underlying the collapsed and extended conformations as the chain crosses the interface.

With a uniform density, the total number of contacts is given by $z_c = \frac{4\pi}{3}b^3\rho - 1$, where ρ is the segment density in the multichain system. In the high-density limit, we can obtain an approximate relation between z_c and the invariant degree of polymerization, $\bar{N}$.

$$z_c \approx \frac{4\pi}{3}\left(\frac{R_e}{\sqrt{N-1}}\right)^3\rho - 1 \approx \frac{4\pi}{3}\sqrt{\frac{\bar{N}}{N}} \tag{2.14}$$

In the following, the polymer contains $N = 32$ segments, $\epsilon = 0.02$, and $z_c = 50$. This corresponds to a system with $\chi N \approx 64$, and $\sqrt{\bar{N}} \approx 67.5$. See Figure 2.6 for a schematic of the system setup.

Monte Carlo Simulation

We run Metropolis Monte Carlo simulations of $O(10^6)$ independent chains. One MC step consists of selecting a polymer bead, updating its position via $\mathbf{r}_{v'} = \mathbf{r}_v + (\sigma/\sqrt{N-1})\hat{\boldsymbol{N}}(0,1)$, computing the new Hamiltonian, and accepting or rejecting the moved based on the Metropolis criterion. Here, $\hat{\boldsymbol{N}}(0,1)$ is the standard normal distribution. The order of polymer beads is chosen randomly without replacement. This updating scheme is intended to mimic the Rouse dynamics of a polymer chain in a melt [10, 58, 59], which is appropriate for diffusion of a polymer chain perpendicular to an interface [30, 31, 48]. A single MC step is conducted as follows:

1. The initial value of the Hamiltonian is computed, H_v
2. A single bead is moved by drawing from an independent random Normal distribution for each Cartesian coordinate. The Normal distributions have mean 0 and standard deviation 1.

$$x_{v'} = x_v + (\sigma/\sqrt{N-1})\hat{\boldsymbol{N}}(0,1) \tag{2.15}$$

$$y_{v'} = y_v + (\sigma/\sqrt{N-1})\hat{\boldsymbol{N}}(0,1) \tag{2.16}$$

$$z_{v'} = z_v + (\sigma/\sqrt{N-1})\hat{\boldsymbol{N}}(0,1) \tag{2.17}$$

   where $\hat{\boldsymbol{N}}(0,1)$ is the standard normal distribution from the PCG family of generators [60]. We set $\sigma = 1$ for simplicity. Note that these moves are used to reproduce Rouse dynamics.
3. The new value of the Hamiltonian is computed, $H_{v'}$.
4. The Metropolis-Hastings algorithm is used to accept or reject the move. Namely, the move is accepted if $\beta(H_{v'} - H_v) = \beta\Delta H_{v,v'} \leq 0$. Additionally, if $\beta(H_{v'} - H_v) = \beta\Delta H_{v,v'} > 0$, then the move is accepted with probability $\exp(-\beta\Delta H_{v,v'})$. If neither condition is satisfied, then the move is rejected, and microstate v is restored.

Forward-flux Sampling

We utilize forward flux sampling (FFS)[44, 45, 61] to compute the rate for chains localized to an interface to fully escape into solution. FFS is a transition path

sampling (TPS) technique that is used to compute the rate of rare events in a way that introduces no external biasing potential or forces. In FFS, virtual interfaces in collective variable (CV) space are placed at regular intervals between the starting and ending basin of the transition path. Transition trajectories are built up by simulating small transitions from one interface to the next, which are by themselves much more probable than the full transition. A *generating CV* is used to define the location of the virtual interfaces and track the progress of each chain from one interface to the next. Ultimately, the trajectories and transition rates can be accumulated from all of the interfaces to compute the overall rate and the ensemble of completed reaction trajectories.

If we have a set of N_i configurations that were saved at interface i, then the FFS algorithm amounts to selecting M configurations out of N_i and continuing each trajectory until they either reach the next interface, or fall back into the basin. This is continued until a minimum threshold of configurations N_{i+1} reach the next interface. If M is the number of required trajectories to reach N_{i+1} *successes*, then the transition rate between interface i and $i+1$ can be computed using

$$k_{i,i+1} = \frac{N_{i+1}}{M} \,. \tag{2.18}$$

Additionally, we need to estimate the flux from the starting Basin1 across the first interface, Φ_0, which can be computed by running a long simulation in Basin1, and monitoring the rate at which the particle crosses over the interface in the forward direction. The rate is computed as,

$$\Phi_0 = \frac{N_0}{\tau} \tag{2.19}$$

where N_0 is the number of forward crossings, and τ is the total simulation time. Each of the N_0 crossing configurations can be saved and used in the next step of the FFS algorithm to propagate from interface 0 to interface 1. The transition rate for the complete transition is computed by accumulating the transition probabilities between each interface. The equation for the transition rate is,

$$k = \Phi_0 \prod_i k_{i,i+t} \tag{2.20}$$

where Φ_0 is the flux of trajectories across the first interface, and $k_{i,i+1}$ is the transition probability from interface i to $i+1$. We define a free energy for the transition according to

$$\beta \Delta F = -\ln \frac{k}{\Phi_0} \tag{2.21}$$

which is motivated by the Arrhenius relationship, $k = A\exp(-\beta\Delta F)$ where A is an unknown kinetic prefactor. It is important to note that the rate k is a physical observable and should be insensitive to the definition of the basin. For example, if the first interface is placed at a larger x, then Φ_0 will necessarily decrease, but there will also be some interfaces omitted which will cause $\prod_i k_{i,i+t}$ to increase. The overall effect is for k to remain constant. Our definition of $\beta\Delta F$ will shift with the placement of the first interface, but not by enough to impact the scaling behavior.

We choose the inhomogeneous external fields, w_A and w_B, such that there is an interface located at $x_I = 2.5$ in units of $R_{\mathrm{e2e}} = \sigma\sqrt{N-1}$. For $x < x_I$, the external field mimics an A-rich domain at the mean-field level, while $x > x_I$ mimics a B-rich domain. We define Basin1 to be when the chain is localized to the interface, $x_{\mathrm{jp}} \approx x_I$, where x_{jp} is the component of the junction point displacement that is normal to the interface. We start with the A-block in the A-rich domain, and the B-block in the B-rich domain, such that both blocks behave approximately as ideal Gaussian chains with chain-lengths N_A and N_B respectively. When the chain has escaped into the B-rich domain, the A block takes on a partially collapsed conformation.

Due to the planar geometry, we utilize the 1-dimensional analogs of the collective variables from the MD portion of this work, CV1 (x_{jp}) and CV1′ (x_{cmA}) to conduct different FFS simulations. We place the first interface slightly outside of the A-rich domain, $x_1 > x_I$. We place additional interfaces further and further out from the interface, with the final interface located at a sufficient distance for the chain to be fully detached from the interface.

Results and Discussion

First, we compute the transition rate for the chain to escape from the interface using either the position of the junction point, x_{jp}, or the position of the center of mass of the A block, x_{cmA}, as the generating CV. We run FFS simulations for several core-block lengths, $N_A \in \{6, 8, 10, 12, 14, 16, 18\}$, to elucidate the scaling relationship of the free energy barrier. Figure 2.7 shows the free energy profiles and scaling behavior for the x_{jp} CV. In addition, we provide free energy profiles and barriers for the x_{cmA} CV in Figure 2.8.

The scaling of the free energy barrier with core-block length appears to be linear, regardless of the choice of generating CV. The inset of Figure 2.7b also shows that the rate computed from Equation (2.20) decays exponentially with N_A. This is the expected scaling for the case when the core block does not collapse into a dry globule

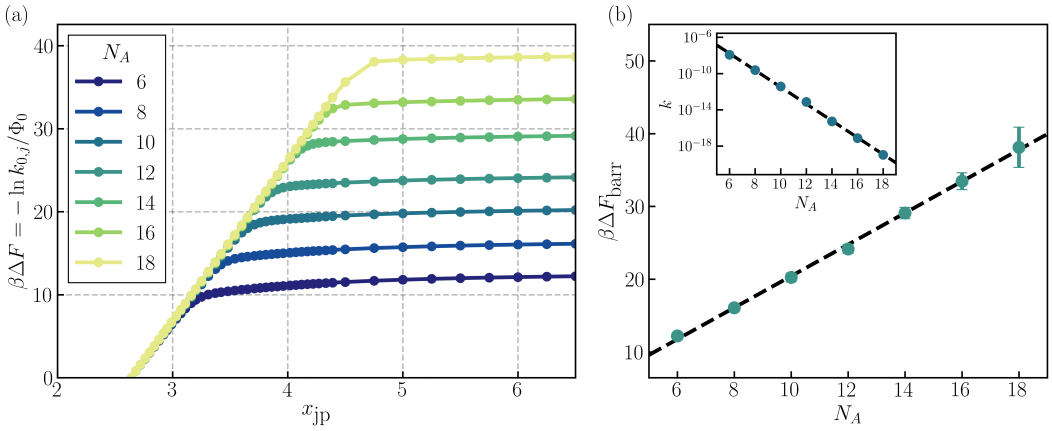

Figure 2.7: FFS results for the x_{jp} generating CV with various core-block lengths, N_A. All lengths are scaled by R_{e2e}, with the interface placed at $x = 2.5$. In all cases, the total chain length is $N = 32$. (a) The cumulative free energy change. (b) The total free energy change from Equation (2.21) versus core-block length, with the dashed line being the optimized linear fit. Error bars represent a 95% confidence interval from averaging 5 independent FFS simulations. The inset is the rate constant from Equation (2.20).

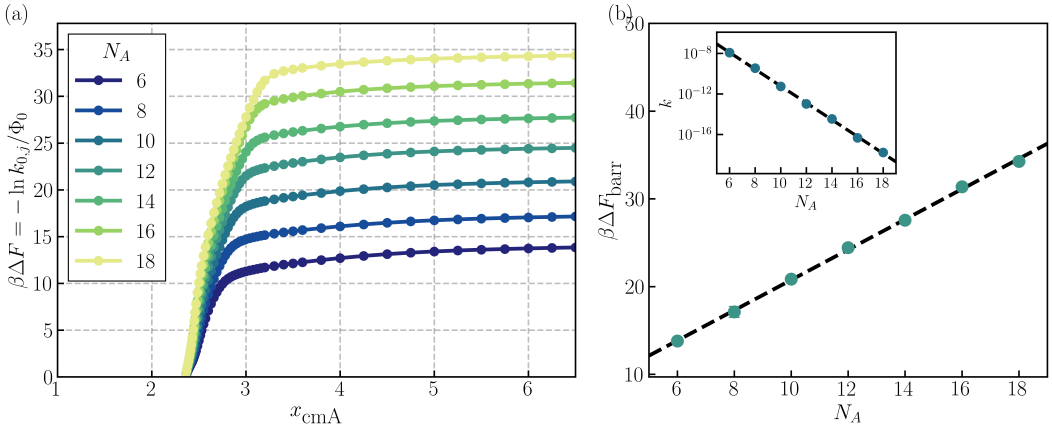

Figure 2.8: FFS results for the x_{cmA} generating CV with various core-block lengths. (left) The natural logarithm of the cumulative transition rate. (right) The total free energy change versus core-block length, with optimized linear fit. Error bars represent a 95% confidence interval from averaging 4 simulations.

upon entering the B domain. Since a linear scaling of the barrier is also observed in experiments, this indicates that the experimental conditions could be such that the core block of an isolated chain is not fully collapsed after escaping. This would occur if the core block is too short to form a statistically probable globule. As argued by Lund et al., it could also occur if the corona block is sufficiently dense

such that the core block cannot collapse fully upon entering the corona domain [28]. As argued by Choi et al., it could also be due to solvent penetrating the collapsed globule such that all or most of the monomers are contacting the solvent [62–64]. In our FFS simulations, the linear scaling is expected since the core block shrinks only slightly upon entering the B domain due to the high value of $\bar{N}$.

Note that even after the chain has fully detached from the interface the free energy continues to gradually increase. This behavior is perfectly explained using the Markov chain for symmetric diffusion on a number line with an absorbing boundary condition on the left. After the chain has escaped, the chain still has a probability to diffuse backwards and fall into the starting basin. This probability decreases the further the chain is from the transition state. If we consider the absorbing boundary to be at the transition state, which we define as node 0, then we can compute the probability of reaching node $n+1$ starting from node 0 before falling back into the starting basin; we define this probability as $P(n+1|0) = P_0$, and more generally we define $P(n{+}1|i) = P_i$ for $i \geq 0$. Starting from P_0 we can recursively compute all P_i up to P_n. Lastly, we assume that the forward and backwards transition probabilities are both $1/2$ at all interfaces. By induction, we find that $P_n = P(n{+}1|n) = (n{+}1)/(n{+}2)$, and therefore $P_0 \sim 1/(n+2)$ and $-\ln P_n \to 0$ as $n \to \infty$. We could subtract out this contribution to obtain a flat plateau, however, we elect not to since the transition state is not well-defined for the monotonic free energy curves in Figures 2.7. The small contribution does not affect the scaling of the free energy with N_A.

Forward-Flux Ensemble (FFE)

From this point, it is of interest to evaluate the distributions of different chain properties along the trajectories to better understand the mechanism by which the chain is able to escape. We analyze different ensembles of trajectories specifically for the system with $N_A = N_B = 16$, and $\epsilon = z_c^{-1} = 0.02$. The forward flux ensemble (FFE) is the ensemble containing properties on the FFS interfaces for chains that were frozen immediately after reaching an interface.

The distribution for the end-to-end distance of the core-block and the minimum monomer position computed using the x_{jp} CV is given in Figure 2.9. A complementary plot for the x_{cmA} CV is given in Figure S3 in the ESI†. Each interface is plotted as an independent normalized probability distribution. The distribution in x_{jp} or x_{cmA} at each interface is not considered in these particular figures. Thus, the distribution is shown as uniform in the abscissa for the domains in between

FFS interfaces for easier visualization. The purple dots prior to the first interface represent initial configurations from equilibration runs in Basin1. The black line traces the mean value of the property along the interfaces.

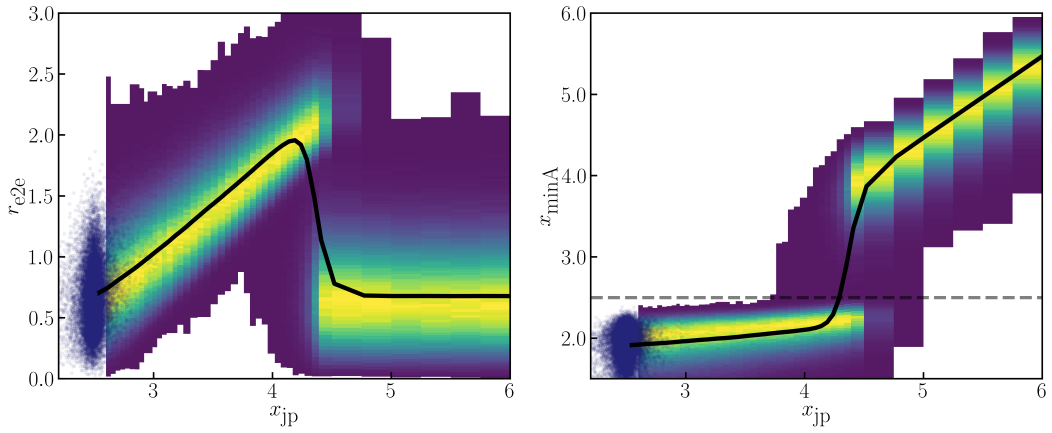

Figure 2.9: FFE of the (top) core-block end-to-end distance, r_{e2e} and (bottom) core-block minimum bead position, x_{minA} as a function of the junction position, x_{jp}. Here, x_{jp} is used as the generating CV. Scatter points represent initial configurations within Basin1.

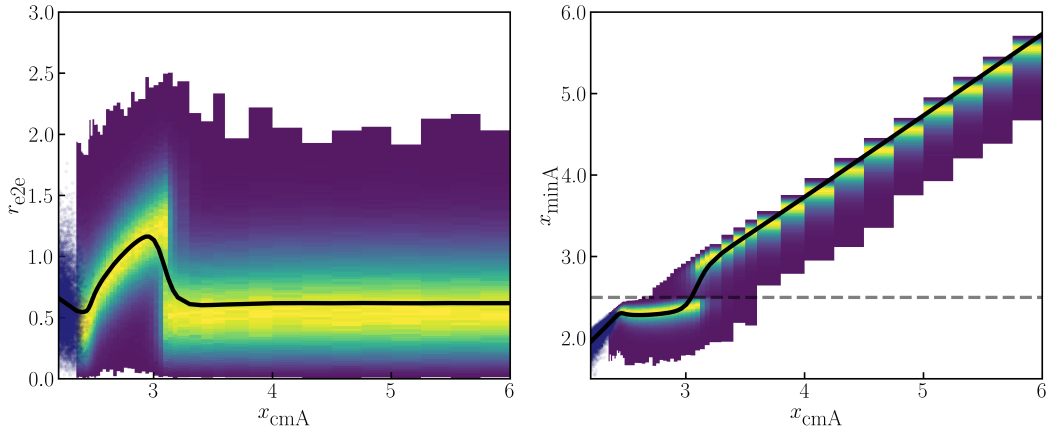

Figure 2.10: FFE of the (left) core-block end-to-end distance and (right) core-block minimum bead position, as a function of the core-block center-of-mass. Here, x_{cmA} is used as the generating CV.

It is clear from Figure 2.9 that the chain prefers to extend before eventually collapsing and fully escaping from the interface. If we consider the chain to be fully escaped when the last bead leaves the micelle core, then this implies that the transition state is when $x_{jp} \approx 4.25 - 4.50$. Thus, the chain is significantly extended, with

$\langle r_{\mathrm{e2e}} \rangle_{TS} \approx 2.0$, which is much greater than the Basin1 average of ≈ 0.68. Note that r_{e2e} is the end-to-end distance of the core (A) block only. While still present, the extension mechanism becomes less pronounced when referring to Figure 2.10, with $\langle r_{\mathrm{e2e}} \rangle_{TS} \approx 1.2$. This discrepancy arises from the unique definition of the FFE, which freezes chains the first time that they cross each interface. As a result, these chain conformations have an implicit bias. In addition, most of the chains that are saved at FFS interfaces will go on to fall back into Basin1, which means the ensemble may not be representative of the pathway that chains must take to successfully escape. In practice, it is more appropriate and meaningful to look at the chain properties from the ensemble of chain trajectories that successfully completed the transition between the starting and ending basin, with monomer coordinates written at regular intervals, as opposed to only at first-crossing. We denote this ensemble of transition paths as the *reactive ensemble* (RE), which we discuss in the following section.

Reactive Ensemble (RE)

While the FFE is simple to compute and analyze since polymer configurations on the interfaces are saved during the FFS simulation, it is hard to extract meaning from this ensemble due to the bias introduced through the *first-crossing* condition. As a result, the amount of extension present in the FFE is exaggerated compared to reality due to the uniqueness of the *first-crossing* condition. In practice, it is more appropriate and meaningful to look at the chain properties from the ensemble of chain trajectories that successfully completed the transition between the starting and ending basin, with monomer coordinates written at regular intervals, as opposed to only at first-crossing. We denote this ensemble of transition paths as the *reactive ensemble* (RE), which we discuss in this section.

The *reactive* trajectories can be constructed by starting from chain conformations at the final interface and tracing them back to the first interface. These trajectories may cross each interface multiple times before reaching the final basin and may share common ancestors at intermediate interfaces. The only constraint on the reactive trajectories is that the chain must not fall back into the starting basin before reaching the ending basin.

Since the coordinates are output at regular intervals, the properties along the trajectories can be binned using any choice of collective variable (CV), which we denote as the *selecting* CV. To track the progress of chain escape, we define a selecting CV based on the fraction of core-block monomers that have crossed the interface. To

make this CV continuous, we employ a hyperbolic tangent switching function,

$$f = \frac{1}{2N_A} \sum_{i=1}^{N_A} \left[1 + \tanh\left(-\frac{x_i - x_I}{c} \right) \right], \tag{2.22}$$

where $c = 0.1$ modulates the width of the function, and x_I is the interface position. By definition, $f \in [0, 1]$. Example trajectories up to the point of detachment are shown in Figure 2.11a, which indicate that the primary mechanism for a chain to cross the interface is through extension.

The full ensemble of trajectories can generate any univariate or multivariate probability distribution. Here, we focus on $P(r_{\mathrm{e2e},x}, f)$ and, more specifically, the conditional distribution $P(r_{\mathrm{e2e},x}|f)$, plotted in Figure 2.11b. This distribution quantifies the degree of chain stretching (normal to the interface) as a function of chain expulsion during successful escape attempts. Figures 2.11a and 2.11b show that the main escape pathway requires chains first to extend into solution (increasing both f and $r_{\mathrm{e2e},x}$) and then fully collapse and detach from the interface (increasing f while decreasing $r_{\mathrm{e2e},x}$).

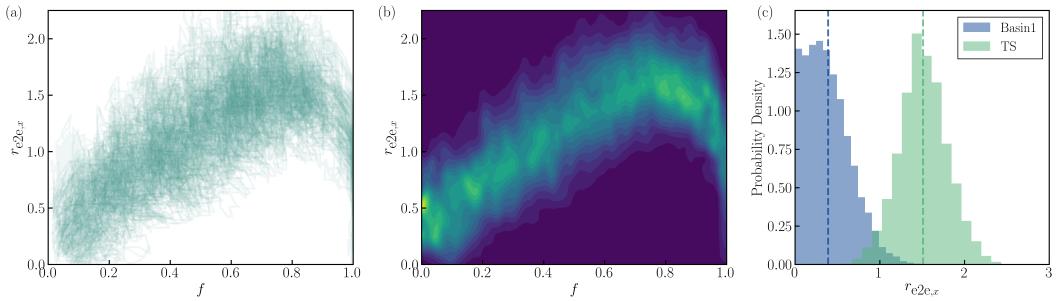

Figure 2.11: Results from the reactive ensemble for $N_A = N_B = 16$, $z_c^{-1} = \epsilon = 0.02$. (a) Example escape trajectories, (b) conditional probability distribution, $P(r_{\mathrm{e2e},x}|f)$, where $r_{\mathrm{e2e},x}$ is the x-component of the end-to-end distance of the core block and f is the fraction CV defined in Equation (2.22), and (c) the distributions of $r_{\mathrm{e2e},x}$ in Basin1 and just before detaching from the interface, denoted as the transition state (TS). Vertical dashed lines mark the means of the two distributions.

To clarify this pathway and the stretched transition state, we compare the probability distributions $P(r_{\mathrm{e2e},x}|f_0)$ and $P(r_{\mathrm{e2e},x}|f_{TS})$ in Figure 2.11c. The term "transition state" is not used formally here, but instead is simply used to indicate the point along the trajectory where f becomes 1. In other words, we define the "transition state" to be the step when the final bead crosses over the interface. The distributions in Figure 2.11c indicate the degree of extension for chains localized at the interface or actively detaching from it, respectively, confirming that the chains adopt an extended conformation immediately prior to detachment.

Our enhanced sampling MD simulations revealed that "bead-by-bead" extension of the chain into the solvent is a relatively low free energy pathway, even in the case where the core block collapsed into a dry globule. However, in that case the MFEP was still the HA mechanism. In the high density limit, the FFS simulations revealed that the chain escapes almost exclusively through an extension mechanism. This hints at the possibility that the MFEP crosses over from the HA mechanism (lower pathway on FES) to the stretching mechanism (upper pathway on FES) as the propensity for core collapse decreases.

2.4 Single-Chain Monte Carlo Umbrella Sampling

In this section we employ the same single-chain Hamiltonian that we used in the FFS simulations in order to better understand how the transition pathways fit into the overall thermodynamic picture. We employ umbrella sampling to compute the underlying free energy surfaces and compare them with the transition pathways discovered in the previous section.

Umbrella Sampling

We compute the 2d free energy surface (FES) using umbrella sampling and the weighted histogram analysis method (WHAM). Here, we briefly describe the method for completeness and we direct the reader to more thorough discussions provided by Hub et al. [65] and Roux [66]. The principal goal of umbrella sampling is to compute the free energy change when going from one state to another in a system. For transitions that are rare, and even for those that are frequent, accurately sampling the transition and estimating the free energy change is challenging. Umbrella sampling seeks to solve this issue by restraining the system at different points along a reaction coordinate ξ, usually via a harmonic biasing potential. If you discretize the pathway between the initial and final states into M windows in the collective variable ξ, then you will apply M harmonic potentials denoted as

$$w_i(\xi) = \frac{\kappa_i}{2}(\xi - \xi_i)^2 \tag{2.23}$$

where κ_i is the spring constant used at window i, and ξ_i is the center of the window. As simulations progress under the biasing potentials, histograms of the CV values, $h_i(\xi)$, are collected in each window. The weighted histogram analysis method (WHAM) is the most common way to construct the free energy or PMF from the biased histograms. The WHAM equations are

$$P(\xi) = \frac{\sum_i^M h_i(\xi)}{\sum_i^M n_i \exp\left[-\beta w_i(\xi) + \beta F_i\right]} \tag{2.24}$$

and

$$e^{-\beta F_i} = \int d\xi e^{-\beta w_i(\xi)} P(\xi) \tag{2.25}$$

where $\beta = 1/k_B T$, n_i is count in window i, and F_i are the free energy constants. Since $P(\xi)$ and all of the F_i are unknown, these equations must be solved iteratively. In this work, we utilize the WHAM software created by Alan Grossfield which can be used for 1- and 2-dimensional umbrella sampling analysis [67].

We start by computing 2d free energy surfaces similar to the ones we computed using sABF in DPD simulations. To elucidate the chain conformation during escape, we bias both an escape coordinate and a conformation coordinate. All calculations use the distance between the junction point and the interface as an escape collective variable. In addition we consider a few collective variables to bias the chain conformation:

1. $r_{\text{e2e}} = |\mathbf{r}_{\text{jp}} - \mathbf{r}_0|$
2. $r_{\text{e2e,x}} = |x_{\text{jp}} - x_0|$
3. $\Delta x_{\text{jp}} = x_{\text{jp}} - x_0$

First we show an example of the sampling achieved in a representative umbrella sampling simulation in Figure 2.12. Here we show the window centers as red dots and the corresponding histograms in blue. In our simulations we use the same spring constant, $k = 10$, for the harmonic bias in both collective variables.

Results for Polymer Melt Hamiltonian

Here we utilize the same simulation Hamiltonian as the FFS simulations which mimics a single polymer chain immersed in a polymer melt that has phase separated into a lamellar microphase. Below are the 2d free energy surfaces using the three different collective variables computed for parameters $N_A = N_B = 16$ and $\chi N = 64$ ($\epsilon = 0.02$ and $z_c^{-1} = 0.02$).

These free energy surfaces contain many of the same features as those computed from our DPD simulations. The main difference is that the end-to-end distance does not significantly decrease upon expulsion because the background is a polymeric solvent. Instead the core block shrinks very slightly. In Figure 2.15 we plot the a dashed line corresponding to $r_{\text{e2e,x}} = x_{\text{jp}}$. This line also by definition corresponds to x_0 lying on the interface. As expected, the ridge in the FES corresponds well with this line.

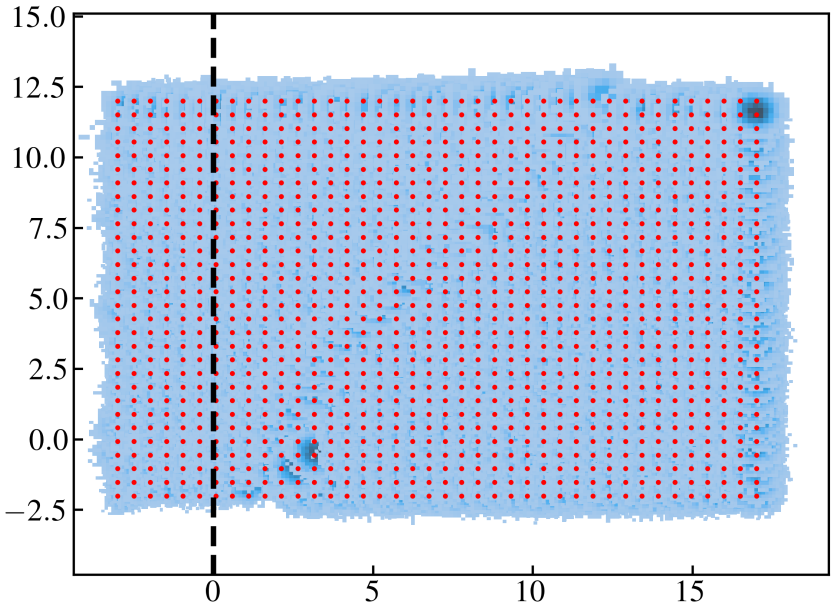

Figure 2.12: Sampling from 2d umbrella sampling simulation.

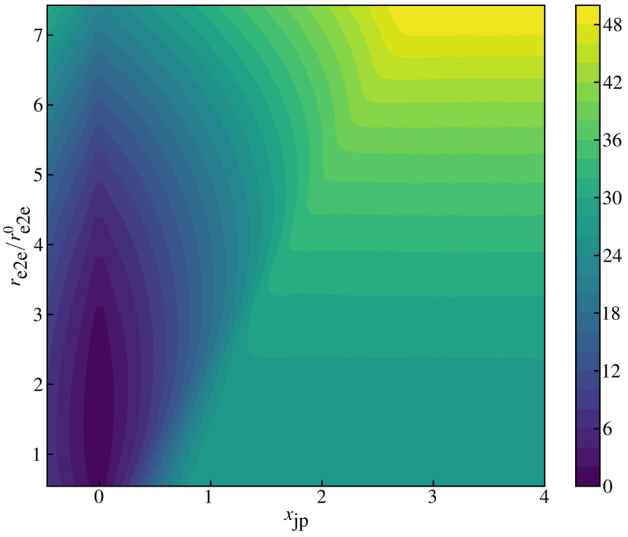

Figure 2.13: 2d FES using the junction point and the core block end to end distance.

In Figure 2.16 we show the reactive trajectories from FFS on top of the FES from umbrella sampling using the same simulation parameters ($N_A = N_B = 16$ and $\chi N = 64$). These plots reveal that the polymers indeed escape by first extending into the upper region of the FES. After achieving some maximum extension, the chains slightly contract before fully detaching from the interface. Note that none of the chains have a relaxed coil conformation at escape.

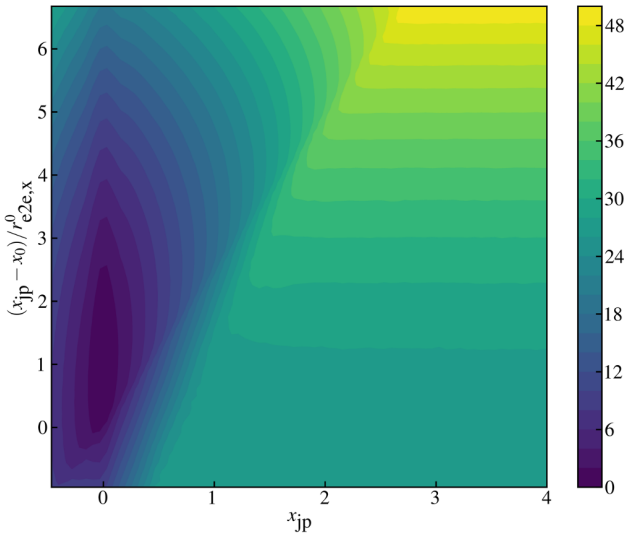

Figure 2.14: 2d FES using the junction point and the x-component of the displacement between the end and junction point.

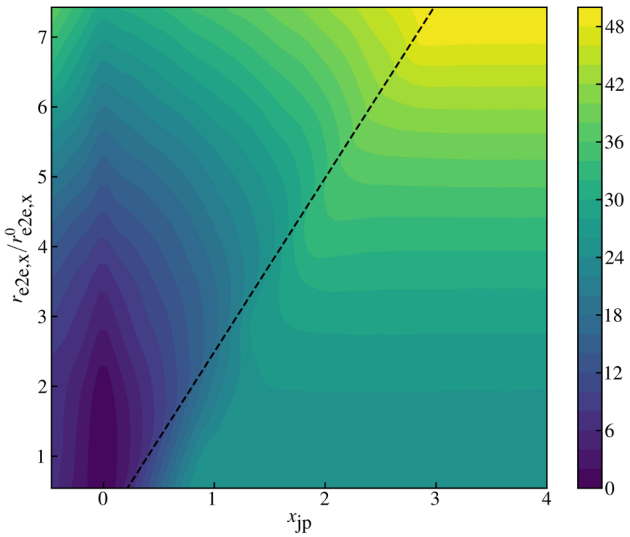

Figure 2.15: 2d FES using the junction point and the x-component of the core block end to end distance.

In addition, we plot an estimate of the most probable pathway computed using the reactive trajectories from FFS in Figure 2.17. Once the chain has extended into the unfavorable domain, it cannot escape simply by increasing x_{jp} due to the additional free energy barrier. Instead, the chain can follow a constant free energy contour on the FES by slightly decreasing x_{jp} while collapsing, and then eventually escaping by increasing x_{jp}.

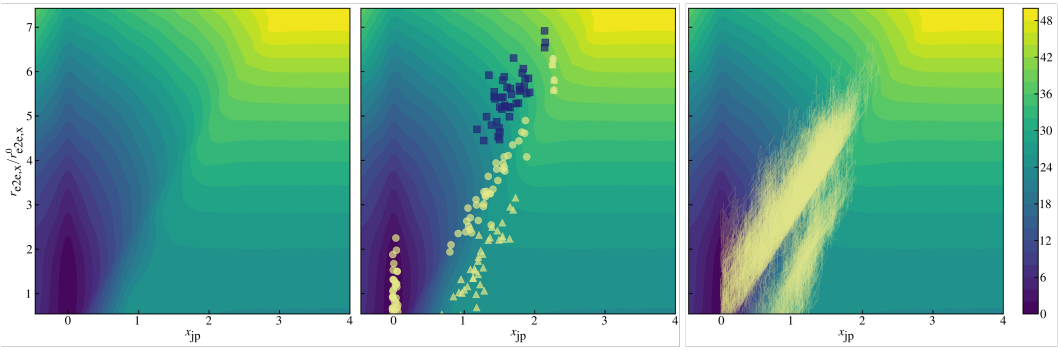

Figure 2.16: (left) Free energy surface using x-component of end-to-end distance in umbrella sampling simulations with $N_A = N_B = 16$ and $\chi N = 64$. (middle) Free energy surface with important points from FFS reactive trajectories. Yellow circles within the basin are starting configurations. Blue Squares are the point of maximum $r_{e2e,x}$ along the trajectory. Yellow circles on the ridge are the point when the final bead detached from the interface. Yellow triangles are configurations shortly after detaching. (right) Trajectories from reactive ensemble computed using FFS.

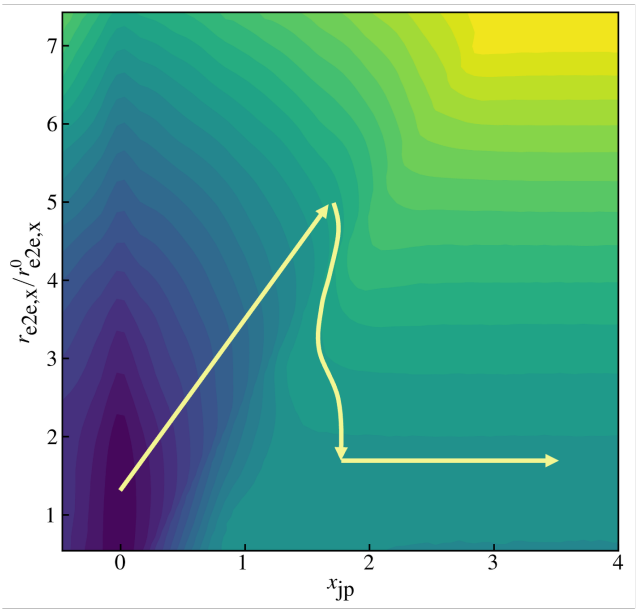

Figure 2.17: 2d FES with arrow showing most probably path computed using reactive trajectories from FFS.

To further describe this pathway, we overlay a single reactive trajectory on top of the FES plotted as a surface in 3d in Figure 2.18. From this plot, it is clear that the chain drifts gradually up the gentle region of the free energy surface without escaping due to the sharp edge along $r_{e2e,x} = x_{jp}$. Instead, once the chain meets this edge, it slides up simultaneously increasing x_{jp} and $r_{e2e,x}$, which corresponds to

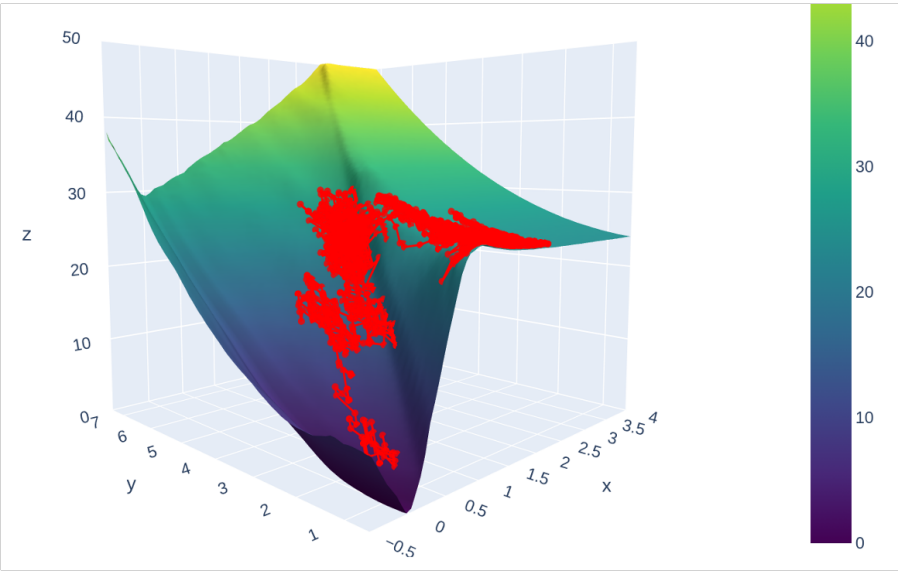

Figure 2.18: Umbrella sampling FES plotted as a 3d surface plot with a single reactive trajectory from FFS plotted on top.

the "bead-by-bead" escape mechanism. Eventually the free energy of this extended conformation becomes almost degenerate to that of the escaped chain, and then it will escape. This is exactly the picture proposed by Seeger et al. [39].

Namely, they used a simple scaling argument to predict the free energy of a chain that is escaping the interface by stretching out into the solution. They write the free energy of the stretched chain as:

$$\beta F = f N_A \Delta a + \frac{x_{\mathrm{jp}}^2}{f N_A b^2} \tag{2.26}$$

where the first term is the energy due to unfavorable contacts with the solvent, and the second term is the stretching energy of the core block. Here, Δa is the penalty for moving a single bead from the core into the solvent, N_A is the length of the core block, f is the fraction of extracted monomers, and b is the statistical segment length. At a given position of the junction point x_{jp}, one can determine the optimal fraction of expelled core block (assuming this stretched conformation) by minimizing the free energy

$$\frac{\partial \beta F}{\partial f} = N_A \Delta a - \frac{x_{\mathrm{jp}}^2}{f^2 N_A b^2} = 0 \tag{2.27}$$

which results in the following expression for f,

$$f \sim \frac{x_{\mathrm{jp}}}{N_A b (\Delta a)^{1/2}} \tag{2.28}$$

which increases linearly with x_{jp} as expected, and decreases with Δa. Plugging this back into the free energy we get,

$$\beta F^* \sim \frac{x_{\text{jp}}}{b}(\Delta a)^{1/2} \tag{2.29}$$

which indicates that the free energy linearly increases with x_{jp} under this stretching assumption. It is interesting to note that the slope is independent of N_A which is expected if the chain is escaping bead-by-bead. They then argue that when the chain is wetted by the solvent, the maximum free energy is achieved when all core beads are expelled. This leads to a barrier

$$\beta F_{\text{barr}} \sim N_A \Delta a \tag{2.30}$$

which is exactly what is expected for a core block that does not collapse. The assumption that the core block is wetted by solvent is key in achieving the linear scaling of the free energy barrier with N_A. On the other hand, if the core escapes without changing its conformation or end-to-end distance at all, then the free energy profile should increase more rapidly, since multiple beads are exposed to the solvent at the same time, rather than one-by-one. If we assume the core block forms an ideal coil and does not change its conformation whatsoever, then we can estimate how f scales with x_{jp}. First we assume that the coil is roughly spherical, with an ideal radius of gyration $R_g = b\sqrt{N_A/6}$. If the beads are uniformly distributed throughout the sphere, then the actual sphere radius is $R = R_g\sqrt{5/3}$. The junction point is located at the right edge of the sphere, so we can compute the fraction of A monomers that have entered the B domain by integrating the volume between $x = 0$ and $x = x_{\text{jp}}$.

$$f = \frac{v}{V} = \frac{2\pi}{\frac{4}{3}\pi R^3}\int_0^{x_{\text{jp}}} dx \int_0^{\sqrt{R^2-(x-R)^2}} dr\, r = \frac{1}{2} + \frac{3}{4}\left[\left(\frac{x_{\text{jp}}}{R} - 1\right) - \frac{1}{3}\left(\frac{x_{\text{jp}}}{R} - 1\right)^3\right] \tag{2.31}$$

Thus, the free energy to escape without changing conformation should obey

$$\beta F \sim f N_A \Delta a \sim N_A \Delta a \left\{\frac{1}{2} + \frac{3}{4}\left[\left(\frac{x_{\text{jp}}}{R} - 1\right) - \frac{1}{3}\left(\frac{x_{\text{jp}}}{R} - 1\right)^3\right]\right\} \tag{2.32}$$

up to $x_{\text{jp}} = 2R$. We use our 2d FES to extract the free energy along the hyperstretching and unperturbed pathways, and compare it to the free energy profile projected onto the x_{jp} CV in Figure 2.19.

From the bottom panel of Figure 2.19, we can see that the free energy of the hyperstretched mechanism is lower up until the transition state, where the free

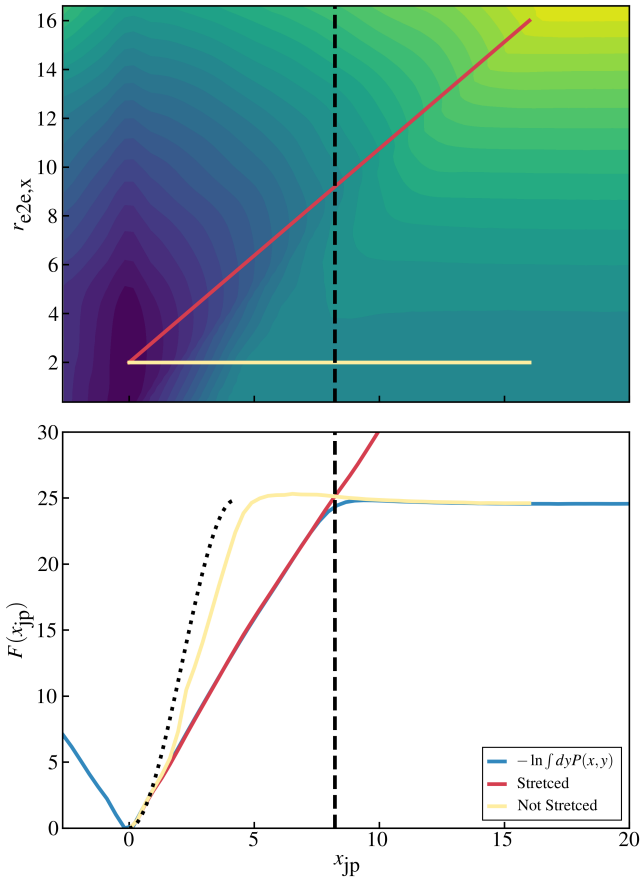

Figure 2.19: (top) Free energy surface for $N_A = N_B = 16$ and $\chi N = 64$. The red line follows the hyperstretched pathway, and the yellow line follows the unperturbed pathway. (bottom) The blue line is the projection of the 2d FES into 1d, and the colored profiles correspond to the paths in the top panel. The dashed vertical line is the point where the free energies of the two paths become equal. The dotted line is Equation (2.32) with the magnitude scaled by the true barrier.

energy of the unperturbed and the stretched chains are equal. At that point, we can predict that the chain will shrink back to its normal size to escape because further stretching would increase the free energy significantly beyond the unperturbed state. Initially, however, the chain will prefer to stretch into the B domain since the free energy gradient is much gentler. This is exactly what we observed in Figure 2.18 where the chain extended into the solution first until the free energy of the stretched and unperturbed states were roughly equal. We also find that our crude model in Equation 2.32 does a good job at predicting the shape of the free energy profile for the chain that escapes without stretching, as shown by the dotted line in the bottom panel of Figure 2.19.

To elucidate the scaling relationship of the free energy barrier, we compute the free energy profile for several N_A and plot the results in Figure 2.20. As expected, we find that the free energy barrier scales linearly with the core block length since the core is exposed to the solvent.

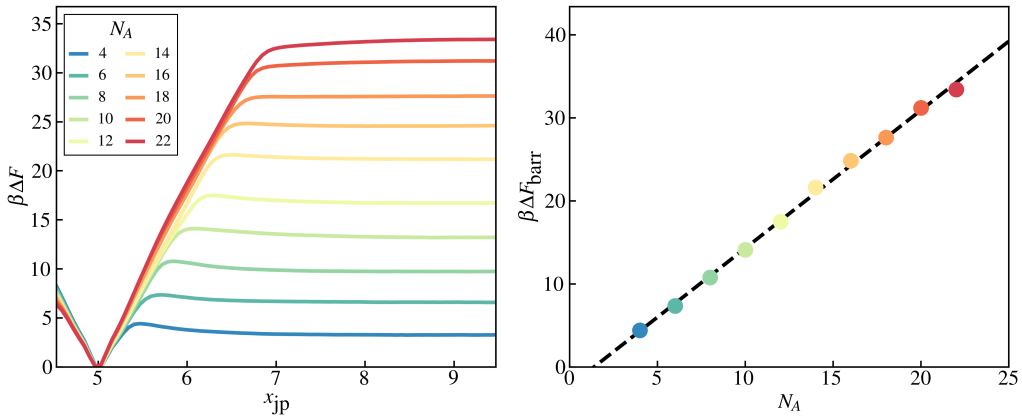

Figure 2.20: (left) 1d free energy profiles computed by projecting 2d surface onto x_{jp} coordinate. (right) Free energy barrier as a function of core block length N_A.

We note here that the analysis of the stretching mechanism presented by Seeger et al. [39] was under the assumption that the core block would be wetted by the solvent after escape. However, for core block lengths exceeding roughly $N_A \approx 6$, the core block in their DPD model forms a globule with interior monomers that are not in fact exposed to the solvent. This effect becomes more and more pronounced for larger core block lengths, which causes the scaling relationship to crossover from linear to $2/3$. This is what we showed in the Enhanced Sampling Molecular Dynamics section by going to much longer core block lengths (up to $N_A = 100$).

In the case of a polymeric solvent with high $\bar{N}$, we have shown through both 2d umbrella sampling and forward flux sampling simulations that the stretching mechanism is indeed correct, but does not lead to a higher or lower free energy barrier than an unperturbed escape mechanism. It has yet to be verified whether the stretching mechanism is still relevant in the case of a collapsed core block. In the following section we will conduct the same simulations but with the many-body dpd model which can model core collapse.

Many-Body Simulation for Polymer in Solution

So far we have shown that the linear scaling of the free energy barrier is achieved in the case of a dense polymer background where the core block does not collapse. We

were able to show that the chain escapes through a bead-by-bead mechanism at first, until the exposure of more beads to the solvent becomes too unfavorable, at which point the polymer collapses and escapes. This is in contrast to the minimum free energy pathway (MFEP) computed from the string method, which predicts that the chain escapes nearly unperturbed. Nevertheless, the free energy barrier remains the same regardless of the mechanism, and the scaling remains linear and in agreement with experiments.

It is now of interest to discover how the minimum free energy pathway and the kinetic pathway for chain expulsion relate in the case of a monomeric solvent where the core block does collapse in the solution as in the Halperin–Alexander theory. We already computed free energy surfaces and minimum free energy pathways from DPD simulations with the spectral ABF enhanced sampling method in a previous section. However, FFS simulations are far too computationally expensive to run with the DPD model due to the high density of particles, the explicit solvent, and the large box sizes required for long polymer chains. To remedy this, we develop a many-body simulation technique for a single chain immersed in an implicit solvent. The model developed here can accurately capture the coil-to-globule transition of a polymer in solution, and therefore will allow us to bridge the gap between the linear scaling regime and the 2/3 scaling regime, and determine if the true kinetic pathways is in line with the Halperin–Alexander mechanism.

Simulation Model

Here I describe a many-body simulation model that is similar to many-body DPD which is a soft-particle model capable of describing liquid–vapor coexistence [68–71]. In this case, we utilize a similar method to describe the coil-to-globule transition in polymers.

The system contains a single copolymer with N total beads divided into two blocks of size N_A and N_B. The A block represents the core species while the B block is the corona and shares chemical identity with the solvent. The monomers interact whenever they have any volume overlapping and have their mass uniformly distribution over a sphere of diameter σ.

$$\rho_i(\mathbf{r}) = \begin{cases} 1/v & , |\mathbf{r} - \mathbf{r}_i| < \sigma/2 \\ 0 & , |\mathbf{r} - \mathbf{r}_i| \geq \sigma/2 \end{cases} \tag{2.33}$$

where $v = \pi\sigma^3/6$ is the volume of a monomer. This choice ensures that $\rho_i(\mathbf{r})$ integrates to 1. I assume that the interaction of two particles is local and quadratic,

$$w_c(|\mathbf{r}_i - \mathbf{r}_j|) = \int d\mathbf{r} \int d\mathbf{r}' \rho_i(\mathbf{r}) \delta(\mathbf{r} - \mathbf{r}') \rho_j(\mathbf{r}') \tag{2.34}$$

which results in the following interaction kernel,

$$w_c(r) = \begin{cases} \frac{1}{2v}\left(2 + \frac{r}{\sigma}\right)\left(1 - \frac{r}{\sigma}\right)^2 & , r \leq \sigma \\ 0 & , r > \sigma \end{cases} \tag{2.35}$$

In the framework of manybody-DPD (MDPD), each particle has a self-energy that is a function of two densities [68].

$$u_i = A\bar{\rho}_i + B\bar{\bar{\rho}}_i^2 \tag{2.36}$$

where $\bar{\rho}_i$ is the sum of the interactions with neighbors,

$$\bar{\rho}_i = \sum_{j \neq i} w_c(r_{ij}) \tag{2.37}$$

and the choice of $A < 0$ makes this an attractive term. This first term is simply just the pairwise interactions with all neighbors within the cutoff radius $r_c = \sigma$. If you choose $A > 0$ and $B = 0$ then this is the typical DPD model. The density $\bar{\bar{\rho}}$ uses the same kernel but with a smaller cutoff,

$$\bar{\bar{\rho}}_i = \frac{6}{2\pi r_d^3} \sum_{j \neq i} \left(2 + \frac{r_{ij}}{r_d}\right)\left(1 - \frac{r_{ij}}{r_d}\right)^2 = \sum_{j \neq i} w_d(r_{ij}) \tag{2.38}$$

where the potential is

$$w_d(r_{ij}) = \frac{1}{2v_d}\left(2 + \frac{r_{ij}}{r_d}\right)\left(1 - \frac{r_{ij}}{r_d}\right)^2 \tag{2.39}$$

with $v_d = \pi r_d^3/6$, and $r_d < \sigma$. Here we use $r_d = 0.75\sigma$, which is a typical choice in the literature. Thus, the second term in Equation 2.36 can be written as,

$$B\bar{\bar{\rho}}^2 = B\bar{\bar{\rho}} \sum_{j \neq i} w_d(r_{ij}) \tag{2.40}$$

where $B > 0$ makes this term repulsive. The combination of the two terms in Equation 2.36 ensures the particles are attractive at "long" range and repulsive at short range. In addition, the repulsion grows with the local density. It has been shown that this is sufficient to enable a VDW loop, and can therefore model a liquid-vapor interface.

In addition to the two interaction terms, we include an additional one-body term that accounts for the interaction of a particle with the background. This will account for the change in energy as a particle crosses from the micelle core into the solution. Thus, the self-energy of a particle including the one-body term is

$$u_i = \chi_i + A\bar{\rho}_i + B\bar{\bar{\rho}}_i^2 \tag{2.41}$$

where χ_i is the interaction strength between the particle and the background, and is a function of the particle position. When a particle is immersed within a background of its own type (e.g., A in A, or B in B) then $\chi_i = 0$. When a particle is immersed within a background of the opposing type (e.g., A in B or B in A), then $\chi_i > 0$. We vary χ smoothly across the interface using a tanh switching function.

The presence of the interface also complicates the 2-body interaction terms, since the effective interaction between two particles should depend on the nature of the background fluid. For example, when two A particles are within the A domain, then their interactions should correspond to the theta condition. On the other hand, when two A particles are in the B domain, then their interaction potential should result in overall attraction. As a result, at each step, we assign each particle a value A_i based on the particle type and position relative to the interface. If the particle is in its own domain, then $A_i = A_0$, otherwise $A_i = A$. Then we compute $A_{ij} = (A_i + A_j)/2$ if i and j are of the same type, otherwise $A_{ij} = 0$. These choices ensure that a chain will take a coil conformation in it's own domain and take a collapsed conformation in the opposite domain. We vary the parameters smoothly across the interface using a tanh switching function. Note that all 3-body interaction have the same repulsive constant, $B > 0$. For a given B, we determine the value $A_0 < 0$ that corresponds to the theta-solvent condition.

By summing the self-energies and correcting for overcounting, one can express the total non-bonded potential energy in terms of pairwise interactions only.

$$\beta U = \sum_i \chi_i + \sum_i \sum_{j \neq i} A_{ij} w_c(r_{ij}) + \sum_i \sum_{j \neq i} B(\bar{\bar{\rho}}_i + \bar{\bar{\rho}}_j) w_d(r_{ij}) \tag{2.42}$$

For two isolated particles, we plot the individual components of, and the total interaction potential in Figure 2.21. Obviously, this is only the interaction between two isolated particles, and the repulsive part will grow stronger as particles accumulate more than a single contact.

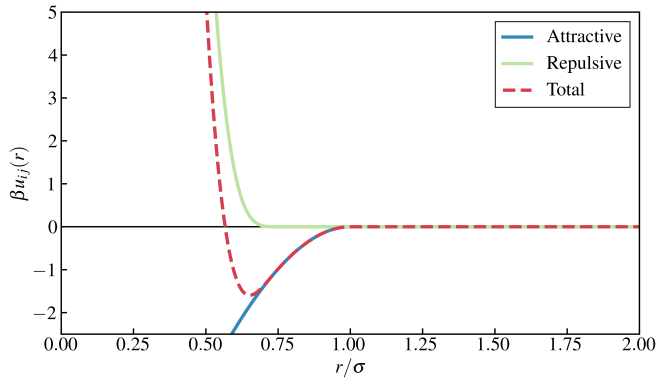

Figure 2.21: Potential between two isolated particles with $A = -6$, $B = 10$, and $r_d = 0.75\sigma$.

Neighboring particles along the backbone also interact via a stiff harmonic bond potential:

$$\beta U_{\mathrm{b}}(r) = \frac{\kappa}{2}(r - b)^2 \tag{2.43}$$

where κ is the spring constant and b is the bond length, which we choose as $b = \sigma$.

Calibration

For a given value of B, we need to determine A_0 such that the polymer takes an ideal conformation within its own domain. We can get an approximate value for A_0 by finding where the second virial coefficient vanishes for two interacting monomers. Figure 2.22 indicates that the theta condition should be near $A_0 = -2.5$. However, we expect the true A_0 to be lower than this value because the repulsion will become stronger when multiple particles overlap.

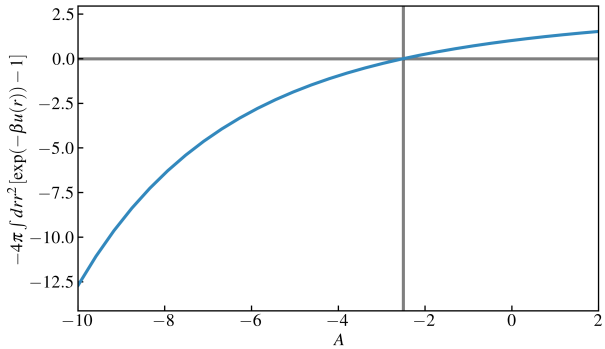

Figure 2.22: 2nd virial coefficient for $B = 10$, $r_d = 0.75$, and $\sigma = 1$.

To determine the actual value of A_0, we compute the radius of gyration for various values of N and A. As shown in Figure 2.23, we find that the actual theta condition

is achieved for approximately $A_0 \approx -4$. Thus, two particles immersed within a fluid of their own kind will interact with $A = -4$ and $B = 10$, while two particles immersed in the poor solvent domain will interact with $A < -4$ and $B = 10$. We choose $A = -6$ to force a collapse without freezing the micelle cores.

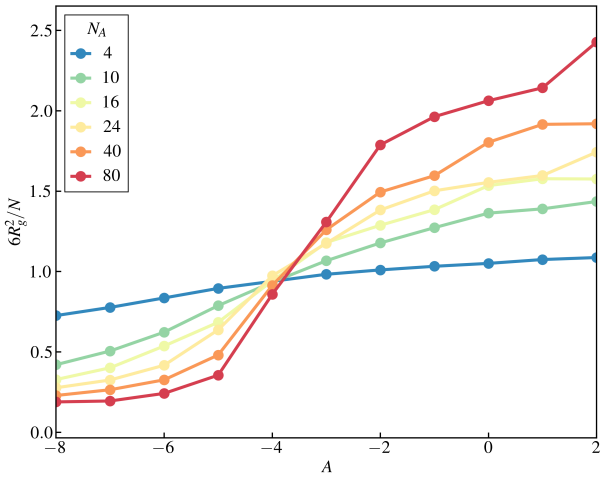

Figure 2.23: Radius of gyration as a function of A for various N with $B = 10$, $\sigma = 1$, and $r_d = 0.75$.

In Figure 2.24, we plot the radius of gyration of a homopolymer for both $A = -4$ and $A = -6$ to show the size-scaling behavior.

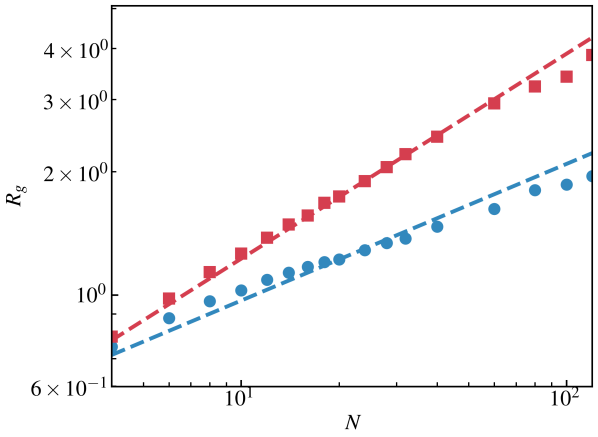

Figure 2.24: Radius of gyration of homopolymers for (red) $A = -4$ and (blue) $B = -6$. The dashed lines correspond to (red) $N^{1/2}$ and (blue) $N^{1/3}$.

Algorithm

To efficiently evaluate the many-body interactions we keep track of the neighbors and local density of each particle. Each polymer has a neighborlist $n[N][z_{\max}+1]$ where the first index is over the monomers, and the second is over the neighbors. The first element is the current number of neighbors, and the remaining elements are the indices of those neighbors. We choose $z_{\max}$ large enough to avoid exceeding the neighborlist limit throughout the simulation, but small enough to avoid excessive memory usage. We also store the particle densities in an array, $\rho[N]$. In addition to these two arrays we create copies n' and ρ' that are used as temporary arrays while making MC attempts.

During an MC move, we endeavor to conduct as few operations as possible using the following set of steps:

1. Compute the interaction of particle i with the background, χ_i.
2. Compute the bonded energy between $i, i-1$ and $i, i+1$.
3. Compute the 2-body interactions between particle i and all other $N-1$ particles. While looping over particles, also do the following:
   a) Count and store the neighbors in $n[i]$
   b) Accumulate the density ρ_i and store in $\rho[i]$
4. Compute the 3-body interactions that will by affected by particle i moving, by doing the following:
   a) Loop over neighbors j of particle i in neighborlist $n[i]$ and compute the 3-body interactions for those particles by looping over their neighbors k in $n[j]$.
      i. If particle k is also a neighbor of i, then multiply 3-body energy between particles j and k, E_{jk}, by $1/2$ to avoid overcounting (since E_{kj} will be addressed as well due to k being in $n[i]$).
      ii. If particle k is not a neighbor of i, then count the full 3-body energy, E_{jk}.
5. Generate a new position for particle i.
6. Compute the new interaction of particle i with the background, χ_i.

7. Compute the new bonded energy between $i, i-1$ and $i, i+1$.

8. Compute the new 2-body interactions between particle i and all other $N-1$ particles. While looping over particles, also do the following:

    a) Count and store the new neighbors in $n'[i]$

    b) Accumulate the new density ρ_i and store in $\rho'[i]$

9. Set the particle coordinates back to their old values

10. Compute old 3-body interactions of particles that were not neighbors of i in $n[i]$, but are neighbors of i in $n'[i]$, by doing the following:

    a) Loop over neighbors j of particle i in neighborlist $n'[i]$

    b) Determine if j is also a neighbor of i in neighborlist $n[i]$

        i. If it is, then break since that old interaction was already counted

        ii. If not, then loop over the old neighbors k of particle j in neighborlist $n[j]$ and add their 3-body interaction with j according to the following criteria...

    c) If particle k is an old neighbor of i in neighborlist $n[i]$, then break since that kj interaction was already counted in Step 4.

    d) If particle k is not an old neighbor of i, then evaluate the 3-body interaction between j and k

        i. If particle k is also a new neighbor of i, then only add $1/2$ the energy E_{jk} to avoid overcounting (since E_{kj} will also be counted)

        ii. If particle k is not a new neighbor of i, then add the full energy E_{jk}.

11. Set coordinates of i back to the values that were generated in Step 5.

12. Compute the new density ρ_i by looping over only neighbors $n'[i]$ and store it in $\rho'[i]$

13. Update neighborlists of new neighbors of i.

    a) Loop over new neighbors j of particle i in list $n'[i]$.

    b) Check if j is an old neighbor of i, if not, then add i to the new neighborlist of j, $n'[j]$.

    c) Either way, compute the new density of particle j and store in $\rho'[j]$.

14. Update neighborlists of old neighbors of i.

    a) Loop over old neighbors j of particle i in list $n[i]$.

    b) Check if j is a new neighbor of i, if not, then remove i from the new neighorlist of j, $n'[j]$.

    c) Either way, compute the new density of particle j and store in $\rho'[j]$.

15. Compute 3-body interactions of new neighbors j of i in neighborlist $n'[i]$.

    a) Loop over neighbors j of particle i in neighborlist $n'[i]$ and compute the 3-body interactions for those particles by looping over their neighbors k in $n'[j]$.

        i. If particle k is also a neighbor of i, then multiply 3-body energy between particles j and k, E_{jk}, by $1/2$ to avoid overcounting (since E_{kj} will be addressed as well due to k being in $n'[i]$).

        ii. If particle k is not a neighbor of i, then count the full 3-body energy, E_{jk}.

16. Compute new 3-body interactions of particles that were neighbors of i in $n[i]$, but are not neighbors of i in $n'[i]$, by doing the following:

    a) Loop over old neighbors j of particle i in neighborlist $n[i]$

    b) Determine if j is also a neighbor of i in new neighborlist $n'[i]$

        i. If it is, then break since that new interaction was already counted in step 15.

        ii. If not, then loop over the new neighbors k of particle j in neighborlist $n'[j]$ and add their 3-body interaction with j according to the following criteria...

    c) If particle k is a new neighbor of i in neighborlist $n'[i]$, then break since that kj interaction was already counted in Step 15.

    d) If particle k is not a new neighbor of i, then evaluate the 3-body interaction between j and k.

        i. If particle k is also an old neighbor of i, then only add $1/2$ the energy E_{jk} to avoid overcounting (since E_{kj} will also be counted)

        ii. If particle k is not an old neighbor of i, then add the full energy E_{jk}.

17. Compute energy difference between the new and old configurations by accumulating all the energy terms that have been computed.

18. Accept move according to Metropolis criterion

    a) If the move is accepted then overwrite n with n'

    b) If the move is rejected then overwrite n' with n

Results and Discussion

Unfortunately, I was not able to collect and analyze enough results with this model this prior to submitting my thesis. I decided to still include the model as inspiration for future work in this area.

2.5 Conclusions

In this study, we utilized coarse-grained molecular dynamics with spectral ABF enhanced sampling to compute the 2d free energy surface for the escape of a copolymer chain from a micelle at high segregation strength, and relatively low density. Our use of two collective variables ensured that the chain conformation was properly sampled during the escape process, and allowed us to observe a bimodal distribution in the chain conformation. In particular, near the transition state, we found that the chain can readily take either a collapsed or an extended conformation where some of the polymer beads remain in the micelle core. While the two conformations have commensurate free energies, they are separated by a large free energy barrier, further indicating the need for explicit biasing of the chain conformation. We computed the minimum free energy path using the string method on the free energy landscape and found it to be in agreement with the originally proposed Halperin–Alexander mechanism, both qualitatively and quantitatively. Namely, the MFEP featured a collapsed core block at the transition state that ultimately yielded a free energy barrier that scaled as $N_A^{2/3}$. Our 2d FES using the $R_{\text{cm-jp}}$ CV featured a broad region where the chain is still tethered to the micelle with a portion of the core block extended into the solution, indicating a high propensity for the extended conformation to exist. While these results are compelling in their validation of the Halperin–Alexander mechanism, they do not agree with experimentally observed scaling relationships of several TR-SANS experiments. This provides support for the idea that the core block is not fully collapsed during escape, which prompted us to study the escape mechanism for chains in a lamellae-forming diblock copolymer melt.

To compute the transition pathway in the high-density limit we conducted single-chain Monte Carlo simulations with forward flux sampling. We utilized a simplified model with a single bead-spring copolymer chain immersed in a mean-field background containing a sharp interface. We computed the rate and free energy barrier for escape using millions of independent forward flux sampling trajectories. The resulting free energy barrier scaled linearly with N_A for different choices of collective variables. The linear scaling is in good agreement with experimental observations from TR-SANS measurements. We analyzed the properties of the polymer chains along the escape trajectories using the forward flux ensemble and the reactive ensemble and found that a large majority of the chains escape via an extended conformation, rather than the collapsed conformation of the Halperin–Alexander mechanism. We also employed umbrella sampling to compute the 2d FES of the single-chain model and found that the reactive trajectories collected from FFS were described well by the shape of the landscape. We found that the bead-by-bead mechanism manifests as a gentle gradient pathway on the FES as compared to an unperturbed escape mechanism. Overlaying the reactive trajectories on top of the FES revealed that chains do in fact prefer to escape bead-by-bead initially, up until the point where the stretched chain has a free energy nearly commensurate with the escaped chain, at which point the chain will collapse and escape. We note that this picture agrees very well with the mechanism proposed by Seeger et al. [38, 39].

In this work we provided a detailed analysis of the different possible mechanisms for a diblock copolymer chain to escape from a micelle using two different simulation techniques. While the simulations were restricted to a narrow range of parameters, we were able to identify different pathways and their relative importance to chain exchange. In a future work we plan to use forward flux sampling simulations to do a more comprehensive study of the effect of the chain and matrix properties on the escape rate and mechanism. In addition, we hope to conduct studies using the many-body simulation in order to determine the kinetic pathway within the Halperin–Alexander regime.

References

(1) Varner, S.; Müller, M.; Gallegos, A., et al. Mechanisms of Chain Exchange in Diblock Copolymer Micelles, 2025, DOI: 10.48550/arXiv.2509.06528.

(2) Halperin, A.; Alexander, S. Polymeric micelles: their relaxation kinetics. *Macromolecules* **1989**, *22*, 2403–2412, DOI: 10.1021/ma00195a069.

(3) Halperin, A. On Micellar Exchange: The Role of the Insertion Penalty. *Macromolecules* **2011**, *44*, 5072–5074, DOI: 10.1021/ma200811x.

(4) Nyrkova, I. A.; Semenov, A. N. On the Theory of Micellization Kinetics. *Macromolecular Theory and Simulations* **2005**, *14*, 569–585, DOI: 10.1002/mats.200500010.

(5) Cao, T.; Munk, P.; Ramireddy, C.; Tuzar, Z.; Webber, S. E. Fluorescence studies of amphiphilic poly(methacrylic acid)-block-polystyrene-block-poly(methacrylic acid) micelles. *Macromolecules* **1991**, *24*, 6300–6305, DOI: 10.1021/ma00023a036.

(6) Creutz, S.; van Stam, J.; Antoun, S.; De Schryver, F. C.; Jérôme, R. Exchange of Polymer Molecules between Block Copolymer Micelles Studied by Emission Spectroscopy. A Method for the Quantification of Unimer Exchange Rates. *Macromolecules* **1997**, *30*, 4078–4083, DOI: 10.1021/ma961922i.

(7) Creutz, S.; van Stam, J.; De Schryver, F. C.; Jérôme, R. Dynamics of Poly((dimethylamino)alkyl methacrylate-block-sodium methacrylate) Micelles. Influence of Hydrophobicity and Molecular Architecture on the Exchange Rate of Copolymer Molecules. *Macromolecules* **1998**, *31*, 681–689, DOI: 10.1021/ma970987y.

(8) Müller, M. Single-Chain Conformations in Symmetric Binary Polymer Blends: Quantitative Comparison between Self-Consistent Field Calculations and Monte Carlo Simulations. *Macromolecules* **1998**, *31*, 9044–9057, DOI: 10.1021/ma9807973.

(9) Helfand, E.; Tagami, Y. Theory of the Interface between Immiscible Polymers. II. *J. Chem. Phys.* **1972**, *56*, 3592–3601, DOI: 10.1063/1.1677735.

(10) Müller, M. Dynamics of Nonequilibrium Single-Chain Conformations in Triblock Copolymers. *Macromolecules* **2021**, *54*, 6296–6311, DOI: 10.1021/acs.macromol.1c00781.

(11) Prochazka, K.; Bednar, B.; Mukhtar, E., et al. Nonradiative energy transfer in block copolymer micelles. *The Journal of Physical Chemistry* **1991**, *95*, 4563–4568, DOI: 10.1021/j100164a069.

(12) Wang, Y.; Kausch, C. M.; Chun, M.; Quirk, R. P.; Mattice, W. L. Exchange of Chains between Micelles of Labeled Polystyrene-block-poly(oxyethylene) As Monitored by Nonradiative Singlet Energy Transfer. *Macromolecules* **1995**, *28*, 904–911, DOI: 10.1021/ma00108a016.

(13) Smith, C. K.; Liu, G. Determination of the Rate Constant for Chain Insertion into Poly(methyl methacrylate)-block-poly(methacrylic acid) Micelles by a Fluorescence Method. *Macromolecules* **1996**, *29*, 2060–2067, DOI: 10.1021/ma951338u.

(14) Underhill, R. S.; Ding, J.; Birss, V. I.; Liu, G. Chain Exchange Kinetics of Polystyrene-block-poly(2-cinnamoylethyl methacrylate) Micelles in THF/Cyclopentane Mixtures. *Macromolecules* **1997**, *30*, 8298–8303, DOI: 10.1021/ma9710545.

(15) Rager, T.; Meyer, W. H.; Wegner, G. Micelle formation of poly(acrylic acid)-block-poly(methyl methacrylate) block copolymers in mixtures of water with organic solvents. *Macromolecular Chemistry and Physics* **1999**, *200*, 1672–1680, DOI: 10.1002/(SICI)1521-3935(19990701)200:7<1672::AID-MACP1672>3.0.CO;2-V.

(16) Van Stam, J.; Creutz, S.; De Schryver, F. C.; Jérôme, R. Tuning of the Exchange Dynamics of Unimers between Block Copolymer Micelles with Temperature, Cosolvents, and Cosurfactants. *Macromolecules* **2000**, *33*, 6388–6395, DOI: 10.1021/ma992174a.

(17) Willner, L.; Poppe, A.; Allgaier, J.; Monkenbusch, M.; Richter, D. Time-resolved SANS for the determination of unimer exchange kinetics in block copolymer micelles. *Europhysics Letters* **2001**, *55*, 667, DOI: 10.1209/epl/i2001-00467-y.

(18) Won, Y.-Y.; Davis, H. T.; Bates, F. S. Molecular Exchange in PEO-PB Micelles in Water. *Macromolecules* **2003**, *36*, 953–955, DOI: 10.1021/ma021439+.

(19) Lu, J.; Bates, F. S.; Lodge, T. P. Remarkable Effect of Molecular Architecture on Chain Exchange in Triblock Copolymer Micelles. *Macromolecules* **2015**, *48*, 2667–2676, DOI: 10.1021/acs.macromol.5b00294.

(20) Aniansson, E. A. G.; Wall, S. N. Kinetics of step-wise micelle association. *The Journal of Physical Chemistry* **1974**, *78*, 1024–1030, DOI: 10.1021/j100603a016.

(21) Aniansson, E. A. G.; Wall, S. N. Kinetics of step-wise micelle association. Correction and improvement. *The Journal of Physical Chemistry* **1975**, *79*, 857–858, DOI: 10.1021/j100575a019.

(22) Lund, R.; Willner, L.; Stellbrink, J.; Lindner, P.; Richter, D. Logarithmic Chain-Exchange Kinetics of Diblock Copolymer Micelles. *Physical Review Letters* **2006**, *96*, 068302, DOI: 10.1103/PhysRevLett.96.068302.

(23) Lund, R.; Willner, L.; Richter, D.; Dormidontova, E. E. Equilibrium Chain Exchange Kinetics of Diblock Copolymer Micelles: Tuning and Logarithmic Relaxation. *Macromolecules* **2006**, *39*, 4566–4575, DOI: 10.1021/ma060328y.

(24) Lund, R.; Willner, L.; Richter, D., et al. Unraveling the equilibrium chain exchange kinetics of polymeric micelles using small-angle neutron scattering – architectural and topological effects. *Journal of Applied Crystallography* **2007**, *40*, s327–s331, DOI: 10.1107/S0021889807005201.

(25) Choi, S.-H.; Lodge, T. P.; Bates, F. S. Mechanism of Molecular Exchange in Diblock Copolymer Micelles: Hypersensitivity to Core Chain Length. *Physical Review Letters* **2010**, *104*, 047802, DOI: 10.1103/PhysRevLett.104.047802.

(26) Zinn, T.; Willner, L.; Lund, R.; Pipich, V.; Richter, D. Equilibrium exchange kinetics in n-alkyl–PEO polymeric micelles: single exponential relaxation and chain length dependence. *Soft Matter* **2011**, *8*, 623–626, DOI: 10.1039/C1SM06809A.

(27) Lu, J.; Choi, S.; Bates, F. S.; Lodge, T. P. Molecular Exchange in Diblock Copolymer Micelles: Bimodal Distribution in Core-Block Molecular Weights. *ACS Macro Letters* **2012**, *1*, 982–985, DOI: 10.1021/mz300285x.

(28) Lund, R.; Willner, L.; Pipich, V., et al. Equilibrium Chain Exchange Kinetics of Diblock Copolymer Micelles: Effect of Morphology. *Macromolecules* **2011**, *44*, 6145–6154, DOI: 10.1021/ma200532r.

(29) Ma, Y.; Lodge, T. P. Chain Exchange Kinetics in Diblock Copolymer Micelles in Ionic Liquids: The Role of χ. *Macromolecules* **2016**, *49*, 9542–9552, DOI: 10.1021/acs.macromol.6b02212.

(30) Cavicchi, K. A.; Lodge, T. P. Self-Diffusion and Tracer Diffusion in Sphere-Forming Block Copolymers. *Macromolecules* **2003**, *36*, 7158–7164, DOI: 10.1021/ma0346815.

(31) Yokoyama, H.; Kramer, E. J. Self-Diffusion of Asymmetric Diblock Copolymers with a Spherical Domain Structure. *Macromolecules* **1998**, *31*, 7871–7876, DOI: 10.1021/ma9805250.

(32) Yokoyama, H.; Kramer, E. J. Diffusion of Triblock Copolymers in a Spherical Domain Structure. *Macromolecules* **2000**, *33*, 954–959, DOI: 10.1021/ma991202m.

(33) Li, Z.; Dormidontova, E. E. Kinetics of Diblock Copolymer Micellization by Dissipative Particle Dynamics. *Macromolecules* **2010**, *43*, 3521–3531, DOI: 10.1021/ma902860j.

(34) Li, Z.; Dormidontova, E. E. Equilibrium chain exchange kinetics in block copolymer micelle solutions by dissipative particle dynamics simulations. *Soft Matter* **2011**, *7*, 4179–4188, DOI: 10.1039/C0SM01443E.

(35) Prhashanna, A.; Khan, S. A.; Chen, S. B. Kinetics of Chain Exchange between Diblock Copolymer Micelles. *Macromolecular Theory and Simulations* **2016**, *25*, 383–391, DOI: 10.1002/mats.201600016.

(36) Prhashanna, A.; Chen, S. B. Chain exchange kinetics between linear ABA-type triblock copolymer micelles. *Polymer* **2017**, *118*, 22–29, DOI: 10.1016/j.polymer.2017.04.049.

(37) Prhashanna, A.; Dormidontova, E. E. Micelle Self-Assembly and Chain Exchange Kinetics of Tadpole Block Copolymers with a Cyclic Corona Block. *Macromolecules* **2020**, *53*, 982–991, DOI: 10.1021/acs.macromol.9b02398.

(38) Seeger, S. C.; Dorfman, K. D.; Lodge, T. P. Free Energy Trajectory for Escape of a Single Chain from a Diblock Copolymer Micelle. *ACS Macro Letters* **2021**, *10*, 1570–1575, DOI: 10.1021/acsmacrolett.1c00508.

(39) Seeger, S. C.; Lodge, T. P.; Dorfman, K. D. Mechanism of Escape of a Single Chain from a Diblock Copolymer Micelle. *Macromolecules* **2022**, *55*, 10220–10228, DOI: 10.1021/acs.macromol.2c01742.

(40) Yuan, F.; Wang, S.; Larson, R. G. Potentials of Mean Force and Escape Times of Surfactants from Micelles and Hydrophobic Surfaces Using Molecular Dynamics Simulations. *Langmuir* **2015**, *31*, 1336–1343, DOI: 10.1021/la5044393.

(41) Wen, B.; Bai, B.; Larson, R. G. Surfactant desorption and scission free energies for cylindrical and spherical micelles from umbrella-sampling molecular dynamics simulations. *Journal of Colloid and Interface Science* **2021**, *599*, 773–784, DOI: 10.1016/j.jcis.2021.04.138.

(42) Barducci, A.; Bonomi, M.; Parrinello, M. Metadynamics. *WIREs Computational Molecular Science* **2011**, *1*, 826–843, DOI: 10.1002/wcms.31.

(43) Van Erp, T. S.; Moroni, D.; Bolhuis, P. G. A novel path sampling method for the calculation of rate constants. *The Journal of Chemical Physics* **2003**, *118*, 7762–7774, DOI: 10.1063/1.1562614.

(44) Allen, R. J.; Frenkel, D.; ten Wolde, P. R. Forward flux sampling-type schemes for simulating rare events: Efficiency analysis. *The Journal of Chemical Physics* **2006**, *124*, 194111, DOI: 10.1063/1.2198827.

(45) Borrero, E. E.; Escobedo, F. A. Reaction coordinates and transition pathways of rare events via forward flux sampling. *The Journal of Chemical Physics* **2007**, *127*, 164101, DOI: 10.1063/1.2776270.

(46) Groot, R. D.; Warren, P. B. Dissipative particle dynamics: Bridging the gap between atomistic and mesoscopic simulation. *The Journal of Chemical Physics* **1997**, *107*, 4423–4435, DOI: 10.1063/1.474784.

(47) Mysona, J. A.; McCormick, A. V.; Morse, D. C. Simulation of diblock copolymer surfactants. I. Micelle free energies. *Physical Review E* **2019**, *100*, 012602, DOI: 10.1103/PhysRevE.100.012602.

(48) Lodge, T. P.; Seitzinger, C. L.; Seeger, S. C., et al. Dynamics and Equilibration Mechanisms in Block Copolymer Particles. *ACS Polymers Au* **2022**, *2*, 397–416, DOI: 10.1021/acspolymersau.2c00033.

(49) Eastman, P.; Galvelis, R.; Peláez, R. P., et al. OpenMM 8: Molecular Dynamics Simulation with Machine Learning Potentials. *Journal of Physical Chemistry B* **2023**, *128*, 109–116, DOI: 10.1021/acs.jpcb.3c06662.

(50) Ye, B. B.; Walker, P. J.; Wang, Z.-G. MDCraft: A Python assistant for performing andanalyzing molecular dynamics simulations of soft matter systems. *Journal of Open Source Software* **2024**, *9*, 7013, DOI: 10.21105/joss.07013.

(51) Zubieta Rico, P. F.; Schneider, L.; Pérez-Lemus, G. R., et al. PySAGES: flexible, advanced sampling methods accelerated with GPUs. *npj Computational Materials* **2024**, *10*, 1–12, DOI: 10.1038/s41524-023-01189-z.

(52) Zubieta Rico, P. F.; Pérez-Lemus, G. R.; de Pablo, J. J. Efficient sampling of free energy landscapes with functions in Sobolev spaces. *The Journal of Chemical Physics* **2025**, *162*, 084109, DOI: 10.1063/5.0221263.

(53) McGovern, M.; de Pablo, J. A boundary correction algorithm for metadynamics in multiple dimensions. *The Journal of Chemical Physics* **2013**, *139*, 084102, DOI: 10.1063/1.4818153.

(54) E, W.; Ren, W.; Vanden-Eijnden, E. String method for the study of rare events. *Physical Review B* **2002**, *66*, 052301, DOI: 10.1103/PhysRevB.66.052301.

(55) E, W.; Ren, W.; Vanden-Eijnden, E. Simplified and improved string method for computing the minimum energy paths in barrier-crossing events. *The Journal of Chemical Physics* **2007**, *126*, 164103, DOI: 10.1063/1.2720838.

(56) E, W.; Vanden-Eijnden, E. Transition-Path Theory and Path-Finding Algorithms for the Study of Rare Events. *Annual Review of Physical Chemistry* **2010**, *61*, 391–420, DOI: 10.1146/annurev.physchem.040808.090412.

(57) Müller, M. Studying Amphiphilic Self-assembly with Soft Coarse-Grained Models. *Journal of Statistical Physics* **2011**, *145*, 967–1016, DOI: 10.1007/s10955-011-0302-z.

(58) Daoulas, K. C.; Müller, M. Single chain in mean field simulations: Quasi-instantaneous field approximation and quantitative comparison with Monte Carlo simulations. *The Journal of Chemical Physics* **2006**, *125*, 184904, DOI: 10.1063/1.2364506.

(59) Schneider, L.; Müller, M. Multi-architecture Monte-Carlo (MC) simulation of soft coarse-grained polymeric materials: SOft coarse grained Monte-Carlo Acceleration (SOMA). *Computer Physics Communications* **2019**, *235*, 463–476, DOI: 10.1016/j.cpc.2018.08.011.

(60) O'Neill, M. E. *PCG: A Family of Simple Fast Space-Efficient Statistically Good Algorithms for Random Number Generation*; tech. rep. HMC-CS-2014-0905; Claremont, CA: Harvey Mudd College, 2014.

(61) Hussain, S.; Haji-Akbari, A. Studying rare events using forward-flux sampling: Recent breakthroughs and future outlook. *The Journal of Chemical Physics* **2020**, *152*, 060901, DOI: 10.1063/1.5127780.

(62) Choi, S.-H.; Bates, F. S.; Lodge, T. P. Molecular Exchange in Ordered Diblock Copolymer Micelles. *Macromolecules* **2011**, *44*, 3594–3604, DOI: 10.1021/ma102788v.

(63) Wu, C.; Wang, X. Globule-to-Coil Transition of a Single Homopolymer Chain in Solution. *Physical Review Letters* **1998**, *80*, 4092–4094, DOI: 10.1103/PhysRevLett.80.4092.

(64) Wang, X.; Qiu, X.; Wu, C. Comparison of the Coil-to-Globule and the Globule-to-Coil Transitions of a Single Poly(N-isopropylacrylamide) Homopolymer Chain in Water. *Macromolecules* **1998**, *31*, 2972–2976, DOI: 10.1021/ma971873p.

(65) Hub, J. S.; de Groot, B. L.; van der Spoel, D. g_wham—A Free Weighted Histogram Analysis Implementation Including Robust Error and Autocorrelation Estimates. *Journal of Chemical Theory and Computation* **2010**, *6*, 3713–3720, DOI: 10.1021/ct100494z.

(66) Roux, B. The calculation of the potential of mean force using computer simulations. *Computer Physics Communications* **1995**, *91*, 275–282, DOI: 10.1016/0010-4655(95)00053-I.

(67) Grossfield, A. An implementation of WHAM: the Weighted Histogram Analysis Method Version 2.1.0.

(68) Warren, P. B. Vapor-liquid coexistence in many-body dissipative particle dynamics. *Physical Review E* **2003**, *68*, DOI: 10.1103/PhysRevE.68.066702.

(69) Han, Y.; Jin, J.; Voth, G. A. Constructing many-body dissipative particle dynamics models of fluids from bottom-up coarse-graining. *The Journal of Chemical Physics* **2021**, *154*, 084122, DOI: 10.1063/5.0035184.

(70) Di Giusto, D.; Castagna, J. A scalable algorithm for many-body dissipative particle dynamics using multiple general purpose graphic processing units. *Computer Physics Communications* **2022**, *280*, 108472, DOI: 10.1016/j.cpc.2022.108472.

(71) Hendrikse, R. L.; Amador, C.; Wilson, M. R. A many-body dissipative particle dynamics parametrisation scheme to study behaviour at air–water interfaces. *Soft Matter* **2023**, *19*, 3590–3604, DOI: 10.1039/D3SM00276D.

Chapter 3

KINETIC PATHWAY TO COPOLYMER MICELLES VIA THIN FILM DISSOLUTION

Surfactant and polymer-based micelles are abundant in nature and widely utilized across diverse applications, from drug delivery to viscosity modification in oils and consumer products. Micelles equilibrate via two principal processes: chain expulsion/insertion and micelle fission/fusion. For surfactants and lipids, these processes occur on subsecond timescales, but in longer-chain diblock copolymers, higher free energy barriers significantly slow equilibration. This presents challenges for achieving equilibrium in micelle size and concentration, making it desirable to develop reliable methods for producing micelle solutions with targeted, narrow size distributions. In this chapter, we use coarse-grained molecular dynamics simulations and a version of self-consistent field theory to explore a kinetic pathway for forming large diblock copolymer micelles by dissolving a lamellar phase in a selective solvent. This pathway circumvents kinetic traps due to large free energy barriers in equilibration processes such as single-chain exchange and micelle fusion.

I am very thankful for many fruitful discussions with Prof. Tim Lodge. The opportunity to work and collaborate with such an incredible experimentalist has inspired me greatly and shaped the way that I think about problems immensely.

3.1 Introduction

Diblock copolymers in selective solvents can self-assemble into a variety of micellar structures such as spheres, cylinders, and vesicles [1, 2], similar to surfactants and other amphiphiles. Unlike small-molecule surfactants, however, diblock copolymers typically have large molecular weights and strongly hydrophobic core blocks. As a result, micelle equilibration processes such as single-chain exchange and micelle fusion can be exceedingly slow, requiring hours, days, or even years to reach equilibrium [3]. Nyrkova and Semenov [4] proposed that quenching a copolymer solution deeply into the micellar regime leads to the formation of small, kinetically trapped micelles. Initially, small aggregates form rapidly, and their average size increases slowly through fusion and exchange. However, as aggregates grow, the barriers to these processes increase as well [4, 5]. Thus, micellization is better described by a continuous spectrum of relaxation times that lengthen with aggregate size, rather

than by a simple two-step process consisting of one fast and one slow step. If the interfacial tension γ is sufficiently large, the system may remain trapped at a smaller, relatively polydisperse size distribution and never reach true equilibrium [3, 6]. This kinetic trapping has been observed in experiments [7–13] and simulations [14–16].

A traditional method for preparing copolymer solutions involves the use of a co-solvent. In the cosolvent-assisted dissolution (CS) method, the copolymer is first dissolved in a good solvent for both blocks so that no micellization occurs. A selective solvent is then slowly added, triggering micellization once the effective solvent quality for the core block becomes poor enough. Alternatively, the copolymer can be dissolved in a good solvent mixture, followed by slow removal of one component through evaporation. This approach often produces small, polydisperse micelles due to kinetic trapping [9, 10, 17]. In contrast, the direct dissolution (DD) method involves dissolving the copolymer directly in a selective solvent while heating at a moderate temperature. A related approach, thin film dissolution (TF), entails casting the copolymer into a thin film and subsequently dissolving it directly in a selective solvent [18].

Meli and Lodge investigated the path dependence of micellization using PB-PEO diblock copolymers dissolved in an ionic liquid selective solvent. In their original study [9], they examined PB-PEO (8-7), which has a core block fraction of $f_{\mathrm{PB}} = 0.61$. They found that micelles formed via the DD and TF methods were significantly larger and more polydisperse than those produced by the CS method. Upon annealing at elevated temperature, the DD/TF micelles shrank by a factor of approximately 2, while the CS micelles remained essentially unchanged. The annealed DD/TF micelles maintained stable size distributions upon further annealing, despite still being larger than the CS micelles, strongly suggesting that equilibrium had been reached. In a subsequent study [10], they extended their work to PB-PEO (8-15), with a smaller core fraction of $f_{\mathrm{PB}} = 0.40$. For these chains, the DD/TF micelles were about twice as large as those produced by the CS method. Extended thermal annealing caused only a slight size decrease in the DD/TF micelles and no measurable change in the CS micelles. They also observed that the PB-PEO (8-15) micelles were much less polydisperse than the PB-PEO (8-7) micelles, with polydispersities comparable to or even lower than those of the CS micelles from the same composition. Thus, two stable yet distinct and narrow size distributions were obtained from the two different methods. They hypothesized that the small CS micelles are trapped in a metastable state due to significantly slowed equilibration

dynamics at large core-solvent incompatibility. They also hypothesized that the narrow size distribution in the CS micelles originates from the slow evaporation of the cosolvent, which allows the micelles to reach equilibrium at an intermediate cosolvent concentration before the equilibration dynamics are frozen. As proposed by Nyrkova and Semenov [4], the distribution should be broader if the quench occurs more rapidly.

In this work, we investigate the kinetic pathway of the TF method in the star-like regime using dissipative particle dynamics (DPD) simulations. We also examine micellization kinetics when chains dissolved in a cosolvent are rapidly quenched deep into the micellar region of the phase diagram by swapping the cosolvent for a highly selective solvent. We compare the final size distributions from the two methods and their dependence on the core block fraction. We then develop a self-consistent field theory based on DPD (DPD-SCFT) to compute the free energy of intermediate states along the kinetic pathway and determine whether the final micelles from the TF method are close to their equilibrium size, as hypothesized by Meli and Lodge [10].

3.2 Dissipative Particle Dynamics

We model diblock copolymers in an explicit solvent using highly coarse-grained molecular dynamics simulations. We employ a variant of a dissipative particle dynamics (DPD) [19] model that has been used previously to study microphase separation in polymer melts [20–22] and confined thin films [23–25], and micellization in copolymer solutions [26–29].

Polymers are made up of N total beads that are divided into a core block with N_A beads and a corona block with N_B beads, and the solvent is monomeric. For simplicity, we set the effective bead size, d_p, to be same for all species (A, B, S). Adjacent monomers within the same polymer chain are connected via a harmonic potential that gives rise to the force

$$\mathbf{F}_{ij}^{b} = \kappa(r_{ij} - b)\hat{\mathbf{r}}_{ij} \tag{3.1}$$

where κ is the spring constant, b is the equilibrium bond distance, and r_{ij} and $\hat{\mathbf{r}}_{ij}$ are the distance and unit vector (respectively) between the two particles. We use a spring constant of $\kappa = 100\, k_B T/d_p^2$ and $b = d_p$. Since we simulate relatively short chains, the traditional Gaussian chain model with $r_0 = 0$ and $\kappa \approx 4\, k_B T/d_p^2$ is not appropriate. It has been shown previously that those parameters can result in the blocks collapsing to minimize their bond energy, even after phase separation occurs,

and therefore should only be applied to very long chains. This collapse does not occur with the freely-jointed chain model used here.

In addition to the bonded interactions, particles interact with a purely repulsive, short-ranged, soft force that is commonly employed in DPD simulations [19],

$$\mathbf{F}_{ij}^{c} = \begin{cases} -a_{ij}(1 - r_{ij}/d_p)\hat{\mathbf{r}}_{ij} & , r_{ij} \leq d_p \\ 0 & , r_{ij} > d_p \end{cases} \tag{3.2}$$

where a_{ij} is the repulsion strength. For DPD, Groot and Warren argued that the density and base repulsion parameter should obey the relationship $a_{ii}\rho = 75k_BT/d_p$ where k_B is the Boltzmann constant and T is the temperature. Since we conduct simulations at a reduced density of $\rho_0 d_p^3 = \rho = 3$, we set the base repulsion accordingly to $a_{ii} = 25\, k_BT/d_p$. In addition to the conservative forces, there are two additional forces employed in DPD that represent thermal fluctuations and drag forces. The combination of these forces act to thermostat the system and also preserve hydrodynamics. These are given by,

$$\mathbf{F}_{ij}^{R} = \sigma w(r_{ij})\theta_{ij}(\Delta t)^{-1/2}\hat{\mathbf{r}}_{ij} \tag{3.3}$$

$$\mathbf{F}_{ij}^{D} = -\gamma w^2(r_{ij})(\hat{\mathbf{r}}_{ij} \cdot \mathbf{v}_{ij})\hat{\mathbf{r}}_{ij} \tag{3.4}$$

where $w(r) = (1 - r/d_p)$ for $r \leq d_p$ and 0 otherwise, $\mathbf{v}_{ij}$ is the difference in the velocities of the two particles $\mathbf{v}_{ij} = \mathbf{v}_i - \mathbf{v}_j$, σ is the amplitude of the random force, $\gamma = \sigma^2/(2k_BT)$ is the friction coefficient of the drag force, θ_{ij} is a random Gaussian variable with zero mean and unit variance, and Δt is the timestep size. In line with previous DPD simulations of diblock copolymer thin films [23], we set $\sigma = 0.10\, k_BT\tau^{1/2}/d_p$, and therefore $\gamma = 0.005\, k_BT\tau/d_p^2$, where $\tau = (md_p^2/k_BT)^{1/2}$ is the unit of time. For simplicity, we set $m = 1$, $d_p = 1$, and $k_BT = 1$. In most cases, we use a timestep of $\Delta t = 0.015\tau$, however, in some cases such as immediately following a parameter quench, we use a much smaller timestep of $\Delta t = 0.001\tau$ to stabilize the simulation. ALl simulations are conducted with the LAMMPS software (v. June 27, 2024) [30]. In the remainder of this work, we will omit units from parameters for simplicity.

Lamellar Domain Spacing

The starting point for the TF method is a microphase separated copolymer melt, usually in the lamellar phase. To determine the equilibrium domain spacing of the lamellar phase for each set of parameters, we simulate a single lamellar period (one

A domain and one B domain) in the NPT ensemble. We determined the correct pressure at $\rho = 3$ and $a_{ii} = 25$ to be $P \approx 21.4\, k_B T / d_p^3$ by running a long NVT simulation and measuring the stress tensor. We use the Berendsen barostat to set equal pressure in all dimensions and couple the size of two dimensions. The size of the coupled dimensions remains proportional according to the initial state. The choice of which dimensions to couple depends on whether the initial domain spacing D_0 is greater than or less than the equilibrium spacing D. If the initial state is not significantly far from equilibrium, the barostat and size coupling allows for the lamellae to grow or shrink in the normal direction (and adjust the other dimensions accordingly) until the stress vanishes in all dimensions. We found that if $D_0 < D$, then coupling the two dimension parallel to the interface is effective. On the other hand, if $D_0 > D$, then it is better to couple the normal dimension to one of the parallel dimensions.

We note that one could instead run many simulations with different cubic box sizes, $V = L^3$, and the stress tensor will become isotropic at $L = D$ [31]. However, we prefer the method presented here since it only requires a single relatively short simulation.

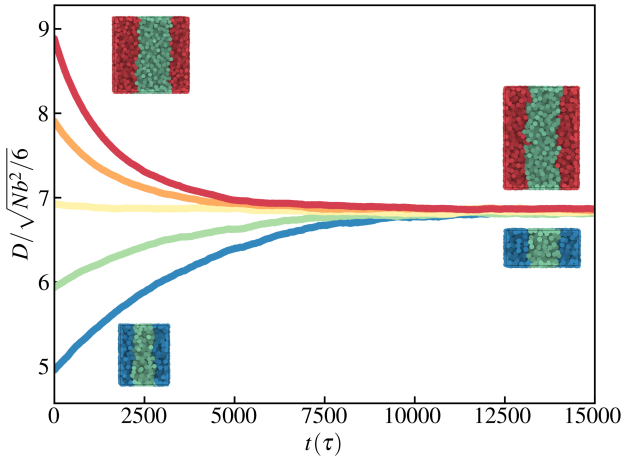

Figure 3.1: Lamellar domain spacing relaxation from NPT simulations for $N_A = 12$, $N_B = 15$, $\Delta a = 20$. Different curves correspond to different initial domain spacings. Lower snapshots correspond to $D_0 = 5R_g^0$, where x and y were coupled. Upper snapshows correspond to $D_0 = 9R_g^0$ where y and z were coupled. The surface normal to the lamellar interface is in the x-direction.

Thin Film Dissolution

In the thin film (TF) dissolution method, a diblock copolymer thin film (usually in the ordered state) is exposed directly to a selective solvent. In this section, we

outline how we conduct *in silico* experiments of the TF method.

Using the domain spacing obtained from the melt simulations, we create a thin film with 4 lamellar periods sandwiched in between two non-solvent bulks. In the experiment, the thin film is usually formed against a substrate so that only one face is exposed to the air/vacuum [9, 10]. This means that the selective solvent is also only introduced to a single face. Since the DPD model used here is purely repulsive and incompressible, this poses a challenge for attaching the thin film to a solid substrate, and makes it impossible to model a true vapor phase. Instead, we start by making the solvent a non-solvent to both polymer blocks. After the polymer and solvent undergo macrophase separation, the polymer thin film undergoes microphase separation into a lamellar morphology. We use a dragging force to orient the 4 lamellar domains perpendicular to the solvent-polymer interface. Once the domains are oriented, we release the dragging force and allow the system to equilibrate for $5 \cdot 10^5$ timesteps. An example of the equilibrated thin film is given in Figure 3.2. For independent productions runs, we start with an additional $5 \cdot 10^5$ timesteps of equilibration to produce completely uncorrelated initial configurations.

To replicate the dissolution of a thin film in a selective solvent, we take an initial lamellar structure in a nonsolvent, as in Figure 3.2, and instantaneously decrease Δa_{BS} down to 0. In other words, the nonsolvent is swapped for solvent that is

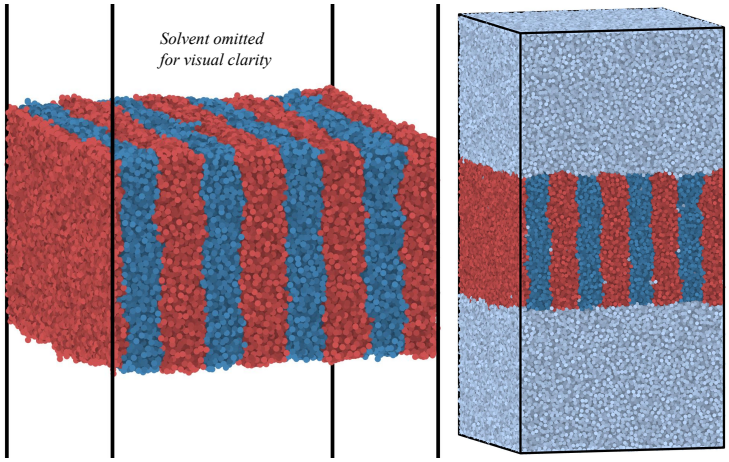

Figure 3.2: Initial structure of thin film dissolution simulations meant to replicate the experimental case of a thin film in contact with air/vacuum. Diblock copolymer lamellae with 4 domains are created by setting $a_{AB} = a_{AS} = a_{\mathrm{BS}} = 45 = a_{ii} + 20$ and dragging the polymer to $z = L_z/2$. This particular simulation has $N_A = 12$, $N_B = 15$, $n_p = 12,220$ and $n_s = 669,878$, where n_p is the number of polymers and n_s is the number of solvent molecules.

selective for the B block. In this case we choose the selective solvent to have the same chemical identity as the monomers of the B block in order to limit the number of independent parameters in the simulations. Immediately after $\Delta a_{\mathrm{BS}} = 0$, the solvent rushes into the B block rapidly which can cause the simulation to become unstable with $\Delta t = 0.015$. To combat this, we use a smaller timestep of $\Delta t = 0.001$ until the solvent has fully penetrated the lamellar domain, at which point we increase it back to $\Delta t = 0.015$. After the solvent quench step, the simulation is run for an additional $3 \cdot 10^6$ steps, or until the lamellae are fully dissolved into spherical micelles.

To ensure that the process is independent of the specific initial state, and to collect sufficient statistics on the final micelle sizes, we conduct simulations of 5 replicas for each value of N_A. All simulations are done in the NVT ensemble since we already determined the optimal lamellar spacing from the small diblock melt simulations.

Cosolvent Assisted Dissolution

There are two common variants of the cosolvent (CS) assisted dissolution method. In one approach, copolymer is dissolved in a mixture of the target selective solvent and a volatile cosolvent. As the cosolvent evaporates the interfacial tension increases and micelles form. Alternatively, a copolymer dissolved in a cosolvent is titrated into the target selective solvent, where micelles form immediately upon mixing [9, 10]. In this section, we describe how we conduct *in silico* experiments of the CS method.

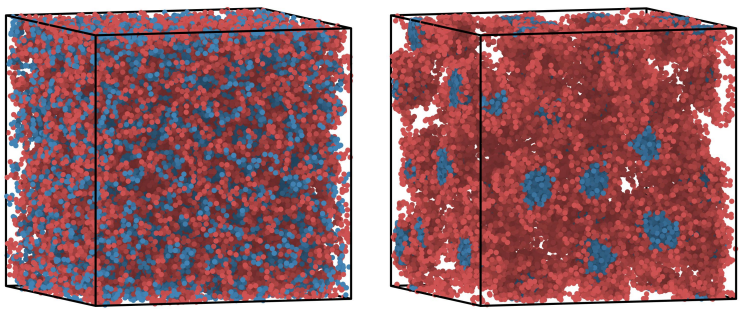

Figure 3.3: (left) initial and (right) final structure of the cosolvent assisted dissolution simulations. This particular visualization is for $\Delta a_{AS} = 20$, $N_A = 12$, $N_B = 15$, $n_p = 1,925$ and $n_s = 347,832$, where n_p is the number of polymers and n_s is the number of solvent molecules. This corresponds to a 13 %v/v solution.

We start with the copolymer dissolved in a cosolvent at a concentration of 13 %v/v. The polymer is uniformly mixed by conducting NVT simulations with $\Delta a = 0$ for

$1.5 \cdot 10^5$ timesteps. We then swap the cosolvent instantaneously for a selective solvent with $\Delta a_{\mathrm{BS}} = 0$ and $\Delta a_{AS} = 20$, and conduct an NVT simulation with $\Delta t = 0.001$ for $2.5 \cdot 10^5$ timesteps, followed by a production simulation with $\Delta t = 0.015$ for $7.5 \cdot 10^6$ timesteps where the polymers form micelles. An example of the initial and final configuration are given in Figure 3.3.

We note here that these simulations represent a rapid quench into the micellar regime, rather than a gradual change. It was shown by Johnson and coworkers [7] as well as Meli and Lodge [9, 10] that slow titration of the cosolvent into the selective solvent can keep exchange dynamics active for long enough to reach equilibrium at an intermediate solvent quality. While the final micelles at the target solvent quality are still kinetically trapped below equilibrium, this slow titration procedure produces more monodispersed micelles than rapid quenching. In this study we do not consider a slow titration technique, but this would be an interesting avenue for future work.

This micellization process simulated here differs from that of Li and Dormidontova [5, 26] since they simulate short chains with lower core hydrophobicity. As a result, exchange and fusion remain active throughout the entire micellization process, and they are able to reach an equilibrium state where unimers are at equilibrium with micelles. As discussed previously, equilibrium is often not attainable in copolymer micelles with longer, more hydrophobic core blocks due to the freezing of unimer exchange and fusion dynamics. In addition, it has been observed experimentally that unimer concentrations at equilibrium are often vanishingly small [32], which is in contrast to the conditions simulated previously by Li and Dormidontova [26]. In this work, we focus on the common experimental regime where micelles rapidly form and then become kinetically trapped with negligible unimer concentration.

3.3 DPD Self-Consistent Field Theory

It is of interest to determine how close the micelles created from the TF and CS methods are to the equilibrium size. It is very difficult to determine the equilibrium size directly from simulation, so instead we utilize self-consistent field theory to compute an approximation to the free energy for an isolated micelle [33, 34]. To ensure the theoretical model is as close to the simulation as possible, we utilize the same bonded potential and conservative non-bonded potential as DPD. As far as we know, this has not been done before for the DPD model, and we call the theory DPD-SCFT. We note that it is possible to determine the free energy from

simulation using a grand canonical Monte Carlo approach as was shown by Mysona and coworkers [27–29], however, this approach is only feasible when a polymeric solvent is used with the same total number of monomers. This method cannot be readily applied to the current case of a monomeric solvent.

The system contains n bead-spring polymers that each contain N total monomers divided into two block of length N_A and N_B. In the canonical ensemble, there are m total solvent molecules that are represented as single beads that are the same size as the polymer beads. The system has a total segment density of $\rho_0 d_p^3 = \rho = 3$, where d_p is the effective particle size of all species. We define the shorthand $\mathbf{C} = \{\mathrm{A}, \mathrm{B}, \mathrm{S}\}$ for the vecor of species in the system. As in the MD simulations, particles interact via a soft, purely repulsive potential given by,

$$\beta U^{ij}_{\mathrm{dpd}}(r_{ij}) = \begin{cases} \frac{1}{2} a_{ij}(1 - r_{ij}/d_p)^2 & , r_{ij} \leq d_p \\ 0 & , r_{ij} > d_p \end{cases} \tag{3.5}$$

where a_{ij} is the repulsion strength, r_{ij} is the distance between particles i and j, and d_p is the range of the interaction. In addition, adjacent particles along a polymer backbone interact via a stiff spring bonded potential of the form,

$$\beta U_b(r_{ij}) = \frac{\kappa}{2 d_p^2}(r_{ij} - b)^2 \tag{3.6}$$

where κ is the spring constant, and b is the equilibrium bond length. Once again, we choose $\kappa = 100$ and $b = d_p = 1$ to match with the MD simulations.

The total interaction energy is thus,

$$\begin{aligned} \beta U(\mathbf{r}^{nN+m}) = {} & \frac{\kappa}{2 d_p^2} \sum_{i=1}^{n} \sum_{j=1}^{N-1} (|\mathbf{r}_{i,j+1} - \mathbf{r}_{i,j}| - b)^2 \\ & + \frac{\beta}{2} \sum_{\alpha \in \mathbf{C}} \sum_{\gamma \in \mathbf{C}} \int d\mathbf{r} \int d\mathbf{r}' \hat{\rho}_\alpha(\mathbf{r}) U_{\mathrm{dpd}}(|\mathbf{r} - \mathbf{r}'|) \hat{\rho}_\gamma(\mathbf{r}') \end{aligned} \tag{3.7}$$

where $\hat{\rho}_\alpha(\mathbf{r}) = \sum_{i=1}^{N_\alpha} \delta(\mathbf{r} - \mathbf{r}_i)$ is the microscopic density operator of species α. The configurational partition function in the canonical ensemble is,

$$Z = \frac{1}{n! m! v^{nN+m}} \int \prod d\mathbf{r}_j \exp\left[-\beta U(\mathbf{r}^{nN+m})\right] \tag{3.8}$$

where $v = d_p^3$ is an arbitrary volume scale for normalization. To transform to a field-based representation, we introduce coarse-grained density for each species using the

Fourier representation of the delta functional,

$$\delta\left[\rho_\alpha(\mathbf{r}) - \hat{\rho}_\alpha(\mathbf{r})\right] = \int Dw_\alpha \exp\left\{ i \int d\mathbf{r}\, w_\alpha(\mathbf{r}) \left[\rho_\alpha(\mathbf{r}) - \hat{\rho}_\alpha(\mathbf{r})\right] \right\} \tag{3.9}$$

where ρ_α is the coarse-grained density that is coupled to the fluctuating field w_α. The field-based canonical partition function can now be written as,

$$Z = \int \prod_{\alpha\in\mathbf{C}} D\rho_\alpha Dw_\alpha \frac{Q_P^n Q_S^m}{n!m!} \prod_{j=1}^{nN+m} \exp\Bigg\{ \sum_{\alpha\in\mathbf{C}} \int d\mathbf{r}\, i w_\alpha \rho_\alpha - \\ - \frac{\beta}{2} \sum_{\alpha\in\mathbf{C}} \sum_{\gamma\in\mathbf{C}} \int d\mathbf{r} \int d\mathbf{r}' \rho_\alpha(\mathbf{r}) U_{\mathrm{dpd}}^{\alpha\gamma}(|\mathbf{r}-\mathbf{r}'|) \rho_\gamma(\mathbf{r}') \Bigg\} \tag{3.10}$$

where $Q_P[w_A, w_B]$ and $Q_S[w_S]$ are the single polymer and single particle partition functions, respectively. These are the partitions functions for a single polymer chain and a single solvent molecule subject to external fields w_A, w_B, and w_S, and they are defined below.

$$Q_P[w_A, w_B] = \frac{1}{v^N} \int d\mathbf{r}^N \exp\Bigg\{ -\frac{\kappa}{2d_p^2} \sum_{j=1}^{N-1} (|\mathbf{r}_{j+1} - \mathbf{r}_j| - b)^2 \\ - \sum_{j=1}^{N_A} i w_A(\mathbf{r}_j) - \sum_{j=N_A+1}^{N} i w_B(\mathbf{r}_j) \Bigg\} \tag{3.11}$$

$$Q_S[w_S] = \frac{1}{v} \int d\mathbf{r}\, e^{-i w_S(\mathbf{r})} \tag{3.12}$$

In order to model an isolated micelle of aggregation number n, we transform to a semigrand ensemble where a subvolume containing the micelle is connected to an infinite reservoir of solvent molecules. To make this transformation, we perform the discrete Laplace transform,

$$\Xi(n, \mu, V, T) = \sum_{m=0}^{\infty} e^{\beta\mu m} Z(n, m, V, T) \tag{3.13}$$

where μ is the solvent chemical potential. The full semigrand partition function can then be written compactly,

$$\Xi = \int Dw_A \int Dw_B \int Dw_S \int D\rho_A \int D\rho_B \int D\rho_S\, e^{-\beta H} \tag{3.14}$$

where H is the field-based Hamiltonian.

$$\beta H = \ln(n!) - n \ln Q_P - e^{\beta\mu} Q_S - \sum_{\alpha\in\mathbf{C}} \int d\mathbf{r}\, i w_\alpha \rho_\alpha \\ + \frac{\beta}{2} \sum_{\alpha\in\mathbf{C}} \sum_{\gamma\in\mathbf{C}} \int d\mathbf{r} \int d\mathbf{r}' \rho_\alpha(\mathbf{r}) U_{\mathrm{dpd}}^{\alpha\gamma}(|\mathbf{r}-\mathbf{r}'|) \rho_\gamma(\mathbf{r}') \tag{3.15}$$

The partition function in Equation (3.14) cannot be evaluated in closed form, so we approximate its value using the saddle-point of the Hamiltonian, H^*. At the saddle point, the fields w_A are purely imaginary, and thus we define new fields, $\xi_\alpha = iw_A$, that are purely real. We can then approximate the equilibrium free energy $\beta\Omega = -\ln\Xi \approx -\ln\Xi^* = \beta H^*$. The equilibrium density and field profiles can be computed by extremizing the Hamiltonian with $\delta H/\delta\xi_\alpha = 0$ and $\delta H/\delta\rho_\alpha = 0$, which gives rise to the following saddle-point (mean-field) equations.

$$\rho_A(\mathbf{r}) = \frac{ne^{\xi_A(\mathbf{r})}}{vQ_P}\sum_{i=1}^{N_A} q(\mathbf{r};i)q^\dagger(\mathbf{r};N-i) \tag{3.16}$$

$$\rho_B(\mathbf{r}) = \frac{ne^{\xi_B(\mathbf{r})}}{vQ_P}\sum_{i=N_A+1}^{N} q(\mathbf{r};i)q^\dagger(\mathbf{r};N-i) \tag{3.17}$$

$$\rho_S(\mathbf{r}) = \frac{e^{\beta\mu}}{v}\int d\mathbf{r}\, e^{-\xi_S(\mathbf{r})} \tag{3.18}$$

$$\xi_\alpha(\mathbf{r}) = \sum_{\gamma\in\mathbf{C}}\int d\mathbf{r}'\rho_\gamma(\mathbf{r}')\beta U^{\alpha\gamma}_{\text{dpd}}(|\mathbf{r}-\mathbf{r}'|) \tag{3.19}$$

The forward and reverse chain propagators, q and $q^\dagger$, are computed in a recursive manner,

$$q(\mathbf{r};1) = e^{-\xi_A(\mathbf{r})} \tag{3.20}$$

$$q(\mathbf{r};i) = \frac{e^{-\xi_{t(i)}(\mathbf{r})}}{C}\int d\mathbf{r}' e^{-\frac{\kappa}{2d_p^2}(|\mathbf{r}-\mathbf{r}'|-b)^2} q(\mathbf{r}';i-1) \tag{3.21}$$

$$q^\dagger(\mathbf{r},1) = e^{-\xi_B(\mathbf{r})} \tag{3.22}$$

$$q^\dagger(\mathbf{r};i) = \frac{e^{-\xi_{t(N-i)}(\mathbf{r})}}{C}\int d\mathbf{r}' e^{-\frac{\kappa}{2d_p^2}(|\mathbf{r}-\mathbf{r}'|-b)^2} q^\dagger(\mathbf{r}';i-1) \tag{3.23}$$

where $t(i) = A$ for $i \le N_A$ and $t(i) = B$ otherwise. C is the normalization constant,

$$C = 4\pi\int_0^\infty dr\, r^2 e^{-\frac{\kappa}{2d_p^2}(r-b)^2}, \tag{3.24}$$

and the polymer partition function can be computed from

$$Q_P = \frac{1}{v}\int d\mathbf{r}\, q(\mathbf{r};N)\ . \tag{3.25}$$

The solvent fugacity, $e^{\beta\mu}$, can be computed using the properties of the homogeneous reservoir according to,

$$\frac{\langle m\rangle v}{V} = \rho = \frac{v}{V}\frac{\partial\ln\Xi}{\partial\beta\mu} = e^{\beta\mu}e^{-\frac{\pi}{15}a_{ii}\rho} \ \longrightarrow\ e^{\beta\mu} = \rho e^{\frac{\pi}{15}a_{ii}\rho} \tag{3.26}$$

where the reservoir is a bulk fluid of solvent at a uniform density of $\rho = 3$. By inserting the saddle-point equations into Equation (3.15), we obtain the simplified mean-field free energy,

$$\beta\Omega(n,\mu,V,T) = \ln(n!) - n\ln Q_P - \int d\mathbf{r}\rho_S(\mathbf{r}) - \frac{1}{2}\sum_{\alpha\in\mathbf{C}}\int d\mathbf{r}\,\xi_\alpha(\mathbf{r})\rho_\alpha(\mathbf{r}). \quad (3.27)$$

By solving Equations (3.16)-(3.23) and (3.25), we can obtain the equilibrium fields and density profiles. In this work we consider 3 different geometries: (1) a lamellar copolymer melt, (2) a spherical micelle, and (3) an infinitely long cylindrical micelle. The necessary mathematical reduction for each geometry is different, as well as the relevant free energy. Details of the transformation of the saddle-point equations and propagators for each geometry are provided in the ESI†. For a copolymer melt in the lamellar microphase, we reduce the variation to the dimension normal to the lamellar interface and compute the Helmholtz free energy per chain per unit area, $F^{\text{lam}}_{\hat{m}}/\hat{m}$, where $\hat{m} = n/A_{||}$ and $A_{||}$ is the area of the lamellar interface. For a spherical micelle, we reduce the variation to only the spherical radial dimension and compute the internal free energy per chain, F^{sph}_n/n. For an infinitely long cylindrical micelle, we reduce the variation to only the cylindrical radial dimension and compute the internal free energy per chain per unit length F^{cyl}_m/m, where $m = n/L$ and L is the length of the cylinder.

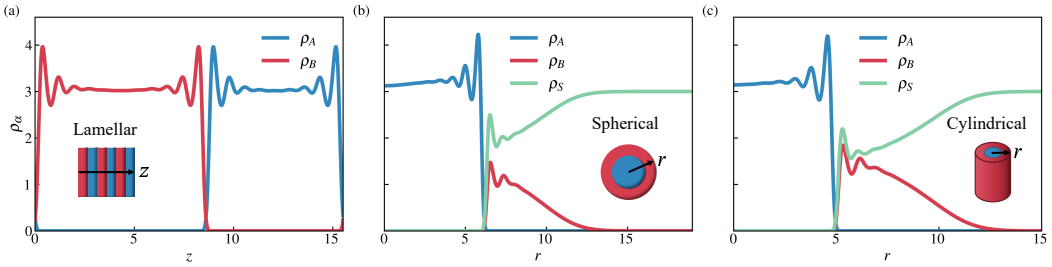

Figure 3.4: Example density profiles from DPD-SCFT for $\rho = 3$, $N_A = 12$, $N_B = 15$, $a_{ii} = 25$, $a_{AS} = a_{AB} = 45$, $\kappa = 100$, and $b = d_p = 1$. Density profiles are for (a) lamellar, (b) spherical and (c) cylindrical morphologies all with 1-dimensional variation.

Example density profiles for the lamellar, spherical, and cylindrical morphologies are given in Figure 3.4. Note that there are significant density oscillations near interfaces due to the large excess repulsion parameter ($\Delta a = 20$) between the core block and the corona+solvent.

Micelle Thermodynamics

The relevant quantity for determining the optimal micelle aggregation number is the free energy difference for n isolated chains to aggregate into a micelle,

$$\Delta F_n = F_n - nF_1 \tag{3.28}$$

where F_n is the internal free energy of a micelle at aggregation number n, and F_1 is the internal free energy of an isolated chain [35]. Since the association takes place within a constant total volume containing a constant number of solvent molecules, the solvent term $\int d\mathbf{r}\rho_S$ can be removed from the internal free energy. However, since we vary the system volume for different aggregation numbers (to ensure sufficient grid resolution), we have to ensure the internal free energies are independent of the system volume. The free energy densities due to the polymer interactions, $\frac{1}{2}\xi_A\rho_A$ and $\frac{1}{2}\xi_B\rho_B$, both decay to zero sufficiently far from the system boundary to avoid dependence on the system size. The remaining free energy density due to the solvent, $\frac{1}{2}\xi_S\rho_S$, does not vanish at the system boundary, but rather goes to $\frac{\pi}{30}a_{ii}\rho^2$. To remove the volume dependence of the internal free energy, we subtract this contribution, resulting in the final expression,

$$\beta F_n = \ln(n!) - n\ln Q_P - \frac{1}{2}\sum_{\alpha\in\mathbf{C}}\int d\mathbf{r}\,\xi_\alpha(\mathbf{r})\rho_\alpha(\mathbf{r}) + \frac{\pi}{30}a_{ii}\rho^2 V \tag{3.29}$$

where the final term on the right accounts for contributions to the free energy that only appear due to additional volume beyond the extent of the micelle. Note that Equation (3.29) is completely independent of the system volume as long as the system is larger than the furthest extent of the micelle.

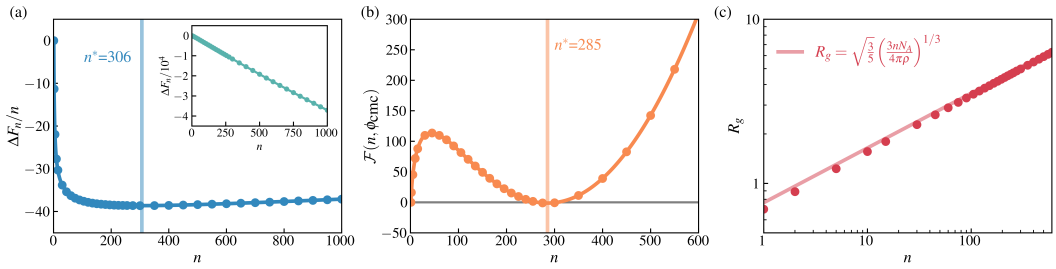

Figure 3.5: Various properties computed from DPD-SCFT for spherical micelles with $\rho = 3$, $N_A = 12$, $N_B = 15$, $a_{ii} = 25$, $a_{AS} = a_{AB} = 45$, $\kappa = 100$, and $b = d_p = 1$. (a) Free energy of aggregation per chain with inset being the free energy of aggregation from Equation (3.28). (b) Free energy of n-mer at critical micelle concentration, $c_1 = c_{\text{cmc}}$. (c) Micelle radius of gyration.

In general, ΔF_n decreases monotonically with n, but $\Delta F_n/n$ features a minimum, as shown in Figure 3.5a. In early treatments of micelle thermodynamics, this minimum

is taken as the optimal micelle aggregation number. However, this is only accurate if the minimum is deep and occurs at a sufficiently large n such that translational entropy of the micelles can be neglected. In dilute solution thermodynamics, the total free energy including the translational entropy is given by,

$$\frac{F}{V} = \sum_{n=1}^{\infty} c_n \left\{ F_n + k_B T \left[\ln \left(c_n v_n \right) - 1 \right] \right\} \tag{3.30}$$

where c_n is the number concentration of n-mers and v_n is the volume of an n-mer [4, 5, 35–39]. Thus, $c_n v_n$ is the volume fraction ϕ_n of n-mers. The concentration of n-mers can be determined by minimizing the free energy in Equation (3.30) subject to a given total unimer concentration $1 = \sum_{n=1}^{\infty} n\phi_n$, resulting in the distribution,

$$\phi_n = \phi_1^n \exp\left(-\frac{\Delta F_n}{k_B T} \right) \tag{3.31}$$

which can be further rearanged into the form,

$$\phi_n = \phi_1 \exp\left[-\beta \mathcal{F}(n, \phi_1) \right] \tag{3.32}$$

where $\mathcal{F}(n, \phi_1)$ is the semi-grand free energy of an n-mer at a specified concentration of unimer volume fraction, ϕ_1. This free energy is defined as

$$\beta \mathcal{F}(n, \phi_1) = F_n - nF_1 - k_B T (n-1) \ln \phi_1 \tag{3.33}$$

Thus, the thermodynamics of micelle formation are completely governed by F_n and ϕ_1. If ΔF_n displays a minimum, then the behavior of $\mathcal{F}(n, \phi_1)$ can be predicted. For very low unimer concentrations, $\mathcal{F}$ will monotonically increase and the only minimum is at $n = 1$, indicating that no micelles will form. At some concentration below the CMC, $\phi_1 < \phi_{\text{cmc}}$, a second minimum appears at some aggregation number n. At the critical micelle concentration, $\phi_1 = \phi_{\text{cmc}}$, the free energy of the unimer and n^*-mer are equal, $\mathcal{F}(n^*, \phi_{\text{cmc}}) = \mathcal{F}(1, \phi_{\text{cmc}}) = 0$. At a concentration above the CMC, $\phi_1 > \phi_{\text{cmc}}$, the n^*-mer minimum is much lower than 0, indicating that the concentration of micelles is much greater than unimers. An example of $\mathcal{F}(n, \phi_{\text{cmc}})$ is given in Figure 3.5b.

In diblock copolymer solutions, it is unclear what the *equilibrium* micelle size should be, given that the critical micelle concentration is exceedingly low, and chain exchange is practically frozen [3, 4]. We believe that the appropriate micelle size should be determined by the optimization of the internal free energy per chain, F_n/n for spherical micelles, and F_m/m for cylindrical micelles. We note that the difference in optimal aggregation number between the two is less than 10%.

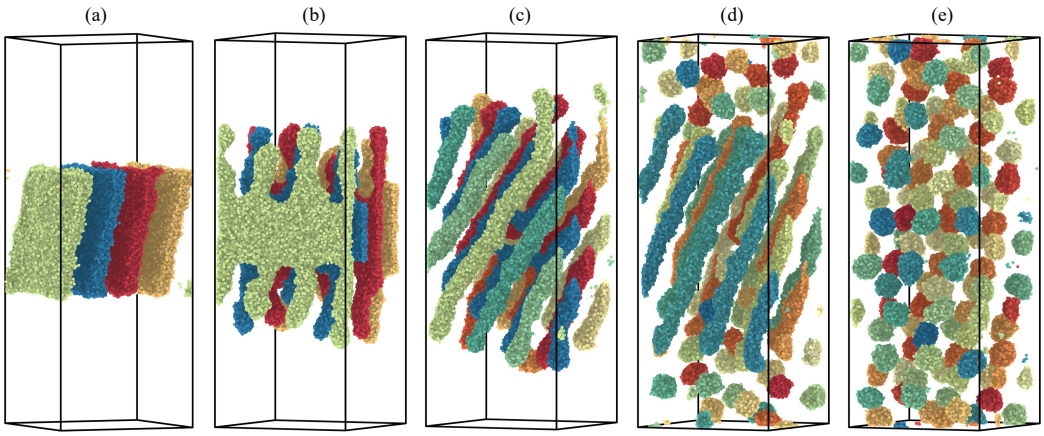

Figure 3.6: Kinetic pathway from lamellar thin film to copolymer micelles for $N_A = 7$ and $N_B = 15$. The solvent and B block are omitted and A beads are colored by cluster for visual clarity. (a) Initial thin film. (b) Partial penetration of solvent into lamellar phase creates finger-like structures. (b) Lamellae fully transform into cylinders that pack onto a hexagonal lattice. (d) Cylinders extend to relieve stress and micelles pinch off from cylinder ends. (e) Final solution containing only spherical micelles.

3.4 Results and Discussion

Thin Film Dissolution

First, we explore the kinetic mechanism for micelle formation via the TF method by following the procedure outline in the methods section. We perform *in silico* experiments for $N_A \in [4, 5, \ldots, 12]$, $N_B = 15$, $a_{ii} = 25$, and $a_{AS} = a_{AB} = 45$. As N_A approached N_B, the timescale for complete dissolution of the thin film became prohibitively long for our simulations. Thus, $N_A = 12$ was the largest core block we could reasonably study for this set of parameters. We will explore the reason for this behavior later in this work.

In Figure 3.6, we give a representative example of the kinetic pathway by showing five different points along the trajectory for $N_A = 7$. In these snapshots, we omit the solvent and the B (corona) block, and we color the polymers using the clustering algorithm available in OVITO. The colors are meaningless beyond indicating polymers belong to the same cluster. The initial state in Figure 3.6a is the lamellar thin film sandwiched in between layers of nonsolvent ($a_{AS} = a_{BS} = a_{AB} = 45$). Immediately after the solvent is swapped for a selective solvent ($a_{AS} = a_{AB} = 45, a_{BS} = 25$), the solvent rushes into the B block causing it to swell. This swelling makes the lamellar structure unstable, causing it to break up into cylinders behind the moving solvent front (Figure 3.6b). We refer to this as a finger-like state. Once the solvent

fronts meet in the middle of the thin film, the fingers become cylinders (Figure 3.6c). At this point, the cylinders are packed closely and therefore have heavily overlapping corona blocks. At this point the cylinders extend to relieve stress felt due to the coronal overlap, as well as the stress resulting from the cylinder radius being larger than optimal. Simultaneously, spherical micelles begin to pinch off from the cylinder ends (Figure 3.6d). It is well known that the ends of cylindrical micelles are bulbous compared to the interior shaft, which allows for the ends to pinch off more easily. Eventually, the cylinders stop extending, presumably because they have reached their optimal radius and relieved as much stress as possible due to the overlapping coronas. The cylinders also align and arrange onto a hexagonal lattice during this time to further relieve stress. For a much thicker thin film that is exposed to the solvent on a single face, we expect that cylinders may only align with their ends pointing into the solvent near the polymer-solvent interface. Deeper into the film the cylinders can curve and form a network like structure, or even align perpendicular, similar to how integro-asymmetric diblock copolymer membranes form. Although, we note that copolymer membranes are form through macrophase separation between the polymer and a non-solvent, as opposed to micelle formation in a selective solvent.

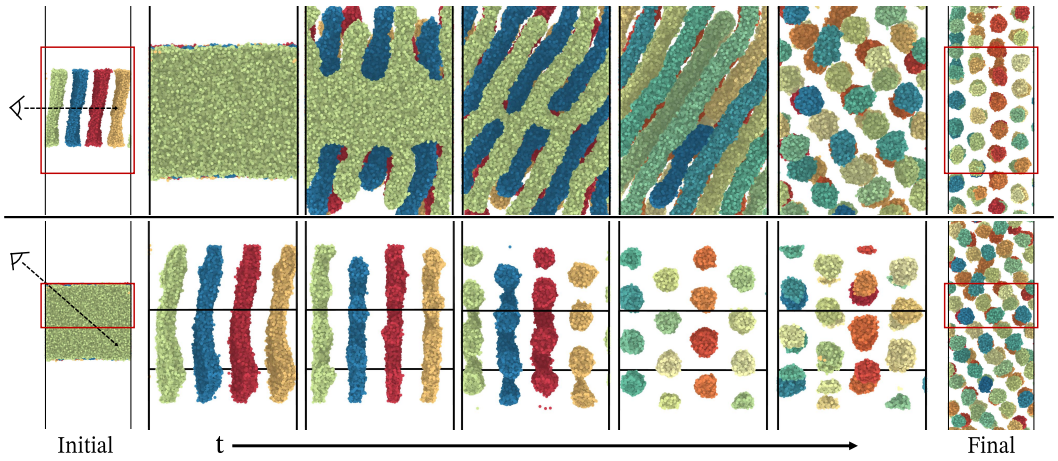

Figure 3.7: Kinetic pathway with different viewing angles for $N_A = 7$ and $N_B = 15$. The eye symbols and arrows indicate the viewing angle and the red box indicates the subregion being shown in the snapshots within the same row. The initial and final snapshots are shown in a zoomed out view. The top row is viewed directly normal to the lamellae to show the finger formation and how they break into cylinders. The bottom row is viewed straight down the axis of the cylinders that form. In all snapshots we omit the solvent and corona (B) block, and we color the polymers according to the cluster they belong to.

In Figure 3.7 we provide visuals of the TF process from two different angles. The top panel shows a zoomed-in view normal to the lamellae to better show the formation of the finger-like structures and how the fingers later disconnect to form cylinders. In this case, the cylinders form on a slant because $L_x = L_y$, which is not commensurate with the unit cell dimensions for hexagonal close packed cylinders. The bottom panel shows a sliced portion of the system viewed from the angle directly down the axis of the cylinders that form. It is clear from this angle that the cylinders are aligned and arranged into a hexagonal close packed structure. Additionally, the final micellar solution is ordered with micelles on a lattice due to the high volume fraction of polymer ($\phi_P \approx 0.3$). We have checked that the micelles are not simply stabilized by their presence in an ordered structure by running separate simulations of individual micelles at the same average size where we observed that the micelles remained stable indefinitely. We will discuss the size of the micelles produced from the TF method after first discussing results for the CS method.

Cosolvent Assisted Dissolution

To simulate the CS method, we create a dispersed solution of copolymer in a cosolvent ($a_{AS} = a_{BS} = 25$) and allow the system to equilibrate for $2 \cdot 10^5$ timesteps. We then instantaneously swapped the cosolvent for a selective solvent by setting $a_{AS} = 45$. During the quenching period we set the timestep to $\Delta t = 0.001$ for $2.5 \cdot 10^5$ timesteps to ensure the simulation remained stable. After that, the timestep was increased back to $\Delta t = 0.015$ and the simulation was run for an additional $9 \cdot 10^6$ timesteps.

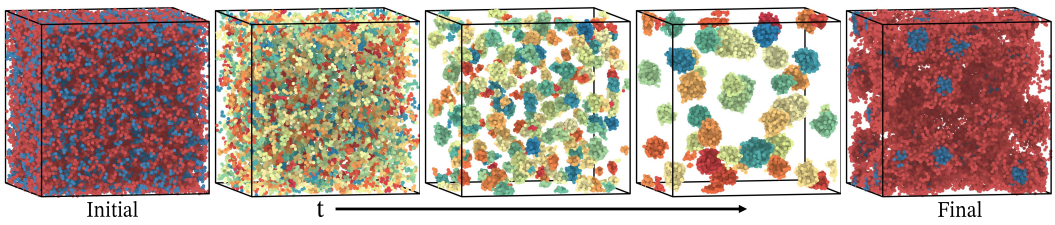

Figure 3.8: Micellization process extracted from simulations of CS method with $N_A = 7$ and $N_B = 15$. The initial and final snapshot are shown with both the core and corona, with the solvent omitted. The intermediate snapshots are shown with the corona (B) block and solvent omitted, and polymers are colored according to the cluster they belong to.

In Figure 3.8 we show snapshots throughout the micellization process using the CS method. In our simulations, micellization progresses through two main steps. The first step, which is also the fast step, is the initial aggregation of neighboring chains

into small clusters/aggregates. After all of the free chains have been incorporated into small micelles, then the micellization process slows precipitously. The second step is the equilibration process wherein the distribution of micelle sizes slowly converges towards the equilibrium distribution. Equilibration is known to proceed via two main mechanisms: single chain exchange, and micelle fission/fusion. For the strong degree of segregation and moderate chain lengths considered here, we find that both initial micellization and equilibration are dominated by fusion events, and single-chain exchange is essentially frozen. As the micelles grow, the rate of fusion decreases due to the decreasing micelle concentration and the increasing corona repulsion. It is possible that the free energy barrier for fusion could surpass the single-chain exchange barrier once the micelles are sufficiently close to equilibrium, as predicted with previous theories and simulations [5, 26]. However, in our simulations the micelles here become kinetically frozen after a certain point and neither exchange nor fusion occurs at an appreciable rate within a practical simulation timescale.

In Figure 3.9 we plot various properties of the aggregates throughout the micellization process in a similar manner to Li and Dormidontova [26]. The main difference here is the use of a higher Δa and longer core and corona blocks with $N_A = 8$ and $N_B = 15$. As discussed, the significantly higher barriers to fusion and exchange lead to slowed dynamics and kinetic trapping of the micelles. Figure 3.9a shows how the proportion of different aggregate numbers evolves over time. Initially, the system is mainly comprised of free chains and small clusters with less than 3 chains. Note that the solution is not 100% free chains at the initial state due to random mixing and the moderate segment volume fraction of $\phi_p = 0.13$. Figure 3.9b shows the evolution of the number averaged and weight averaged aggregation numbers. Similar to Li and Dormidontova, we find that the weight average aggregation number equilibrates more rapidly. Unlike Li and Dormidontova, the average aggregation number does not fluctuate around a steady state at long time, since chain exchange and small aggregate exchange are essentially frozen. Instead, the average aggregation number slowly grows in a stepwise fashion through fusion events that become progressively less probable as the aggregate concentration decreases and the fusion barrier increases. Figure 3.9c shows the distribution of aggregation numbers over time. Initially the distribution is peaked at $n = 1$ which corresponds to the randomly mixed solution. The free chains are depleted rapidly ($t < 10^2$) as small aggregates of size $n = 2 - 10$ form. Over time, the small aggregates find each other in solution and combine to form aggregates of size $10 < n < 25$ which last significantly longer

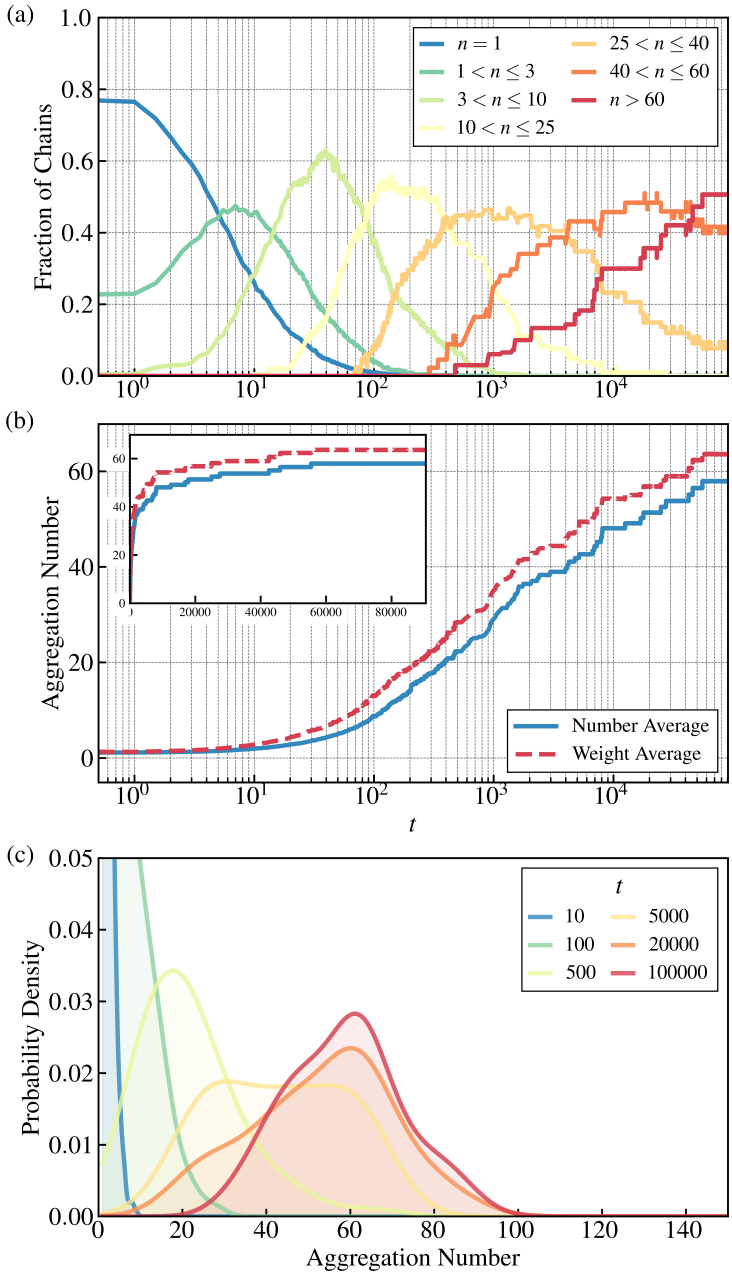

Figure 3.9: Micellization dynamics from CS method for various $N_A = 8$, $N_B = 15$, $\Delta a = 20$, and $\phi_p = 0.13$. (a) Fraction of chains within different sized aggregates over time. (b) Number averaged and weight averaged aggregation numbers over time. The inset is on a linear-linear scale to show the significant slowing of dynamics. (c) Aggregation number probability distribution at different simulation times.

(note the logarithmic scale of the time axis). This process continues until fusion of the most frequent aggregate size becomes unprobable and all smaller aggregates are exhausted. For example, all aggregates of size $10 < n < 25$ are depleted by $t = 10^4$. We also note that the depletion of the aggregates within a particular size grouping

becomes significantly slower as n increases, as evidenced by the much longer tails in the orange and red curves.

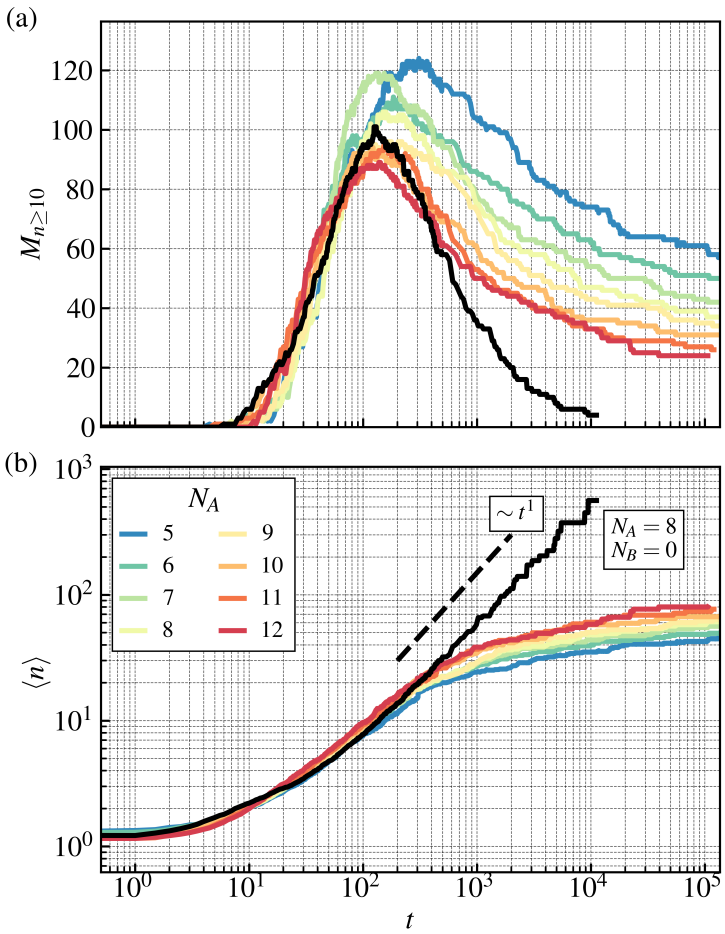

Figure 3.10: Micellization dynamics from CS method for various N_A, with $N_B = 15$. (a) The number of micelles with greater than 10 chains, $M_{n\geq 10}$, over time. (b) The average micelle aggregation number over time. The black solid lines are curves for a homopolymer solution with $N_A = 8$, $N_B = 0$, and $\phi_p = 0.045$ (i.e., $8/23 \cdot 0.13$ to keep the same A fraction). The dashed black line is a linear power law characteristic of spinodal decomposition where $n \sim R^3 \sim t$ for spherical droplets/micelles.

We explore the effect of core block length on the micellization dynamics in Figure 3.10. Figure 3.10a shows the number of micelles containing 10 or more chains as a function of time. This curve shows a rapid growth as free chains form into small aggregates, followed by a maximum due to the exhaustion of free chains. After all of the free chains are exhausted, the number of micelles slowly drops (note the logarithmic scale of the time axis) as small to moderate aggregates undergo fusion. Figure 3.10b shows the coarsening dynamics of the micelle aggregation number as a function of time. The micelles first grow according to a sublinear power-law

dependence, but at $t/t_0 \approx 10^2$ the dynamics slow significantly as shown by the plateauing of $\langle n \rangle$. As discussed, this is due to the diminishing concentration of small aggregates and the rising fusion barrier. We contrast this with the coarsening dynamics of a homopolymer solution, represented by the solid black curves in Figure 3.10. The homopolymer solution has the same number concentration of polymers as the copolymer case, corresponding to an A-segment volume fraction of $\phi_p = 0.045$. Unlike the copolymer solution, the dynamics in the homopolymer solution follow the expected behavior for spinodal decomposition, $\langle R \rangle^3 \sim \langle n \rangle \sim t^1$. It is clear that the progressive slowing of the micellization process in copolymer micelles is a direct consequence of both the fusion barrier and the finite optimal aggregation number.

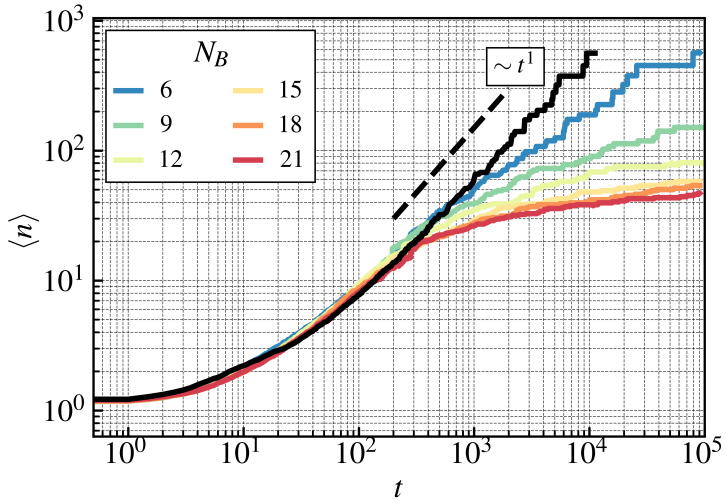

Figure 3.11: Micellization dynamics from CS method for various N_B with $N_A = 8$ and $\Delta a = 20$. The black solid curve is for a homopolymer solution with $N_A = 8$, $N_B = 0$. We keep the A monomer fraction constant at $\phi_A = 0.045$. The dashed black line is a linear power law characteristic of spinodal decomposition where $n \sim R^3 \sim t$ for spherical droplets/micelles.

In addition to the core length effect, we also study the effect of the corona length on the micellization kinetics in the CS method. In Figure 3.11 we plot the average aggregation number over time for various corona block lengths for a constant core block length and constant core monomer concentration. We find that the short time dynamics are unaffected by the corona block length and align well with homopolymer aggregation (black line). This is because at short times the micellization process is dominated by fusion events between aggregates containing small numbers of chains. For these small aggregates, there is no well defined corona domain and

therefore little to no repulsion between the aggregates. Thus, the rate of aggregation is determined almost solely by the chain concentration at short times.

Once the free chains are exhausted and the average aggregation number reaches a moderate value ($n > 10$), the corona domain becomes appreciable and aggregates begin to repel, increasing the barrier to fusion. Since the micellization is driven almost completely by fusion for the parameters studied here, an increase in the fusion barrier necessarily slows the rate. In addition, the fusion barrier will continue to increase with aggregation number since the corona will become denser and denser. This means that whenever two micelles fuse together, fusion of the new micelle with another micelle is even less probable. As explained by Li and Dormidontova [26], fusion events during early stages of micellization are largely between aggregates of similar sizes, while fusion events during later stages are mostly between aggregates of unequal sizes. The latter case is due to more corona repulsion during fusion of two large micelles versus one small and one large micelle. For the largest corona blocks studied, $N_B = 12 - 21$, the micelles essentially become frozen after $t > 10^4\tau$. This is typically where single chain exchange would become important [5], however, the exchange barriers are exceedingly high for the parameters studied here, $\Delta a = 20$ and $N_A = 8$. In our previous work, we computed an exchange barrier of $\beta\Delta F_{\text{barr}} \approx 20$ [40].

We study the effect of polymer concentration on the micellization process in Figure 3.12. Here, polymer concentration refers to the volume fraction of polymer segments including both A and B. Unsurprisingly, increasing the polymer concentrations speeds up the micellization process. Not only is the initial aggregation more rapid, but the steady state is also reached more quickly, as shown in Figure 3.12a. We also find that the final micelle distribution shifts to larger aggregation numbers as concentration increases, and the final average aggregation number is impacted dramatically as shown in Figure 3.12b. At very high concentrations such as $\phi_p = 0.4$, the aggregation process follows a very different pathway compared to more dilute solutions since the system is well above the overlap concentration. Figure 3.13 shows the micellization pathway at high concentration. The initial state is essentially a large cluster since the solution is above the overlap concentration. After the solvent is swapped for a selective solvent, the system aggregates into a network like phase which then further breaks into micelles. While these micelles are bigger than those formed at lower concentrations, these micelles are still smaller than those formed through the TF method as we will show later.

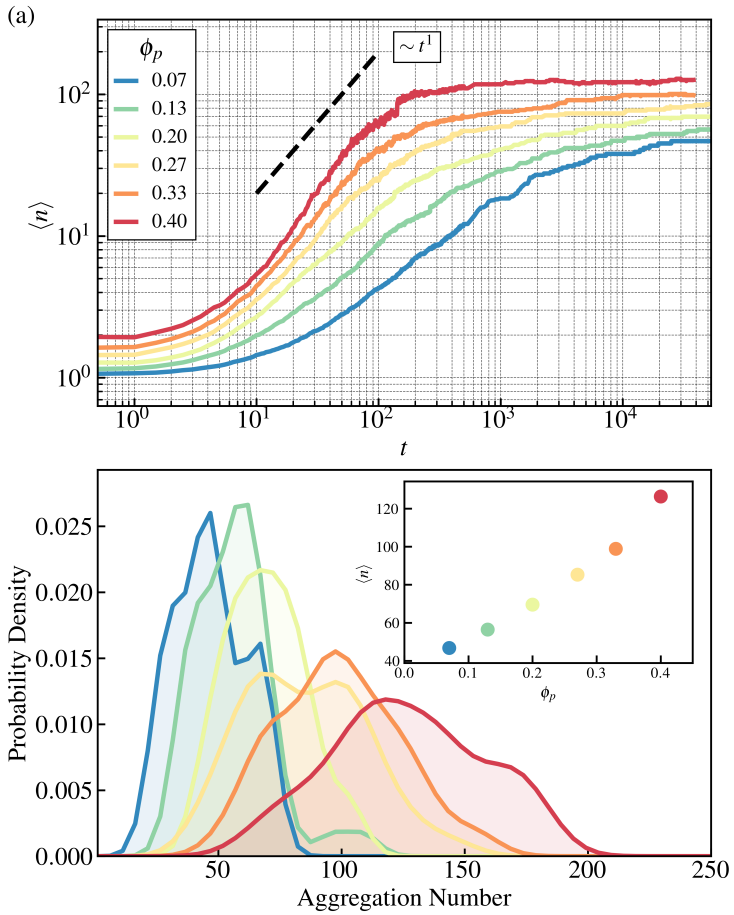

Figure 3.12: Micellization dynamics from CS method for various polymer concentrations ϕ_p with $N_A = 8$, $N_B = 15$, and $\Delta a = 25$. (a) Average aggregation number over time. (b) Final distribution of aggregation numbers with inset for mean aggregation number as a function of polymer concentration.

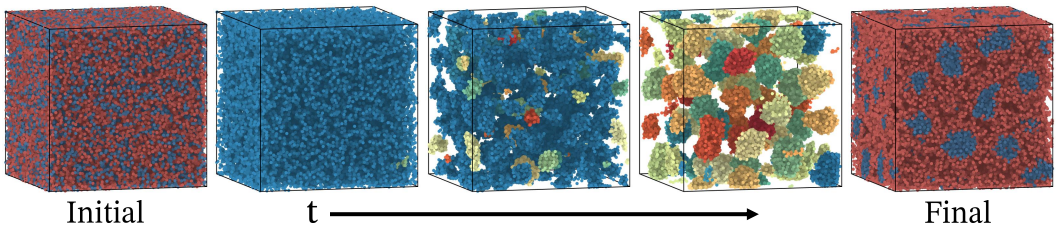

Figure 3.13: Visualization of micellization in highly concentrated solution ($\phi_p = 0.4$) with $N_A = 8$, $N_B = 15$, and $\Delta a = 20$. The left and right plots are colored by A and B blocks. The middle plots only show A blocks and are colored according to cluster.

Comparison Between TF and CS

We now shift our focus to comparing the final micelles produced from the CS and TF methods. We note that the final size distribution achieved from the TF method in our

simulations is stationary and essentially independent of the polymer concentration since the size of the micelles is determined by the size of the intermediate cylinders. As we showed in the previous section, the final size distribution from the CS method depends on the polymer concentration. In addition, the size distribution is still transient but has slowed down so significantly that observing further coarsening is impractical in our simulations.

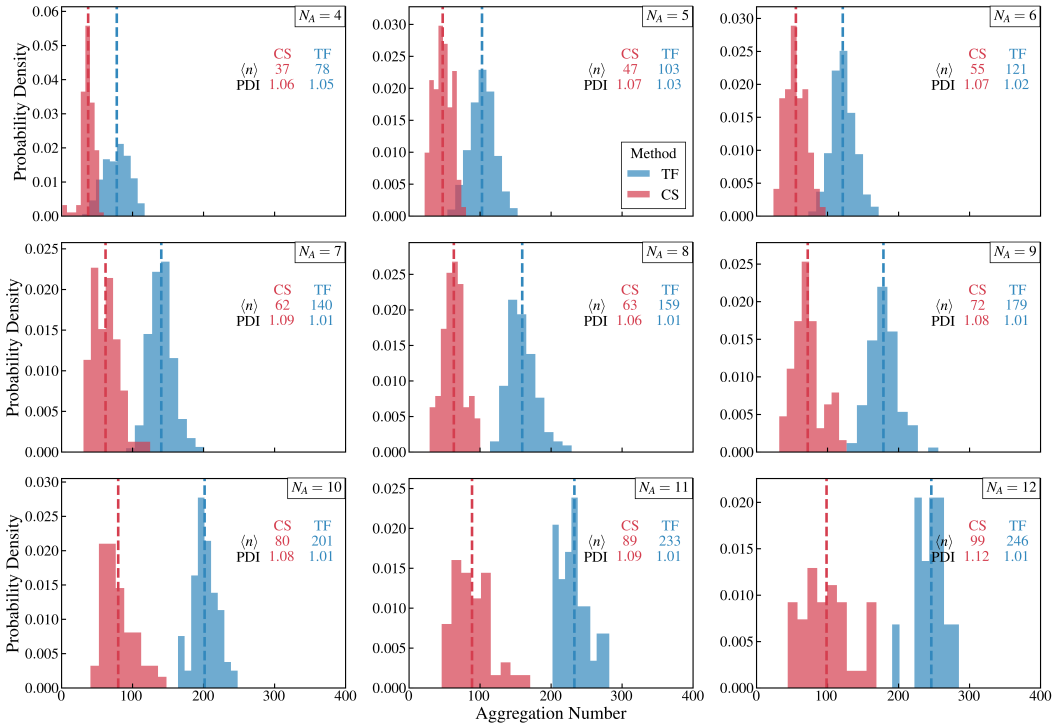

Figure 3.14: Comparison of final micelle distributions of CS and TF methods for various N_A with $N_B = 15$, $\Delta a = 20$. The concentration used for the CS method was $\phi_p = 0.13$. In each panel, the average aggregation numbers and poly dispersive indices are given for both methods.

In Figure 3.14 we compare the final size distributions of the two methods for $N_A = 4 - 12$. In all cases, the size distributions from the TF method are shifted to higher aggregation numbers and have a lower polydispersity index (PDI). This confirms that the route passing through the cylinder phase avoids the kinetic traps of the CS method, since the cylinder pathway does not rely on single chain exchange or micelle fusion. Instead, the micelles form through cylinder extension and pinching which features much lower free energy barriers. The PDI from the TF method is also lower because the size of the micelles that pinch off from the ends of the cylinders are linked to the cylinder radius.

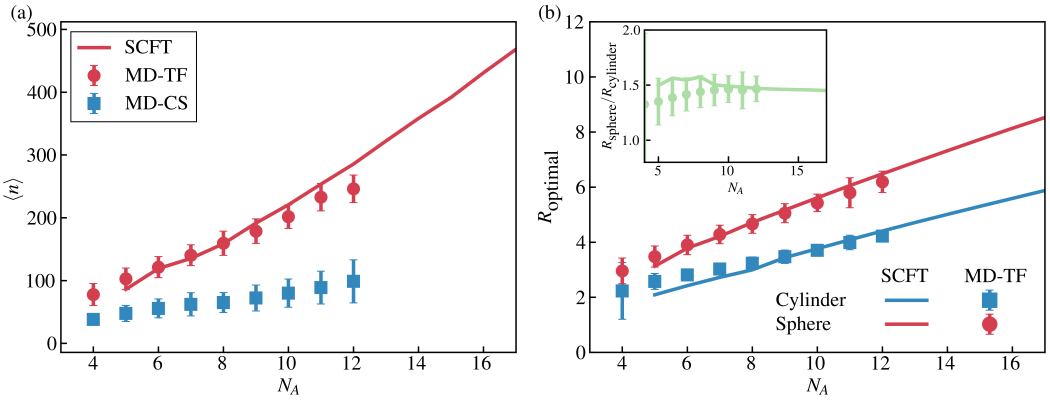

Figure 3.15: Average micelle properties from the two preparation methods and SCFT. (a) Average aggregation number of final micelles from MD simulation compared to optimal aggregation number from SCFT. (b) Average radius of final sphere and intermediate cylinders from the TF method compared to the optimal radii computed from SCFT. The inset is the ratio of the sphere radius to the cylinder radius.

In Figure 3.15 we show the average sizes of the micelles produced from the CS and TF methods. The mean aggregation number is of the final spherical micelles and the error bars are the standard deviation of the distribution. For the larger core block lengths, $N_A \geq 10$, some cylinders persist longer than our simulation runtime, and we exclude these from the distributions and calculation of the mean aggregation number, since we are focused only on the properties of the resulting spherical micelles. It is clear from Figure 3.15a that the mean aggregation number of micelles from the TF method are nearly double the size of those from the CS method. Impressively, the prediction of the optimal size from DPD-SCFT agrees very well with the size of the micelles produced by the TF method, indicating that those micelles are near equilibrium. In Figure 3.15b we plot the average radii of the final spheres and intermediate cylinders and compare them with the optimal values from DPD-SCFT. The sphere radius is defined using the radius of gyration by assuming that the desity is constant throughout the core,

$$R_{\text{sph,MD}} = \sqrt{\frac{5}{3}} R_g = \sqrt{\frac{5}{3}\frac{1}{nN_A}\sum_{i=1}^{nN_A} |\mathbf{r}_i - \mathbf{r}_{\text{com}}|^2} \tag{3.34}$$

$$R_{\text{sph,SCFT}} = \sqrt{\frac{5}{3}\frac{4\pi}{nN_A}\int_0^\infty dr\, r^4 \rho_A(r)} \tag{3.35}$$

where R_g and $\mathbf{r}_{\text{com}}$ are the radius of gyration and the center of mass of the micelle core, respectively. Computing the cylinder radius from MD is challenging since the

cylinders are not always aligned with a cartesian axis, and can even turn and change directions such that there is no principal axis describing the cylinder. To combat this, we instead compute a local principal axis along the cylinder, and then compute the radius of the section of cylinder described by that principal axis using the 2nd and 3rd principal moments. We then average all of the local radii computed from the local 2nd and 3rd principal moments. For a given frame and a given chain in the cylinder, c, we find all other chains within a certain radius that is larger than the radius of the cylinder. We then compute the gyration tensor using only these chains as,

$$\mathbf{G}_c = \frac{1}{mN_A} \sum_{i}^{mN_A} \sum_{i}^{mN_A} \left(\mathbf{r}_i - \mathbf{r}_{\text{com}}\right) \left(\mathbf{r}_j - \mathbf{r}_{\text{com}}\right) \tag{3.36}$$

where the subscript c denotes that the tensor is specific to chain c, m is the number of chains within the chosen range, and r_{com} is the center of mass of the chains (not the entire cylinder). We then compute the principal moments, λ_1^2, λ_2^2, and λ_3^3 which are Eigenvalues of $\mathbf{G}_c$ sorted from largest to smallest. For a cylinder, the 2nd and 3rd moments are related to the cylinder radius by, $R^2_{\text{cyl,MD}} = 2\left(\lambda_2^2 + \lambda_3^2\right)$. Note that a perfect cylinder has $\lambda_2^2 = \lambda_3^2$, however, the moments computed from MD are never exactly equal, so we do not make this simplifying assumption. In DPD-SCFT, we can compute the density profile directly in cylindrical coordinates, which then results in the following equation for the radius

$$R_{\text{cyl,SCFT}} = \sqrt{2\frac{2\pi}{mN_A}\int_0^\infty dr\, r^3 \rho_A(r)} \tag{3.37}$$

where m is the number of chains per units length of the cylinder. From Figure 3.15b, we find striking agreement between the theory and simulation. Interestingly, the radius of the intermediate cylinders during the TF dissolution process is very close to the optimal cylinder radius computed from SCFT, even though the cylinder morphology does not have the lowest free energy. This indicates that there is some local minimum in the free energy of the cylinder where they prefer to sit until something causes them to break apart further into spheres. The inset of Figure 3.15b shows that the ratio of the optimal sphere radius to the optimal cylinder radius remains relatively constant around a value of ≈ 1.4. This indicates that the optimal radii of the sphere and cylinder grow similarly with N_A and that the two radii are intimately linked through the pinching process.

While we did not study it in this work, we hypothesize that the cylinders break up either due to a Plateau–Rayleigh-like instability [41], or via nucleation at the

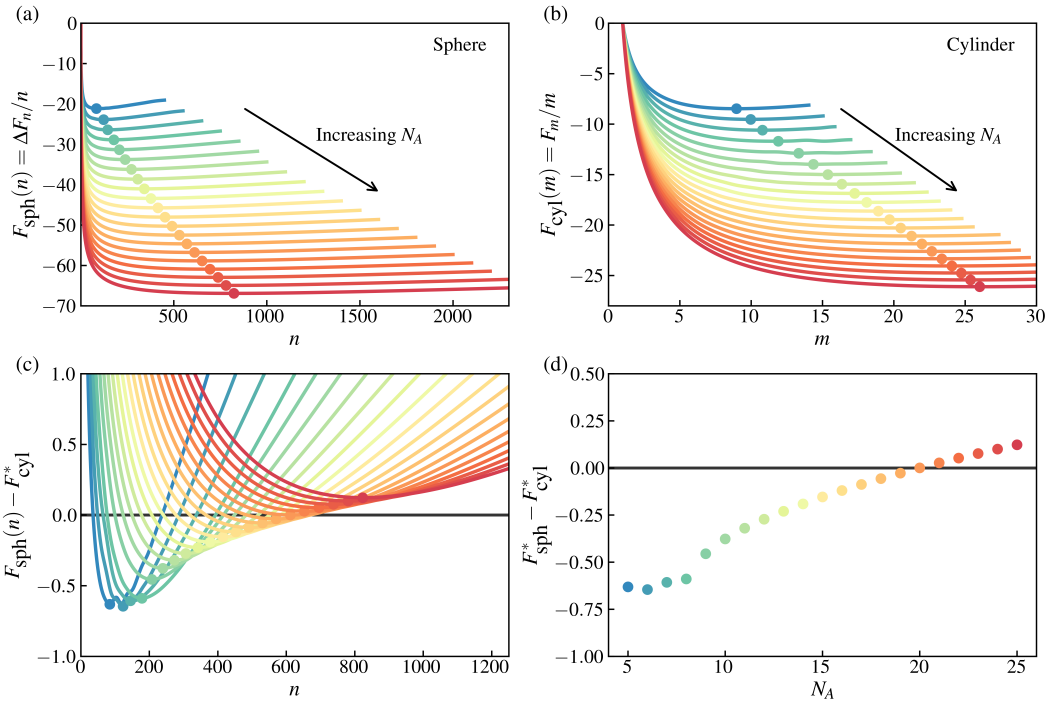

Figure 3.16: Free energy of formation for spheres and cylinders from DPD-SCFT using $\rho = 3$, $N_B = 15$, and $\Delta a = 20$. (a) Free energy of formation per chain for spherical micelles. (b) Free energy of formation per unit length per chain per unit length for infinitely long cylindrical micelles. (c) Formation free energy of sphere of aggregation number n relative to the optimal cylinder free energy. (d) Free energy difference between optimal sphere and optimal cylinder.

cylinder ends. It was discovered by Matsen [42] that there is a low free energy pathway between hexagonal cylinders and BCC spheres in copolymer melts that follows a nucleation and growth mechanism as long as the system is sufficiently far from the cylinder-sphere spinodal. However, the pathway could deviate significantly in copolymer solutions with a free interface between polymer rich and polymer dilute phases. In addition, the spheres that form from the cylinder ends are free to diffuse away, indicating that the pathway need not terminate at the BCC phase. Away from the interface, however, the system may still exhibit a nucleation and growth pathway from cylinders into BCC spheres.

Next, we compare the free energy of an isolated sphere and an isolated cylinder as functions of N_A and aggregation number to determine the location of the phase boundary between the two morphologies. In Figure 3.16a, we show the formation free energy per chain for a spherical micelle as a function of aggregation number. These curves exhibit a single minimum corresponding to the optimal aggregation

number for a spherical micelle. As expected, the optimal aggregation number shifts to higher values as the core block length increases. In Figure 3.16b, we plot the formation free energy for an infinitely long cylinder with m chains per unit length. Similar to the spherical case, these curves display a single minimum corresponding to the optimal number of chains per unit length for the cylinder. Notably, we can compute the sphere (or cylinder) free energy and corresponding optimal aggregation number even outside the respective stability regions because we assume variation only along the radial dimension using spherical (or cylindrical) coordinates. This approach allows direct comparison of formation free energies across morphologies to determine where they intersect.

In Figure 3.16c, we plot the formation free energy per chain for a spherical micelle relative to that of a cylinder at its optimal m. When sufficient chains are available, the cylinder can extend or contract to reach its optimal chain density and radius. From this plot, we observe that shorter core blocks favor spherical morphologies, whereas at very high aggregation numbers, cylindrical morphologies always become energetically preferred. At these large aggregation numbers, micelles tend to form cylinders that extend to their optimal radius before pinching into spheres whose size corresponds to the optimal spherical radius. In the intermediate regime, where the number of chains exceeds the spherical optimum but remains insufficient to form a stable cylinder, the micelle undergoes fission into two smaller micelles. Although not explored in this work, it would be of interest to investigate potential differences in the fission mechanisms of spheres and cylinders. In Figure 3.16d, we present the free energy difference between the optimal sphere and optimal cylinder. Consistent with expectations, spheres are stable for short core blocks, while cylinders dominate for long core blocks. For the DPD model studied here, the morphological boundary occurs at $N_A = 20$, corresponding to $f = N_A/(N_A + N_B) = 0.57$. The crossover occurs at a relatively high value of f because the corona block is solvophilic in our calculations ($\Delta a_{BS} = 0$), which extends the stability region of spherical micelles due to coronal swelling. These results imply that all of our simulations lie within the spherical micelle stability region, and that the cylinders are simply a low free energy metastable intermediate. These results also indicate that the cylinders are able to achieve their optimal radius during the pathway despite being metastable.

3.5 Conclusions

In this work, we provided an in-depth analysis of the kinetic pathway of thin film (TF) dissolution and cosolvent-assisted (CS) dissolution in diblock copolymer mi-

celles. We conducted dissipative particle dynamics (DPD) simulations starting from a copolymer melt in the lamellar microphase, sandwiched between two layers of non-solvent. Upon switching to a selective solvent, the lamellae dissolved into cylinders that aligned axially into a hexagonal close-packed lattice. These cylinders then elongated to relieve transverse stress caused by overlapping coronas from neighboring cylinders. Through elongation, the cylinders reached a local free energy minimum, which was shown to be a metastable state via free energy calculations using DPD-based self-consistent field theory (DPD-SCFT). Over extended simulation times, the cylinders broke up into spherical micelles, with most spheres originating from pinching events at the cylinder ends.

We found that the size of the resulting spherical micelles in the TF method was closely linked to the radius of the intermediate cylinders. To explore this, we varied the core block length, N_A, while keeping the corona block length constant, spanning block fractions in the range $0.21 \leq f \leq 0.44$. Increasing N_A (and therefore f) led to larger cylinders and spheres and also extended the lifespan of the cylindrical intermediates. This is consistent with the expectation that cylindrical micelles become more stable as f increases.

Many of these conclusions were supported by DPD-SCFT calculations of the free energies and optimal sizes of both spherical and cylindrical micelles across a broad parameter space. We found that the parameters used in this study lie within the region of the phase diagram where spheres are thermodynamically stable and cylinders are metastable. There was excellent agreement between the cylinder radii observed in simulations and the metastable values predicted by theory. We also found good agreement between the TF micelle sizes and the theoretical optima, with TF micelles being slightly smaller than optimal. Both simulation and theory revealed that the ratio of sphere to cylinder radii is nearly constant at $R_{\text{sphere}} \approx 1.4 R_{\text{cylinder}}$, providing further evidence that the final sphere size is closely tied to the optimal cylinder radius.

We also analyzed micellization via the cosolvent-assisted (CS) dissolution method using the same simulation parameters. In this case, micelles became kinetically trapped at sizes much smaller than those from the TF method or the optimal sizes predicted by DPD-SCFT. Although increasing the concentration led to larger micelles, their size remained significantly smaller than those from the TF method, even at unrealistically high concentrations. For $\rho = 3$, $\Delta a = 20$, and $N_A = 4$–12, we found that single-chain exchange was essentially halted, except in the case of $N_A = 4$.

This represents a different regime than that studied by Li and Dormidontova, who used much shorter core blocks and achieved equilibrium through a combination of fusion and exchange [26]. In our simulations, the combination of high χ and longer core blocks produced exchange barriers that are insurmountable on our simulation timescale, consistent with our previous work [40] and the findings of Seeger et al. [43, 44]. As a result, fusion becomes the dominant mechanism for micellization and equilibration, with little to no free energy barrier for small aggregates with diffuse coronas. However, as these aggregates fuse and grow larger, their coronas thicken, and the fusion barrier increases. This leads to significantly slowed dynamics and micelles that are kinetically trapped far below their equilibrium size.

Future work in this area should focus on elucidating the mechanism by which intermediate cylinders break up into spheres. We hypothesize that this occurs either through a Plateau–Rayleigh-like instability or a nucleation process at the cylinder ends. In either case, further investigation into the cylinder-to-sphere transition would be highly valuable. Another direction worth exploring is the TF dissolution pathway starting from other copolymer microphases, such as BCC spheres, hexagonally packed cylinders, or even gyroid phases. A natural extension is also to study TF dissolution in triblock copolymers, where we expect the pathway to differ somewhat due to the bridging that occurs in triblock lamellae. Lastly, more work is warranted at higher core block fractions to explore the possibility of forming micelles that are significantly larger than their equilibrium size, as has been observed by Meli and Lodge [9, 10].

3.6 Appendix

Micelle Distribution Properties

DPD-SCFT

As mentioned in the main text, we solve the profiles and free energy of three separate morphologies: (1) lamellar, (2) spherical, and (3) cylindrical. In this section, we outline the mathematical and computational details for how the general equations are reduced to 1 dimensional problems and then solved numerically. As a reminder,

Table 3.1: Final micelle distribution properties from CS and TF methods with $N_B = 15$ and $\Delta a = 20$.

N_A	$\langle n \rangle$		PDI	
	CS	TF	CS	TF
4	38	78	1.04	1.05
5	48	103	1.07	1.03
6	56	121	1.07	1.02
7	62	140	1.09	1.01
8	63	159	1.06	1.01
9	72	179	1.08	1.01
10	80	201	1.08	1.01
11	89	233	1.09	1.01
12	99	246	1.12	1.01

the mean-field equations in 3 dimensions are given by

$$\rho_A(\mathbf{r}) = \frac{n e^{\xi_A(\mathbf{r})}}{v Q_P} \sum_{i=1}^{N_A} q(\mathbf{r}; i) q^\dagger(\mathbf{r}; N - i) \tag{3.38}$$

$$\rho_B(\mathbf{r}) = \frac{n e^{\xi_B(\mathbf{r})}}{v Q_P} \sum_{i=N_A+1}^{N} q(\mathbf{r}; i) q^\dagger(\mathbf{r}; N - i) \tag{3.39}$$

$$\rho_S(\mathbf{r}) = \frac{e^{\beta\mu}}{v} \int d\mathbf{r}\, e^{-\xi_S(\mathbf{r})} \tag{3.40}$$

$$\xi_\alpha(\mathbf{r}) = \sum_{\gamma \in \mathbf{C}} \int d\mathbf{r}' \rho_\gamma(\mathbf{r}') \beta U_{\text{dpd}}^{\alpha\gamma}(|\mathbf{r} - \mathbf{r}'|) \tag{3.41}$$

with propagators

$$q(\mathbf{r}; 1) = e^{-\xi_A(\mathbf{r})} \tag{3.42}$$

$$q(\mathbf{r}; i) = \frac{e^{-\xi_{t(i)}(\mathbf{r})}}{C} \int d\mathbf{r}' e^{-\frac{\kappa}{2d_p^2}(|\mathbf{r}-\mathbf{r}'|-b)^2} q(\mathbf{r}'; i-1) \tag{3.43}$$

$$q^\dagger(\mathbf{r}, 1) = e^{-\xi_B(\mathbf{r})} \tag{3.44}$$

$$q^\dagger(\mathbf{r}; i) = \frac{e^{-\xi_{t(N-i)}(\mathbf{r})}}{C} \int d\mathbf{r}' e^{-\frac{\kappa}{2d_p^2}(|\mathbf{r}-\mathbf{r}'|-b)^2} q^\dagger(\mathbf{r}'; i-1) \tag{3.45}$$

where $t(i) = A$ for $i \leq N_A$ and $t(i) = B$ otherwise. C is the normalization constant,

$$C = 4\pi \int_0^\infty dr\, r^2 e^{-\frac{\kappa}{2d_p^2}(r-b)^2}, \tag{3.46}$$

and the polymer partition function can be computed from

$$Q_P = \frac{1}{v} \int d\mathbf{r}\, q(\mathbf{r}; N)\ . \tag{3.47}$$

The solvent fugacity, $e^{\beta\mu}$, can be computed using the properties of the homogeneous reservoir according to,

$$\frac{\langle m\rangle v}{V} = \rho = \frac{v}{V}\frac{\partial \ln \Xi}{\partial \beta\mu} = e^{\beta\mu}e^{-\frac{\pi}{15}a_{ii}\rho} \;\rightarrow\; e^{\beta\mu} = \rho e^{\frac{\pi}{15}a_{ii}\rho} \tag{3.48}$$

where the reservoir is a bulk fluid of solvent at a uniform density of $\rho = 3$. By inserting the saddle-point equations into the Hamiltonian, we obtain the simplified mean-field free energy,

$$\beta\Omega(n,\mu,V,T) = \ln(n!) - n\ln Q_P - \int d\mathbf{r}\rho_S(\mathbf{r}) - \frac{1}{2}\sum_{\alpha\in\mathbf{C}}\int d\mathbf{r}\,\xi_\alpha(\mathbf{r})\rho_\alpha(\mathbf{r}). \tag{3.49}$$

Lamellar Melt

In the lamellar phase, we take dimensions parallel to the interface to be infinite such that the system can be reduced to variation in only the normal direction (z). Thus, we must reduce all of the equations to only variation in z by integrating out the dependence on x and y.

The propagator can be computed by integrating in cylindrical coordinates where r and θ are used to integrate in the x, y plane.

$$I(\mathbf{r}) = \frac{1}{C}\int d\mathbf{r}' e^{-\frac{\kappa}{2}(|\mathbf{r}-\mathbf{r}'|-b)^2} q(\mathbf{r}') \tag{3.50}$$

$$I(z) = \frac{1}{C}\int_{-\infty}^{\infty} dz'\, q(z') \int_0^\infty dr\, r \exp\left\{-\frac{\kappa}{2}\left[\sqrt{(z-z')^2+r^2}-b\right]^2\right\}\int_0^{2\pi} d\theta \tag{3.51}$$

$$= \frac{2\pi}{C}\int_{-\infty}^{\infty} dz'\, q(z') \int_{|z-z'|}^\infty du\, \exp\left\{-\frac{\kappa}{2}\left[u-b\right]^2\right\} \tag{3.52}$$

$$= \frac{2\pi}{C}\int_{-\infty}^{\infty} dz'\, q(z') \int_{(|z-z'|-b)\sqrt{\kappa/2}}^\infty du\, \left(\frac{2}{\kappa}u + b\sqrt{\frac{2}{\kappa}}\right)e^{-u^2} \tag{3.53}$$

$$= \frac{2\pi}{C}\int_{-\infty}^{\infty} dz'\, q(z')\left\{\frac{1}{\kappa}\exp\left[-\frac{\kappa}{2}\left(|z-z'|-b\right)^2\right]\right.$$
$$\left. + b\sqrt{\frac{\pi}{2\kappa}}\mathrm{erfc}\left[\sqrt{\frac{\kappa}{2}}\left(|z-z'|-b\right)\right]\right\} \tag{3.54}$$

If we define the following function,

$$g(|z-z'|) = \frac{1}{\kappa}\exp\left[-\frac{\kappa}{2}\left(|z-z'|-b\right)^2\right] + b\sqrt{\frac{\pi}{2\kappa}}\mathrm{erfc}\left[\sqrt{\frac{\kappa}{2}}\left(|z-z'|-b\right)\right] \tag{3.55}$$

then the convolutional integral can be performed in Fourier space,

$$I(z) = \frac{2\pi}{C}\mathcal{F}^{-1}\left[\hat{q}(\mathbf{k}) * \hat{g}(\mathbf{k})\right] \tag{3.56}$$

where $\hat{q}$ and $\hat{g}$ are Fourier transforms, and $\mathcal{F}^{-1}$ is the inverse Fourier transform operator.

Next, we evaluate the the integration for field variables involving the DPD potential. Note that the DPD potential is only valid for $r < 1$.

$$W(\mathbf{r}) = \int d\mathbf{r}' \, \frac{1}{2}\left(1 - |\mathbf{r} - \mathbf{r}'|\right)^2 \rho(\mathbf{r}') \tag{3.57}$$

$$W(z) = \frac{1}{2}\int_{z-1}^{z+1} dz' \rho(z') \int_0^{\sqrt{1-(z-z')^2}} dr \, r \left[1 - \sqrt{(z-z')^2 + r^2}\right]^2 \int_0^{2\pi} d\theta \tag{3.58}$$

$$= \frac{\pi}{2}\int_{z-1}^{z+1} dz' \rho(z') \left[\frac{1}{6} - \frac{1}{2}|z-z'|^4 + \frac{4}{3}|z-z'|^3 - |z-z'|^2\right] \tag{3.59}$$

Again, if we define the function $u(|z - z'|)$,

$$u(|z-z'|) = \begin{cases} \frac{1}{6} - \frac{1}{2}|z-z'|^4 + \frac{4}{3}|z-z'|^3 - |z-z'|^2 & , \, |z-z'| \leq 1 \\ 0 & , \, |z-z'| > 1 \end{cases} \tag{3.60}$$

then the integration can be performed in Fourier space using

$$W(z) = \frac{\pi}{2}\mathcal{F}^{-1}\left[\hat{\rho}(\mathbf{k}) * \hat{u}(\mathbf{k})\right] . \tag{3.61}$$

If we set $\rho = 1$, then we find the full weight of the DPD kernel amounts to $\pi/15$. The single polymer partition function results in

$$Q_P = \frac{1}{v}\int d\mathbf{r} \, q(\mathbf{r}; N) = \frac{A_{||}}{v}\int dz \, q(z; N) = A_{||} Q_P^z \, . \tag{3.62}$$

Given that the system is infinite in the x, y-plane, the total number of chains n is not well defined. Instead, we can define the number of chains per unit area, $\hat{m} = n/A_{||}$. Thus, the polymer densities can be written as,

$$\rho_A(z) = \frac{\hat{m} e^{\xi_A(z)}}{v Q_P^z} \sum_{i=1}^{N_A} q(z; i) q^\dagger(z; N - i) \tag{3.63}$$

$$\rho_B(z) = \frac{\hat{m} e^{\xi_B(z)}}{v Q_P^z} \sum_{i=N_A+1}^{N} q(z; i) q^\dagger(z; N - i) \, . \tag{3.64}$$

The indistinguishability factor also needs to be rewritten in terms of the Sterling approximation.

$$\ln(n!) = \ln[(\hat{m}A_{||})!] \approx \hat{m}A_{||}\ln(\hat{m}A_{||}) - \hat{m}A_{||} + \frac{1}{2}\ln(2\pi\hat{m}A_{||}) \tag{3.65}$$

Combining everything, the mean-field free energy per unit area becomes

$$\frac{\beta\Omega}{A} = \hat{m}\ln\hat{m} - \hat{m} + \frac{1}{2A_{||}}\ln(2\pi\hat{m}A_{||}) - \hat{m}\ln Q_P^z - \int_0^L dz\rho_S(z) - \frac{1}{2}\sum_{\alpha\in\mathbf{C}}\int_0^L dz\,\xi_\alpha(z)\rho_\alpha(z) \tag{3.66}$$

where the term $\ln(2\pi\hat{m}A_{||})/2A_{||} \to 0$ as $A_{||} \to \infty$.

Spherical Micelle

If we assume that the micelle is a perfect sphere, then there is no variation in the φ and θ angles. We can exploit this fact and integrate out the angular dependence from all of the mean-field equations. We follow a similar path to that of the lamellar melt section, starting with the propagator integral,

$$I(\mathbf{r}) = \frac{1}{C}\int d\mathbf{x}\, e^{-\frac{\kappa}{2}(|\mathbf{r}-\mathbf{x}|-b)^2} q(\mathbf{x}) \tag{3.67}$$

$$I(r) = \frac{1}{C}\int_0^\infty dx\, x^2 q(x)\int_0^{2\pi} d\varphi \int_0^\pi d\theta\ \sin(\theta)\exp\left\{-\frac{\kappa}{2}\left[(r^2+x^2-2rx\cos\theta) - 2b\sqrt{r^2+x^2-2rx\cos\theta}+b^2\right]\right\} \tag{3.68}$$

$$= \frac{2\pi}{C}\int_0^\infty dx\, x^2 q(x)\int_0^\pi d\theta\ \sin(\theta)\exp\left\{-\frac{\kappa}{2}\left[(r^2+x^2-2rx\cos\theta) - 2b\sqrt{r^2+x^2-2rx\cos\theta}+b^2\right]\right\} \tag{3.69}$$

$$= \frac{2\pi}{C}\int_0^\infty dx\, x^2 q(x)\frac{1}{2rx}\int_{(r-x)^2}^{(r+x)^2} du\ \exp\left[-\frac{\kappa}{2}\left(\sqrt{u}-b\right)^2\right] \tag{3.70}$$

$$= \frac{2\pi}{C}\int_0^\infty dx\, x^2 q(x)\frac{1}{rx}\int_{|r-x|}^{r+x} ds\, s\exp\left[-\frac{\kappa}{2}(s-b)^2\right] \tag{3.71}$$

$$= \frac{2\pi}{C}\int_0^\infty dx\, x^2 q(x)\frac{1}{rx}\int_{|r-x|-b}^{r+x-b} dt\,(t+b)\exp\left[-\frac{\kappa}{2}t^2\right] \tag{3.72}$$

$$= \frac{2\pi}{C}\int_0^\infty dx\, q(x)\frac{x}{r}\left\{\sqrt{\frac{\pi b^2}{2\kappa}}\mathrm{erf}\left[\sqrt{\frac{\kappa}{2}}t\right] - \frac{1}{\kappa}\exp\left[-\frac{\kappa}{2}t^2\right]\right\}_{|r-x|-b}^{r+x-b} \tag{3.73}$$

This cannot be evaluated using Fourier transforms, so we must evaluate the integral over x in real space for each point r. Fortunately, all propagators $q(x;i)$ go to 0 at the boundary as long as the system radius is sufficiently large, and in addition, the integrand decays rapidly for $|r-x| > b$. This allows us to truncate the integral at $x = R + b$.

Next, we evaluate the integration for the field variables involving the DPD potential. Again, note that the DPD potential is only valid for distances less than 1, and so we have to pay close attention to integration bounds.

$$W(\mathbf{r}) = \int d\mathbf{r}' \, \frac{1}{2} \left(1 - |\mathbf{r} - \mathbf{r}'|\right)^2 \rho(\mathbf{r}') \tag{3.74}$$

$$W(r) = \pi \int_{\max(r-1,0)}^{r+1} dx \, x^2 \rho(x) \int d\theta \sin(\theta) \Bigg[1 - 2\sqrt{r^2 + x^2 - 2rx\cos\theta} + r^2 + x^2 - 2rx\cos\theta \Bigg] \tag{3.75}$$

$$= \frac{\pi}{2} \int_{\max(r-1,0)}^{r+1} dx \frac{x}{r} \rho(x) \int_{(r-x)^2}^{\min((r+x)^2,1)} du \left[1 - 2\sqrt{u} + u\right] \tag{3.76}$$

$$= \frac{\pi}{2} \int_{\max(r-1,0)}^{r+1} dx \frac{x}{r} \rho(x) \left[u^2 - \frac{4}{3}|u|^3 + \frac{1}{2}u^4 \right]_{r-x}^{\min(r+x,1)} \tag{3.77}$$

The final integral over x can be evaluated numerically in real space for each value of r. In the special case where $r = 0$, the integral reduces to,

$$W(0) = 2\pi \int_0^1 dx \, \rho(x) x^2 \left[1 - 2x + x^2\right] \tag{3.78}$$

In spherical coordinates, any simple integral is evaluated with the normal Jacobian with the angular components integrated out,

$$\int_V d\mathbf{r} \, f(\mathbf{r}) = 4\pi \int_0^R dr \, r^2 f(r) \tag{3.79}$$

where $f(\mathbf{r})$ is any function that can be expressed in terms of only the radial coordinate $f(r)$. Since the number of chains, n, is well-defined for an isolated micelle in spherical coordinates, we do not have to modify the mean-field free energy.

$$\beta\Omega = \ln(n!) - n \ln Q_P - 4\pi \int_0^R dr \, r^2 \rho_S(r) - 2\pi \sum_{\alpha \in \mathbf{C}} \int_0^R dr \, r^2 \, \xi_\alpha(r) \rho_\alpha(r). \tag{3.80}$$

Cylindrical

If we assume the micelle is an infinitely long cylinder, then there is no variation in z and θ. Thus, we can reduce the problem to variation in the radial dimension of the cylinder by integrating out the z and θ dimensions. We follow a similar path to that of the other two morphologies, starting with the propagator integral,

$$I(\mathbf{r}) = \frac{1}{C}\int d\mathbf{r}' e^{-\frac{\kappa}{2}(|\mathbf{r}-\mathbf{r}'|-b)^2} q(\mathbf{r}') \tag{3.81}$$

$$I(r) = \frac{1}{C}\int_0^\infty dx\, xq(x)\int_0^{2\pi} d\theta \int_{-\infty}^{\infty} dz \exp\left\{-\frac{\kappa}{2}\left[\sqrt{r^2+x^2-2rx\cos\theta+z^2}-b\right]^2\right\} \tag{3.82}$$

None of the integrals can be evaluated in closed form, so we numerically evaluated the double integral over θ and z for each combination of r and x to create a kernel that could be interpolated, $K(r,x)$.

Next, we evaluate the integration for the field variables involving the DPD potential. Again, note that the DPD potential is only valid for distances less than 1, so we have to pay close attention to the integration bounds.

$$W(\mathbf{r}) = \int d\mathbf{r}' \frac{1}{2}\left(1-|\mathbf{r}-\mathbf{r}'|\right)^2 \rho(\mathbf{r}') \tag{3.83}$$

$$W(r) = \frac{1}{2}\int_{\text{max(r-1,0)}}^{r+1} dx\, x\rho(x) \int_{-\arccos\left[\max\left(\frac{x^2+r^2-1}{2rx},-1\right)\right]}^{\arccos\left[\max\left(\frac{x^2+r^2-1}{2rx},-1\right)\right]} d\theta \cdots$$
$$\cdots \int_{-\sqrt{1-r^2-x^2+2rx\cos\theta}}^{\sqrt{1-r^2-x^2+2rx\cos\theta}} dz \left(1-\sqrt{r^2+x^2-2rx\cos\theta+z^2}\right)^2 \tag{3.84}$$

This cannot be solved analytically, so we numerically evaluate the integrals in θ and z over a grid of r and x to make a kernel that can be interpolated for later use, $K(r,x)$. Then in the calculation we simply evaluate the integral,

$$W(r) = \int_{\text{max(r-1,0)}}^{r+1} dx\, x\rho(x)K(r,x) \tag{3.85}$$

In cylindrical coordinates, any simple integral is evaluated with the normal Jacobian with the angular and length coordinates integrated out,

$$\int_V d\mathbf{r}\, f(\mathbf{r}) = 2\pi L\int dr\, rf(r) \tag{3.86}$$

where L is the length of the cylinder and $f(\mathbf{r})$ is any function that can be expressed only in terms of the radial coordinate, $f(r)$. Since the number of chains, n, is not

well defined for an infinitely long cylinder, we define the number of chains per units length, $m = n/L$. The single polymer partition function is,

$$Q_P = \frac{1}{v}\int d\mathbf{r}\, q(\mathbf{r}; N) = \frac{2\pi L}{v}\int dr\, r q(r; N) = L Q_P^r \ . \tag{3.87}$$

The polymer densities can then be written as,

$$\rho_A(z) = \frac{m e^{\xi_A(z)}}{v Q_P^r}\sum_{i=1}^{N_A} q(z; i) q^\dagger(z; N-i) \tag{3.88}$$

$$\rho_B(z) = \frac{m e^{\xi_B(z)}}{v Q_P^r}\sum_{i=N_A+1}^{N} q(z; i) q^\dagger(z; N-i) \ . \tag{3.89}$$

The indistinguishability factor also needs to be rewritten in terms of the Sterling approximation.

$$\ln(n!) = \ln[(mL)!] \approx mL\ln(mL) - mL + \frac{1}{2}\ln(2\pi mL) \tag{3.90}$$

Combining everything, the mean-field free energy per unit length becomes

$$\begin{aligned}\frac{\beta\Omega}{L} = m\ln m - m + \frac{1}{2L}\ln(2\pi mL) - m\ln Q_P^r \\ - 2\pi\int_0^R dr\, r\rho_S(r) - \pi\sum_{\alpha\in\mathbf{C}}\int_0^R dr\, r\xi_\alpha(r)\rho_\alpha(r)\end{aligned} \tag{3.91}$$

where the term $\ln(2\pi mL)/2L \to 0$ as $L \to \infty$.

Numerical Procedure

To solve the set of mean-field equations, we employ a simple fixed-point scheme with a judicious choice of the initial profiles. We use a combination of simple (Picard) mixing and Anderson Acceleration. The steps are as follows:

1. Initialize density profiles to ρ_A^0, ρ_B^0, $\rho_S^0 = \rho - \rho_A^0 - \rho_B^0$.
2. Compute the fields ξ_A, ξ_B, and ξ_S using Equation (3.41)
3. Compute the propagators using Equations (3.42)-(3.45).
4. Compute the single polymer partition function with (3.47).
5. Compute new densities, $\rho^{n+1/2}$, using the field and propagators with Equations (3.38)-(3.40).

6. Compute error between new and old densities with $E = ||\rho^{n+1/2} - \rho^n||_\infty$.

7. If $E > 0.01$, update via simple mixing, $\rho^{n+1} = (1 - \lambda)\rho^n + \lambda\rho^{n+1/2}$. If $E \leq 0.01$ then update using Anderson acceleration.

8. If the error is below some tolerance, $E < \epsilon$, then exit the self-consistent loop. Otherwise, continue at step 2.

References

(1) Zhulina, E. B.; Adam, M.; LaRue, I.; Sheiko, S. S.; Rubinstein, M. Diblock Copolymer Micelles in a Dilute Solution. *Macromolecules* **2005**, *38*, 5330–5351, DOI: 10.1021/ma048102n.

(2) Zhulina, E. B.; Borisov, O. V. Theory of Block Polymer Micelles: Recent Advances and Current Challenges. *Macromolecules* **2012**, *45*, 4429–4440, DOI: 10.1021/ma300195n.

(3) Lodge, T. P.; Seitzinger, C. L.; Seeger, S. C., et al. Dynamics and Equilibration Mechanisms in Block Copolymer Particles. *ACS Polymers Au* **2022**, *2*, 397–416, DOI: 10.1021/acspolymersau.2c00033.

(4) Nyrkova, I. A.; Semenov, A. N. On the Theory of Micellization Kinetics. *Macromolecular Theory and Simulations* **2005**, *14*, 569–585, DOI: 10.1002/mats.200500010.

(5) Dormidontova, E. E. Micellization Kinetics in Block Copolymer Solutions: Scaling Model. *Macromolecules* **1999**, *32*, 7630–7644, DOI: 10.1021/ma9809029.

(6) Nicolai, T.; Colombani, O.; Chassenieux, C. Dynamic polymeric micelles versus frozen nanoparticles formed by block copolymers. *Soft Matter* **2010**, *6*, 3111–3118, DOI: 10.1039/B925666K.

(7) Johnson, B. K. Mechanism for Rapid Self-Assembly of Block Copolymer Nanoparticles. *Physical Review Letters* **2003**, *91*, DOI: 10.1103/PhysRevLett.91.118302.

(8) Zhang, J.; Xu, J.; Liu, S. Chain-Length Dependence of Diblock Copolymer Micellization Kinetics Studied by Stopped-Flow pH-Jump. *The Journal of Physical Chemistry B* **2008**, *112*, 11284–11291, DOI: 10.1021/jp803700n.

(9) Meli, L.; Lodge, T. P. Equilibrium vs Metastability: High-Temperature Annealing of Spherical Block Copolymer Micelles in an Ionic Liquid. *Macromolecules* **2009**, *42*, 580–583, DOI: 10.1021/ma802020a.

(10) Meli, L.; Santiago, J. M.; Lodge, T. P. Path-Dependent Morphology and Relaxation Kinetics of Highly Amphiphilic Diblock Copolymer Micelles in Ionic Liquids. *Macromolecules* **2010**, *43*, 2018–2027, DOI: 10.1021/ma902366c.

(11) Jain, S.; Bates, F. S. Consequences of Nonergodicity in Aqueous Binary PEO-PB Micellar Dispersions. *Macromolecules* **2004**, *37*, 1511–1523, DOI: 10.1021/ma035467j.

(12) Lund, R.; Willner, L.; Richter, D.; Dormidontova, E. E. Equilibrium Chain Exchange Kinetics of Diblock Copolymer Micelles: Tuning and Logarithmic Relaxation. *Macromolecules* **2006**, *39*, 4566–4575, DOI: 10.1021/ma060328y.

(13) Zhang, J.; Farias-Mancilla, B.; Kulai, I., et al. Effect of Hydrophilic Monomer Distribution on Self-Assembly of a pH-Responsive Copolymer: Spheres, Worms and Vesicles from a Single Copolymer Composition. *Angewandte Chemie International Edition* **2021**, *60*, 4925–4930, DOI: 10.1002/anie.202010501.

(14) Rodrigues, K.; Mattice, W. L. Simulation of the steric stabilization of polymer colloids by diblock copolymers. *The Journal of Chemical Physics* **1991**, *94*, 761–766, DOI: 10.1063/1.460344.

(15) Wang, Y.; Mattice, W. L.; Napper, D. H. Simulation of the formation of micelles by diblock copolymers under weak segregation, ACS Publications https://pubs.acs.org/doi/abs/10.1021/la00025a017 (accessed 10/22/2025).

(16) Kazaryan, P. S.; Chertovich, A. V.; Gavrilov, A. A. Tuning polymer micelle size and dynamics with solvophobic block structure. *Journal of Colloid and Interface Science* **2025**, *680*, 496–505, DOI: 10.1016/j.jcis.2024.10.186.

(17) Lund, R.; Willner, L.; Stellbrink, J.; Lindner, P.; Richter, D. Logarithmic Chain-Exchange Kinetics of Diblock Copolymer Micelles. *Physical Review Letters* **2006**, *96*, 068302, DOI: 10.1103/PhysRevLett.96.068302.

(18) Wright, D. B.; Patterson, J. P.; Gianneschi, N. C., et al. Blending block copolymer micelles in solution; Obstacles of blending. *Polymer chemistry* **2016**, *7*, 1577–1583, DOI: 10.1039/C5PY02006A.

(19) Groot, R. D.; Warren, P. B. Dissipative particle dynamics: Bridging the gap between atomistic and mesoscopic simulation. *The Journal of Chemical Physics* **1997**, *107*, 4423–4435, DOI: 10.1063/1.474784.

(20) Glaser, J.; Medapuram, P.; Beardsley, T. M.; Matsen, M. W.; Morse, D. C. Universality of Block Copolymer Melts. *Physical Review Letters* **2014**, *113*, 068302, DOI: 10.1103/PhysRevLett.113.068302.

(21) Groot, R. D.; Madden, T. J. Dynamic simulation of diblock copolymer microphase separation. *The Journal of Chemical Physics* **1998**, *108*, 8713–8724, DOI: 10.1063/1.476300.

(22) Petrov, A.; Huang, H.; Alexander-Katz, A. Simple Calibration of Block Copolymer Melt Models. *Macromolecules* **2024**, *57*, 8212–8222, DOI: 10.1021/acs.macromol.4c00680.

(23) Huang, H.; Alexander-Katz, A. Dissipative particle dynamics for directed self-assembly of block copolymers. *The Journal of Chemical Physics* **2019**, *151*, 154905, DOI: 10.1063/1.5117839.

(24) Petrus, P.; Lísal, M.; Brennan, J. K. Self-Assembly of Symmetric Diblock Copolymers in Planar Slits with and without Nanopatterns: Insight from Dissipative Particle Dynamics Simulations, ACS Publications https://pubs.acs.org/doi/abs/10.1021/la903200j (accessed 10/22/2025).

(25) Feng, J.; Liu, H.; Hu, Y. Mesophase Separation of Diblock Copolymer Confined in a Cylindrical Tube Studied by Dissipative Particle Dynamics. *Macromolecular Theory and Simulations* **2006**, *15*, 674–685, DOI: 10.1002/mats.200600042.

(26) Li, Z.; Dormidontova, E. E. Kinetics of Diblock Copolymer Micellization by Dissipative Particle Dynamics. *Macromolecules* **2010**, *43*, 3521–3531, DOI: 10.1021/ma902860j.

(27) Mysona, J. A.; McCormick, A. V.; Morse, D. C. Mechanism of Micelle Birth and Death. *Physical Review Letters* **2019**, *123*, 038003, DOI: 10.1103/PhysRevLett.123.038003.

(28) Mysona, J. A.; McCormick, A. V.; Morse, D. C. Simulation of diblock copolymer surfactants. I. Micelle free energies. *Physical Review E* **2019**, *100*, 012602, DOI: 10.1103/PhysRevE.100.012602.

(29) Mysona, J. A.; McCormick, A. V.; Morse, D. C. Simulation of diblock copolymer surfactants. II. Micelle kinetics. *Physical Review E* **2019**, *100*, 012603, DOI: 10.1103/PhysRevE.100.012603.

(30) Thompson, A. P.; Aktulga, H. M.; Berger, R., et al. LAMMPS - a flexible simulation tool for particle-based materials modeling at the atomic, meso, and continuum scales. *Computer Physics Communications* **2022**, *271*, 108171, DOI: 10.1016/j.cpc.2021.108171.

(31) Lequieu, J. Combining particle and field-theoretic polymer models with multi-representation simulations. *The Journal of Chemical Physics* **2023**, *158*, 244902, DOI: 10.1063/5.0153104.

(32) Patterson, J. P.; Robin, M. P.; Chassenieux, C.; Colombani, O.; O'Reilly, R. K. The analysis of solution self-assembled polymeric nanomaterials. *Chemical Society Reviews* **2014**, *43*, 2412–2425, DOI: 10.1039/C3CS60454C.

(33) Fredrickson, G. H., *The equilibrium theory of inhomogeneous polymers*; International series of monographs on physics 134; Clarendon Press ; Oxford University Press: Oxford : New York, 2006; 437 pp.

(34) Matsen, M. W. Self-Consistent Field Theory for Melts of Low-Molecular-Weight Diblock Copolymer. *Macromolecules* **2012**, *45*, 8502–8509, DOI: 10.1021/ma301788q.

(35) Wang, J.; Guo, K.; An, L.; Müller, M.; Wang, Z.-G. Micelles of Coil-Comb Block Copolymers in Selective Solvents: Competition of Length Scales. *Macromolecules* **2010**, *43*, 2037–2041, DOI: 10.1021/ma901977h.

(36) Wang, J.; Müller, M.; Wang, Z.-G. Nucleation in A/B/AB blends: Interplay between microphase assembly and macrophase separation. *The Journal of Chemical Physics* **2009**, *130*, 154902, DOI: 10.1063/1.3105340.

(37) Duan, C.; Li, W.; Wang, R. Conformation of a single polyelectrolyte in poor solvents. *The Journal of Chemical Physics* **2020**, *153*, 064901, DOI: 10.1063/5.0017371.

(38) Duan, C.; Wang, R. Electrostatics-Induced Nucleated Conformational Transition of Protein Aggregation. *Physical Review Letters* **2023**, *130*, 158401, DOI: 10.1103/PhysRevLett.130.158401.

(39) Duan, C.; Wang, M.; Ghobadi, A.; Eike, D. M.; Wang, R. Quantifying the Critical Micelle Concentration of Nonionic and Ionic Surfactants by Self-Consistent Field Theory, 2024, DOI: 10.48550/arXiv.2412.03549.

(40) Varner, S.; Müller, M.; Gallegos, A., et al. Mechanisms of Chain Exchange in Diblock Copolymer Micelles, 2025, DOI: 10.48550/arXiv.2509.06528.

(41) Barker, B.; Bell, J. B.; Garcia, A. L. Fluctuating hydrodynamics and the Rayleigh–Plateau instability. *Proceedings of the National Academy of Sciences* **2023**, *120*, e2306088120, DOI: 10.1073/pnas.2306088120.

(42) Matsen, M. W. Cylinder-sphere epitaxial transitions in block copolymer melts. *The Journal of Chemical Physics* **2001**, *114*, 8165–8173, DOI: 10.1063/1.1365085.

(43) Seeger, S. C.; Dorfman, K. D.; Lodge, T. P. Free Energy Trajectory for Escape of a Single Chain from a Diblock Copolymer Micelle. *ACS Macro Letters* **2021**, *10*, 1570–1575, DOI: 10.1021/acsmacrolett.1c00508.

(44) Seeger, S. C.; Lodge, T. P.; Dorfman, K. D. Mechanism of Escape of a Single Chain from a Diblock Copolymer Micelle. *Macromolecules* **2022**, *55*, 10220–10228, DOI: 10.1021/acs.macromol.2c01742.

Part II

Inhomogeneous Thermodynamics of Ionic Liquids and Polar Fluids

Chapter 4

INTRODUCTION

This introductory chapter covers the fundamentals of electrolye solutions, ionics liquids, and polar fluids including basic theory and applications. Subsequent chapters will address three specific research topics including the capacitance and phase behavior of ionic liquid supercapacitors, the entropic origin of ionic interactions in polar solvents, and the spontaneous surface polarization in asymmetric polar fluids.

This chapter includes content from our previously published articles:

Varner, S.; Wang, Z.-G. Effects of dilution in ionic liquid supercapacitors. *Physical Chemistry Chemical Physics* **2022**, *24*, 27362–27374, DOI: 10.1039/D2CP03398D

Varner, S.; Balzer, C.; Wang, Z.-G. Entropic Origin of Ionic Interactions in Polar Solvents. *The Journal of Physical Chemistry B* **2023**, *127*, 4328–4337, DOI: 10.1021/acs.jpcb.3c00588

Varner, S.; Walker, P. J.; Venkatachalam, A.; Zhuang, B.; Wang, Z.-G. Stockmayer Fluid with a Shifted Dipole: Interfacial Behavior, 2025, DOI: 10.48550/arXiv.2509.05523

4.1 Electrolytes

Electrolytes are solutions made up of ions or charged species dissolved in a solvent. The variety of electrolytes is vast, as is their importance in both natural and engineered systems. The extent to which electrolytes play a role in the natural world and society cannot be overstated. The most basic example of an electrolyte is salt water, which contains dissolved sodium and chloride ions. Seawater is another common electrolyte that contains several different ions including sodium, chloride, magnesium, sulfate, calcium, and potassium [4], all of which contribute to the complex ecosystem and geochemistry of the ocean [5, 6]. In our bodies, electrolytes play a crucial role in almost every biological function including nerve conduction [7], muscle contraction [8], and general cellular homeostasis through regulation of osmotic pressure and pH [9, 10].

Polyelectrolytes are another class of electrolytes where polymers containing charged groups are dissolved in a solvent. Polyelectrolyes display different behavior from

both regular electrolytes and neutral polymer solutions due to the complex interplay between electrostatic interactions, polymer conformations, and strong polymer-solvent interactions [11, 12]. Many biomolecules including DNA, RNA, and proteins are polyelectrolytes that control biological function. Most recently, charged biopolymers have been shown to undergo liquid–liquid phase separation to form membraneless organelles that play important roles in cellular organization and regulate cellular functions [13–18].

Electrolytes and polyelectrolytes are also widely used in engineering applications, with energy storage being one of the most prominent use cases. In batteries, electrolytes facilitate the transport of ions between the anode and cathode and even participate in chemical reactions. The most common example is in lithium-ion batteries where lithium ions shuttle between a graphite anode and an $FePO_4$ cathode [19] during discharge. Supercapacitors are another class of energy storage devices where energy is stored by applying a potential difference between two electrodes separated by an electrolyte [20, 21]. Unlike batteries, supercapacitors store energy electrostatically in the electric double layer formed at the electrode–electrolyte interface [22–24], rather than through chemical reactions.

Due to their importance across such a broad range of important applications, understanding the properties of electrolyte solutions in bulk environments and near interfaces is of great scientific and technological interest. At the most basic level, the properties of dilute electrolytes are governed by the Coulombic interactions between ions immersed in a dielectric medium. If the concentration is sufficiently low, the ions can be treated simply as point charges interacting through a screened Coulomb potential [25, 26]. At higher concentrations, the dilute approximation breaks down due to ion–ion correlations and the finite size of ions [24, 27, 28]. A common case where ion–ion correlations and finite ion sizes play a crucial role in the structure and thermodynamics of electrolytes is in ionic liquids where the electrolyte can consist entirely of ions without any solvent [29, 30]. Additionally, for polar solvents such as water, the solvent molecules themselves can play a significant role in mediating ion–ion interactions beyond simple dielectric screening at long distances. In these cases, the structure of the solvent around the ions and specific ion–solvent interactions become important to describing effective interactions and thermodynamics within electrolytes [11, 31].

In the following two sections, we describe ionic liquids and polar fluids in more detail, highlighting their unique properties and challenges associated with modeling

them.

4.2 Ionic Liquids

Ionic liquids (ILs) are a special class of electrolytes that consist entirely of ions without any solvent. Room-temperature ionic liquids (RTILs) are a subclass of ionic liquids that are liquid at or near room temperature [32–34]. RTILs typically consist of bulky organic cations such as imidazolium cations (e.g., EMIM, BMIM) and weakly coordinating anions such as tetrafluoroborate (BF_4^-) or bis(trifluoromethanesulfonyl)imide ($TFSI^-$) [35]. Some examples of common components of RTILs are shown in Figure 5.1c.

RTILs are of great interest for energy storage applications due to their high thermal and electrochemical stability, and low volatility [36–40]. Despite their promise, modeling of RTILs is challenging due to the strong electrostatic correlations, finite size effects, and non-electrostatic interactions that govern their behavior. The combination of these factors poses theoretical challenges as well as computational challenges for simulating RTILs at the atomistic level.

Over the past few decades, several theories have been developed to phenomenologically describe the behavior of ionic liquids near charged interfaces [41–45]. In the following chapter, we describe several of these theories in depth, including their strengths and weaknesses. We then propose a new theory that addresses several of the shortcomings of previous theories, and we apply it to study the capacitance and phase behavir of RTILs in electric double layer capacitors (EDLCs) [1].

4.3 Electrolytes and Polar Fluids

The presence of a polar solvent complicates the picture of ion–ion interactions and electrolyte thermodynamics significantly. While the solvent can often be thought of as a uniform dielectric medium for determining the bulk properties of a dilute electrolyte [25], this picture is not satisfactory for more concentrated electrolytes or electrolytes near interfaces. For sufficiently polar solvents, a uniform dielectric treatment is also not appropriate for considering how ions interact and associate at short distances on the order of the solvent size. In these cases, the discrete nature of the solvent molecules and their specific interactions with ions must be taken into account.

Despite the important role of the solvent in mediating and screening charged interactions, it is common to treat solvents as a uniform dielectric background for simplicity

in what are called implicit solvent models [46]. Implicit solvent models approximate the effect of the solvent by integrating out the solvent degrees of freedom and replacing the bare interaction energy between charged species with an effective interaction energy known as the potential of potential of mean force [17, 46]. This potential of mean force is actually a free energy, since the solvent degrees of freedom have been averaged over. This is especially common in simulations including large biomolecules where the computational cost of explicitely modeling every solvent molecule is prohibitive [47–50]. Most implicit solvent models attempt to maintain the pairwise nature of interactions between charged species for computational efficiency. However, in reality, the presence of the solvent between several charged species in close proximity leads to many-body interactions that cannot be captured by simple pairwise potentials. In very recent years, machine learning approaches have been developed to capture these many-body effects more accurately without suffering from the high computational cost of explicit solvent simulations [51–54].

In two of the following chapters, we explore the consequences on the thermodynamics of electrolytes and surface-containing systems when the solvent is modeled explicitly. We develop theoretical techniques capable of capturing the solvent degrees of freedom, at least at the mean-field level, and we employ explicit solvent molecular simulations to verify our theoretical predictions [2, 3].

References

(1) Varner, S.; Wang, Z.-G. Effects of dilution in ionic liquid supercapacitors. *Physical Chemistry Chemical Physics* **2022**, *24*, 27362–27374, DOI: 10.1039/D2CP03398D.

(2) Varner, S.; Balzer, C.; Wang, Z.-G. Entropic Origin of Ionic Interactions in Polar Solvents. *The Journal of Physical Chemistry B* **2023**, *127*, 4328–4337, DOI: 10.1021/acs.jpcb.3c00588.

(3) Varner, S.; Walker, P. J.; Venkatachalam, A.; Zhuang, B.; Wang, Z.-G. Stockmayer Fluid with a Shifted Dipole: Interfacial Behavior, 2025, DOI: 10.48550/arXiv.2509.05523.

(4) Balzer, C.; Qing, L.; Wang, Z.-G. Preferential Ion Adsorption in Blue Energy Applications. *ACS Sustainable Chemistry & Engineering* **2021**, *9*, 9230–9239, DOI: 10.1021/acssuschemeng.1c01326.

(5) Sillén, L. G. The Ocean as a Chemical System. *Science* **1967**, *156*, Publisher: American Association for the Advancement of Science, 1189–1197, DOI: 10.1126/science.156.3779.1189.

(6) Millero, F. J. In *Chemistry of Marine Water and Sediments*, Gianguzza, A., Pelizzetti, E., Sammartano, S., Eds.; Springer: Berlin, Heidelberg, 2002, pp 3–34, DOI: 10.1007/978-3-662-04935-8_1.

(7) Riggs, J. E. Neurologic Manifestations of Electrolyte Disturbances. *Neurologic Clinics* **2002**, *20*, 227–239, DOI: 10.1016/S0733-8619(03)00060-4.

(8) Bohr, D. F. ELECTROLYTES AND SMOOTH MUSCLE CONTRACTION. *Pharmacological Reviews* **1964**, *16*, 85–111, DOI: 10.1016/S0031-6997(25)07013-9.

(9) Mahendra, A. An overview on electrolytes: Its importance, function, and imbalances. *Clinical Nutrition and Hospital Dietetics* **2023**, *43*.

(10) Pollock, J. S.; Ryan, M. J.; Samson, W. K.; Brooks, D. P. Water and electrolyte homeostasis brings balance to physiology. *American Journal of Physiology-Regulatory, Integrative and Comparative Physiology* **2014**, *307*, R481–R483, DOI: 10.1152/ajpregu.00246.2014.

(11) Muthukumar, M., *Physics of Charged Macromolecules: Synthetic and Biological Systems*; Cambridge University Press: Cambridge, 2023.

(12) Balzer, C. Polyelectrolytes near Solid Surfaces, Ph.D. Thesis, California Institute of Technology, 2023.

(13) Brangwynne, C. P. Phase transitions and size scaling of membrane-less organelles. *Journal of Cell Biology* **2013**, *203*, 875–881, DOI: 10.1083/jcb.201308087.

(14) Brangwynne, C. P.; Tompa, P.; Pappu, R. V. Polymer physics of intracellular phase transitions. *Nature Physics* **2015**, *11*, 899–904, DOI: 10.1038/nphys3532.

(15) Feric, M.; Vaidya, N.; Harmon, T. S., et al. Coexisting Liquid Phases Underlie Nucleolar Subcompartments. *Cell* **2016**, *165*, 1686–1697, DOI: 10.1016/j.cell.2016.04.047.

(16) Shin, Y.; Brangwynne, C. P. Liquid phase condensation in cell physiology and disease. *Science* **2017**, *357*, eaaf4382, DOI: 10.1126/science.aaf4382.

(17) Chen, S.; Wang, Z.-G. Driving force and pathway in polyelectrolyte complex coacervation. *Proceedings of the National Academy of Sciences* **2022**, *119*, e2209975119, DOI: 10.1073/pnas.2209975119.

(18) Sing, C. E.; Perry, S. L. Recent progress in the science of complex coacervation. *Soft Matter* **2020**, *16*, 2885–2914, DOI: 10.1039/D0SM00001A.

(19) Finkelstein, S. H.; Ricci, M.; Bötticher, T.; Schmidt-Rohr, K. How lithium-ion batteries work conceptually: thermodynamics of Li bonding in idealized electrodes. *Physical Chemistry Chemical Physics* **2024**, *26*, Publisher: The Royal Society of Chemistry, 24157–24171, DOI: 10.1039/D4CP00818A.

(20) Conway, B. E., *Electrochemical Supercapacitors: Scientific Fundamentals and Technological Applications*; Springer US: 1999.

(21) Yan, J.; Wang, Q.; Wei, T.; Fan, Z. Recent Advances in Design and Fabrication of Electrochemical Supercapacitors with High Energy Densities. *Advanced Energy Materials* **2014**, *4*, 1300816, DOI: https://doi.org/10.1002/aenm.201300816.

(22) Gouy, M. Sur la constitution de la charge électrique à la surface d'un électrolyte. *Journal de Physique Théorique et Appliquée* **1910**, *9*, 457–468, DOI: 10.1051/jphystap:019100090045700.

(23) Chapman, D. L. LI. A contribution to the theory of electrocapillarity. *The London, Edinburgh, and Dublin Philosophical Magazine and Journal of Science* **1913**, *25*, 475–481, DOI: 10.1080/14786440408634187.

(24) Bikerman, J. XXXIX. Structure and capacity of electrical double layer. *The London, Edinburgh, and Dublin Philosophical Magazine and Journal of Science* **1942**, *33*, 384–397, DOI: 10.1080/14786444208520813.

(25) Debye, P.; Hückel, E. Zur Theorie der Elektrolyte. I. Gefrierpunktserniedrigung und verwandte Erscheinungen. *Physikalische Zeitschrift* **1923**, *24*.

(26) Kirkwood, J. G. On the Theory of Strong Electrolyte Solutions. *The Journal of Chemical Physics* **1934**, *2*, 767–781, DOI: 10.1063/1.1749393.

(27) Wang, Z.-G. Fluctuation in electrolyte solutions: The self energy. *Physical Review E* **2010**, *81*, 021501, DOI: 10.1103/PhysRevE.81.021501.

(28) Levin, Y. Electrostatic correlations: from plasma to biology. *Reports on Progress in Physics* **2002**, *65*, 1577–1632, DOI: 10.1088/0034-4885/65/11/201.

(29) Wakai, C.; Oleinikova, A.; Ott, M.; Weingärtner, H. How Polar Are Ionic Liquids? Determination of the Static Dielectric Constant of an Imidazolium-based Ionic Liquid by Microwave Dielectric Spectroscopy. *The Journal of Physical Chemistry B* **2005**, *109*, 17028–17030, DOI: 10.1021/jp053946+.

(30) Ohno, H. Functional Design of Ionic Liquids. *Bulletin of the Chemical Society of Japan* **2006**, *79*, 1665–1680, DOI: 10.1246/bcsj.79.1665.

(31) Fröhlich, H., *Theory of Dielectrics: Dielectric Constant and Dielectric Loss*; Oxford University: 1958; book.

(32) Frackowiak, E.; Lota, G.; Pernak, J. Room-temperature phosphonium ionic liquids for supercapacitor application. *Applied Physics Letters* **2005**, *86*, 164104, DOI: 10.1063/1.1906320.

(33) Marcus, Y. Ionic and molar volumes of room temperature ionic liquids. *Journal of Molecular Liquids* **2015**, *209*, 289–293, DOI: 10.1016/j.molliq.2015.06.015.

(34) Ghorbani, M.; Simone, M. I. Developing New Inexpensive Room-Temperature Ionic Liquids with High Thermal Stability and a Greener Synthetic Profile. *ACS Omega* **2020**, *5*, 12637–12648, DOI: 10.1021/acsomega.9b04091.

(35) Mousavi, M. P. S.; Wilson, B. E.; Kashefolgheta, S., et al. Ionic Liquids as Electrolytes for Electrochemical Double-Layer Capacitors: Structures that Optimize Specific Energy. *ACS Applied Materials & Interfaces* **2016**, *8*, 3396–3406, DOI: 10.1021/acsami.5b11353.

(36) McEwen, A. B.; Ngo, H. L.; LeCompte, K.; Goldman, J. L. Electrochemical Properties of Imidazolium Salt Electrolytes for Electrochemical Capacitor Applications. *Journal of The Electrochemical Society* **1999**, *146*, 1687, DOI: 10.1149/1.1391827.

(37) Simon, P.; Gogotsi, Y. Materials for electrochemical capacitors. *Nature Materials* **2008**, *7*, 845–854, DOI: 10.1038/nmat2297.

(38) Arbizzani, C.; Biso, M.; Cericola, D., et al. Safe, high-energy supercapacitors based on solvent-free ionic liquid electrolytes. *Journal of Power Sources* **2008**, *185*, 1575–1579, DOI: 10.1016/j.jpowsour.2008.09.016.

(39) Sato, T.; Masuda, G.; Takagi, K. Electrochemical properties of novel ionic liquids for electric double layer capacitor applications. *Electrochimica Acta* **2004**, *49*, 3603–3611, DOI: 10.1016/j.electacta.2004.03.030.

(40) Lewandowski, A.; Olejniczak, A.; Galinski, M.; Stepniak, I. Performance of carbon–carbon supercapacitors based on organic, aqueous and ionic liquid electrolytes. *Journal of Power Sources* **2010**, *195*, 5814–5819, DOI: 10.1016/j.jpowsour.2010.03.082.

(41) Kornyshev, A. A. Double-Layer in Ionic Liquids: Paradigm Change? *The Journal of Physical Chemistry B* **2007**, *111*, 5545–5557, DOI: 10.1021/jp067857o.

(42) Bazant, M. Z.; Storey, B. D.; Kornyshev, A. A. Double Layer in Ionic Liquids: Overscreening versus Crowding. *Physical Review Letters* **2011**, *106*, 046102, DOI: 10.1103/PhysRevLett.106.046102.

(43) Chao, H.; Wang, Z.-G. Effects of Surface Transition and Adsorption on Ionic Liquid Capacitors. *The Journal of Physical Chemistry Letters* **2020**, *11*, 1767–1772, DOI: 10.1021/acs.jpclett.0c00023.

(44) Bossa, G. V.; May, S. Stability of ionic liquid modeled by composite Coulomb-Yukawa potentials. *Physical Review Research* **2020**, *2*, 032040, DOI: 10.1103/PhysRevResearch.2.032040.

(45) Lian, Z.; Chao, H.; Wang, Z.-G. Effects of Confinement and Ion Adsorption in Ionic Liquid Supercapacitors with Nanoporous Electrodes. *ACS Nano* **2021**, 11724-11733, DOI: 10.1021/acsnano.1c02506.

(46) Roux, B.; Simonson, T. Implicit solvent models. *Biophysical Chemistry* **1999**, *78*, 1–20, DOI: 10.1016/S0301-4622(98)00226-9.

(47) Ferrara, P.; Apostolakis, J.; Caflisch, A. Evaluation of a fast implicit solvent model for molecular dynamics simulations. *Proteins: Structure, Function, and Bioinformatics* **2002**, *46*, 24–33, DOI: 10.1002/prot.10001.

(48) Feig, M.; Onufriev, A.; Lee, M. S., et al. Performance comparison of generalized born and Poisson methods in the calculation of electrostatic solvation energies for protein structures. *Journal of Computational Chemistry* **2004**, *25*, 265–284, DOI: 10.1002/jcc.10378.

(49) Baker, N. A. Improving implicit solvent simulations: a Poisson-centric view. *Current Opinion in Structural Biology* **2005**, *15*, 137–143, DOI: 10.1016/j.sbi.2005.02.001.

(50) Chen, J.; Brooks, C. L.; Khandogin, J. Recent advances in implicit solvent-based methods for biomolecular simulations. *Current Opinion in Structural Biology* **2008**, *18*, 140–148, DOI: 10.1016/j.sbi.2008.01.003.

(51) Chen, Y.; Krämer, A.; Charron, N. E., et al. Machine learning implicit solvation for molecular dynamics. *The Journal of Chemical Physics* **2021**, *155*, 084101, DOI: 10.1063/5.0059915.

(52) Batzner, S.; Musaelian, A.; Sun, L., et al. E(3)-equivariant graph neural networks for data-efficient and accurate interatomic potentials. *Nature Communications* **2022**, *13*, 2453, DOI: 10.1038/s41467-022-29939-5.

(53) Zhang, J.; Pagotto, J.; T. Duignan, T. Towards predictive design of electrolyte solutions by accelerating ab initio simulation with neural networks. *Journal of Materials Chemistry A* **2022**, *10*, 19560–19571, DOI: 10.1039/D2TA02610D.

(54) Zhang, J.; Pagotto, J.; Gould, T.; Duignan, T. T. Scalable molecular simulation of electrolyte solutions with quantum chemical accuracy, 2024, DOI: 10.48550/arXiv.2310.12535.

Chapter 5

EFFECTS OF DILUTION IN IONIC LIQUID SUPERCAPACITORS

Electric double layer capacitors (EDLCs) bridge the gap between the high power density of traditional capacitors and the high energy density of batteries by storing energy in the electric double layer formed under an applied electric field. EDLCs use a range of electrolytes, including aqueous, organic, and more recently, ionic liquids. Aqueous and organic electrolytes are volatile and have limited stability windows, which constrain performance. Ionic liquids, while non-volatile and stable over wide voltage ranges, are highly viscous, leading to low ionic conductivity and high resistance. To improve conductivity and power delivery, they are often diluted with organic solvents.

Although many theories describe the electric double layer and capacitance of simple electrolytes and pure ionic liquids, the effects of dilution on the thermodynamics and energy storage performance of ionic liquid EDLCs remain largely unexplored. To address this, we extend existing theories to include dilution and preferential surface interactions. We analyze how dilution impacts double layer structure, surface phase behavior, differential capacitance, and overall energy storage. We also relate tricritical surface phase behavior to the diluted Ising model, known as the Blume Capel model, and introduce an algorithm for solving complex field-theoretic equations.

This chapter includes content from our previously published articles:

Varner, S.; Wang, Z.-G. Effects of dilution in ionic liquid supercapacitors. *Physical Chemistry Chemical Physics* **2022**, *24*, 27362–27374, DOI: 10.1039/D2CP03398D

Varner, S.; Balzer, C.; Wang, Z.-G. A Jacobian-free pseudo-arclength continuation method for phase transitions in inhomogeneous thermodynamic systems. *The Journal of Chemical Physics* **2024**, *161*, 064107, DOI: 10.1063/5.0220849

I am grateful for the guidance and mentorship provided by Dr. Christopher Balzer when first learning the fundamentals and numerical algorithms of self-consistent field theory. I am also very grateful for the many discussions with Dr. Benjamin Ye who worked on a companion project. Our many discussions were invaluable to the progress and understanding of my work.

5.1 Introduction

Electric double-layer capacitors (EDLCs), a subset of supercapacitors (SCs), are devices that store charge in an electric double-layer within an electrolyte near charged electrodes. A schematic of a basic EDLC is provided in Figure 5.1a. EDLCs are extensively studied because they may have the capability to match the power density (PD) of traditional capacitors with the energy density (ED) of batteries [3–5], as shown in Figure 5.1b. When an electric field is applied between two electrodes, the formation of the double-layer is very rapid due to high ion mobility, especially for electrolytes with low bulk resistance (high ionic conductivity). This makes them useful for applications that require high cyclability and power delivery, such as in regenerative braking for electric vehicles [6].

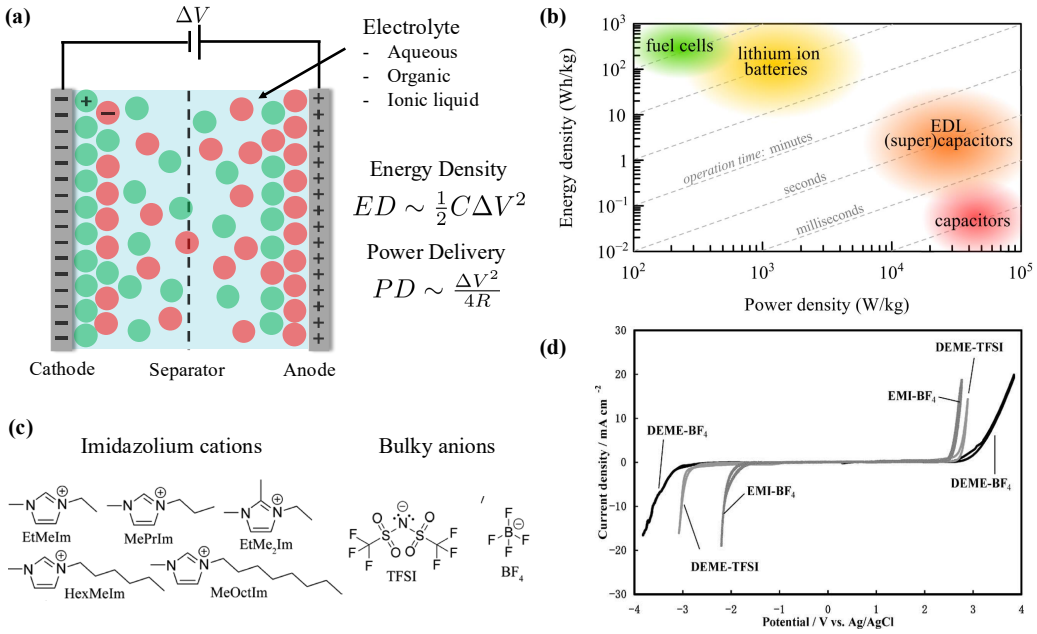

Figure 5.1: (a) Schematic of an electric double layer capacitor. (b) Ragone plot of common energy storage devices reproduced from Yan et al. [7]. (c) Common cations and anions for room-temperature ionic liquids (RTILs) reproduced from Mousavi et al. [8]. (d) Voltammogram of common RTILs reproduced from Sato et al. [9].

Since the maximum energy that can be stored by an EDLC scales as $CV^2/2$ (for constant C), increasing the cell potential V is a very effective way to improve EDLC devices [10]. The cell potential is determined by the electrolyte material being used, which can range from aqueous electrolytes and polyelectrolytes to organic electrolytes and even ionic liquids (ILs) [11]. Both the PD and ED are greatly improved if the cell potential of the EDLC can be increased, *ceteris paribus*. Aqueous

electrolytes remain electrochemically stable up to ~1 V, whereas organic replacements such as acetonitrile (AN) and propylene carbonate (PC) have wider potential windows up to ~2.5 V [12]. More recently, ILs are being studied as electrolytes for EDLCs due to their low volatility, high potential window and improved electrochemical stability [3, 10, 13].

Room temperature ionic liquids (RTILs) are a special class of ILs that differ from traditional molten salts in many ways. A neat RTIL is typically made up of a bulky organic cation (e.g. imidazolium, pyrrolidinium, phosphonium) and a weakly coordinated organic/inorganic anion (e.g. tetrafluoroborate, trifluoromethanesulfonate, trifluoromethanesulfonimide) [8, 10]. Examples of common RTIls are provided in Figure 5.1c. Due to the organic and bulky nature of the ions, RTILs can exist as liquids at room temperature despite strong Coulomb interactions. Additionally, RTILs are non-volatile and can remain stable up to ~5 V, making them much more stable than aqueous and organic electrolytes. Figure 5.1d shows the wide stability window displayed by three common RTILs. Their desirable properties make them prime candidates as electrolytes in EDLCs [9, 14, 15].

Kornyshev studied the finite size effects using a mean-field lattice-gas model with only single-occupation sites [16]. The effect of ion crowding near the electrode with increasing potential gave a bell-shaped capacitance–potential curve, rather than the typical U-shaped curve that was predicted by Helmholtz. More interestingly, Kornyshev also discovered that there is a transition from bell-shaped to camel-shaped capacitance curves when the void space in the system was high enough, specifically for an ion volume fraction of $\gamma < 1/3$.

The Kornyshev model was then extended by Bazant–Storey–Kornyshev (BSK) to allow for electrostatic correlation phenomenologically via the incorporation of a non-local relative permittivity [17]. It was shown that short-ranged electrostatic correlations in neat RTILs can lead to overscreening, where the surface charge is overscreened in subsequent layers, leading to an oscillatory charge density profile that decays to the bulk value away from the electrode. This oscillatory behavior has been observed experimentally and in simulations of dense electrolytes such as RTILs where short-ranged electrostatic correlations are expected to be important [18–20]. While the BSK model was successful at incorporating electrostatic correlations, the model was restricted to a fixed correlation strength, and did not incorporate dilution effects. The non-local relative permittivity introduced in the BSK model maps to a composite Coulomb–Yukawa potential, $U(r) = (1 - \mathrm{e}^{-r/\ell_c})/4\pi\lambda_D^2 r$,

where the Yukawa potential incorporates the short-ranged electrostatic correlations and non-electrostatic interactions [21, 22]. Here ℓ_c is the correlation length, λ_D is the Debye length, and r is the interparticle distance. The BSK model was further expanded upon by allowing for the correlation strength to vary with the parameter α, $U(r) = (1 - \alpha e^{-r/\ell_c})/4\pi\lambda_D^2 r$ [23–25]. The correlation strength α incorporates the strength of electrostatic correlations as well as short-ranged non-electrostatic interactions between the bulky ions of RTILs. Caetano et al. first used this model to describe hydration mediated interactions in aqueous electrolytes [26]. The observed hysteresis in RTIL EDLCs [27, 28] was first explained by Limmer as a result of a fluctuation induced first-order surface phase transition [29]. This spontaneous surface charge separation (SSCS) was also predicted using the composite Coulomb–Yukawa potential with a correlation strength above a critical value $\alpha > \alpha_{s,c}$ [23, 24]. The symmetry breaking transition is made possible by the short-ranged attraction of co-ions resulting from non-electrostatic (dispersion) interactions. Typically, in an inorganic electrolyte with small ions, the Coulomb repulsion would prevent the coions from coalescing at an electrode without a driving force. In the case of ILs, short-ranged dispersion forces offset the Coulomb repulsion and allow coions to gather at an electrode, inducing a surface charge. The result is a stable double layer formed spontaneously through ion density fluctuations and surface polarization. The image charge interactions are crucial for the surface transition. Recent coarse-grained molecular dynamics simulations show that SSCS is possible only with attractive image charges from a metal electrode [30]. The discussed mean-field theories (MFTs) do not distinguish the electrode type.

While there have been many studies about neat RTILs near electrified interfaces, there has been little work on diluted RTILs with account for finite size and electrostatic correlation, and little discussion on their capacitance and energy storage behavior. The high viscosity of RTILs at room temperature causes a low ionic conductivity and thus low PD [12, 31]. High bulk resistance gives rise to slow charging/discharging dynamics. This is one of the main issues faced when using RTILs as the electrolyte for EDLCs. The most popular way to get around the high viscosity is by using mixtures of ILs and organic solvents, such as AN [32–34]. While the addition of organic solvents generally decreases the cell potential, exploratory studies have discovered RTIL–solvent mixtures that maintain a cell potential above 3V with high cyclability [15, 34]. In most commercial applications, RTILs are diluted with AN or PC to achieve acceptable power delivery [31]. Incorporating neutral solvent into existing theories of RTIL EDLCs is crucial to more

accurately model real systems and predict trends in ED and PD.

In the following sections, we provide a historical perspective on previous theories for electric double layer capacitors. While none of this is novel, we believe there is significant value in providing a comprehensive accounting of these theories including their similarities, differences, strengths, and weaknesses. We hope that this can serve as a helpful review for future scientists aiming to learn the history mean-field modeling of EDLCs.

In our own work, we extend the MFT used in recent works [24, 25] by incorporating a neutral solvent. We investigate the effect of dilution on SSCS, capacitance, and energy storage for a single plate system. We also investigate the effects of preferential adsorption of solvent on the phase behavior, capacitance, and energy storage.

5.2 Electric Double Layer

For practical application of RTILs in EDLCs, it is crucial to understand the structure and behavior of the electric double-layer (EDL). The capacitance and energy storage are directly determined by the response of the EDL to applied potentials. The study of EDL structure goes back to Helmholtz in 1853 [35]. At that time the EDL was described as a single layer of ions adjacent to a charged electrode which yielded a constant capacitance at all potentials. Now, more sophisticated theories incorporate physics like electrostatic correlation, non-electrostatic interactions and finite ion size [16, 17, 23, 26, 36–39]. The advent of more advanced theories was motivated by the discovery that electrostatic correlation and finite size effects are essential to the EDL behavior of RTILs [40–42]. In the following subsections, we step through the history of inhomogeneous EDL modeling, starting with the Poisson–Boltzmann theory.

Poisson-Botzmann / Gouy–Chapman Theory

In the original theory, Helmholtz assumed that only a single layer of oppositely charged ions would adsorb to the electrode [35], when in fact there is actually a distribution of ions going away from the electrode. The meaning of the "double layer" is then extended beyond the surface charge on the electrode and the immediate layer of ions nears the surface, to now include the diffuse distribution of ions moving away from the surface. The shape of the charge and the resulting electrostatic potential is determined by the competition of electrostatic forces that draw counterions and repel coions, and mixing entropy which favors even mixing as in the bulk condition. The simplest model to capture these two affects is that of an ideal gas of point charges

near a planar charged wall. To derive the ion distribution and electrostatic potential in this system, we could start from the canonical partition function and proceed via particle-to-field transformation [43–45], however, we instead proceed through a simpler route by starting directly from the free energy functional. We direct the reader to the appendix for the full derivation using particle-to-field transformations. Here, we write the Helmholtz free energy functional as the sum of only two parts, $F = F_{\text{id}} + F_{\text{el}}$, where F_{id} is the free energy of an ideal gas, and F_{el} is the free energy due to electrostatic interactions between charged species. Thus, the form of the free energy functional is:

$$\beta F = \sum_{\alpha=+,-} \int d\mathbf{r} \rho_\alpha(\mathbf{r}) \left[\ln \rho_\alpha(\mathbf{r}) - 1\right] + \frac{\beta e^2}{8\pi\epsilon} \int d\mathbf{r} \int d\mathbf{r}' \frac{\rho_c(\mathbf{r})\rho_c(\mathbf{r}')}{|\mathbf{r} - \mathbf{r}'|} \tag{5.1}$$

where $\rho_\alpha(\mathbf{r})$ is the inhomogeneous number density of species α, $\beta = 1/k_B T$, e is the elementary charge, and ϵ is the permittivity. Note that we are treating the solvent implicitly by assuming a uniform permittivity in the Coulomb interaction kernel. $\rho_c(\mathbf{r}) = \rho_+(\mathbf{r}) - \rho_-(\mathbf{r}) + \rho_{\text{ex}}(\mathbf{r})$ is the charge density (reduced by e), and $\rho_{\text{ex}}(\mathbf{r})$ is the fixed external charge distribution (e.g., electrode, charged nanoparticle, pore wall, etc.). From here, we can define the electrostatic potential, $\psi(\mathbf{r})$,

$$\psi(\mathbf{r}) = -\frac{e}{4\pi\epsilon} \int d\mathbf{r}' \frac{\rho_c(\mathbf{r}')}{|\mathbf{r} - \mathbf{r}'|} \tag{5.2}$$

which allows the Helmholtz free energy to be simplified,

$$\beta F = \sum_{\alpha=+,-} \int d\mathbf{r} \rho_\alpha(\mathbf{r}) \left[\ln \rho_\alpha(\mathbf{r}) - 1\right] + \frac{\beta e}{2} \int d\mathbf{r} \rho_c(\mathbf{r}) \psi(\mathbf{r}) \ . \tag{5.3}$$

For a given charge distribution, the electrostatic potential can be computed using the convolution in Equation (5.2). Alternatively, one can recognize that the Coulomb kernel is the Green's function for Poisson's equation,

$$\nabla^2_{\mathbf{r}} \psi(\mathbf{r}) = \frac{e}{4\pi\epsilon} \int d\mathbf{r}' \rho_c(\mathbf{r}') \nabla^2_{\mathbf{r}} \left(\frac{1}{|\mathbf{r} - \mathbf{r}'|} \right) \tag{5.4}$$

$$= -\frac{e}{\epsilon} \int d\mathbf{r}' \rho_c(\mathbf{r}') \delta(\mathbf{r} - \mathbf{r}') \tag{5.5}$$

$$= -\frac{e}{\epsilon} \rho_c(\mathbf{r}) \tag{5.6}$$

where $\nabla^2(|\mathbf{r} - \mathbf{r}'|^{-1}) = -4\pi\delta(\mathbf{r} - \mathbf{r}')$. Note that the elementary charge, e, appears because we have reduced the charge density. We can arrive at a nondimensional version of Poisson's equation by reducing the potential by the thermal voltage,

k_BT/e, the length scale by the effective particle size $b = v^{1/3}$, and converting the number density to a volume fraction, $\phi_c = \rho_c v$. The nondimensional equation is given by,

$$-\lambda_0^2 \nabla^2 \psi = \phi_c \tag{5.7}$$

where $\lambda_0^2 = \epsilon b/\beta e^2 = b/4\pi l_B$ is the nominal screening length, and $l_B = \beta e^2/4\pi\epsilon$ is the Bjerrum length. Note that ψ is now in units of k_BT/e. The Bjerrum length is the length scale at which the interaction energy between two monovalent charges is equal to the thermal energy, k_BT. The nominal screening length is a measure of the ratio between the Bjerrum length and the particle size. Now, the electrostatic potential can be computed by solving the simple partial differential equation in Equation (5.7), rather than the convolutional integral in Equation (5.2).

Since we are interested in computing the distribution of ions at an electrode that is immersed in an electrolyte, we can assume that the system containing the EDL is connected to an infinitely large reservoir at fixed concentrations of ions, $\rho_\pm^b$, and therefore also fixed chemical potentials $\mu_\pm$. This also implies that the ion concentrations will approach their bulk values as the distance from the electrode goes to infinity. To this end, we transform the Helmholtz free energy to the Grand free energy using the Legendre transform

$$\Omega = F - \sum_{\alpha=\pm} \mu_\alpha n_\alpha = F - \sum_{\alpha=\pm} \mu_\alpha \int d\mathbf{r} \rho_\alpha(\mathbf{r}) \tag{5.8}$$

where Ω is the Grand free energy (or Grand potential), and n_α and μ_α are the number of particles and the chemical potential of species α, respectively. Thus, the Grand free energy functional is given by,

$$\beta\Omega = \sum_{\alpha=\pm} \int d\mathbf{r} \rho_\alpha(\mathbf{r}) \left[\ln \rho_\alpha(\mathbf{r}) - 1 - \mu_\alpha\right] + \int d\mathbf{r} \rho_c(\mathbf{r}) \psi(\mathbf{r}) \ . \tag{5.9}$$

The equilibrium density profiles can be determined by extremizing the free energy with respect to $\rho_\pm$ using functional variation, $\delta\beta\Omega/\delta\rho_\pm = 0$, which yields the equations,

$$-\mu_\pm + \ln(\phi_\pm) \pm \psi = 0 \tag{5.10}$$

for a monovalent salt solution. In the reservoir, the electrostatic potential is 0, and the bulk volume fraction of ions is $\phi_\pm^b$ which yields the chemical potentials, $\mu_\pm = \ln \phi_\pm^b$. Finally, inserting the values of the chemical potentials yields the familiar Boltzmann distribution,

$$\phi_\pm = \phi_\pm^b e^{\mp\psi} \tag{5.11}$$

which must be self-consistent with Poisson's equation in Equation (5.7). Combining these two equations yields the Poisson–Boltzmann (PB) equation/theory,

$$-\lambda_0^2 \nabla^2 \psi = \phi_+^b e^{-\psi} - \phi_-^b e^{\psi} + \phi_{\text{ex}} \tag{5.12}$$

$$= -2\phi_\pm^b \sinh \psi + \phi_{\text{ex}} \tag{5.13}$$

where the second equality is only true if $\phi_+^b = \phi_-^b$. Recall that ϕ_{ex} is the fixed external charge distribution and will determine the boundary conditions. For an EDLC, we are interested in a planar electrode carrying a surface charge σ. If the electrode is significantly larger in the transverse directions relative to the width of the EDL, then we can approximate the 3d profiles as 1d profiles with variation only in the direction normal to the electrode. In this case the external charge distribution is expressed as $\phi_{\text{ex}}(z) = \sigma\delta(z)$, and the PB equation becomes,

$$-\lambda_0^2 \frac{\partial^2 \psi}{\partial z^2} = \phi_+ e^{-\psi} - \phi_- e^{\psi} + \sigma\delta(z) \tag{5.14}$$

where it is understood that all profiles vary in the z-dimension only. Integrating over the domain, accounting for charge neutrality, and recognizing that $\partial_z \psi = 0$ inside the electrode results in the following boundary condition,

$$-\lambda_0^2 \left.\frac{\partial \psi}{\partial z}\right|_{z=0} = \sigma \ . \tag{5.15}$$

Note that one can either solve the equation subject to a fixed surface charge, σ, or fixed surface potential, ψ_s. In both cases the second boundary condition is $\psi \to 0$ as $z \to \infty$ where a vanishing bulk potential is chosen for simplicity. If a fixed surface potential is used, then the surface charge can be computed using Equation (5.15).

This equation can be solved analytically for a planar electrode at a fixed surface charge ϕ_s using the integrating factor method. The key result of the Gouy–Chapman theory is the differential capacitance computed from the solution of the non-linearized PB equation,

$$C_{\text{diff}}^{\text{GC}} = \frac{\partial \sigma}{\partial \psi_s} = \frac{\epsilon}{\lambda_D} \cosh\left(\frac{\psi_s}{2}\right) \tag{5.16}$$

where $\lambda_D = \sqrt{\epsilon k_B T / (\sum_\alpha z_\alpha^2 \phi_\alpha^b)}$ is the Debye length, and ψ_s is still reduced by the thermal voltage. At no applied potential, the differential capacitance is simply $C_{\text{diff}}^{\text{GC}}(0) = \epsilon/\lambda_D$, which is the same result one would get from the linearized PB equation for small surface potentials. Notably, the differential capacitance has a "U"

shape, with the differential capacitance increasing exponentially as $\psi_s \to \infty$. While the GC model applies well for dilute systems at low surface potential, it breaks down at high potential because the ions are taken as point charges, meaning they can accumulate infinitesimally close to the electrode up to an infinite density. This gives the nonphysical exponential divergence in capacitance, as in reality, ions have a finite size and cannot occupy the same space.

In 1923, Stern offered a solution for high surface potential called the Stern Layer [46]. The Stern Layer is simply the original Helmholtz layer added in series to the diffuse GC layer.

$$C_{\text{diff}}^{\text{GCS}} = \frac{1}{C_H} + \frac{1}{C_{\text{diff}}^{\text{GC}}} \tag{5.17}$$

At high potential, the Stern layer contribution dominates the GC contribution and the capacitance approaches a constant value, rather than increasing exponentially. The Gouy-Chapman-Stern (GCS) theory works well for sufficiently dilute electrolytes, but for concentrated RTILs the dilute approximation breaks down and the GCS theory no longer accurately predicts experimental capacitance curves.

The two main reasons that the GC and GCS theories give incorrect predictions for concentrated electrolytes and moderate-to-high potentials are *crowding* and *ion correlations*. The GC and GCS models are mean-field models, derived by considering the self-consistent relationship between the mean electrostatic potential and the mean charge density in a system with only long-ranged Coulomb interactions. In the mean-field approximation, local ion structure (correlation) is neglected since the charge density is averaged out. For dilute systems this is often a good approximation because the Debye length is much greater than the correlation length. In dense electrolytes, however, there is some level of ordering around any given ion. In ILs for example, the Debye length is smaller than the ions themselves, and the relevant length scale for correlations is the ion size. Experiments have shown that the local charge environment around an ion within an IL is oscillatory in sign (for a cation it is -+-+-+-) moving away from the ion, and decays to zero in the bulk [18, 20, 47]. Similarly, the charge density shows the same oscillatory profile at the interface between an IL and an electrode. Theories developed since the GC theory have aimed to address the areas where the GC fails to make predictions in ILs with strong ion correlations and significant crowding.

Kornyshev

In 2007, Kornyshev proposed a lattice based mean-field model to study the effect of crowding [16]. The free energy in the Kornyshev model is given in Eq (5.18).

$$F = e\Psi(N_+ - N_-) + B_+N_+^2 + B_-N_-^2 + CN_+N_- - k_BT \ln W_{LG} \tag{5.18}$$

Neglecting the short ranged interactions yields $B_+ = B_- = C = 0$. The total number of microstates is given by considering the number of ways the positive and negative ions can be placed on a lattice of N sites. In this case, the total number of ions need not equal the total number of sites, there may unfilled sites (holes).

$$W_{LG} = \binom{N}{N_+}\binom{N - N_+}{N_-} = \frac{N!}{N_+!N_-!(N - N_+ - N_-)!} \tag{5.19}$$

Since there are a finite number of lattice sites in the system, the density at the electrode cannot grow infinitely. This form of the conformational entropy leads to a *Fermi* distribution for the ion concentrations, rather than the typically used Boltzmann distribution.

$$c_\pm = c_0 \frac{\exp\left(\mp \frac{e\Psi}{k_BT}\right)}{1 - \gamma + \gamma \cosh\left(\frac{e\Psi}{k_BT}\right)} \tag{5.20}$$

γ here is the amount of ions in the bulk divided by the total number of sites available for them. When $\gamma \to 0$, the ion densities are Boltzmann distributed, as expected for very dilute systems.

With the Fermi distribution for ions, Kornyshev goes on to solve for the ion density and potential profiles in one dimension using the Poisson–Fermi Equation (rather than Poisson–Boltzmann). The Poisson Equation can be obtained by taking the saddle-point solutions of the functional integrals which are obtained from the partition function, neglecting all fluctuations. This is the hallmark of the mean-field approximation. Substituting the Fermi-distributed ion densities gives the simple differential equation for the nondimensional electrostatic potential $\psi = e\Psi/k_BT$:

$$\frac{d^2\psi}{dX^2} = \frac{\sinh(\psi)}{1 + 2\gamma \sinh^2(\psi/2)} \tag{5.21}$$

Solving this differential equation gives the potential distribution. The surface charge (density) σ is related to the slope of the potential at the surface via Gauss' law. The differential capacitance is the derivative of the surface charge with respect to the

potential drop between two electrodes. In the case of the Kornyshev model, there is only one electrode and the potential decays to 0 as $X \rightarrow \infty$

$$C_{diff} = \frac{d\sigma}{d\Delta\psi} = \frac{\varepsilon_0 \varepsilon_r}{4\pi\lambda_D} \frac{d}{d\Delta\psi} \left\{ - \left. \frac{d\psi}{dX} \right|_{X=0} \right\} \tag{5.22}$$

$$= C_0 \frac{\cosh(\Delta\psi/2)}{1 + 2\gamma \sinh^2(\Delta\psi/2)} \sqrt{\frac{2\gamma \sinh^2(\Delta\psi/2)}{\ln\left[1 + 2\gamma \sinh^2(\Delta\psi/2)\right]}} \tag{5.23}$$

For a neat RTIL, Kornyshev predicted a bell shaped capacitance curve where increasing the potential extends the double layer and decreases the capacitance. For sufficiently dilute RTILs, $\gamma < 1/3$, he predicted a camel-shaped capacitance curve. These two regimes are shown in Figure 5.2.

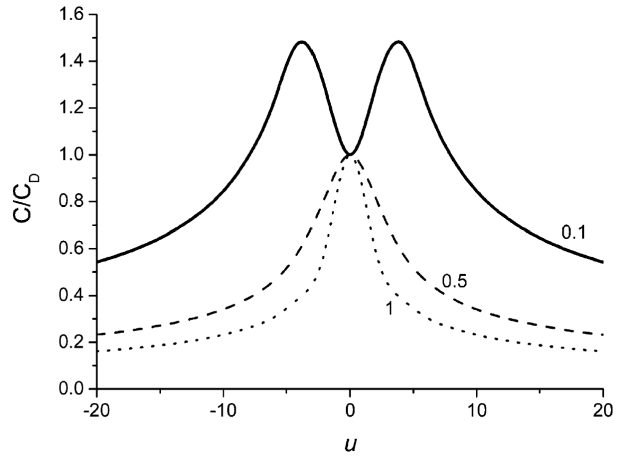

Figure 5.2: Differential capacitance from the Kornyshev model. The transition from bell to camel shaped capacitance occurs for $\gamma < 1/3$. Figure reproduced from Kornyshev [16].

At low potential, the voids in the first layer begin to fill with counterions, which increases the capacitance in the same manner as in the GC theory. At high potential, the first layer becomes full and the double layer extends into more layers, decreasing the capacitance. The bell and camel shaped capacitance, and the transition between them, are a direct result of *crowding* or *lattice saturation* effects. For high potentials, in the lattice saturation regime, the capacitance decays as $\sim\Delta V^{-1/2}$. This can be obtained using simple scaling arguments and equating the cumulative charge in the double layer with the surface charge.

The predictions of the theory were successfully compared to some results of both experiments and simulations. This simple theory, while addressing ion crowding,

completely neglects ion correlations which are expected to have a large role in concentrated ionic systems like ILs as mentioned before. For this reason, the Kornyshev model cannot correctly predict charge density profiles.

All-in-all, as the title of his seminal paper suggests, Kornyshev sparked a *paradigm change* in the way that RTIL EDL theories would develop in subsequent years and up to this day.

Bazant, Storey, and Kornyshev

In 2011, Bazant, Storey and Kornyshev addressed the issue of correlations through introduction of non-locality in the dielectric permittivity [17]. Their Landau-Ginzburg-like free energy functional incorporated an additional potential gradient term, shown in Eq (5.24), where Ψ is the electrostatic potential, g is the enthalpy density, $\phi = e\left(c_+ - c_-\right)$ is the mean charge density, ℓ_c is the correlation length, and σ is the surface charge.

$$G = \int_V d\mathbf{r}\left\{g + \phi\Psi - \frac{\varepsilon}{2}\left[|\nabla\Psi|^2 + \ell_c^2\left(\nabla^2\Psi\right)^2\right]\right\} + \oint_S d\mathbf{r}\sigma\Psi \tag{5.24}$$

In Fourier space, this appears as a non-local dielectric, while in real space it gives rise to a fourth-order gradient term in the electrostatic potential that is not present in the Kornyshev model (Eq (5.21)). The result upon extremization of the free energy is a modified Poisson Equation which includes the fourth-order gradient term.

$$\ell_c^2\tilde{\nabla}^4\psi - \tilde{\nabla}^2\psi = -\frac{\sinh\left(\psi\right)}{1 + 2\gamma\sinh^2\left(\psi/2\right)} \tag{5.25}$$

Notice that the only difference between this model and the original Kornyshev model is the fourth-order gradient term which accounts for short ranged electrostatic correlations.

The BSK model predicted oscillatory charge density profiles at low potential, termed *overscreening* and *crowding* at high potentials. See Figure 5.3 for a visual representation. *Overscreening* occurs when the surface charge is overcompensated in the layer(s) of counterions adjacent to the electrode, and the extra charge in the counterion layer(s) is then overcompensated by an adjacent coion layer. The layers alternate and decay until eventually zero charge density is reached in the bulk. This is a direct result of the consideration of electrostatic correlations. *Crowding* occurs at high potential when a single layer of counterions adsorbed onto the surface is not enough to screen the surface charge. Since the particles have finite volume, as more come towards the surface, the double layer extends further out into the

solution occupying 2 or more layers. This is the same crowding/saturation effect as the original Kornyshev model, and in both cases the capacitance decays as $\sim\Delta V^{-1/2}$ for high potential.

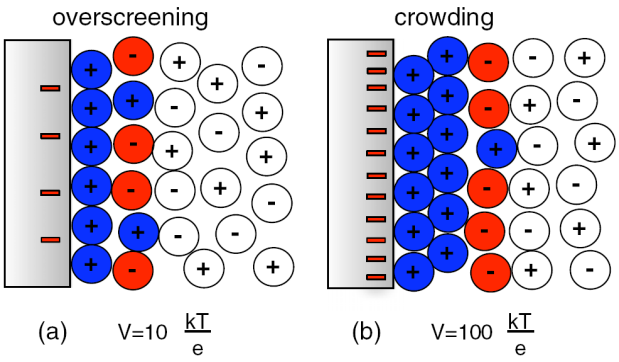

Figure 5.3: *Overscreening* vs *crowding* visual representation for RTIL EDLs reproduced from Bazant, Storey, and Kornyshev [17].

Bazant and de Souza [48] later discovered that the non-local dielectric is mathematically equivalent to introducing a composite Coulomb-Yukawa pair potential of the form $U(r) = (1 - e^{-r/\ell_c})/r$, where ℓ_c is an effective correlation length. Applying the Hubbard-Stratonovich transformation to the operator in Fourier space and expanding in powers of k results identically in the BSK formulation. In this respect, the BSK model is fairly restrictive since the strength of the Yukawa interaction relative to the Coulomb interaction is specified rather arbitrarily. We can rewrite the composite potential without making this restriction as $U(r) = (1 - \alpha e^{-r/\ell_c})/r$ with α representing the combined strength of short-ranged non-electrostatic interactions and electrostatic correlations. The BSK model corresponds to $\alpha = 1$, but there is no reason this should be the case for any real system.

In Appendix B I provide an alternative derivation to the BSK model valid for $0 \leq \alpha \leq 1$. In the derivation I similarly consider only a single field that combines the effects of the Yukawa and Coulomb interactions. The result is an integro-differential equation for a modified electrostatic potential which reduces to the Kornyshev model for $\alpha = 0$ and the BSK model for $\alpha = 1$. The restriction on α arises from the restriction on the Hubbard-Stratonivich transformation, where the operator must be positive definite. I do not provide further analysis of this model beyond the derivation since the next models described allow for a wider range on α and easier numerical solutions simply by introducing different fields for the two interaction potentials. One of which is the theory used by Chao and Wang in 2020

which expanded the BSK model by allowing for variation of the strength α through the introduction of an auxiliary Yukawa field [23].

Chao and Wang

In 2020, Chao and Wang proposed a mean-field theory [23] to explain the origin of the observed hysteresis upon charging and discharging [27, 29]. I refrain from providing derivations here because this is the theory that my own research is built upon, and in-depth derivations will be provided in a later section.

In addition to the normal long ranged Coulomb interactions, they included a Yukawa potential to model the short ranged non-electrostatic interactions and electrostatic correlations. The origin of the non-electrostatic interactions in RTILs comes from the organic composition of the molecular ions. Bossa and May also postulated that the nonelectrostatic interactions are hydration mediated [26]. At short ranges, there will be some amount of attraction between like-charged ions due to dispersion. Chao and Wang modified the BSK model by adding a strength α to the Yukawa part of the potential which encapsulates the combined strength of the non-electrostatic interactions and the correlations. The particle pair-potential thus has the form $U(r) = (1 - \alpha e^{-r/\ell_c})/r$ as mentioned before.

To analyze the physics at the mean-field level they introduced two fluctuating fields: the electrostatic potential ψ; and an auxiliary Yukawa field Y, accounting for the Coulomb and Yukawa components of the pair-potential respectively. Applying the mean-field approximation, they discovered a spontaneous surface charge separation which is second order at the mean-field level but weakly first order beyond the mean-field level. At a critical correlation strength α_{sc} below the bulk transition critical value α_c, there is spontaneous surface charge separation at no applied potential.

They show that above this transition value, there can be metastability in the $\sigma - \Delta V$ equation of state, which could be responsible for experimentally observed hysteresis. They further supported this claim by showing through structure factor calculation from molecular dynamics simulations that many common RTILs have $\alpha_{sc} < \alpha < \alpha_c$. Lastly, they show that proximity to the transition can result in enhanced energy storage, especially when applying different electrode materials for preferential adsorption, which shifts the divergent capacitance to a nonzero cell potential.

The CW model was later discovered to have an incorrect boundary condition, namely they did not include the penetration of the Yukawa field into the electrode. Despite

this, their results remain qualitatively valid and they still capture the essential physics.

Bossa and May

In 2020, Bossa and May corrected the boundary condition error from the CW model. They introduced a different field for each of the Yukawa interactions cation-cation, anion-anion, and cation-anion [24]. In this way they allowed for a different strength of interaction/correlation between the different types of ions. This model is more realistic as it is unfair to assume that these interactions would have the same exact strength. They ultimately assumed that the system has no solvent and thus is binary. This assumption collapses the three fields into a single field that is identical to the one proposed in the CW model. Their results with the correct boundary condition proved qualitatively identical to the results of the CW model, but they found the CW model slightly overestimated the effects of SSCS.

The Bossa and May model provided the framework for inclusion of solvent, but results for dilute RTILs were not reported in their work.

Lian, Chao, and Wang

Lian, Chao, and Wang (LCW) revisited the CW theory (now with the correct Yukawa boundary condition) and used it to study the effects of confinement on the differential capacitance [25]. Experiments have shown an anomalous capacitance increase as the pore size of the electrode approaches the diameter of the ions [49]. LCW showed that as the pore size approaches the ion diameter, the $\alpha_{s,c}$ drops dramatically, enabling spontaneous surface charge separation to occur for much weaker ion correlations. During the transition, counterions migrate into the pore while coions migrate out, leading to the experimentally observed anomalous capacitance increase for small pore sizes. This study was for neat RTILs, but the presence of solvent can have a drastic impact on how the EDL and capacitance respond to confinement.

With a grasp on the previous theories and the information they provided, I move onto discussion of the theory used in our work.

5.3 Diluted Ionic Liquid Mean-Field Theory

The MFT used in our work is similar to that developed earlier [26] to describe hydration mediated interactions in dilute electrolyte where a Yukawa potential was used to account for correlations, and the Bikerman mixing entropy was used to account for finite ion size [50]. The model was more recently used to study the thermodynamic stability of neat ionic liquids and the spontaneous surface phase

transition arising from ion–ion correlations [23–25]. These theories, however, have not yet been used to study the thermodynamic stability of diluted ionic liquids and the capacitance behavior in the charge separated regime. Briefly, a planar electrode is immersed in a size-symmetric 1:1 diluted RTIL where each ion carries unit charge $\pm e$ and has volume v and we define $b = v^{1/3}$ as the length scale of the ion. For simplicity, we assume the solvent also has molecular volume v. In the framework of the lattice-gas-like model, v corresponds to the volume of a lattice site where each lattice site can be occupied by a single particle. In principle, ion size asymmetry could be accounted for either phenomenologically as was done by Kornyshev [16], or in an asymmetric lattice gas model as done by Han et al which uses a Flory–Huggins entropy [51]. We focus on the symmetric case in order to study the effects of dilution and ion–ion correlations. The dielectric constant of the RTIL is ϵ. The bulk ion volume fractions are $\phi_{\pm}^B = v c_{\pm}^B$ where c_i^B is the bulk number density of species i. A neat RTIL corresponds to $\phi_+^B = \phi_-^B = 1/2$. The solvent volume fraction is given by the incompressibility condition $\phi_s^B = 1 - \phi_+^B - \phi_-^B$. We use the B superscript to denote bulk values, while the inhomogeneous system profiles are denoted $\phi_+ = \phi_+(\mathbf{r})$, $\phi_- = \phi_-(\mathbf{r})$ and $\phi_s = \phi_s(\mathbf{r}) = 1 - \phi_+ - \phi_-$. The electrode carries surface charge σ while the system remains charge neutral.

We start with the modified BSK equation [17, 25, 26, 48] with the addition of the chemical potential in the grand canonical ensemble,

$$\begin{aligned}
\beta\Omega = &\int d\mathbf{r}\,[\phi_+ \ln\phi_+ + \phi_- \ln\phi_- + (1-\phi_+-\phi_-)\ln(1-\phi_+-\phi_-)] \\
&+ \frac{1}{8\pi\lambda_0^2}\int d\mathbf{r}\int d\mathbf{r}\frac{\phi(\mathbf{r})\phi(\mathbf{r}')}{|\mathbf{r}-\mathbf{r}'|} \\
&- \frac{\alpha}{8\pi\lambda_0^2}\int d\mathbf{r}\int d\mathbf{r}'\frac{\phi(\mathbf{r})\mathrm{e}^{-\frac{|\mathbf{r}-\mathbf{r}'|}{\ell_c}}\phi(\mathbf{r}')}{|\mathbf{r}-\mathbf{r}'|} \\
&- \int d\mathbf{r}_{||}\int dz\,[H_+(z)\phi_+(\mathbf{r}) + H_-(z)\phi_-(\mathbf{r})] \\
&- \int d\mathbf{r}\,[\mu_+\phi_+(\mathbf{r}) + \mu_-\phi_-(\mathbf{r})] \qquad (5.26)
\end{aligned}$$

where the integration dimensions are normalized by the ion size b. The first integral is the translational entropy of the mixture proposed by Bikerman [50] with the incompressibility condition enforced. This is the most widely used model to account for finite ion size in MFTs of ionic liquids [16, 17, 23–26]. We drop the explicit notation for spatial dependence as it is understood that these profiles can be inhomogeneous. The second term is the coulombic interactions where $\phi =$

$\phi_+ - \phi_-$ is the local dimensionless charge density. The nondimensionalized nominal screening length is given by $\lambda_0 = [\epsilon_r \epsilon_0 b/\beta e^2]^{1/2}$ with $\beta = 1/k_B T$, elementary charge e, temperature T, Boltzmann constant k_B, vacuum permittivity ϵ_0, and relative permittivity ϵ_r. The third term is a Yukawa potential which accounts for the ion–ion correlations and the non-electrostatic interactions between the bulky organic ions, with α controlling the strength and the correlation length ℓ_c controlling the range. In principle, as shown by de Souza and Bazant [48], α and ℓ_c will vary with concentration; however, we assume they are independent and choose a particular section of the parameter space to explore. One could expand the model to include more chemical specificity by using a different α and ℓ_c for each pair of species [24]. Alternatively a Flory χ could be included between each species pair which is a much simpler local interaction that would still allow for chemical specificity [52]. The fourth term models the preferential adsorption/desorption of ions with the electrode, where $\mathbf{r}_{||}$ is the 2-dimensional position in the directions parallel to the electrode, z is position normal to the electrode, and $H_\pm$ are the adsorption potentials for the ions relative to the solvent. Note that the adsorption potentials $H_\pm(z)$ only depend on position normal to the surface, z. The last term contains the contributions from the chemical potentials μ_+ and μ_- where the solvent term is eliminated using the incompressibility condition. The system is grand canonical as it is connected to a bulk reservoir at fixed species chemical potentials.

For the single plate geometry, assuming the transverse directions are vast compared to the normal direction, we can reduce the model to a one-dimensional system. Instead of the vector position, $\mathbf{r}$, dependence is reduced to the coordinate z normal to the electrode face (normalized by b). Since the single-plate system is semi-infinite, we introduce a second plate at a sufficiently large distance L from the first plate to simplify numerical calculations. The two plates have the same magnitude of surface charge σ with opposite sign, and are located at $z = \pm L/2$. They are far enough that a significant region centered at $z = 0$ is at the bulk condition of $\phi_\pm = \phi_\pm^B$.

The Coulomb term, the second term in Eq. (5.26) can be rewritten identically using an identity transform for quadratic interactions [43, 44]. This introduces the nondimensional electrostatic potential $\psi = \beta e \Psi$ that is coupled to the mean charge density, ϕ. We also include preferential adsorption potentials to account for non-electrostatic electrode–electrolyte interactions [23]. The nondimensional grand free

energy per unit area for the single plate system is

$$\begin{aligned}\frac{\beta\Omega}{A} &= \int_{-L/2}^{L/2} dz\ [\phi_+ \ln \phi_+ + \phi_- \ln \phi_- + (1-\phi_+-\phi_-)\ln(1-\phi_+-\phi_-)] \\ &+ \int_{-L/2}^{L/2} dz \left\{ \left[\phi + \sigma\delta\left(z+\frac{L}{2}\right) - \sigma\delta\left(z-\frac{L}{2}\right)\right]\psi - \frac{\lambda_0^2}{2}\left|\frac{\partial\psi}{\partial z}\right|^2 \right\} \\ &+ \frac{\alpha}{2\lambda_0^2}\int_{-L/2}^{L/2} dz \int_{-L/2}^{L/2} dz'\, U(z-z')\phi(z)\phi(z') \\ &- \int_{-L/2}^{L/2} dz\ [H_+\phi_+ + H_-\phi_-] \\ &- \int_{-L/2}^{L/2} dz\, [\mu_+\phi_+ + \mu_-\phi_-] \end{aligned} \tag{5.27}$$

where the Yukawa potential is $U(z-z') = -\frac{\ell_c}{2}\mathrm{e}^{-|z-z'|/\ell_c}$ and A is the electrode area. The fourth term accounts for the preferential adsorption/desorption of ions and solvent. The solvent contribution is eliminated from this term using the incompressibility condition. We use the same short-ranged preferential adsorption potential that was used by Chao and Wang (CW) in their study of preferential adsorption of ionic liquids [23]. This form was invoked for numerical stability and to maintain consistency with the length scale of the RTIL, b. In principle the potential could be a delta function at each surface, rather than be position dependent. We choose to use a smooth potential for numerical stability.

$$H_\pm(z) = \begin{cases} (1-z-\frac{L}{2})^2\Delta h_\pm & -L/2 \le z < -L/2+1 \\ 0 & -L/2+1 \le z < L/2-1 \\ (1+z-\frac{L}{2})^2\Delta h_\pm & L/2-1 \le z \le L/2 \end{cases} \tag{5.28}$$

where strength of the harmonic adsorption for each ion type relative to the solvent is denoted $\Delta h_\pm = h_\pm - h_s$ [23]. In general, the strength of the interaction can be different for cations and anions. However, for simplicity, we assume that $\Delta h = \Delta h_+ = \Delta h_-$, and therefore $H = H_+ = H_-$. Note, the negative sign in front of the adsorption term of eqn (5.27) means that when Δh is negative, the electrode has a higher affinity for the solvent than the ions.

Setting the variation of the free energy Ω with respect to ψ and $\phi_\pm$ to zero, we obtain

the following set of self-consistent equations

$$-\lambda_0^2 \frac{\partial^2 \psi}{\partial z^2} = \phi + \sigma\delta\left(z + \frac{L}{2}\right) - \sigma\delta\left(z - \frac{L}{2}\right) \tag{5.29}$$

$$\ln\left(\frac{\phi_+}{1-\phi_+-\phi_+}\right) + \psi + Y - H_+ - \mu_+ = 0 \tag{5.30}$$

$$\ln\left(\frac{\phi_-}{1-\phi_+-\phi_-}\right) - \psi - Y - H_- - \mu_- = 0 \tag{5.31}$$

where we have introduced the Yukawa field Y defined by the convolutional integral

$$Y(z) = \frac{\alpha}{\lambda_0^2}\int_{-L/2}^{L/2} dz'\, U(z-z')\phi(z') \tag{5.32}$$

Since the system is symmetric, we have the condition $\partial_z\psi|_{z=0} = 0$. Integrating over the domain and noting that inside the electrodes $\partial_z\psi = 0$ yield the boundary conditions

$$-\lambda_0^2 \left.\frac{\partial\psi}{\partial z}\right|_{z=\pm L/2} = \sigma \tag{5.33}$$

The Poisson equation, eqn (5.29), can be solved efficiently via finite difference, or can be solved via direct integration

$$\psi(z) = \psi(0) - \frac{1}{\lambda_0^2}\int_0^z dz'(z-z')\phi(z') \tag{5.34}$$

where $\psi(0) = 0$ for the symmetric two-plate system. Although one can obtain $Y(z)$ in terms of $\phi(z)$ using the integral form of eqn (5.32), computationally it is more convenient to solve for $Y(z)$ from a differential equation. To this end, differentiating eqn (5.32) twice yields

$$\frac{\partial^2 Y}{\partial z^2} - \frac{Y}{\ell_c^2} = \frac{\alpha}{\lambda_0^2}\phi(z) \tag{5.35}$$

Differentiating eqn (5.32) once and setting $z = 0$ yields the boundary condition

$$\left.\frac{\partial Y}{\partial z}\right|_{z=\pm L/2} = \mp\frac{Y(\pm L/2)}{\ell_c} \tag{5.36}$$

which agrees with previously obtained results [24, 25] for no Yukawa source at the electrode. Assuming the bulk is a homogeneous 1:1 ionic liquid with ion volume fractions $\phi_\pm^B = \phi^B$, we may set $\psi = Y = H = \phi = 0$. Using the bulk conditions in addition to the equilibrium conditions $\mu_+ = \mu_+^B$ and $\mu_- = \mu_-^B$, we obtain an equation for the chemical potential.

$$\mu = \mu_+ = \mu_- = \ln\left(\frac{\phi^B}{1-2\phi^B}\right) \tag{5.37}$$

Inserting eqn (5.37) into eqn (5.30) and eqn (5.31) gives equations for the ion density profiles in terms of the potentials ψ, Y, and H,

$$\phi_+ = \frac{\mathrm{e}^{-(\psi+Y)}}{(1/\phi^B - 2)\mathrm{e}^{-H} + 2\cosh(\psi + Y)} \tag{5.38}$$

$$\phi_- = \frac{\mathrm{e}^{\psi+Y}}{(1/\phi^B - 2)\mathrm{e}^{-H} + 2\cosh(\psi + Y)} \tag{5.39}$$

Equations (5.29), (5.35), (5.38) and (5.39), along with boundary conditions in eqn (5.33) and eqn (5.36) constitute a set of self-consistent equations which can be solved iteratively with an initial guess for $\phi(z)$. For all calculations we set $T = 300\,\mathrm{K}$ and $b = 1\,\mathrm{nm}$. BSK predicted that the correlation length is on the order of the molecular size; therefore, we set $\ell_c = b = v^{1/3}$ [17]. We choose $\epsilon_r = 10$ in accordance with experimental measurements of imidazolium-based ionic liquids [53]. These values result in a nominal screening length of $\lambda_0 = 0.12$.

Zero applied field

For the case of no applied potential, the electrostatic potential difference between the two separated plates is zero, $\Delta V = \psi_{-L/2} - \psi_{L/2} = 0$. The mean-field equations are solved self-consistently via the following algorithm. An initial guess is made for $\phi(z)$. $\psi(z)$ is calculated from eqn (5.29) with the boundary conditions in eqn (5.33). $Y(z)$ is calculated from eqn (5.35) with the boundary condition given in eqn (5.36), and $H(z)$ is calculated from eqn (5.28). ψ, Y, and H are used in eqn (5.38) and eqn (5.39) to calculate new profiles ϕ_+ and ϕ_-, and therefore $\phi(z) = \phi_+ - \phi_-$. This process is repeated until the maximum difference in local charge density between subsequent iterations is below a tolerance, set to 10^{-10} for our calculations.

Applied field

In the case of an applied field, $\psi_{-L/2} = -\psi_{L/2} \neq 0$ and we specify the surface charge on the left and right plate to be σ and $-\sigma$ respectively. For each σ, we calculate the equilibrium profiles and extract the surface potential on each plate, which effectively yields the relationship $\sigma(\Delta V)$, where ΔV is the difference in surface potential between the two plates. The differential capacitance is calculated as

$$C_{\mathrm{diff}} = \frac{\partial|\sigma|}{\partial \Delta V} \tag{5.40}$$

and the energy storage per surface area is calculated as

$$\Delta F = \int_{\sigma(0)}^{\sigma(\Delta V)} u\, d\sigma = \int_0^{\Delta V} C u\, du \tag{5.41}$$

where σ, ΔV, C_{diff} and ΔF are in units of e/b^2, k_BT/e, e^2/k_BTb^2 and k_BT/b^2 respectively.

5.4 Results and Discussion

Effect of dilution on spontaneous surface charge separation

We first study the effect of dilution on spontaneous surface charge separation when there is no applied potential, $\Delta V = 0$. We vary the Yukawa interaction strength from $\alpha = 0$ to $\alpha = 1$, and the bulk ion volume fraction from $\rho^B = \phi_+^B + \phi_-^B = 0.05$ to $\rho^B = 1$. It is expected that dilution should weaken the effect of correlations [25], making the critical correlation strength for SSCS, $\alpha_{s,c}$, larger. Thus, a neat RTIL that undergoes SSCS at a particular $\alpha_{s,c}$ may not undergo any SSCS after dilution. We can observe SSCS by varying the bulk ion concentration ρ^B at a fixed correlation strength α.

We find that when α is moderately above the transition value for neat IL SSCS, the transition density decreases, but the transition remains second-order. When α is well above the transition value for neat IL SSCS, the transition can happen at a lower density and the nature of the transition changes from second-order to first-order. Figure 5.4 shows SSCS in systems with α moderately (a) and significantly (b) above the neat ionic liquid transition value of $\alpha_{s,c} = (\lambda_0/\ell_c)^2 + 2(\lambda_0/\ell_c) = 0.25$ for $\lambda_0/\ell_c = 0.12$ [25]. Figure 5.4a shows a second-order transition in the surface charge density with increasing ρ^B while Figure 5.4b shows a first-order transition. Additionally, as conjectured in Ref. 31, stronger correlations lead to a lower transition density.

The first-order behavior is characterized by metastability. When starting from a charge separated state and slowly decreasing the bulk concentration, the charge separated state remains metastable until a lower ρ^B value than when starting from a homogeneous state and slowly increasing ρ^B, as shown in Figure 5.4b. Furthermore, note that the surface charge no longer increases continuously from 0 upon SSCS. Instead, the surface charge jumps from 0 to a finite value at the disordered spinodal and similarly jumps from a finite value down to 0 at the ordered spinodal. The true equilibrium transition ρ^B value is determined by the equality of the grand free energy density between the two branches. See the Appendix for more information on determining the transition point. The grand free energy is obtained by using the converged profiles ψ, Y, and $\phi_\pm$.

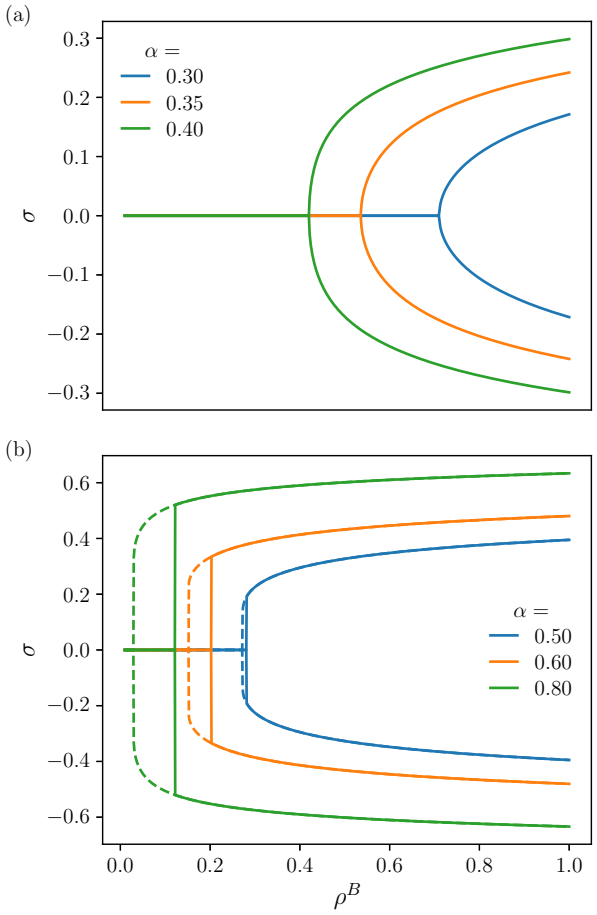

Figure 5.4: (a) second-order SSCS transition, for a specified α, the transition occurs at a critical bulk ion concentration. Note, $\rho^B = \phi_+^B + \phi_-^B = 2\phi^B$ is the total ion concentration in the bulk. There are two branches because the symmetry can spontaneously break in either direction. (b) first-order SSCS transition, for a specified α, the transition occurs at different bulk ion concentrations depending on the initial state of the system, indicating metastability of the two phases. Solid lines and dashed lines correspond to paths taken starting from homogeneous and charge-separated states, respectively.

Charge overscreening and crowding

SSCS is accompanied by the presence of decaying oscillatory charge density profiles away from a charged electrode. The overcompensation of surface charge and the resulting oscillatory charge density and electrostatic potential profiles have been described as *overcharging*, or *overscreening* [17, 20, 54]. This phenomenon has been well documented for dense ionic systems near charged surfaces. In the case of BSK, the surface is charged and the ionic liquid overcompensates the surface charge, whereas in our case the surface charge is generated by the spontaneous

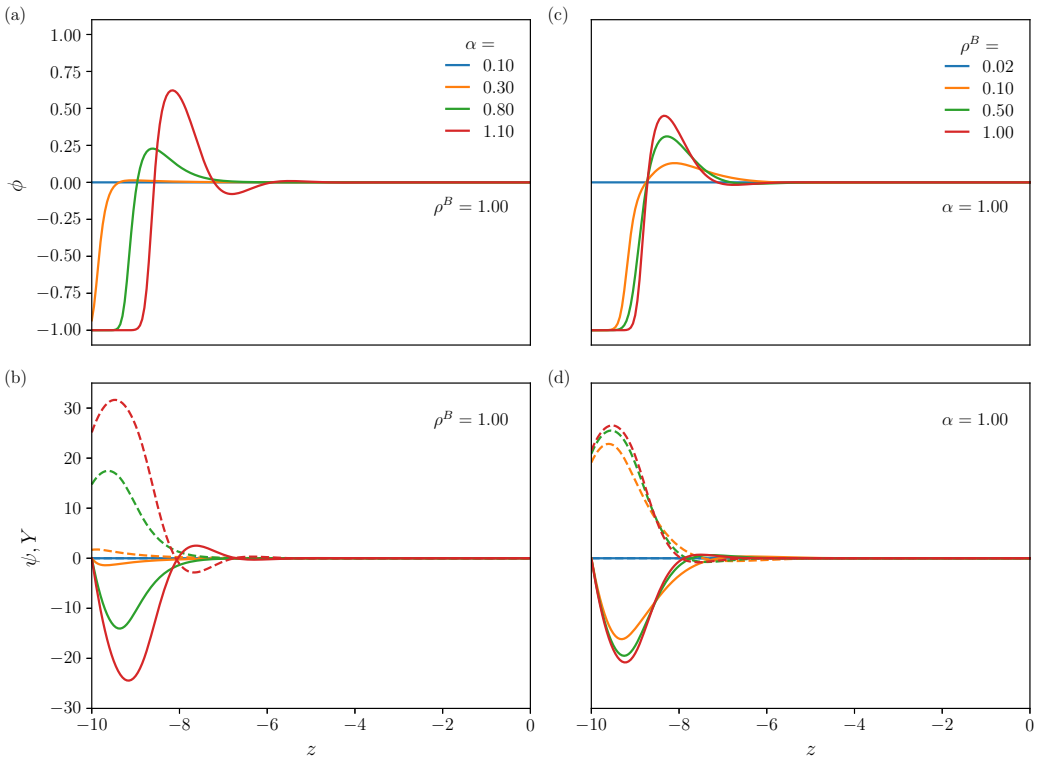

Figure 5.5: (a) Charge density profiles near a positively charged electrode for a neat RTIL, $\rho^B = 1$. Profiles for various α are shown, all with $\Delta V = 0$. (b) Potential profiles corresponding to the charge density profiles in (a) where the electrostatic potential is given by solid lines and the Yukawa potential is given by dashed lines. (c) Charge density profiles near a positively charged electrode for a diluted RTIL with $\alpha = 1$ and $\Delta V = 0$. (d) Potential profiles corresponding to the charge density profiles in (c) where the electrostatic potential is given by solid lines and the Yukawa potential is given by dashed lines.

charge separation of the ionic liquid. In either case, *overscreening* of the charge occurs. An example of an oscillatory charge density profile for a neat RTIL is given in Figure 5.5a. The oscillations become more pronounced as the correlation strength α increases.

For very strong correlations (e.g. $\alpha = 1.1$), the effects of lattice saturation, or *crowding*, are observed. For the red and green curves in Figure 5.5a, the layer adjacent to the electrode extends out into the solution. This is a result of the finite size of the ions in the lattice-gas-like model. Since the charge density cannot exceed unity, as the driving force for separation increases, the counterion layer adjacent to the electrode grows.

As the RTIL is diluted, the effect of correlations decreases and the driving force for SSCS decreases with it. As a result, both *overscreening* and *crowding* should be diminished as the RTIL concentration decreases. Indeed this is shown in Figure 5.5c. As the RTIL is diluted, the extent of overscreening is diminished until eventually SSCS no longer occurs.

Phase diagram for SSCS at zero potential

For neat RTILs, the CW model shows a second-order transition at a critical alpha value, $\alpha_{s,c}$, at zero potential ($\Delta V = 0$) [23]. The spontaneous surface charge separation is similar to the spontaneous magnetization in the mean-field Ising model, where the surface charge is the analog of the magnetization.

It is of interest to determine the exact nature of the first-order and second-order behavior in the relevant parameter space. Specifically, what is the location of the tricritical point with respect to concentration (or μ) and correlation strength? To answer this question a phase diagram in $\alpha - \mu$ space was generated numerically. For a comprehensive description of the algorithm, see the Appendix.

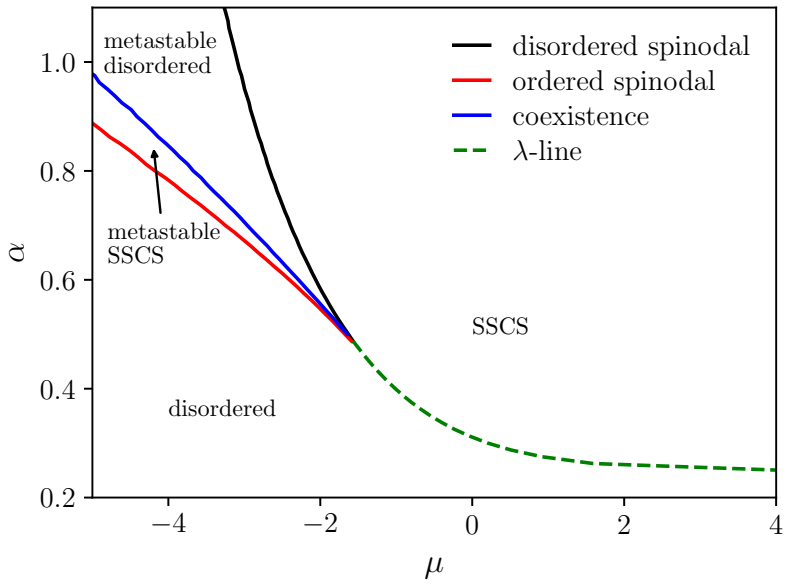

Figure 5.6: RTIL SSCS phase diagram in $\alpha - \mu$ space. The dashed λ-line is a line of critical points where second-order transitions occur. The blue coexistence line and the black and red spinodals are a region of first-order transitions. The transition from second-order to first-order occurs at the *tricritical point*.

As shown, dilution decreases the effects of SSCS, meaning that a dilute system

will have a higher $\alpha_{s,c}$ than a neat RTIL. This can be easily understood since the neutral solvent increases the average distance between ions, reducing the effects of short-ranged correlations. The CW model shows that for neat RTILs the transition value is determined by $\alpha_{sc,neat} = 2\lambda_0/\ell_c + \lambda_0^2/\ell_c^2$ [25]. For any dilute system, it should hold that $\alpha_{sc,dilute} > \alpha_{sc,neat}$. Thus, For any $\alpha < \alpha_{sc,neat}$ there will never be SSCS at any bulk ion density. This sets a lower bound for the value of α in the α–μ phase diagram.

The phase diagram in $\alpha - \mu$ space is given in Figure 5.6. At the lower right part of the phase diagram, the SSCS transition is second-order as indicated by a line of critical points (the λ-line; the dashed green curve). For larger α and low bulk density, the transition becomes first-order indicated by the solid blue binodal, which is flanked by the spinodals of the disordered phase (solid black line) and the spinodal of the SSCS state (solid red line). The λ-line and the binodal meet at the tricritical point, where the two spinodal lines also terminate with a common tangent. The tricritical point occurs at $\mu = -\ln 4$ or $\rho_B = 1/3$. We note that this volume fraction is the same value that results in a transition from bell to camel-shaped capacitance curves, as shown by Kornyshev [16]. The transition in the shape of the capacitance curves occurs even without consideration of correlations and is a result of the finite ion size as treated with the lattice model. We see in the case of the diluted RTIL with correlations that the transition in the shape of the capacitance curve at critical dilution coincides with a transition in the phase behavior.

Beyond the mean-field, fluctuations will change the nature of the transition. It has been shown that the transition in concentrated ILs is weakly first-order rather than second-order, putting it in the Brazovski universality class [29, 55]. Coarse-grained molecular dynamics simulations of neat RTILs also indicate a weakly first-order transition [30].

Connection to Blume–Capel Model

The SSCS is a transition involving spontaneous symmetry breaking in the presence of a diluent. This is reminiscent of the spontaneous magnetization in the diluted Ising model, the spin-1 Ising model or the Blume–Capel (BC) model (a subset of the well known Blume–Emery–Griffiths model) [56–59].

The BC/BEG model accurately captures the tricritical behavior of $He^4 - He^3$ mixtures, where the fluid-superfluid transition goes from second-order to first-order at a critical amount of He^3 impurity. The diluted RTIL shows a transition from

second-order to first-order phase behavior below a certain ion concentration, where the neutral solvent plays the role of impurities. To show the comparison, we briefly derive results of the BC model.

The Hamiltonian of the BC model in the constrained grand canonical ensemble is given by,

$$H(\{\mathbf{s}\}, N, T, \mu_A, \mu_B) = -\frac{J}{2}\sum_i \sum_j^{n.n.} s_i s_j - \Delta\mu \sum_i s_i^2 \tag{5.42}$$

where s_i is the spin on particle i (± 1 for interacting particles, A, and 0 for impurities, B), $J > 0$ is the ferromagnetic interaction strength, and $\Delta\mu = \mu_A - \mu_B$ is the chemical potential difference between particle types. The sum over j is over the nearest neighbors of spin i.

We define the relative magnetization order parameter $m = \sum_i s_i / N_A$ and the type A spin concentration $x = N_A/N$ in order to write the mean-field Hamiltonian. The Gibbs Entropy is used with the mean-field Hamiltonian to write a variational free energy, $G = \langle H \rangle - TS$. The non-dimensional variational free energy per spin is

$$\begin{aligned} g = \frac{G}{Nk_BT} = -\frac{1}{2}\alpha x^2 m^2 - \mu x + x\frac{1+m}{2}\ln\left(x\frac{1+m}{2}\right) + \\ + x\frac{1-m}{2}\ln\left(x\frac{1-m}{2}\right) + (1-x)\ln(1-x) \end{aligned} \tag{5.43}$$

where $\alpha \equiv zJ/k_BT$, $\mu \equiv \Delta\mu/k_BT$, and z is the coordination number of the lattice. Minimizing the free energy gives the mean field equations

$$m = \tanh(\alpha x m) \tag{5.44}$$

$$\mu = \ln\frac{x}{1-x} - \alpha x m^2 + \frac{1+m}{2}\ln\frac{1+m}{2} + \frac{1-m}{2}\ln\frac{1-m}{2} \tag{5.45}$$

which can be analyzed to obtain a phase diagram for the fluid-superfluid transition. The $\alpha - \mu$ phase diagram for the BC model has the same characteristic shape as the phase diagram for the dilute RTIL model in this study. We observe tricritical behavior at the same chemical potential, which corresponds to $\mu = -\ln 4$ or $x = \rho^B = 1/3$. Note, this is the same concentration, $\gamma = 1/3$, discovered by Kornyshev [16] where the capacitance curve transitions from bell to camel-shaped. This analysis confirms the strong analogy between the currently studied dilute RTIL model and the *dilute Ising model*. The BC model and variants have also been used to study confined ionic liquids, and similar tricritical phase behavior is reported [60, 61]. That the tricritical point for both the SSCS transition and the BC/BEG model occurs at $\rho = 1/3$ is striking. However, the exact reason for this remains to be understood.

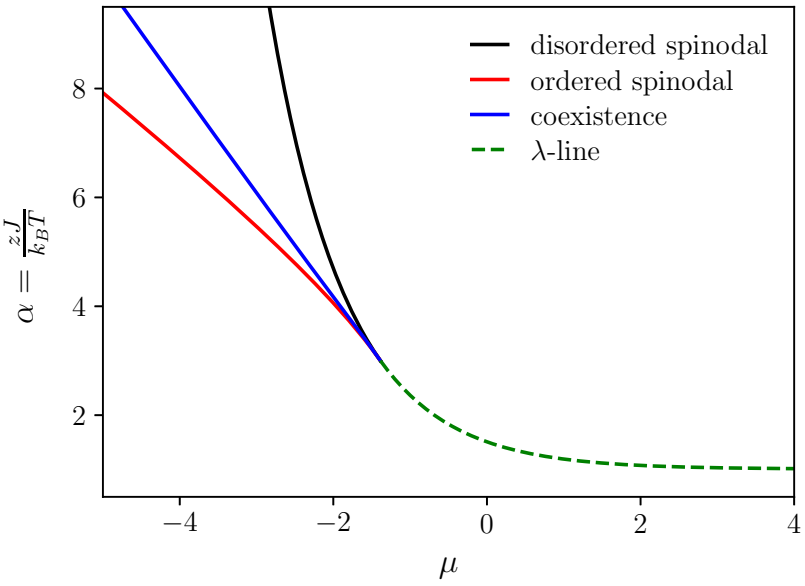

Figure 5.7: $\alpha - \mu$ phase diagram for the mean-field BC model.

Capacitance and energy storage of dilute RTIL

Modulation of the distance to the $\alpha_{s,c}$ can be beneficial in multiple ways, first by preventing unwanted hysteresis in charging and discharging, but also by allowing for a large zero-potential capacitance. We have shown that addition of neutral solvent increases $\alpha_{s,c}$; here we discuss how this affects the capacitance and energy storage.

In order to see the effect of α in dilute systems, we first look at the $\alpha = 0$ case that was studied by Kornyshev [16]. He observed a transition from bell to camel-shaped capacitance curves at significant dilution [16]. The framework developed in our theory successfully reproduces the results of Kornyshev when $\alpha = 0$, as shown in Figure 5.15 in the Appendix. The transition from bell to camel-shaped curves occurs at $\rho^B = 1/3$, as expected. While the zero-potential capacitance is lower for the dilute RTIL, at high potentials, the more dilute RTILs have higher capacitance. As pointed out by May [62], the increase in capacitance with dilution at high potential comes from a frustration relief of the EDL, where coions near the surface are replaced by solvent molecules. Recent works have discovered a "bird-shaped" capacitance curve that occurs near the RTIL–solvent demixing transition when ionophilic electrodes are used [63]. While we did not observe this shape with the given model, we believe this shape can be achieved by adding a local repulsion between ions and solvent via a Flory χ parameter. Ionophilic electrodes can be modeled by setting Δh to a

positive value. We leave this exploration for a future study.

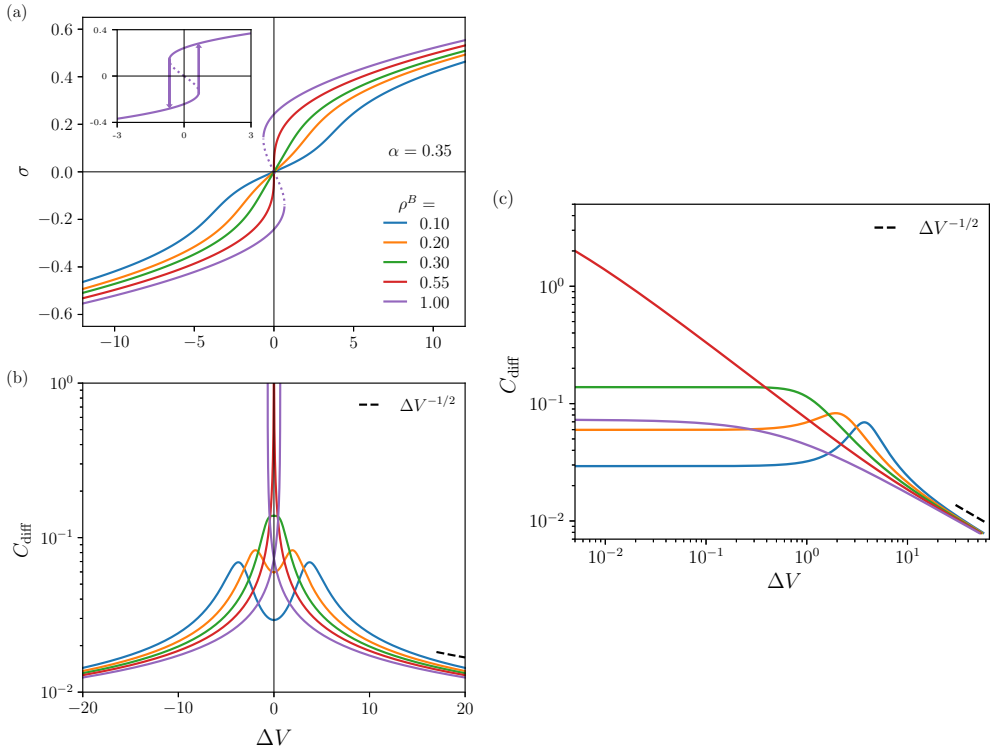

Figure 5.8: (a) σ vs ΔV plotted for a RTILs with varying dilution and $\alpha = 0.35$. The dashed portion of $\rho_B = 1.0$ (purple) curve is the region of instability. The inset shows the $\rho_B = 1.0$ curve with arrows indicating the trajectory the system would follow when slowly charging or discharging. The arrow is located at the spinodal, where the system must jump to the stable positive branch. (b) and (c) C_{diff} vs ΔV plotted for RTILs with varying dilution on semi-log and log-log scales respectively. The capacitance curves are calculated using only the stable and metastable portions of the $\sigma - \Delta V$ curves.

With correlations accounted for in the Yukawa potential, dilution effectively raises $\alpha_{s,c}$. Figure 5.8a shows that hysteresis in charging/discharging can be minimized or even prevented via dilution. The $\sigma - \Delta V$ curve for $\rho_B = 1.0$ (purple) exhibits metastability where σ and ΔV have opposite signs, while the stability condition $\partial\sigma/\partial\Delta V > 0$ is still satisfied. There is also a region of instability indicated by a dashed line where $\partial\sigma/\partial\Delta V < 0$. For a given α, instability and metastability can be mitigated by diluting enough with a neutral solvent such that $\alpha \leq \alpha_{s,c}$. For $\alpha = 0.35$ we see that at the corresponding critical concentration of $\rho_B = 0.55$ the slope diverges at $\Delta V = 0$. See the red curve in Figure 5.8a. This means that for an RTIL with $\alpha = 0.35$, one can maximize the zero-potential capacitance by diluting

the RTIL down to 55% v/v. We again acknowledge that α for a given RTIL could generally depend on the ion concentration;[48] however, the extent and form of the dependence is not the focus of this study. Here, we assume that α is independent of the concentration and explore the parameter space.

Capacitance curves for $\alpha = 0.35$ are shown in Figure 5.8b and c. The zero-potential capacitance first increases upon dilution (purple to red). The maximum capacitance is reach when the concentration is such that $\alpha = \alpha_{s,c}$. Further dilution results in a decrease in zero-potential capacitance (red to green to orange to blue) because it brings the system further below $\alpha_{s,c}$. For $\rho^B < 1/3$ the maximum in capacitance characteristic of the camel shaped capacitance curves is still present. Similarly, for high enough potentials, the capacitance increases with dilution due to EDL frustration relief.

Figure 5.9 show the zero-voltage capacitance as a function of ρ^B at different values of α. The capacitance diverges for a critical ρ^B value whose $\alpha_{s,c}$ becomes equivalent to α for the given RTIL.

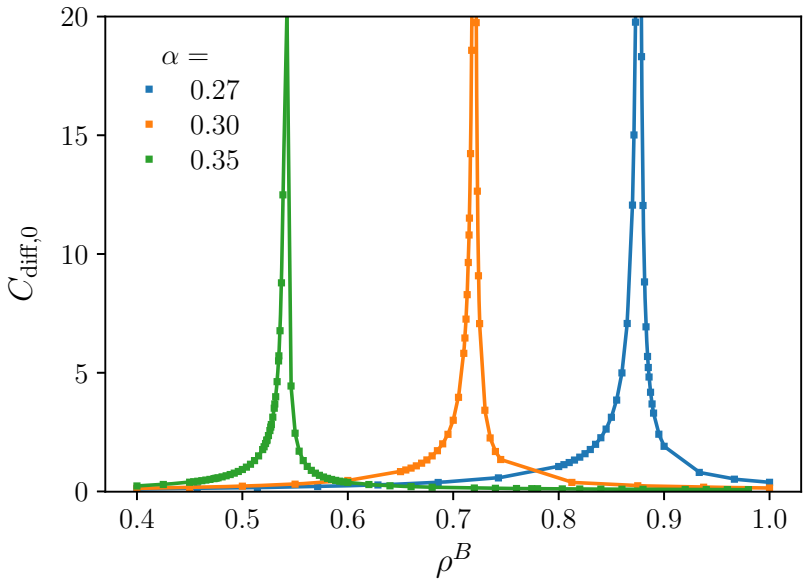

Figure 5.9: $C_{\text{diff}}(\Delta V = 0)$ vs ρ_B for different values of α. Note that α is below the value at the tricritical point, and therefore the transition remains second-order.

Since dilution leads to a higher capacitance at high potentials, it is conceivable that the energy storage could be higher in more dilute RTILs at the same charging potential. The energy storage is calculated via eqn (5.41) and plotted in Figure 5.10

for an RTIL with $\alpha = 0.35$. If the capacitor is charged to higher potentials, it is evident that more dilute RTILs can store more energy per unit area. This is because of the higher capacitance in dilute RTILs at high potential, which is shown in Figure 5.8b and c. We see that even at the critical concentration of $\rho^B = 0.55$ where the zero-voltage capacitance diverges, the energy storage is relatively low. As explained by Chao and Wang[23], this is due to the peak in capacitance being counterbalanced by the zero of potential in the integral in eqn (5.41). In order to combat this, Chao and Wang proposed preferential adsorption where one ion is preferentially attracted to a particular electrode. The result was a shifted diverging capacitance which leads to a substantial increase in energy storage. We would expect similar results with asymmetric ion adsorption in diluted RTILs, so we instead focus on solvent adsorption which is specific to our work.

Preferential adsorption of solvent

We assume the same short-ranged preferential adsorption for the solvent that has previously been used to describe preferential adsorption of ions in neat RTILs [23, 25]. The form of the potential is given in eqn (5.28). We assume that the two ions have the same interaction with the electrodes while the solvent interaction differs. Under the assumption of indifferent adsorption between the cation and anion, the

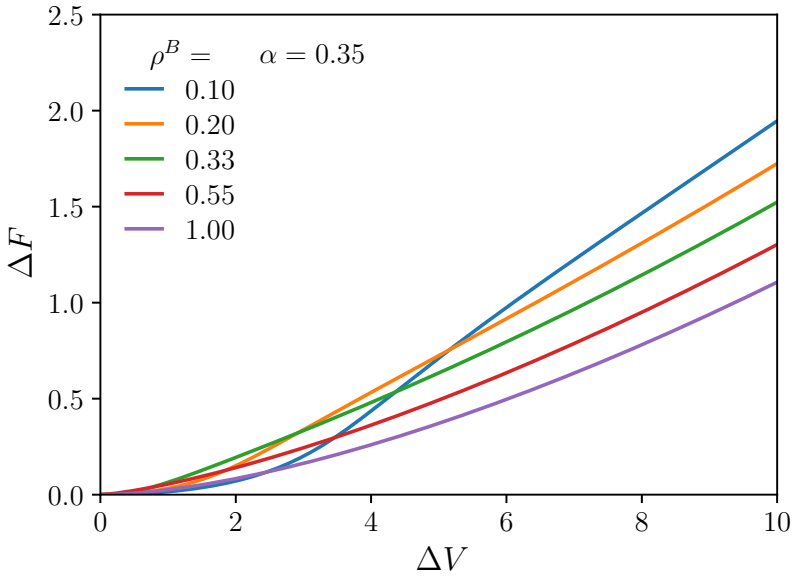

Figure 5.10: Energy storage per unit area for an RTIL with $\alpha = 0.35$ at various levels of dilution.

relevant interaction is the difference between the solvent and the ions with the surface. A negative Δh implies that the solvent is preferentially attracted to the electrode, or that the electrode is solvophilic. We expect that a solvophilic electrode will diminish unfavorable hysteresis and SSCS by drawing solvent to the electrode and pushing ions away. To study the SSCS behavior we set zero surface potential and vary the bulk ion concentration. The $\alpha - \mu$ phase diagram for a diluted RTIL with $\Delta h = -5$ is given in Figure 5.11. The main effect on the zero-voltage behavior is that for a given chemical potential, a higher α is required to induce SSCS.

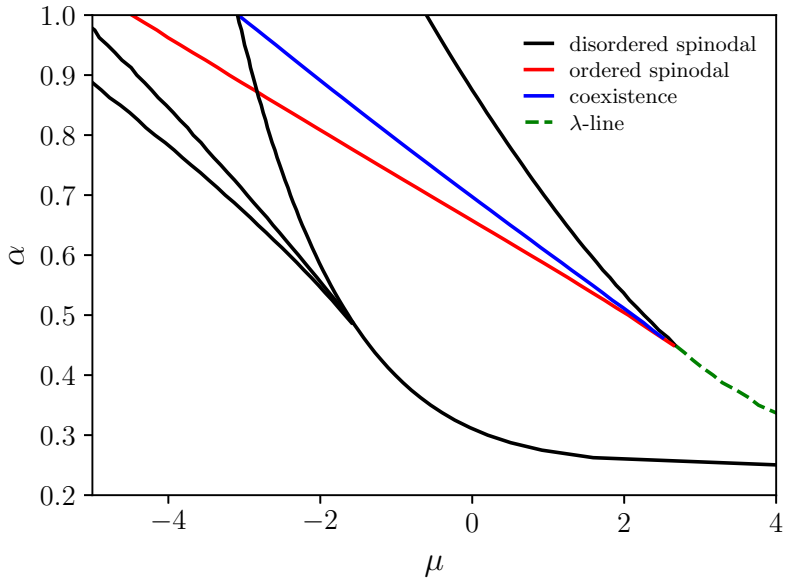

Figure 5.11: $\alpha - \mu$ phase diagram for a dilute RTIL with a solvophilic electrode, $\Delta h = -5$. The black superimposed phase diagram is the result for no preferential adsorption.

Preferential adsorption of solvent repels ions away from the electrode. At low potential, this leads to a lower differential capacitance as the driving force for ions to replace the solvent molecules is low. As the potential increases, the system undergoes a surface transition where the solvent molecules are replaced with counterions. We note that this finite potential transition can occur in systems with no preferential adsorption, so long as the RTIL concentration is sufficiently low, and the correlation strength is sufficiently high. Preferential adsorption of solvent enhances the effect and shifts the transition to higher concentrations where RTILs are typically used. Near the transition at finite potential, the capacitance becomes very large.

In Figure 5.12, the surface charge, differential capacitance, and energy storage are

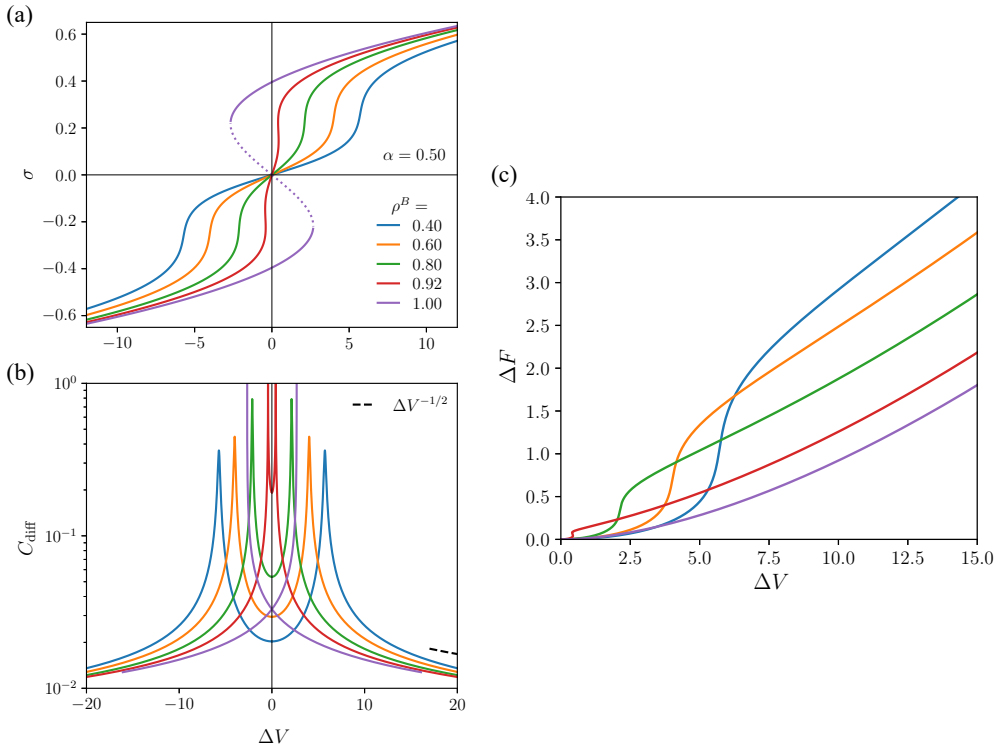

Figure 5.12: (a) σ vs ΔV plotted for a RTILs with varying dilution, $\alpha = 0.50$, and a solvophilic electrode ($\Delta h = -5.0$). The dashed portion of $\rho_B = 1.0$ (purple) curve is the region of instability. (b) C_{diff} vs ΔV plotted on semi-log scale and (c) energy storage ΔF vs ΔV.

plotted as a function of the applied potential for a solvophilic electrode. We see that the spike in capacitance (Figure 5.12b) at a finite potential difference leads to a sudden rapid increase in the energy storage (Figure 5.12c), which naturally comes from the definition of energy storage given in eqn (5.41). Previous studies that focused on ion adsorption into nanopores have shown a similar increase in energy storage when using *ionophobic* electrodes [64–67]. Generally, wider peaks in capacitance shifted to larger applied potentials lead to more energy storage. Also, we still observe the trend that more dilute RTILs store more energy when charged to relatively higher potentials. This is due to the higher differential capacitance at higher potential. In the high potential limit we still observe the expected $\Delta V^{-1/2}$ behavior [16].

5.5 Conclusions

The RTIL concentration is a powerful design handle for EDLCs. While some factors such as the correlation strength and length, or the chemical nature of the electrode can be difficult and expensive to vary, concentration is very simple, yet effective for tuning capacitance and energy storage. For example, the hysteresis in RTILs due to strong correlation effects [23, 27–29] can be mitigated by dilution. Addition of a neutral solvent works to separate ions and decrease the effect of the short-ranged correlations. By diluting, one can modulate the proximity to SSCS to fine tune and bolster the capacitance.

When a neutral solvent is added, there is also a rich phase behavior similar to that of the well known BC (or BEG) model. At high concentrations SSCS is a second-order transition at the mean-field level, whereas at low concentrations SSCS is a first-order transition. The transition from second-order to first-order occurs at the tricritical point which exists at a bulk ion volume fraction of $\rho^B = 1/3$, the same volume fraction of the tricritical point in the BC model. This volume fraction also corresponds to the transition between bell and camel-shaped capacitance curves as discovered by Kornyshev [16].

If the electrode shows preference for the solvent, this further reduces the effect of SSCS, pushing the transition to finite potentials where ions are attracted to the charged electrodes. This preference for solvent can lead to a surface charge transition at a *finite potential* where the surface charge rapidly increases (or even jumps), and the electric double layer is flooded with ions to counteract the charge. The rapid increase in surface charge is favorable when continuous due to the increased capacitance and energy storage. However, a jump in surface charge could lead to unfavorable hysteresis in charging and discharging similarly to neat RTILs [27, 28]. We achieved a significant increase in energy storage without considering asymmetric adsorption of the ions as in Ref. 18. The presence of solvent allows for the phase transition at finite potential, which could not occur in a neat RTIL without introducing asymmetry.

Based on these results, the ideal charging behavior is achieved when the concentration and correlation strength are such that the system is near but not above the critical concentration for a finite potential surface phase transition. The solvent choice and concentration serve as easy handles for modulating the phase behavior and maximizing the capacitance.

While we only apply a mean-field treatment of RTILs with a phenomenological cor-

rection for ion–ion correlations, similar models have been used to predict qualitative behavior observed in experiments [16, 23–26]. The lattice-gas-like model used here is not able to incorporate any ion packing effects. Future works should consider more sophisticated theories that account for liquid structure such as classical density functional theory (cDFT) and weighted density theories. Size asymmetry can be incorporated into future studies where the solvent, cation, and anion can be treated explicitly with different sizes. Size asymmetry has been previously considered using Monte Carlo, cDFT [68], MFT without ion–ion correlations [51], and continuum theory [69], but there has not been work looking at the phase behavior and energy storage performance in asymmetric systems. Size asymmetry will shift the peak in the capacitance from zero potential in a similar manner to preferential adsorption, enhancing the energy storage from charging. It is also of interest to look at RTIL behavior in curved environments. Some studies are already looking at the EDL structure for RTILs near curved surfaces [10, 70, 71], but there is still work to be done specifically in confined systems with curvature. With the advent of wearable technology, supercapacitors are being targeted for power delivery in flexible electronics, where electrode curvature is of utmost importance [72]. Much work can be done even at the mean-field level. Future works should incorporate the effects explored in this work such as dilution, correlations, and non-electrostatic interactions, while including additional effects such as size asymmetry, curvature, and confinement.

5.6 Appendix

Locating the SSCS Transition

The second-order λ-line in the phase diagram in Figure 5.6 was calculated by stepping the bulk volume fraction from low to high, and identifying the volume fraction where the surface charge becomes finite. This process is done for various α below the tri-critical point. The continuous SSCS transition is shown in Fig. 5.13.

The binodal, disordered spinodal, and SSCS spinodal are found by analyzing the Ω–μ plot for various α above the tri-critical point. The free energy curve for the disordered state at a given α is calculated by stepping the bulk volume fraction from low to high starting from a homogeneous state. The free energy curve for the SSCS state is calculated by stepping the bulk volume fraction from high to low starting from a charge separated state. The spinodal of each state is the limit of stability, where thermodynamic stability is defined as $\partial^2\Omega/\partial\mu^2 < 0$. The coexistence point is where the separate free energy curves cross. At this point $\mu^I = \mu^{II}$ and $\Omega^I = \Omega^{II}$

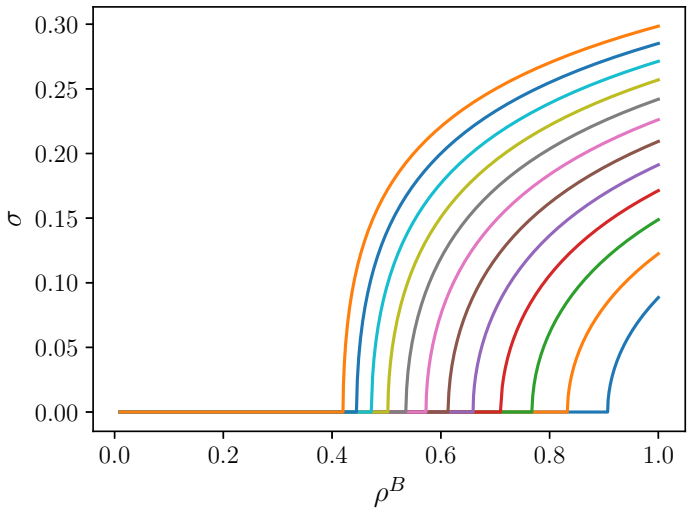

Figure 5.13: Surface charge vs. bulk concentration for $0.26 < \alpha < 0.4$, which is below the tri-critical point. The curves are ordered by their α value which is decreasing from left to right. Note that the second-order transition from disordered to surface charge separated is continuous.

where I and II represent the disordered and SSCS states, respectively. The Ω–μ plot for $\alpha = 0.8$ is given in Fig. 5.14.

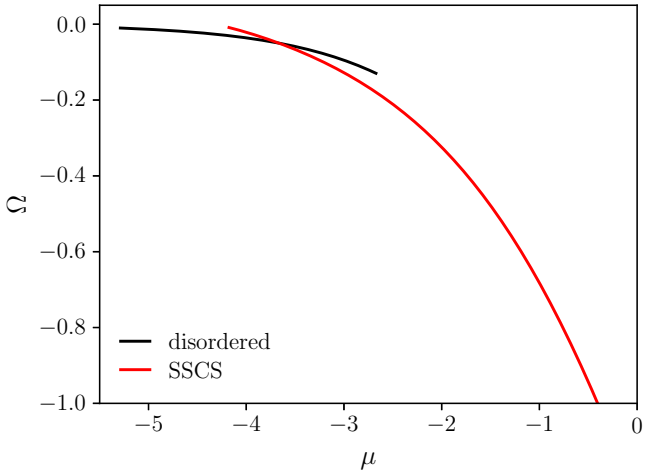

Figure 5.14: Free energy vs. chemical potential for $\alpha = 0.8$. Note that $\alpha = 0.8$ is above the tri-critical point. Metastable regions are regions that obey $\partial^2\Omega/\partial\mu^2 < 0$ but are not the lowest free energy states. Once a spinodal is reached, the system jumps to the stable branch.

The location of the two spinodals was also confirmed by observing the surface

charge. Starting from a near homogeneous state and stepping the chemical potential up while calculating the equilibrium charge and potential profiles at each step, the spinodal of the disordered (homogeneous) phase is reached at the first instance where a finite surface charge is observed. A finite surface charge indicates that the system has charge separated and is no longer disordered. Similarly, starting from a charge separated state and stepping the ion concentration (or chemical potential) down while calculating the charge and potential profiles at each step, the ordered spinodal is reached at the first instance where a zero surface charge is observed.

$\alpha = 0$ **Results**

The results for $\alpha = 0$ are presented to serve as a comparison to the finite α cases highlighted in the main text. In the $\alpha = 0$ case, the model without preferential adsorption reduces to the model developed by Kornyshev [16].

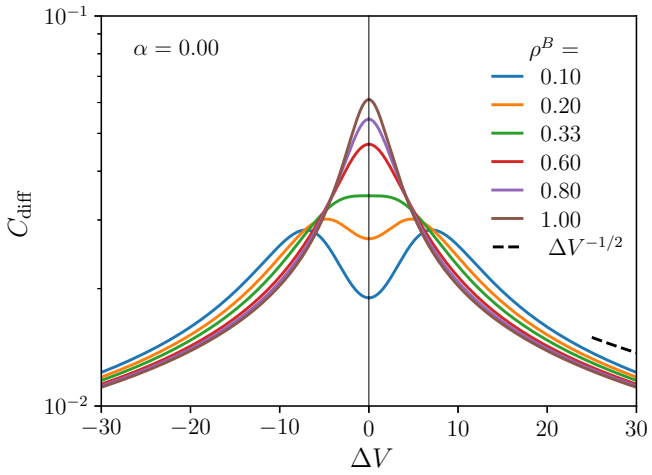

Figure 5.15: C_{diff} vs ΔV plotted for RTILs with varying dilution at $\alpha = 0$. Note the transition from bell to camel-shaped curves at $\rho^B = 1/3$ (green).

Generalized BSK Model with Combined Coulomb–Yukawa Potential

We start with the BSK formulation of the free energy in Fourier space, and specifically we start with the form where we have already extremized over ψ and replaced ψ, thus giving a quadratic interaction term of the form:

$$\beta F_c = \frac{V}{(2\pi)^3}\int d\mathbf{k}\left[2\pi\ell_B\left(\frac{1}{k^2}-\frac{\ell_c^2}{1+\ell_c^2k^2}\right)\right]\hat{\rho}_c(-\mathbf{k})\hat{\rho}_c(\mathbf{k}) \tag{5.46}$$

The first term gives the Coulomb interactions while the second term represents the non-electrostatic Yukawa interactions with a correlation length of ℓ_c. In order to add a strength to the Yukawa interaction, we introduce α:

$$\beta F_c = \frac{V}{(2\pi)^3}\int d\mathbf{k}\left[2\pi\ell_B\left(\frac{1}{k^2}-\alpha\frac{\ell_c^2}{1+\ell_c^2k^2}\right)\right]\hat{\rho}_c(-\mathbf{k})\hat{\rho}_c(\mathbf{k}) \tag{5.47}$$

In order to invert this operator we recombine into a single term which gives the following:

$$\beta F_c = \frac{V}{(2\pi)^3}\int d\mathbf{k}\left[2\pi\ell_B\frac{1+(1-\alpha)\ell_c^2k^2}{k^2(1+\ell_c^2k^2)}\hat{\rho}_c(\mathbf{\text{-}k})\hat{\rho}_c(\mathbf{k})\right] \tag{5.48}$$

To decouple the pair-wise interactions at the expense of adding a fluctuating field, we use the following identity for quadratic terms:

$$\frac{1}{2}\mathbf{x}\cdot\mathbf{A}\cdot\mathbf{x} = -\min_{\mathbf{y}}\left(\frac{1}{2}\mathbf{y}\cdot\mathbf{A}^{-1}\cdot\mathbf{y}-\mathbf{x}\cdot\mathbf{y}\right) = \max_{\mathbf{y}}\left(-\frac{1}{2}\mathbf{y}\cdot\mathbf{A}^{-1}\cdot\mathbf{y}+\mathbf{x}\cdot\mathbf{y}\right) \tag{5.49}$$

It is important to note that this operator can only be inverted when $\alpha <= 1$, otherwise there will be singular points and the matrix will not be invertible. The result is a variational Hamiltonian.

$$\begin{aligned} H_{var} &= \frac{V}{(2\pi)^3}\int d\mathbf{k}\left[\hat{\rho}_{\mathbf{k}}\hat{\psi}_{-\mathbf{k}}-\frac{1}{8\pi\ell_B}\frac{k^2(1+\ell_c^2k^2)}{1+(1-\alpha)\ell_c^2k^2}\hat{\psi}_{\mathbf{k}}\hat{\psi}_{-\mathbf{k}}\right] \\ &= \frac{V}{(2\pi)^3\nu}\int d\mathbf{k}\left[\hat{\phi}_{\mathbf{k}}\hat{\psi}_{-\mathbf{k}}-\frac{\nu}{8\pi\ell_B}\frac{k^2(1+\ell_c^2k^2)}{1+(1-\alpha)\ell_c^2k^2}\hat{\psi}_{\mathbf{k}}\hat{\psi}_{-\mathbf{k}}\right] \end{aligned} \tag{5.50}$$

Where the charge density is $\phi = \nu\rho_c$. The second term here is unwieldy but can be simplified down a lot via some algebra. First pull out a k^2, leaving:

$$\frac{k^2(1+\ell_c^2k^2)}{1+(1-\alpha)\ell_c^2k^2} = k^2+\frac{\alpha\ell_c^2k^4}{1+(1-\alpha)\ell_c^2k^2} \tag{5.51}$$

Next we introduce two lumped constants defined as:

$$A = \alpha\ell_c^2 \tag{5.52}$$

$$B = (1-\alpha)\ell_c^2 \tag{5.53}$$

Then the algebraic steps to simplify the 4th order term are as follows:

$$\begin{aligned}
\frac{k^2(1+\ell_c^2k^2)}{1+(1-\alpha)\ell_c^2k^2} &= k^2 + \frac{\alpha\ell_c^2k^4}{1+(1-\alpha)\ell_c^2k^2} \\
&= k^2 + \frac{Ak^2(k^2+1/B-1/B)}{1+Bk^2} \\
&= k^2 + \frac{A}{B}k^2 - \frac{A(k^2+1/B-1/B)}{B(1+Bk^2)} \\
&= k^2 + \frac{A}{B}k^2 - \frac{A}{B^2} + \frac{A}{B^2(1+Bk^2)} \\
&= \left(1+\frac{A}{B}\right)k^2 - \frac{A}{B^2} + \frac{A}{B^2(1+Bk^2)} \qquad (5.54)
\end{aligned}$$

Thus (5.50) can be written equivalently as,

$$\begin{aligned}
H_{var} = \frac{V}{(2\pi)^3\nu}\int d\mathbf{k}\Bigg\{&\hat{\phi}_{\mathbf{k}}\hat{\psi}_{-\mathbf{k}} \\
&- \frac{\nu}{8\pi\ell_B}\left[\left(1+\frac{A}{B}\right)k^2 - \frac{A}{B^2} + \frac{A}{B^2(1+Bk^2)}\right]\hat{\psi}_{\mathbf{k}}\hat{\psi}_{-\mathbf{k}}\Bigg\} \qquad (5.55)
\end{aligned}$$

Performing a variation w.r.t $\hat{\psi}$ we have:

$$\begin{aligned}
H_{var}\left[\hat{\psi}+\delta\hat{\psi}\right] = &\frac{V}{(2\pi)^3\nu}\int d\mathbf{k}\hat{\phi}_{\mathbf{k}}\left(\hat{\psi}_{-\mathbf{k}}+\hat{\psi}_{-\mathbf{k}}\right) - \\
&-\frac{V}{(2\pi)^3\nu}\int d\mathbf{k}\frac{\nu}{8\pi\ell_B}\left[\left(1+\frac{A}{B}\right)k^2 - \frac{A}{B^2} + \frac{A}{B^2(1+Bk^2)}\right]\left(\hat{\psi}_{\mathbf{k}}+\delta\hat{\psi}_{\mathbf{k}}\right)\left(\hat{\psi}_{-\mathbf{k}}+\delta\hat{\psi}_{-\mathbf{k}}\right) \qquad (5.56)
\end{aligned}$$

This gives the first order functional derivative of H_{var} w.r.t $\hat{\psi}$:

$$\frac{\delta H_{var}}{\delta\hat{\psi}} = \frac{V}{(2\pi)^3\nu}\left\{\hat{\phi}_{\mathbf{k}} - \frac{\nu}{4\pi\ell_B}\left[\left(1+\frac{A}{B}\right)k^2 - \frac{A}{B^2} + \frac{A}{B^2(1+Bk^2)}\right]\hat{\psi}_{\mathbf{k}}\right\} \qquad (5.57)$$

Finally, setting the first functional derivative to 0, we have:

$$\frac{\delta H_{var}}{\delta\hat{\psi}} = \hat{\phi}_{\mathbf{k}} - \frac{\nu}{4\pi\ell_B}\left[\left(1+\frac{A}{B}\right)k^2 - \frac{A}{B^2} + \frac{A}{B^2(1+Bk^2)}\right]\hat{\psi}_{\mathbf{k}} = 0 \qquad (5.58)$$

$$\hat{\phi}_{\mathbf{k}} = \frac{\nu}{4\pi\ell_B}\left[\left(1+\frac{A}{B}\right)k^2 - \frac{A}{B^2} + \frac{A}{B^2(1+Bk^2)}\right]\hat{\psi}_{\mathbf{k}} \qquad (5.59)$$

Multiplying both sides by $\exp(i\mathbf{k}\cdot\mathbf{r})$ and integrating over $\mathbf{k}$ gives:

$$\int d\mathbf{k}\hat{\phi}_{\mathbf{k}}e^{i\mathbf{k}\cdot\mathbf{r}} = \int d\mathbf{k}\frac{\nu}{4\pi\ell_B}\left[\left(1+\frac{A}{B}\right)k^2 - \frac{A}{B^2} + \frac{A}{B^2(1+Bk^2)}\right]\hat{\psi}_{\mathbf{k}}e^{i\mathbf{k}\cdot\mathbf{r}} \tag{5.60}$$

$$\frac{4\pi\ell_B}{\nu}(2\pi)^3\phi(\mathbf{r}) = \left(1+\frac{A}{B}\right)\int d\mathbf{k}k^2\hat{\psi}_{\mathbf{k}}e^{i\mathbf{k}\cdot\mathbf{r}} - \frac{A}{B^2}\int d\mathbf{k}\hat{\psi}_{\mathbf{k}}e^{i\mathbf{k}\cdot\mathbf{r}} + \frac{A}{B^2}\int d\mathbf{k}\frac{1}{1+Bk^2}\hat{\psi}_{\mathbf{k}}e^{i\mathbf{k}\cdot\mathbf{r}} \tag{5.61}$$

The first term on the right hand side of (5.60) simply gives the Laplacian of ψ.

$$\begin{aligned}\left(1+\frac{A}{B}\right)\int d\mathbf{k}k^2\hat{\psi}_{\mathbf{k}}e^{i\mathbf{k}\cdot\mathbf{r}} &= -\left(1+\frac{A}{B}\right)\int d\mathbf{k}\hat{\psi}_{\mathbf{k}}\nabla_{\mathbf{r}}\cdot\nabla_{\mathbf{r}}\left[e^{i\mathbf{k}\cdot\mathbf{r}}\right] \\ &= -\left(1+\frac{A}{B}\right)\nabla_{\mathbf{r}}\cdot\nabla_{\mathbf{r}}\left[\int d\mathbf{k}\hat{\psi}_{\mathbf{k}}e^{i\mathbf{k}\cdot\mathbf{r}}\right] \\ &= -(2\pi)^3\left(1+\frac{A}{B}\right)\nabla^2\psi(\mathbf{r})\end{aligned} \tag{5.62}$$

The second term is just the inverse inverse Fourier transform of $\hat{\psi}$

$$-\frac{A}{B^2}\int d\mathbf{k}\hat{\psi}_{\mathbf{k}}e^{i\mathbf{k}\cdot\mathbf{r}} = -(2\pi)^3\frac{A}{B^2}\psi(\mathbf{r}) \tag{5.63}$$

For the last term we need to invoke the definition of the Fourier transform in place of $\hat{\psi}_{\mathbf{k}}$ and compute the $\mathbf{k}$ integral in 3-dimensions using spherical coordinates.

$$\begin{aligned}&\frac{A}{B^2}\int d\mathbf{k}\frac{1}{1+Bk^2}\hat{\psi}_{\mathbf{k}}e^{i\mathbf{k}\cdot\mathbf{r}} = \frac{A}{B^2}\int d\mathbf{k}\frac{1}{1+Bk^2}\int d\mathbf{r'}\psi(\mathbf{r'})e^{-i\mathbf{k}\cdot\mathbf{r'}}e^{i\mathbf{k}\cdot\mathbf{r}} \\ &= \frac{A}{B^2}\int d\mathbf{r'}\psi(\mathbf{r'})\int d\mathbf{k}\frac{1}{1+Bk^2}e^{i\mathbf{k}\cdot(\mathbf{r}-\mathbf{r'})} \\ &= \frac{A}{B^2}\int d\mathbf{r'}\psi(\mathbf{r'})\int_0^{2\pi}d\varphi\int_0^{\pi}\int_0^{\infty}\frac{1}{1+Bk^2}e^{ik|\mathbf{r}-\mathbf{r'}|\cos\theta}\sin\theta d\theta k^2dk \\ &= 2\pi\frac{A}{B^2}\int d\mathbf{r'}\psi(\mathbf{r'})\int_{-1}^{1}\int_0^{\infty}\frac{k^2}{1+Bk^2}e^{ik|\mathbf{r}-\mathbf{r'}|t}dtdk \\ &= 4\pi\frac{A}{B^2}\int d\mathbf{r'}\psi(\mathbf{r'})\int_0^{\infty}\frac{k}{1+Bk^2}\frac{\sin(k|\mathbf{r}-\mathbf{r'}|)}{|\mathbf{r}-\mathbf{r'}|}dk \\ &= 2\pi^2\frac{A}{B^3}\int d\mathbf{r'}\psi(\mathbf{r'})\frac{e^{-|\mathbf{r}-\mathbf{r'}|/\sqrt{B}}}{|\mathbf{r}-\mathbf{r'}|}\end{aligned} \tag{5.64}$$

Therefore, the complete integro-differential equation is:

$$\frac{4\pi\ell_B}{\nu}(2\pi)^3\phi(\mathbf{r}) = -(2\pi)^3\left(1+\frac{A}{B}\right)\nabla^2\psi(\mathbf{r}) - (2\pi)^3\frac{A}{B^2}\psi(\mathbf{r}) + 2\pi^2\frac{A}{B^3}\int d\mathbf{r'}\psi(\mathbf{r'})\frac{e^{-|\mathbf{r}-\mathbf{r'}|/\sqrt{B}}}{|\mathbf{r}-\mathbf{r'}|} \quad (5.65)$$

Cancelling multiplicative factors and combining some terms gives:

$$\begin{aligned}\frac{4\pi\ell_B}{\nu}\phi(\mathbf{r}) &= -\left(1+\frac{A}{B}\right)\nabla^2\psi(\mathbf{r}) - \frac{A}{B^2}\psi(\mathbf{r}) + \frac{1}{4\pi}\frac{A}{B^3}\int d\mathbf{r'}\psi(\mathbf{r'})\frac{e^{-|\mathbf{r}-\mathbf{r'}|/\sqrt{B}}}{|\mathbf{r}-\mathbf{r'}|} \\ &= -\left(1+\frac{A}{B}\right)\nabla^2\psi(\mathbf{r}) - \frac{A}{B^2}\left[\psi(\mathbf{r}) - \frac{1}{2\pi}\int d\mathbf{r'}\psi(\mathbf{r'})\frac{e^{-|\mathbf{r}-\mathbf{r'}|/\sqrt{B}}}{2B|\mathbf{r}-\mathbf{r'}|}\right]\end{aligned} \quad (5.66)$$

Finally, replacing A and B with their definitions in (5.52) we get the final integro-differential equation.

$$\frac{4\pi\ell_B}{\nu}\phi(\mathbf{r}) = -\frac{1}{1-\alpha}\nabla^2\psi(\mathbf{r}) - \frac{\alpha}{(1-\alpha)^2\ell_c^2}\left[\psi(\mathbf{r}) - \frac{1}{2\pi}\int d\mathbf{r'}\psi(\mathbf{r'})\frac{\exp\left(\frac{-|\mathbf{r}-\mathbf{r'}|}{\ell_c\sqrt{1-\alpha}}\right)}{2(1-\alpha)\ell_c^2|\mathbf{r}-\mathbf{r'}|}\right] \quad (5.67)$$

References

(1) Varner, S.; Wang, Z.-G. Effects of dilution in ionic liquid supercapacitors. *Physical Chemistry Chemical Physics* **2022**, *24*, 27362–27374, DOI: 10.1039/D2CP03398D.

(2) Varner, S.; Balzer, C.; Wang, Z.-G. A Jacobian-free pseudo-arclength continuation method for phase transitions in inhomogeneous thermodynamic systems. *The Journal of Chemical Physics* **2024**, *161*, 064107, DOI: 10.1063/5.0220849.

(3) Zhong, C.; Deng, Y.; Hu, W., et al. A review of electrolyte materials and compositions for electrochemical supercapacitors. *Chemical Society Reviews* **2015**, *44*, 7484–7539, DOI: 10.1039/C5CS00303B.

(4) Pell, W. G.; Conway, B. E. Quantitative modeling of factors determining Ragone plots for batteries and electrochemical capacitors. *Journal of Power Sources* **1996**, *63*, 255–266, DOI: 10.1016/S0378-7753(96)02525-6.

(5) Muzaffar, A.; Ahamed, M. B.; Deshmukh, K.; Thirumalai, J. A review on recent advances in hybrid supercapacitors: Design, fabrication and applications. *Renewable and Sustainable Energy Reviews* **2019**, *101*, 123–145, DOI: 10.1016/j.rser.2018.10.026.

(6) Sharma, P.; Bhatti, T. S. A review on electrochemical double-layer capacitors. *Energy Conversion and Management* **2010**, *51*, 2901–2912, DOI: 10.1016/j.enconman.2010.06.031.

(7) Yan, J.; Wang, Q.; Wei, T.; Fan, Z. Recent Advances in Design and Fabrication of Electrochemical Supercapacitors with High Energy Densities. *Advanced Energy Materials* **2014**, *4*, 1300816, DOI: https://doi.org/10.1002/aenm.201300816.

(8) Mousavi, M. P. S.; Wilson, B. E.; Kashefolgheta, S., et al. Ionic Liquids as Electrolytes for Electrochemical Double-Layer Capacitors: Structures that Optimize Specific Energy. *ACS Applied Materials & Interfaces* **2016**, *8*, 3396–3406, DOI: 10.1021/acsami.5b11353.

(9) Sato, T.; Masuda, G.; Takagi, K. Electrochemical properties of novel ionic liquids for electric double layer capacitor applications. *Electrochimica Acta* **2004**, *49*, 3603–3611, DOI: 10.1016/j.electacta.2004.03.030.

(10) Béguin, F.; Presser, V.; Balducci, A.; Frackowiak, E. Carbons and Electrolytes for Advanced Supercapacitors. *Advanced Materials* **2014**, *26*, 2219–2251, DOI: 10.1002/adma.201304137.

(11) Balducci, A. Electrolytes for high voltage electrochemical double layer capacitors: A perspective article. *Journal of Power Sources* **2016**, *326*, 534–540, DOI: 10.1016/j.jpowsour.2016.05.029.

(12) Simon, P.; Gogotsi, Y. Capacitive Energy Storage in Nanostructured Carbon–Electrolyte Systems. *Accounts of Chemical Research* **2013**, *46*, 1094–1103, DOI: 10.1021/ar200306b.

(13) Van Aken, K. L.; Beidaghi, M.; Gogotsi, Y. Formulation of Ionic-Liquid Electrolyte To Expand the Voltage Window of Supercapacitors. *Angewandte Chemie International Edition* **2015**, *54*, 4806–4809, DOI: 10.1002/anie.201412257.

(14) Armand, M.; Endres, F.; MacFarlane, D. R.; Ohno, H.; Scrosati, B. Ionic-liquid materials for the electrochemical challenges of the future. *Nature Materials* **2009**, *8*, 621–629, DOI: 10.1038/nmat2448.

(15) Frackowiak, E.; Lota, G.; Pernak, J. Room-temperature phosphonium ionic liquids for supercapacitor application. *Applied Physics Letters* **2005**, *86*, 164104, DOI: 10.1063/1.1906320.

(16) Kornyshev, A. A. Double-Layer in Ionic Liquids: Paradigm Change? *The Journal of Physical Chemistry B* **2007**, *111*, 5545–5557, DOI: 10.1021/jp067857o.

(17) Bazant, M. Z.; Storey, B. D.; Kornyshev, A. A. Double Layer in Ionic Liquids: Overscreening versus Crowding. *Physical Review Letters* **2011**, *106*, 046102, DOI: 10.1103/PhysRevLett.106.046102.

(18) Reichert, P.; Kjær, K. S.; Driel, T. B. v., et al. Molecular scale structure and dynamics at an ionic liquid/electrode interface. *Faraday Discussions* **2017**, *206*, 141–157, DOI: 10.1039/C7FD00171A.

(19) Lynden-Bell, R. M.; Frolov, A. I.; Fedorov, M. V. Electrode screening by ionic liquids. *Physical Chemistry Chemical Physics* **2012**, *14*, 2693, DOI: 10.1039/c2cp23267g.

(20) Levin, Y. Electrostatic correlations: from plasma to biology. *Reports on Progress in Physics* **2002**, *65*, 1577–1632, DOI: 10.1088/0034-4885/65/11/201.

(21) Santangelo, C. D. Computing counterion densities at intermediate coupling. *Physical Review E* **2006**, *73*, 041512, DOI: 10.1103/PhysRevE.73.041512.

(22) Lee, A. A.; Kondrat, S.; Vella, D.; Goriely, A. Dynamics of Ion Transport in Ionic Liquids. *Physical Review Letters* **2015**, *115*, 106101, DOI: 10.1103/PhysRevLett.115.106101.

(23) Chao, H.; Wang, Z.-G. Effects of Surface Transition and Adsorption on Ionic Liquid Capacitors. *The Journal of Physical Chemistry Letters* **2020**, *11*, 1767–1772, DOI: 10.1021/acs.jpclett.0c00023.

(24) Bossa, G. V.; May, S. Stability of ionic liquid modeled by composite Coulomb-Yukawa potentials. *Physical Review Research* **2020**, *2*, 032040, DOI: 10.1103/PhysRevResearch.2.032040.

(25) Lian, Z.; Chao, H.; Wang, Z.-G. Effects of Confinement and Ion Adsorption in Ionic Liquid Supercapacitors with Nanoporous Electrodes. *ACS Nano* **2021**, 11724-11733, DOI: 10.1021/acsnano.1c02506.

(26) Caetano, D. L. Z.; Bossa, G. V.; de Oliveira, V. M., et al. Role of ion hydration for the differential capacitance of an electric double layer. *Physical Chemistry Chemical Physics* **2016**, *18*, 27796–27807, DOI: 10.1039/C6CP04199J.

(27) Zhou, W.; Inoue, S.; Iwahashi, T., et al. Double layer structure and adsorption/desorption hysteresis of neat ionic liquid on Pt electrode surface — an in-situ IR-visible sum-frequency generation spectroscopic study. *Electrochemistry Communications* **2010**, *12*, 672–675, DOI: 10.1016/j.elecom.2010.03.003.

(28) Drüschler, M.; Huber, B.; Passerini, S.; Roling, B. Hysteresis Effects in the Potential-Dependent Double Layer Capacitance of Room Temperature Ionic Liquids at a Polycrystalline Platinum Interface. *The Journal of Physical Chemistry C* **2010**, *114*, 3614–3617, DOI: 10.1021/jp911513k.

(29) Limmer, D. T. Interfacial Ordering and Accompanying Divergent Capacitance at Ionic Liquid-Metal Interfaces. *Physical Review Letters* **2015**, *115*, 256102, DOI: 10.1103/PhysRevLett.115.256102.

(30) Ye, B. B.; Wang, Z.-G. A coarse-grained model of room-temperature ionic liquids between metal electrodes: a molecular dynamics study. *Physical Chemistry Chemical Physics* **2022**, *24*, 11573–11584, DOI: 10.1039/D2CP00166G.

(31) Bozym, D. J.; Uralcan, B.; Limmer, D. T., et al. Anomalous Capacitance Maximum of the Glassy Carbon–Ionic Liquid Interface through Dilution with Organic Solvents. *The Journal of Physical Chemistry Letters* **2015**, *6*, 2644–2648, DOI: 10.1021/acs.jpclett.5b00899.

(32) Kühnel, R.-S.; Böckenfeld, N.; Passerini, S.; Winter, M.; Balducci, A. Mixtures of ionic liquid and organic carbonate as electrolyte with improved safety and performance for rechargeable lithium batteries. *Electrochimica Acta* **2011**, *56*, 4092–4099, DOI: 10.1016/j.electacta.2011.01.116.

(33) Ruiz, V.; Blanco, C.; Raymundo-Piñero, E., et al. Effects of thermal treatment of activated carbon on the electrochemical behaviour in supercapacitors. *Electrochimica Acta* **2007**, *52*, 4969–4973, DOI: 10.1016/j.electacta.2007.01.071.

(34) Lewandowski, A.; Olejniczak, A.; Galinski, M.; Stepniak, I. Performance of carbon–carbon supercapacitors based on organic, aqueous and ionic liquid electrolytes. *Journal of Power Sources* **2010**, *195*, 5814–5819, DOI: 10.1016/j.jpowsour.2010.03.082.

(35) Helmholtz, H. Ueber einige Gesetze der Vertheilung elektrischer Ströme in körperlichen Leitern mit Anwendung auf die thierisch-elektrischen Versuche. *Annalen der Physik und Chemie* **1853**, *165*, 211–233, DOI: 10.1002/andp.18531650603.

(36) Gouy, M. Sur la constitution de la charge électrique à la surface d'un électrolyte. *Journal de Physique Théorique et Appliquée* **1910**, *9*, 457–468, DOI: 10.1051/jphystap:019100090045700.

(37) Di Caprio, D.; Borkowska, Z.; Stafiej, J. Simple extension of the Gouy–Chapman theory including hard sphere effects.: Diffuse layer contribution to the differential capacity curves for the electrode|electrolyte interface. *Journal of Electroanalytical Chemistry* **2003**, *540*, 17–23, DOI: 10.1016/S0022-0728(02)01270-6.

(38) Di Caprio, D.; Borkowska, Z.; Stafiej, J. Specific ionic interactions within a simple extension of the Gouy–Chapman theory including hard sphere effects. *Journal of Electroanalytical Chemistry* **2004**, *572*, 51–59, DOI: 10.1016/j.jelechem.2004.06.001.

(39) Borukhov, I.; Andelman, D.; Orland, H. Steric Effects in Electrolytes: A Modified Poisson-Boltzmann Equation. *Physical Review Letters* **1997**, *79*, 435–438, DOI: 10.1103/PhysRevLett.79.435.

(40) Netz, R.; Orland, H. Beyond Poisson-Boltzmann: Fluctuation effects and correlation functions. *The European Physical Journal E* **2000**, *1*, 203, DOI: 10.1007/s101890050023.

(41) Levin, D. B.; Chahine, R. Challenges for renewable hydrogen production from biomass. *International Journal of Hydrogen Energy* **2010**, *35*, 4962–4969, DOI: 10.1016/j.ijhydene.2009.08.067.

(42) Skinner, B.; Loth, M. S.; Shklovskii, B. I. Capacitance of the Double Layer Formed at the Metal/Ionic-Conductor Interface: How Large Can It Be? *Physical Review Letters* **2010**, *104*, 128302, DOI: 10.1103/PhysRevLett.104.128302.

(43) Fredrickson, G. H., *The equilibrium theory of inhomogeneous polymers*; International series of monographs on physics 134; Clarendon Press ; Oxford University Press: Oxford : New York, 2006; 437 pp.

(44) Wang, Z.-G. Variational electrostatics for charge solvation. *Journal of Theoretical and Computational Chemistry* **2008**, *07*, 397–419, DOI: 10.1142/S0219633608003824.

(45) Wang, Z.-G. In *Variational Methods in Molecular Modeling*, Wu, J., Ed.; Molecular Modeling and Simulation; Springer: Singapore, 2017, pp 1–29.

(46) Stern, O. Zur Theorie Der Elektrolytischen Doppelschicht. *Zeitschrift für Elektrochemie und angewandte physikalische Chemie* **1924**, *30*, 508–516, DOI: 10.1002/bbpc.192400182.

(47) Mezger, M.; Schröder, H.; Reichert, H., et al. Molecular Layering of Fluorinated Ionic Liquids at a Charged Sapphire (0001) Surface. *Science* **2008**, *322*, 424–428, DOI: 10.1126/science.1164502.

(48) De Souza, J. P.; Bazant, M. Z. Continuum Theory of Electrostatic Correlations at Charged Surfaces. *The Journal of Physical Chemistry C* **2020**, *124*, 11414–11421, DOI: 10.1021/acs.jpcc.0c01261.

(49) Largeot, C.; Portet, C.; Chmiola, J., et al. Relation between the Ion Size and Pore Size for an Electric Double-Layer Capacitor. *Journal of the American Chemical Society* **2008**, *130*, 2730–2731, DOI: 10.1021/ja7106178.

(50) Bikerman, J. XXXIX. Structure and capacity of electrical double layer. *The London, Edinburgh, and Dublin Philosophical Magazine and Journal of Science* **1942**, *33*, 384–397, DOI: 10.1080/14786444208520813.

(51) Han, Y.; Huang, S.; Yan, T. A mean-field theory on the differential capacitance of asymmetric ionic liquid electrolytes. *Journal of Physics: Condensed Matter* **2014**, *26*, 284103, DOI: 10.1088/0953-8984/26/28/284103.

(52) Goodwin, Z. A. H.; Feng, G.; Kornyshev, A. A. Mean-Field Theory of Electrical Double Layer In Ionic Liquids with Account of Short-Range Correlations. *Electrochimica Acta* **2017**, *225*, 190–197, DOI: 10.1016/j.electacta.2016.12.092.

(53) Wakai, C.; Oleinikova, A.; Ott, M.; Weingärtner, H. How Polar Are Ionic Liquids? Determination of the Static Dielectric Constant of an Imidazolium-based Ionic Liquid by Microwave Dielectric Spectroscopy. *The Journal of Physical Chemistry B* **2005**, *109*, 17028–17030, DOI: 10.1021/jp053946+.

(54) Torrie, G. M.; Valleau, J. P. Electrical double layers. I. Monte Carlo study of a uniformly charged surface. *The Journal of Chemical Physics* **1980**, *73*, 5807–5816, DOI: 10.1063/1.440065.

(55) Brazovski?, S. A. In *30 Years of the Landau Institute ? Selected Papers*; World Scientific Series in 20th Century Physics Volume 11, Vol. Volume 11; WORLD SCIENTIFIC: 1996, pp 109–113.

(56) Blume, M. Theory of the First-Order Magnetic Phase Change in U O 2. *Physical Review* **1966**, *141*, 517–524, DOI: 10.1103/PhysRev.141.517.

(57) Capel, H. W. On the possibility of first-order phase transitions in Ising systems of triplet ions with zero-field splitting. *Physica* **1966**, *32*, 966–988, DOI: 10.1016/0031-8914(66)90027-9.

(58) Blume, M.; Emery, V. J.; Griffiths, R. B. Ising Model for the l Transition and Phase Separation in He 3 - He 4 Mixtures. *Physical Review A* **1971**, *4*, 1071–1077, DOI: 10.1103/PhysRevA.4.1071.

(59) Blum, L. Mean spherical model for asymmetric electrolytes. *Molecular Physics* **1975**, *30*, 1529–1535, DOI: 10.1080/00268977500103051.

(60) Dudka, M.; Kondrat, S.; Kornyshev, A.; Oshanin, G. Phase behaviour and structure of a superionic liquid in nonpolarized nanoconfinement. *Journal of Physics: Condensed Matter* **2016**, *28*, 464007, DOI: 10.1088/0953-8984/28/46/464007.

(61) Groda, Y.; Dudka, M.; Kornyshev, A. A.; Oshanin, G.; Kondrat, S. Superionic Liquids in Conducting Nanoslits: Insights from Theory and Simulations. *The Journal of Physical Chemistry C* **2021**, *125*, 4968–4976, DOI: 10.1021/acs.jpcc.0c10836.

(62) May, S. Differential capacitance of the electric double layer: mean-field modeling approaches. *Current Opinion in Electrochemistry* **2019**, *13*, 125–131, DOI: 10.1016/j.coelec.2018.12.002.

(63) Cruz, C.; Ciach, A.; Lomba, E.; Kondrat, S. Electrical Double Layers Close to Ionic Liquid–Solvent Demixing. *The Journal of Physical Chemistry C* **2019**, *123*, 1596–1601, DOI: 10.1021/acs.jpcc.8b09772.

(64) Lee, A. A.; Kondrat, S.; Kornyshev, A. A. Single-File Charge Storage in Conducting Nanopores. *Physical Review Letters* **2014**, *113*, 048701, DOI: 10.1103/PhysRevLett.113.048701.

(65) Kondrat, S.; Kornyshev, A. A. Pressing a spring: what does it take to maximize the energy storage in nanoporous supercapacitors? *Nanoscale Horizons* **2015**, *1*, 45–52, DOI: 10.1039/C5NH00004A.

(66) Lee, A. A.; Vella, D.; Goriely, A.; Kondrat, S. Capacitance-Power-Hysteresis Trilemma in Nanoporous Supercapacitors. *Physical Review X* **2016**, *6*, 021034, DOI: 10.1103/PhysRevX.6.021034.

(67) Lian, C.; Liu, H.; Henderson, D.; Wu, J. Can ionophobic nanopores enhance the energy storage capacity of electric-double-layer capacitors containing nonaqueous electrolytes? *Journal of Physics: Condensed Matter* **2016**, *28*, 414005, DOI: 10.1088/0953-8984/28/41/414005.

(68) Lamperski, S.; Sosnowska, J.; Bhuiyan, L. B.; Henderson, D. Size asymmetric hard spheres as a convenient model for the capacitance of the electrical double layer of an ionic liquid. *The Journal of Chemical Physics* **2014**, *140*, 014704, DOI: 10.1063/1.4851456.

(69) De Souza, J. P.; Pivnic, K.; Bazant, M. Z.; Urbakh, M.; Kornyshev, A. A. Structural Forces in Ionic Liquids: The Role of Ionic Size Asymmetry. *The Journal of Physical Chemistry B* **2022**, *126*, 1242–1253, DOI: 10.1021/acs.jpcb.1c09441.

(70) Feng, G.; Jiang, D.-e.; Cummings, P. T. Curvature Effect on the Capacitance of Electric Double Layers at Ionic Liquid/Onion-Like Carbon Interfaces. *Journal of Chemical Theory and Computation* **2012**, *8*, 1058–1063, DOI: 10.1021/ct200914j.

(71) Caetano, D. L. Z.; de Carvalho, S. J.; Bossa, G. V.; May, S. Monte Carlo simulations and mean-field modeling of electric double layers at weakly and moderately charged spherical macroions. *Physical Review E* **2021**, *104*, 034609, DOI: 10.1103/PhysRevE.104.034609.

(72) Liu, Y.; Lu, C.; Twigg, S., et al. Direct Observation of Ion Distributions near Electrodes in Ionic Polymer Actuators Containing Ionic Liquids. *Scientific Reports* **2013**, *3*, 973, DOI: 10.1038/srep00973.

Chapter 6

ENTROPIC ORIGIN OF IONIC INTERACTIONS IN POLAR SOLVENTS

Implicit solvent models that reduce solvent degrees of freedom into effective interaction potentials are widely used in the study of soft materials and biophysical systems. For electrolyte and polyelectrolyte solutions, coarse-graining the solvent degrees of freedom into an effective dielectric constant embeds entropic contributions into the temperature dependence of the dielectric constant. Properly accounting for this *electrostatic entropy* is essential to discern whether a free energy change is enthalpically or entropically driven. We address the entropic origin of electrostatic interactions in dipolar solvent and provide a clarified physical picture of the solvent dielectric response. We calculate the potential of mean force (PMF) between two oppositely charged ions in a dipolar solvent using molecular dynamics and dipolar self-consistent field theory. We find with both techniques that the PMF is dominated by the entropy gain from the dipole release, owing to the diminished orientational polarization of the solvent. We also find that the relative contribution of the entropy to the free energy change is nonmonotonic with temperature. We expect that our conclusions are applicable to a broad range of problems involving ionic interactions in polar solvents.

This chapter includes content from our previously published article:

Varner, S.; Balzer, C.; Wang, Z.-G. Entropic Origin of Ionic Interactions in Polar Solvents. *The Journal of Physical Chemistry B* **2023**, *127*, 4328–4337, DOI: 10.1021/acs.jpcb.3c00588

I am very thankful for helpful discussions with Prof. Bilin Zhuang on the use of dipolar self-consistent field theory. These discussions were invaluable to the progress of this work. I would also like to thank Prof. Shensheng Chen who pioneered the initial work on the electrostatic entropy in polyelectrolyte complex coacervation.

6.1 Introduction

A wide variety of simulation and theoretical approaches utilize implicit solvent models, where the solvent degrees of freedom are lumped into effective interactions

[2, 3]. Treating the solvent as a background medium can significantly reduce the computational cost[4–6]. In doing so, however, the solvent degrees of freedom become hidden in effective interaction potentials, which are often specified in an approximate manner. Common methods in biological simulations include the accessible surface area (ASA) method and continuum electrostatic methods such as the generalized Born model [7–14].

Dielectric materials with polar molecules respond to an electric field through reorientation of the dipoles[15]. Generally, the presence of an electric field will cause the dipoles to align and increase the order in the system. The free energy change during dipole reorganization is thus composed of both energetic and entropic contributions [16]. The energy comes from the electrostatic interactions of the dipoles with the electric field and with each other, while the entropy arises from the changes in the orientation of the dipoles. For a uniform dielectric material, the *electrostatic entropy* contribution is encapsulated in the temperature dependence of the dielectric constant [17].

$$\Delta S_{\mathrm{el}} = -\frac{\partial \Delta F}{\partial T} = -\frac{\partial}{\partial T}\left(\frac{1}{2}\varepsilon V E^2\right) = -\frac{1}{2}VE^2\frac{\partial \varepsilon}{\partial T} \tag{6.1}$$

where T is the temperature, ΔS_{el} is the electrostatic entropy change due to the application of an electric field, ΔF is the Helmholtz free energy change, ε is the dielectric constant, V is the system volume, and E is the electric field. Capturing the entropic contribution relies on knowing the temperature dependence of the dielectric constant.

In solutions containing ions and charged macromolecules, the presence of charged species generates the electric field that polarizes the solvent[17]. Recently, this phenomenon has been used to explain the apparent discrepancy between experiments[18–21] and coarse-grained molecular dynamics simulations[22–25] in describing the driving force for polyelectrolyte complex coacervation. Chen and Wang showed that the Coulomb potential used in coarse-grained implicit solvent models inherently includes an entropic contribution, which they term the *electrostatic entropy*[26]. By correctly accounting for this electrostatic entropy contribution through the temperature dependence of the dielectric constant, they were able to predict entropy driven coacervation from implicit solvent molecular dynamics, in agreement with experimental observations. Further, they rationalized this entropic driving force as arising from the solvent reorganization using the example of two oppositely charged ions forming an ion pair. The entropic contributions to the potential of mean

force have also been addressed in other studies which used molecular dynamics [27] and the extended reference interaction site model (RISM) [28]. However, these studies were restricted to water which has specific properties and interactions with different types of ions.

The effective interaction potential, or potential of mean force (PMF), between ions in solution is a result of the combined effects of direct ion–ion interactions and interactions of ions with the solvent. At the most basic level, one can assume the solvent has a uniform temperature-dependent dielectric constant. In the Debye approximation [29], for the process of bringing two ions from infinity to a distance r, we have

$$\Delta F = \frac{q_i q_j}{4\pi\varepsilon_0(1+\xi)r} \tag{6.2}$$

$$T\Delta S = -T\frac{\partial \Delta F}{\partial T} = -\frac{q_i q_j}{4\pi\varepsilon_0 r}\frac{\xi}{(1+\xi)^2} \tag{6.3}$$

$$\Delta U = \Delta F + T\Delta S = \frac{q_i q_j}{4\pi\varepsilon_0 r}\frac{1}{(1+\xi)^2} \tag{6.4}$$

where q_i and q_j are the charges on the ions, U is the internal energy, $\xi \equiv \frac{\beta\bar{\mu}^2}{3v\varepsilon_0}$ is a dimensionless measure of the dipole strength, $\bar{\mu}$ is the dipole moment, $\beta = 1/k_B T$, and v is the molecular volume of the solvent. Thus, the electrostatic entropy will dominate the PMF when $\xi > 1$. A similar result can be obtained using a more complete dielectric theory, such as Onsager's theory [30, 31]. While this is a satisfying result, it is phenomenological and does not provide a clear molecular picture, since the solvent degrees of freedom are not explicitly included.

In this study, we address the concept of electrostatic entropy and demonstrate its generality by studying two ions in a dipolar fluid. Using dipolar self-consistent field theory (DSCFT) and molecular dynamics simulations, we analyze the PMF between two oppositely-charged, monovalent ions immersed in a dipolar solvent, explicitly accounting for the solvent degrees of freedom. We separate the PMF into its entropic and energetic contributions to determine the conditions where the electrostatic entropy dominates. Finally, we connect the entropic driving force to the release of dipoles as the ions approach one another, quantified through the decrease in the solvent polarization. While solvent reorganization has long been recognized as a source of entropy in physical processes, especially in the context of binding of small molecules to proteins and multivalent ions to charged macromolecules in water[32–34], the phenomenon is often presented as solvent- or system-specific,

where other effects such as hydrogen bonding may dominate. Our results highlight the generality of the electrostatic entropy and the importance of properly accounting for the solvent degrees of freedom in studying charge-containing systems.

6.2 Enhanced Sampling Molecular Dynamics

To model two ions in a dipolar fluid, we use a Stockmayer fluid model based on work by Shock et al. [35]. The solvent particles possess permanent point dipoles $\boldsymbol{\mu}$ at their center of mass while the ions are described as point charges with no dipole. The nonelectrostatic nonbonded potential energy for all bead types is described by a truncated and shifted Lennard-Jones (LJ) potential [36],

$$U_{ij}^{LJ}(r) = \begin{cases} 4\epsilon_{ij}\left[\left(\frac{\sigma_{ij}}{r}\right)^{12} - \left(\frac{\sigma_{ij}}{r}\right)^{6} + \frac{1}{4}\right] & r \leq 2^{1/6}\sigma_{ij} \\ 0 & r > 2^{1/6}\sigma_{ij} \end{cases} \tag{6.5}$$

where $\epsilon_{ij} = \sqrt{\epsilon_i \epsilon_j}$, $\sigma_{ij} = \sqrt{\sigma_i \sigma_j}$ for all pairs, and r is the distance between beads i and j. With a cutoff of $2^{1/6}\sigma_{ij}$, the LJ potential is purely repulsive and ϵ_{ij} is relatively unimportant. For all of our systems, we set $\epsilon_i = \epsilon_j = 1$. An example of the system setup is given in Figure 6.1.

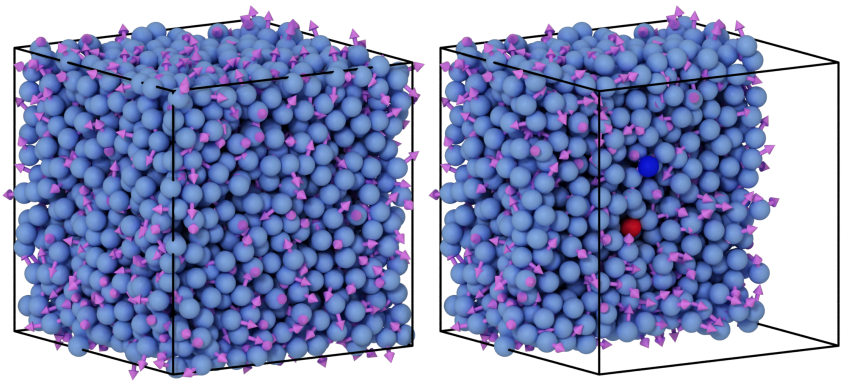

Figure 6.1: Example simulation configuration of two ions (blue/red) in a Stockmayer fluid (light blue). Solvent dipoles are depicted as pink arrows.

The electrostatic interactions are composed of charge–charge, charge–dipole, and dipole–dipole interactions. The standard Coulomb potential describes the charge–charge interactions between the two ions,

$$U_{ij}^{qq}(r) = \frac{1}{4\pi\varepsilon_0}\frac{q_i q_j}{r} \tag{6.6}$$

where ε_0 is vacuum permittivity and q is the charge on each ion. The charge–dipole and dipole–dipole interactions are, respectfully, given as

$$U^{q\mu}(\mathbf{r}) = \frac{1}{4\pi\varepsilon_0}\frac{q(\mathbf{r}_{q\mu}\cdot\boldsymbol{\mu})}{|\mathbf{r}_{q\mu}|^3} \tag{6.7}$$

where $|\mathbf{r}_{q\mu}|$ is the center of mass distance between the charge and the solvent dipole, and

$$U_{ij}^{\mu\mu}(\mathbf{r}) = \frac{1}{4\pi\varepsilon_0}\frac{\boldsymbol{\mu}_i\cdot\boldsymbol{\mu}_j}{|\mathbf{r}_{\mu\mu}|^3} - \frac{3}{4\pi\varepsilon_0}\frac{(\boldsymbol{\mu}_i\cdot\mathbf{r}_{\mu\mu})(\boldsymbol{\mu}_j\cdot\mathbf{r}_{\mu\mu})}{|\mathbf{r}_{\mu\mu}|^5} \tag{6.8}$$

where $|\mathbf{r}_{\mu\mu}|$ is the center of mass distance between point dipoles $\boldsymbol{\mu}_i$ and $\boldsymbol{\mu}_j$. We reiterate that only the ions carry charge. All long-range electrostatic interactions are computed using a standard Ewald summation.

The solvent dipoles reorient due to the torque arising from charge–dipole or dipole–dipole interactions. We use a Langevin thermostat that takes into account the angular degrees of freedom of the solvent. The LJ size parameter σ_s is used to describe the spherical diameter required to update the angular velocity via the solvent bead's moment of inertia.

Throughout the work, we consider a coarse-grained model solvent based on water[35]. Namely, the number density is $\rho = 0.03344/\text{Å}^3$ at $T = 300\,\text{K}$ with diameter $\sigma_s = 3.0\,\text{Å}$ and mass $18.015\,\frac{\text{g}}{\text{mol}}$. Water has a gas-phase dipole moment of 1.85 D; however, we vary the magnitude of the dipole moment to highlight the role of the dipoles, ranging from $\bar{\mu} = 0\,\text{D}$ to 2 D. For simplicity, we treat the anion and cation as monovalent ions $\pm 1e$ with the same size parameter as the solvent, $\sigma_+ = \sigma_- = \sigma_s$. For all simulations, we use reduced units with the length scale $1\sigma = 3\,\text{Å}$, energy scale $1\epsilon = 2.49\frac{\text{kJ}}{\text{mol}}$, and mass scale $1m = 18.015\frac{\text{g}}{\text{mol}}$ that give a corresponding timescale $\tau = \sqrt{\frac{\epsilon}{m\sigma^2}}$.

The PMF between two ions is calculated using the adaptive biasing force (ABF) method [37, 38]. In the ABF method, the average force is computed as the system evolves and explores the collective variable (CV) space. After some amount of sampling in a particular region of the CV space, a biasing force is applied that counteracts the mean force. This biasing force allows the system to efficiently climb free energy barrier and explore high free energy configurations. The ion separation distance is divided into 8 windows in the range of 0.75σ to 8.5σ. In each window, the system was equilibrated for 5×10^6 timesteps ($\delta t = 0.005\tau$) and production of 10^7 timesteps. Each simulation consists of 5000 solvent particles, corresponding to a simulation box length of 17.69σ. We use the GPU [39, 40]

and Colvars [41] packages in LAMMPS [42] for simulations and OVITO [43] for visualizations. Example LAMMPS and Colvars scripts for calculating the PMF are available at `https://github.com/chrisbalzer/Stockmayer-Two-Ions`.

6.3 Ion-Dipole Field Theory

In recent years, several groups have developed statistical field theories that explicitly account for solvent polarization and the dielectric response [44–48]. Here, we adapt a dipolar self-consistent field theory that was previously developed and used to study ion solvation energy and electron transfer reorganization energy [49–51]. Alternatively, we could have used the Ornstein–Zernike integral equation theory with the hypernetted-chain (HNC) approximation, or the extended RISM equation which have both been used to study the potential of mean force between ions at infinite dilution [28, 52–55]. The purpose of the theoretical model is not to compare or validate the simulation, but rather to provide an alternative approach for studying the ionic interaction in dipolar fluids to emphasize the generality of the presented behavior. We believe any theory which can capture the solvent orientational polarization in the vicinity of ions can capture the presented results, which includes all of the mentioned theories. We consider two ions at fixed separation immersed in a dipolar solvent. The solvent dipole is composed of a permanent dipole $\boldsymbol{\mu}$ and an induced dipole $\boldsymbol{p}$. The induced dipole is related to the electronic degrees of freedom. This contribution is not essential for this work, but we include it for completeness as it does not add much complexity to the theory or calculations. The ions are modeled as Gaussian smeared charges inside a spherical solute cavity, where the solvent is excluded. The use of smeared charges is for convenience, to avoid the diverging self-energy. The cavities are modeled using a spherically symmetric cavity function [56–58]. The ions are treated as fixed external charges to the solvent in this field theory. The microscopic charge density in the system is given by the contributions from the two ions and the solvent dipoles.

$$\hat{\rho}(\mathbf{r}) = \hat{\rho}_c(\mathbf{r}) + \hat{\rho}_{\mathrm{or}}(\mathbf{r}) + \hat{\rho}_{\mathrm{el}}(\mathbf{r}) \tag{6.9}$$

Here, $\hat{\rho}_c(\mathbf{r}) = \hat{\rho}_1(\mathbf{r}) + \hat{\rho}_2(\mathbf{r})$ is the total charge density of the ions, modeled as Gaussian smeared charges,

$$\hat{\rho}_c(\mathbf{r}) = z_1 e \left(\frac{1}{2b_1^2}\right)^{\frac{3}{2}} \exp\left(-\frac{\pi|\mathbf{r}-\mathbf{R}_1|^2}{2b_1^2}\right) + z_2 e \left(\frac{1}{2b_2^2}\right)^{\frac{3}{2}} \exp\left(-\frac{\pi|\mathbf{r}-\mathbf{R}_2|^2}{2b_2^2}\right) \tag{6.10}$$

where z_i are the ion valencies, b_i are the radii of the charge spread, $\mathbf{R}_i$ are the ion positions, and e is the elementary charge. $\hat{\rho}_{\mathrm{or}}(\mathbf{r})$ and $\hat{\rho}_{\mathrm{el}}(\mathbf{r})$ are the charge densities

due to the permanent and induced dipoles of the solvent, respectively. The charge density due to the orientational and electronic contributions of the solvent can be expressed in terms of their dipole moments as

$$\hat{\rho}_{\mathrm{or}}(\mathbf{r}) = -\sum_{i=1}^{N} \boldsymbol{\mu}_i \cdot \nabla\delta(\mathbf{r} - \mathbf{r}_i) \tag{6.11}$$

$$\hat{\rho}_{\mathrm{el}}(\mathbf{r}) = -\sum_{i=1}^{N} \boldsymbol{p}_i \cdot \nabla\delta(\mathbf{r} - \mathbf{r}_i) \tag{6.12}$$

where N is the number of solvent molecules, $\boldsymbol{\mu}_i$ is the permanent dipole moment on molecule i, and $\boldsymbol{p}_i$ is the induced dipole moment on molecule i. In the energy, we only consider the Coulomb interactions between all charges, and a harmonic penalty associated with the induced dipoles

$$U(\mathbf{r}^N, \boldsymbol{\mu}^N, \boldsymbol{p}^N) = \frac{1}{2}\int d\mathbf{r} \int d\mathbf{r}' \, \frac{\hat{\rho}(\mathbf{r})\hat{\rho}(\mathbf{r}')}{4\pi\varepsilon_0|\mathbf{r} - \mathbf{r}'|} + \sum_{i=1}^{N} \frac{|\boldsymbol{p}_i|^2}{2\alpha} \tag{6.13}$$

where α is the polarizability. We work in the grand canonical ensemble with volume V, temperature T, and solvent chemical potential μ. We assume the system is incompressible. The grand canonical partition function is given by

$$\Xi = \sum_{N=0}^{\infty} \frac{e^{\beta\mu N}}{N!} \left(\prod_{i=1}^{N} \frac{1}{\eta} \int d\mathbf{r}_i \int d\boldsymbol{\mu}_i \int d\boldsymbol{p}_i \right) \delta[v\hat{n}(\mathbf{r}) + \varphi_0(\mathbf{r}) - 1] e^{-\beta U} \tag{6.14}$$

where $\hat{n}$ is the solvent density operator, φ_0 is the volume fraction occupied by the ions, and η is a factor similar to the cube of the thermal wavelength, which has no thermodynamic consequence. The solvent density operator is given by $\hat{n}(\mathbf{r}) = \sum_{i=1}^{N} \delta(\mathbf{r} - \mathbf{r}_i)$. The local volume fraction due to the two ions, is modeled by the superposition of two cavity functions,

$$\varphi_0(\mathbf{r}) = 1 + \frac{1}{2}\tanh\left[-\frac{|\mathbf{r} - \mathbf{R}_1| - m\frac{\sigma_1}{2}}{c} \right] + \frac{1}{2}\tanh\left[-\frac{|\mathbf{r} - \mathbf{R}_2| - m\frac{\sigma_2}{2}}{c} \right] \tag{6.15}$$

where σ_i are the diameters of the two ions, m is a positive parameter for shifting the boundary of the cavity, and c is a positive parameter for tuning the width of the interface between the ion and the solvent. In practice, any reasonable choice of m and c will yield the same qualitative results. We choose $c = 0.01$ for a rapid but continuous decay near the ion boundary, and we choose $m = 0.95$ such that the ion volume fraction practically decays to zero by σ_i.

We take advantage of the Fourier representation of a delta functional to introduce the incompressibility field w

$$\delta[v\hat{n}(\mathbf{r}) + \varphi_0(\mathbf{r}) - 1] = \int \mathcal{D}w \exp\left\{i \int d\mathbf{r}\, w\, [v\hat{n}(\mathbf{r}) + \varphi_0(\mathbf{r}) - 1]\right\} \tag{6.16}$$

To turn the partition function into a field theory, we introduce coarse-grained density fields ρ_{or} and ρ_{el} through the identities

$$\begin{aligned} 1 &= \int \mathcal{D}\rho_{\text{or}} \delta[\rho_{\text{or}}(\mathbf{r}) - \hat{\rho}_{\text{or}}(\mathbf{r})] \\ &= \int \mathcal{D}\rho_{\text{or}} \int \mathcal{D}w_{\text{or}} \exp\left\{i \int d\mathbf{r}\, w_{\text{or}}\, [\rho_{\text{or}}(\mathbf{r}) - \hat{\rho}_{\text{or}}(\mathbf{r})]\right\} \end{aligned} \tag{6.17}$$

$$\begin{aligned} 1 &= \int \mathcal{D}\rho_{\text{el}} \delta[\rho_{\text{el}}(\mathbf{r}) - \hat{\rho}_{\text{el}}(\mathbf{r})] \\ &= \int \mathcal{D}\rho_{\text{el}} \int \mathcal{D}w_{\text{el}} \exp\left\{i \int d\mathbf{r}\, w_{\text{el}}\, [\rho_{\text{el}}(\mathbf{r}) - \hat{\rho}_{\text{el}}(\mathbf{r})]\right\} \end{aligned} \tag{6.18}$$

where w_{or} and w_{el} are auxiliary fields introduced through the Fourier representation of the delta functional. In eqs (6.16)-(6.18), the notation $\int \mathcal{D}[\cdots]$ denotes functional integration. Applying these identities to the partition function results in

$$\begin{aligned} \Xi = &\int \mathcal{D}w \int \mathcal{D}w_{\text{or}} \int \mathcal{D}w_{\text{el}} \int \mathcal{D}\rho_{\text{or}} \int \mathcal{D}\rho_{\text{el}} \sum_{N=0}^{\infty} \frac{e^{\beta\mu N}}{N!} \\ &\times \prod_{i=1}^{N} \frac{1}{\eta} \int d\mathbf{r}_i \int d\boldsymbol{\mu}_i \int d\boldsymbol{p}_i \exp\Bigg[-\frac{\beta}{2} \int d\mathbf{r} \int d\mathbf{r}'\, \frac{\rho(\mathbf{r})\rho(\mathbf{r}')}{4\pi\varepsilon_0|\mathbf{r} - \mathbf{r}'|} \\ &- \sum_{i=1}^{N} \frac{\beta|\boldsymbol{p}_i|^2}{2\alpha} + i \int d\mathbf{r}\, w_{\text{or}}(\mathbf{r})[\rho_{\text{or}}(\mathbf{r}) - \hat{\rho}_{\text{or}}(\mathbf{r})] \\ &+ i \int d\mathbf{r}\, w_{\text{el}}(\mathbf{r})[\rho_{\text{el}}(\mathbf{r}) - \hat{\rho}_{\text{el}}(\mathbf{r})] \\ &+ i \int d\mathbf{r}\, w(\mathbf{r})\, [v\hat{n}(\mathbf{r}) + \varphi_0(\mathbf{r}) - 1]\Bigg] \end{aligned} \tag{6.19}$$

where $\rho(\mathbf{r}) = \hat{\rho}_c(\mathbf{r}) + \rho_{\text{or}}(\mathbf{r}) + \rho_{\text{el}}(\mathbf{r})$. Through these identity transformations, the particle–particle interactions are turned into particles interacting with fluctuating fields. The particle degrees of freedom can be easily integrated out to yield the single-particle partition function, $Q[w, w_{\text{or}}, w_{\text{el}}]$, given by,

$$Q = \frac{4\pi\bar{\mu}^2}{\eta} \left(\frac{2\pi\alpha}{\beta}\right)^{3/2} \int d\mathbf{r} \left\{\frac{\sin\left(\bar{\mu}|\nabla w_{\text{or}}|\right)}{\bar{\mu}|\nabla w_{\text{or}}|} \exp\left[ivw(\mathbf{r}) - \frac{\alpha}{2\beta}\,|\nabla w_{\text{el}}(\mathbf{r})|^2\right]\right\} \tag{6.20}$$

The transformed grand canonical partition function is now written as

$$\Xi = \int \mathcal{D}w \int \mathcal{D}w_{\text{or}} \int \mathcal{D}w_{\text{el}} \int \mathcal{D}\rho_{\text{or}} \int \mathcal{D}\rho_{\text{el}}\, e^{-\beta H} \tag{6.21}$$

where the Hamiltonian, $H = H[w, w_{\text{or}}, w_{\text{el}}, \rho_{\text{or}}, \rho_{\text{el}}]$, is a functional of the field variables only, and is given by

$$\begin{aligned}\beta H = i \int d\mathbf{r}\, w(\mathbf{r})\,[1 - \varphi_0(\mathbf{r})] - i \int d\mathbf{r}\, w_{\text{or}}(\mathbf{r})\rho_{\text{or}}(\mathbf{r}) - i \int d\mathbf{r}\, w_{\text{el}}(\mathbf{r})\rho_{\text{el}}(\mathbf{r}) \\ + \frac{\beta}{2} \int d\mathbf{r} \int d\mathbf{r}'\, \frac{\rho(\mathbf{r})\rho(\mathbf{r}')}{4\pi\varepsilon_0|\mathbf{r} - \mathbf{r}'|} - e^{\beta\mu} Q[w, w_{\text{or}}, w_{\text{el}}]\end{aligned} \tag{6.22}$$

The integrals in the partition function cannot be evaluated in closed form, so we use the saddle-point configuration as an approximation to the full partition function. The saddle point is found by extremizing the Hamiltonian with respect to all the field variables [59]. The grand free energy is given by $\beta\Omega = -\ln\Xi \approx -\ln\Xi^*$, where Ξ^* is the saddle-point contribution to the partition function. Extremizing the free energy results in a set of self-consistent equations that can be solved to find the equilibrium field configurations, and therefore observables such as the free energy and the electric field. Since the saddle-points for the w fields lie on the imaginary axis, to avoid the use of imaginary numbers, we define real potentials $\beta u = -iw$ and $\beta\phi = iw_{\text{or}} = iw_{\text{el}}$ ($w_{\text{or}} = w_{\text{el}}$ at equilibrium). The set of self-consistent equations obtained from extremizing Ω with respect to w, ρ_{or} (and ρ_{el}), w_{or}, and w_{el} respectively, is given by

$$1 - \varphi_0(\mathbf{r}) = e^{-\beta v u(\mathbf{r}) + \frac{\beta\alpha}{2}|\nabla\phi(\mathbf{r})|^2} \frac{\sinh\left(\beta\bar{\mu}|\nabla\phi(\mathbf{r})|\right)}{\beta\bar{\mu}|\nabla\phi(\mathbf{r})|} \tag{6.23}$$

$$-\varepsilon_0 \nabla \cdot [(1 + \chi_{\text{or}}(\mathbf{r}) + \chi_{\text{el}}(\mathbf{r}))\nabla\phi(\mathbf{r})] = \hat{\rho}_c(\mathbf{r}) \tag{6.24}$$

$$\chi_{\text{or}}(\mathbf{r}) = \frac{\beta\bar{\mu}^2}{v\varepsilon_0} e^{-\beta v u(\mathbf{r}) + \frac{\beta\alpha}{2}|\nabla\phi(\mathbf{r})|^2} G(\beta\bar{\mu}|\nabla\phi(\mathbf{r})|) \tag{6.25}$$

$$\chi_{\text{el}}(\mathbf{r}) = \frac{\alpha}{v\varepsilon_0}\,[1 - \varphi_0(\mathbf{r})] \tag{6.26}$$

where $G(x) = [1/\tanh(x) - 1/x]\sinh(x)/x^2$. Additionally, we have defined the orientational electric susceptibility, χ_{or}, and the electronic electric susceptibility, χ_{el}. For convenience, The Poisson equation, eq (6.24), is written in a way that separates the ion charge density from the bound solvent charge density (reflected in χ_{or} and χ_{el}). Equation (6.24) can be rewritten as

$$\nabla \cdot \mathbf{D} = \hat{\rho}_c(\mathbf{r}) \tag{6.27}$$

where $\mathbf{D} = -\varepsilon_0[1+\chi_{\text{or}}(\mathbf{r})+\chi_{\text{el}}(\mathbf{r})]\nabla\phi(\mathbf{r})$ is the electric displacement. Conveniently, the electric displacement can be determined solely from the location of the free charges. We simplify the solution to eq (6.27) by assuming that the total electric displacement is the superposition of the electric displacement due to each of the ions. (The superposition principle is used as an approximation to avoid solving the full Poisson equation. In general it does not hold exactly for nonlinear dielectrics. The approximation becomes less accurate for strong interactions, and in particular when the ions are at close approach[50].) The displacement at a distance r_i from an isolated Gaussian smeared charge i is

$$\mathbf{D}_i(\mathbf{r}) = \frac{ez_i}{4\pi r_i^2}\left[\operatorname{erf}\left(\sqrt{\frac{\pi}{2}}\frac{r_i}{b_i}\right) - \sqrt{2}\,\frac{r_i}{b_i}\exp\left(-\frac{\pi r_i^2}{2b_i^2}\right)\right]\hat{\mathbf{r}}_i \tag{6.28}$$

where $\mathbf{r}_i = \mathbf{r} - \mathbf{R}_i$, and $\hat{\mathbf{r}}_i$ is the unit vector in the direction of $\mathbf{r}_i$. The equilibrium electric field is found by iterating $\mathbf{D}(\mathbf{r}) = -\varepsilon(\mathbf{r})\nabla\phi(\mathbf{r})$ using eqs (6.23), (6.25) and (6.26) to calculate the dielectric function $\varepsilon(\mathbf{r}) = \varepsilon_0[1 + \chi_{\text{or}}(\mathbf{r}) + \chi_{\text{el}}(\mathbf{r})]$. For all self-consistent calculations, we iterate until the maximum difference in the electric field between two consecutive steps is less than 10^{-13}.

The equilibrium free energy can be simplified by plugging the saddle-point equations into the Hamiltonian,

$$\begin{aligned}\Omega\left(\hat{\rho}_c, \varphi_0, |\nabla\phi|, \chi_{\text{or}}, \chi_{\text{el}}\right) = \int d\mathbf{r}\Bigg\{&\frac{1}{2}\varepsilon_0(1 + 2\chi_{\text{or}}(\mathbf{r}) + \chi_{\text{el}}(\mathbf{r}))|\nabla\phi(\mathbf{r})|^2 \\ &- \frac{vn(\mathbf{r})}{\beta v}\ln\left[\frac{\sinh\left(\beta\bar{\mu}|\nabla\phi(\mathbf{r})|\right)}{\beta\bar{\mu}|\nabla\phi(\mathbf{r})|}\right] - \frac{vn(\mathbf{r})}{\beta v}\left[1 - \ln\left(vn(\mathbf{r})\right)\right]\Bigg\}\end{aligned} \tag{6.29}$$

where $vn(\mathbf{r}) = 1 - \varphi_0(\mathbf{r})$ is the coarse-grained solvent volume fraction. The system is rotationally-symmetric about the axis connecting the ions, allowing the integral in eq (6.29) to be calculated in cylindrical coordinates with variation restricted to the r, z-plane. We use a large enough domain to avoid cutting off the long-range tail of the electric field from the ions.

When calculating the PMF, the quantity of interest is the difference between the free energy at separation r and that at infinite separation. We call this difference $\Delta\Omega = \Omega(r) - \Omega(\infty)$. The entropic contribution to $\Delta\Omega$ can be calculated with the derivative

$$\Delta S = -\left(\frac{\partial\Delta\Omega}{\partial T}\right)_{\mu,V} \tag{6.30}$$

Note that the change in grand free energy is equal to the change in Helmholtz free energy for this process as the chemical potential and particle number do not change

when bringing the ions together at a fixed T and V due to the incompressibility constraint. Mathematically, we can write the following

$$\begin{aligned}\Delta\Omega &= U - TS - \mu N - [U_\infty - TS_\infty - (\mu N)_\infty] \\ &= (U - U_\infty) - T(S - S_\infty) \\ &= \Delta F \end{aligned} \tag{6.31}$$

where the subscript ∞ denotes a quantity at infinite ion separation. We then decompose $\Delta\Omega$ into entropic and energetic contributions by calculating ΔS with eq (6.30) and internal energy with $\Delta U = \Delta F + T\Delta S = \Delta\Omega + T\Delta S$. We give examples of the profiles for the ion density, the charge density, and the dielectric displacement in Figure 6.2.

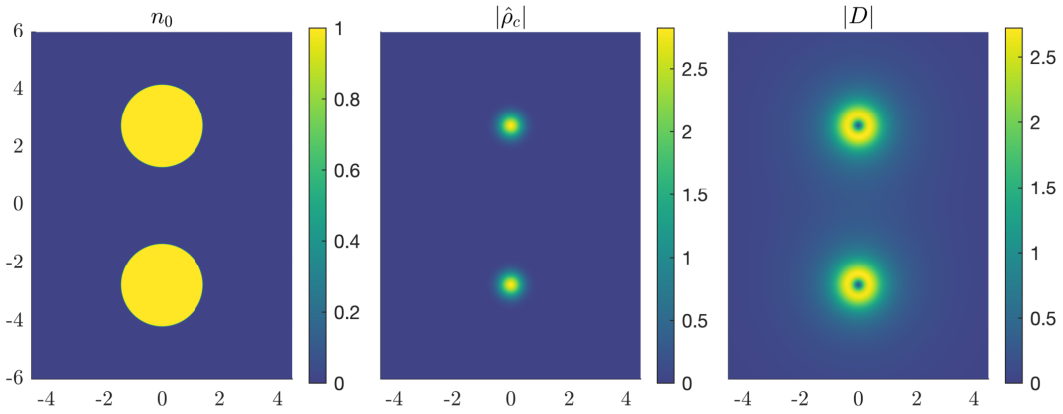

Figure 6.2: Example plot of ion mass density (left), ion charge density (middle) and electric displacement (right). The plots represent a slice in the x,z-plane. Note that the simulated domain is cylindrical and rotationally symmetric around the axis connecting the ions.

6.4 Results and Discussion

We start with a discussion of the behavior of the PMF for bringing two oppositely-charged monovalent ions together in a dipolar solvent; this is shown in Figure 6.3. Both panels show that increasing the dipole moment of the solvent decreases the attraction between the two ions. This behavior can be easily understood as due to the increase in the effective dielectric constant with the dipole moment. The diverging behavior below $r = 1\sigma$ in Figure 6.3b is due to the diverging LJ potential from simulation. Above $r = 1\sigma$, we see close agreement between the DSCFT and simulation results at low to moderate dipole moment; a direct comparison is given in Figure 6.9 in the Appendix. At higher dipole moments (insets of Figure

6.3), oscillations appear in the PMFs for simulations, indicating that there are strong solvation shells of the dipolar solvent around the ions, with each maximum corresponding to the energy barrier for breaking a solvation shell [60]. Interestingly, for large dipole moments, even DSCFT captures (though to a lesser degree) this nonmonotonic behavior, despite it only accounting for the solvent excluded volume through the incompressibility constraint without explicitly considering the packing of the solvent molecules.

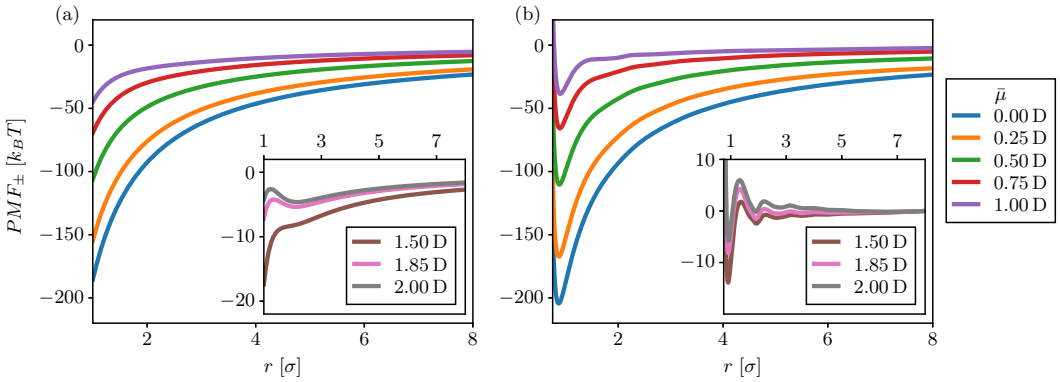

Figure 6.3: PMFs for various dipole moments calculated from (a) DSCFT and (b) molecular dynamics simulation with $\sigma = 3$ Å, $T = 300$ K, $q_1 = -q_2 = e$, $v = 30$ Å^3. The insets of both panels show PMFs for larger dipole moments. For reference, $\bar{\mu} = 1.85$ D corresponds to the gas-phase dipole moment of water.

For large ion separations, the PMF from both DSCFT and simulation reproduces the expected Coulomb behavior, $\Delta F(r) = -e^2/4\pi\varepsilon r$, where ε is the effective dielectric constant for the given dipole moment. Table S1 gives the effective dielectric constants obtained by fitting the long-range part of the PMF to a Coulomb potential. The dielectric constants so obtained from the simulation are consistent with literature values for small dipole moment [61–64]. The effective bulk dielectric constant from DSCFT is equivalent to that of Debye [29, 48] ($\varepsilon_r = 1 + \frac{\beta\bar{\mu}^2}{3v\varepsilon_0} = 1 + \xi$). The effective bulk dielectric constant from MD simulations is higher than from DSCFT, since the simulations inherently include the reaction field due to dipole–dipole correlations[30, 63]. It is possible to include the reaction field effect in the field theory, as was done by Zhuang and Wang [48, 65]; however, this would add significant complexity and would not affect the qualitative behavior observed in this study.

We decompose the PMF into its energetic and entropic contributions in Figure 6.4. From the MD simulation, the entropic contribution is calculated using $-T\Delta S = \Delta F - \Delta U$, where ΔU is the potential energy calculated from the pair potentials (the

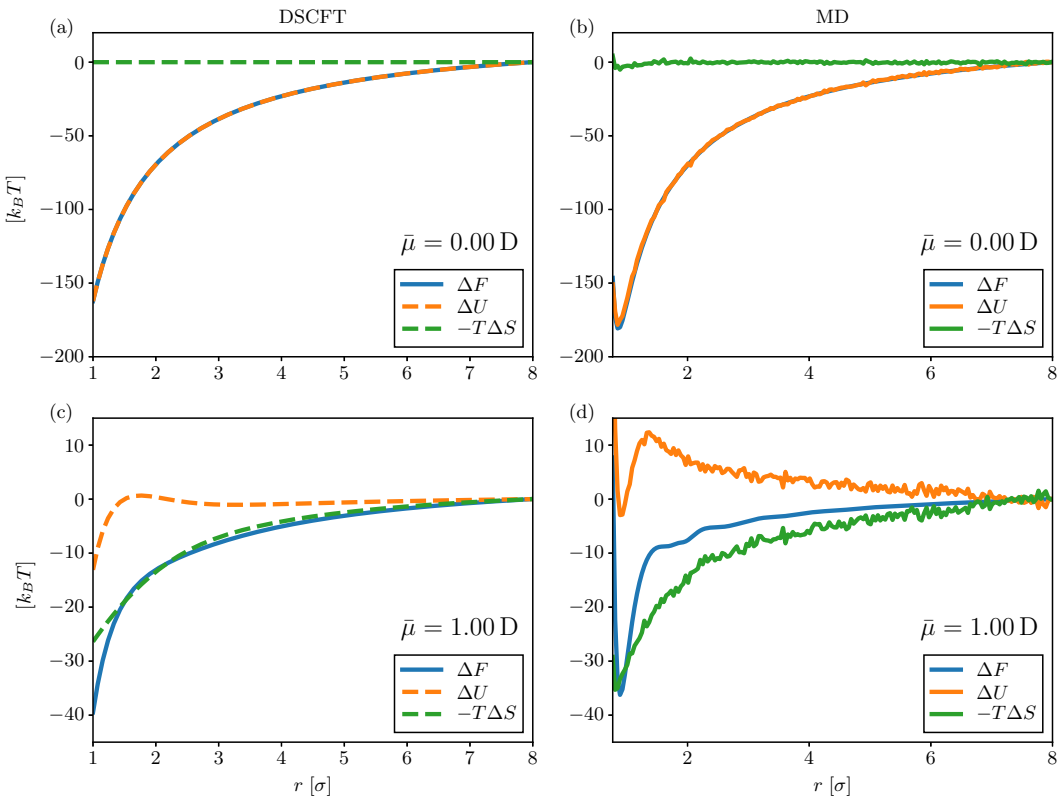

Figure 6.4: PMFs decomposed into their energetic and entropic contributions with solvent dipoles of (a,b) $\bar{\mu} = 0\,\mathrm{D}$ and (c,d) $\bar{\mu} = 1\,\mathrm{D}$. The PMFs are calculated from DSCFT in (a,c) and MD simulation in (b,d). Other parameters are the same as in Figure 6.3.

kinetic energy is constant at any given temperature and thus does not contribute to the energy change). From DSCFT, the entropy is calculated via eq (6.30). Since it is difficult to calculate these differences with respect to infinite separation in simulation, we choose a reference point of $r = 8\sigma$ (the largest simulated separation). The DSCFT is not limited by this constraint but we use the same reference point for consistency.

In Figure 6.4a,b, we see that there is essentially no entropic contribution to the PMF when there is no solvent dipole, indicating that the PMF is only made up of the electrostatic interaction energy. When the solvent does have a permanent dipole, as in Figure 6.4c,d, we see that the PMF is dominated by the entropic contribution. The energetic contribution even becomes unfavorable, which was similarly observed by Chen and Wang [26]. The shape and magnitude of the free energy, internal energy, and entropy are similar to those observed in previous simulation and theoretical studies that focused on ions in water [27, 28]. As we discuss later, this significant

entropy increase comes from the diminished polarization of the solvent around the ions. The unfavorable energetic contribution comes from the fact that ion–dipole interactions are weakened when the ions are close. Physically, the two ions form an effective dipole upon close-contact, and dipole–dipole interactions are weaker than ion–dipole interactions. We provide similar plots for additional values for the dipole moment in Figure 6.10 in the Appendix.

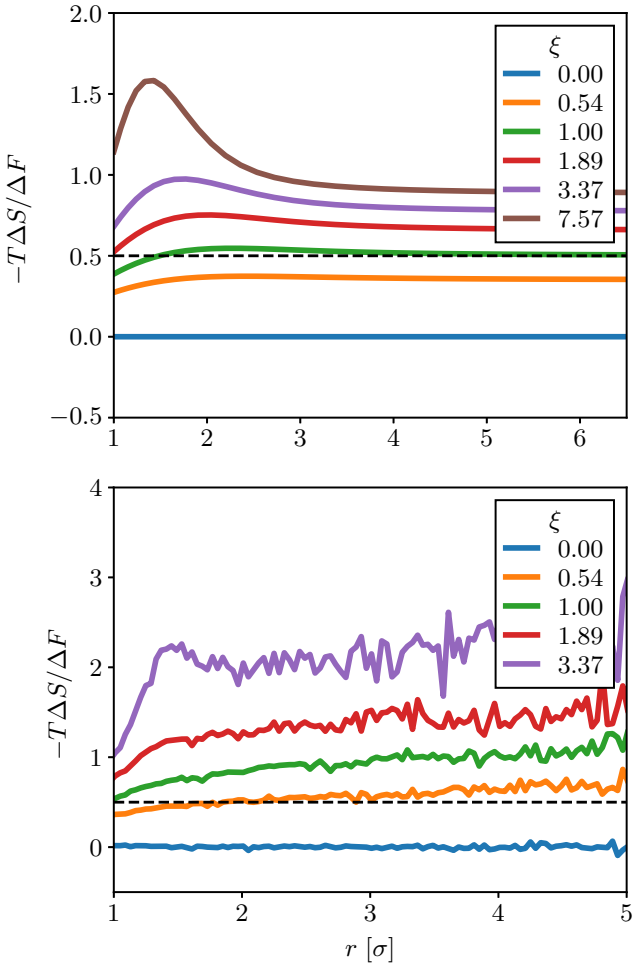

Figure 6.5: Ratio of PMF due to entropy for $\sigma = 3\,\text{Å}$, $q_1 = -q_2 = e$ and various $\xi = \frac{\beta\tilde{\mu}^2}{3v\varepsilon_0}$ calculated via (a) DSCFT and (b) molecular dynamics.

For clarity, we explicitly calculate the entropic contribution as a ratio to the total free energy difference in Figure 6.5 for different values of the dimensionless dipole parameter ξ. For $\xi = 1$, the entropic and energetic contributions are equal at long range for DSCFT. This is exactly what is predicted when using the Debye approximation for the dielectric constant in the Coulomb potential, as shown in eqs (6.2)–(6.4). Similarly, the MD simulations predict a crossover from energetically

to entropically dominated, but the crossover is actually below $\xi = 1$ because of the stronger dipole–dipole correlations discussed earlier. However, determining the exact crossover from simulation is computationally demanding owing to both the required system size and sampling of the potential energy, particularly at large ξ, so we mostly focus on the qualitative features. Importantly, Figure 6.5 shows that the crossover from energy to entropy driven is obtained by increasing the dipole moment or decreasing the temperature.

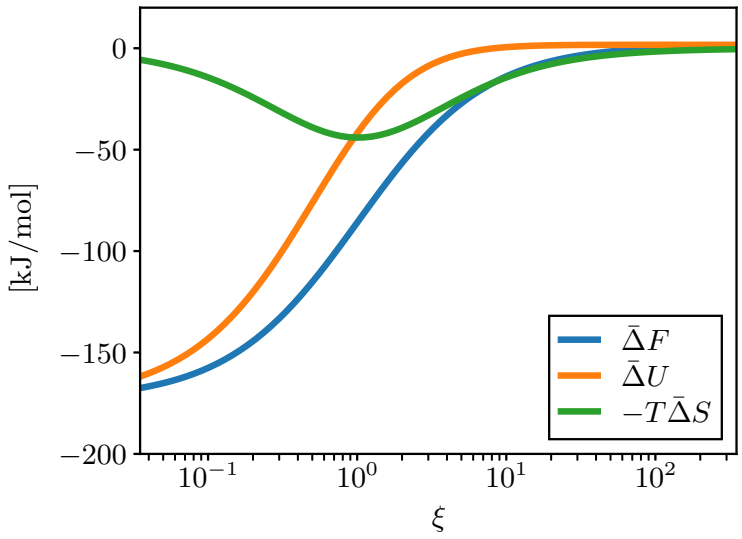

Figure 6.6: Free energy, internal energy, and entropy change from infinite separation to $r = 5\sigma$ versus $\xi = \frac{\beta\bar{\mu}^2}{3v\varepsilon_0}$ for $\sigma = 3$ Å and $q_1 = -q_2 = e$. Calculations were done using DSCFT.

In the Debye theory, ξ is a universal parameter that quantifies the importance of polarization in the system. It is of interest to see how the electrostatic entropy contribution changes with this parameter. To this end, we consider the various components of the PMF in the DSCFT at a fixed distance $r = 5\sigma$, where the symbol $\bar{\Delta}$ denotes the difference from the infinite separation. The result is shown in Figure 6.6. We see that for low ξ (weak dipoles or high temperature) the entropy change is small. Near $\xi = 1$ there is the crossover from energy to entropy dominance, consistent with the Debye analysis and the results of Figure 6.5. In the high ξ regime (strong dipoles or low temperature), the process is practically fully entropy driven. The free energy and entropy change are small in the high ξ regime due to the large effective dielectric constant. At the mean-field level, the same curves are observed regardless of whether the temperature or solvent dipole is changed, indicating that ξ is a universal parameter for determining the entropic contribution

to the free energy. This holds true as long as the ions are not too close together.

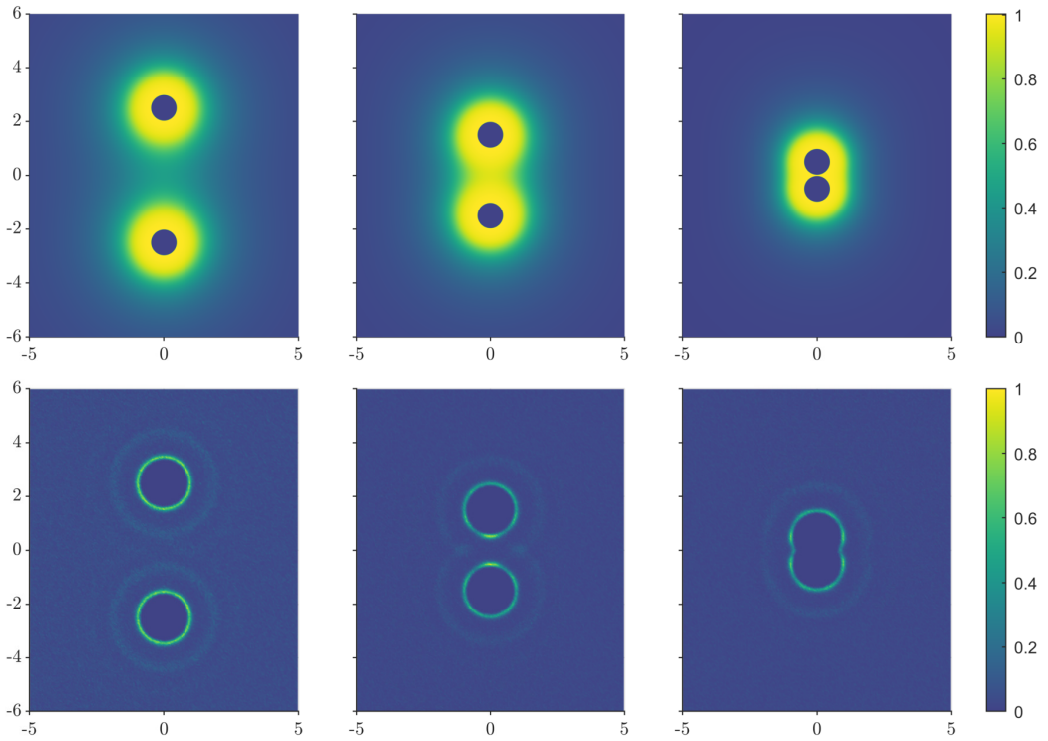

Figure 6.7: Solvent polarization at the midplane of the ions for both theory (top row) and simulation (bottom row). Spatial positions are in units of σ. The ions are at separations of $r = 5\sigma$, 3σ and 1σ going from left to right. Both ions have size $\sigma = 3$ Å and charges $q_1 = -q_2 = e$.

To visualize the decrease in the orientational order when the two oppositely charged ions approach each other, Figure 6.7 shows a heatmap of the local polarization induced by oppositely-charged ions from both theory and simulation. One could also plot the dielectric function, $\varepsilon_r(\mathbf{r})$, as was done in previous work using lattice Monte Carlo simulations [66]. We have provided an example of this type of plot calculated using the DSCFT (See Figure 6.11 in the Appendix). The conclusions drawn from both types of plots are the same; however, we believe the plot of local polarization provides a clearer picture of solvent release. In DSCFT the measure of local orientational polarization is taken to be the orientational susceptibility times the electric field, or $|P| = \chi_{\text{or}}|\nabla\phi|$. Note that far away from the ions, the orientational polarization is zero due to the random orientation of the dipoles. In the simulation, the measure is given by the magnitude of the local, time-averaged solvent dipole, $|\langle\boldsymbol{\mu}(\mathbf{r})\rangle|$ (simulation details are in the Appendix). Both rows of Figure 6.7 are normalized by each row's maximum value to emphasize the qualitative features.

The qualitative difference between the simulation and theory comes from the strong ordering and solvation shells present in the simulation, of which the first two are clearly visible in Figure 6.7b. This strong spatial ordering is not captured in the DSCFT, and therefore the polarization is continuous and decreases with distances away from the ions. The shrinking of the cloud surrounding the ions indicates that the polarization around the ions weakens as the ions move closer together. The total polarization due to two separated ions is greater than that of the paired ions, meaning that a portion of the solvent is released to freely translate and rotate upon bringing the ions together. This solvent release is responsible for the large entropy increase, which dominates the ion interactions at a sufficiently large dipole moment or low temperature.

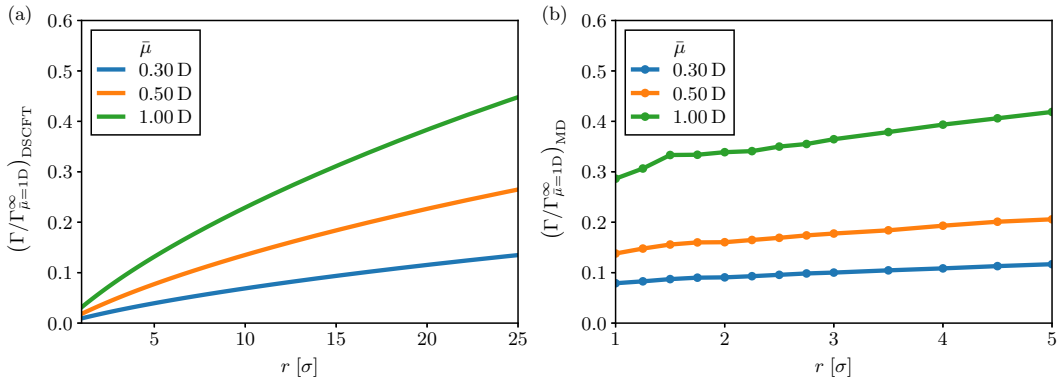

Figure 6.8: Normalized excess polarization versus the ion separation for various dipole moments $\bar{\mu}$, near the energy/entropy crossover, with $\sigma = 3\,\text{Å}$ and $q_1 = -q_2 = e$. Here, the excess polarization is normalized by the infinite separation excess polarization for $\bar{\mu} = 1.0\,\text{D}$. Calculations were done using (a) DSCFT and (b) simulation.

While the visual representation is helpful it does not provide a quantitative measure of the change in polarization. Therefore, in Figure 6.8 we quantify the change in excess polarization of the solvent when bringing the ions together. The excess polarization calculated from DSCFT is defined as $\Gamma_{\text{DSCFT}} = \int d\mathbf{r}\, \chi_{\text{or}}(\mathbf{r})|\nabla\phi(\mathbf{r})|$, which is the local orientational polarization of the solvent integrated over the system volume. From MD simulations, we measure the excess polarization by integrating the time-averaged dipole moment with the local solvent density, $\Gamma_{\text{MD}} = \int d\mathbf{r}|\langle\boldsymbol{\mu}(\mathbf{r})\rangle|\rho_s(\mathbf{r})$. To highlight the dependence of the magnitude of the excess on the dipole moment, we normalize each panel by the same value. We opt to use the excess polarization at infinite separation from the largest dipole moment, $\bar{\mu} = 1\,\text{D}$.

From theory and simulation, the excess polarization decreases as the ion separation

decreases. The magnitude of the decrease becomes more substantial with increasing dipole strength. This supports the idea that the solvent dipoles are released as the ions come together, which is responsible for the significant increase in the system entropy. We see that the solvent reorganization is significant even at large separations, where the DSCFT has not plateaued even at $r = 25\sigma$. Interestingly, in DSCFT, the curves at different dipole moments collapse onto a single curve when each curve is normalized by its excess polarization at infinite separation (see Figure 6.12 in the Appendix). The collapse of the curves indicates that the magnitude of the decrease in solvent polarization is what causes the crossover from energy- to entropy-driven, rather than a new physical process.

6.5 Conclusions

For two monovalent ions in a dipolar fluid, the solvent plays a major role in the interaction of the ions. At the mean-field level, the interaction is entropy dominated when $\xi = \frac{\beta\vec{\mu}^2}{3v\varepsilon_0} > 1$, as is the case of water at room temperature. The physical origin of the entropy is the reorganization of solvent dipoles as the two ions approach one another. This entropy is purely electrostatic in nature, arising from the polarization due to the electric field generated by the ions. We emphasize that this entropy and the solvent reorganization will occur in *any* polar solvent. In implicit solvent models, the solvent contribution to the entropy may be buried in effective interaction parameters, requiring careful treatment to calculate the entropy of the system. For weakly or moderately charged systems, using the temperature dependence of the bulk dielectric constant may be sufficient to extract the entropic contribution. Such an approach will likely become inadequate in systems with stronger correlations[67] (i.e. packing effects, multivalent ions, polyelectrolytes, etc.) or nonaqueous solvents[68], where explicitly considering the solvent becomes necessary. Even in the model systems considered in this work, for large dipole strengths, the effective interaction (PMF) can no longer be described as a simple Coulombic potential with an effective dielectric constant at short distances.

The implications of these conclusions are important since assembly in charged systems is ubiquitous[69–72]. For instance, in drug discovery, researchers often discuss enthalpy-entropy compensation, where a strong enthalpic interaction between two species (i.e. protein–ligand) invariably comes with an equivalent entropic compensation. As reemphasized by Dragan et al. [73], a significant part of this entropy likely comes from the solvent release. Emphasizing solvation rather than high-affinity ligands could lead to new design strategies in drug discovery.

On the simulation side, implicit solvent models are growing increasingly complex, including many machine-learned models [74]. These models are excellent in their ability to reproduce thermodynamic quantities like the PMF. We hope that our study motivates future efforts toward understanding the components of the PMF, such as the entropic vs. energetic contributions, and the specific molecular mechanisms that are responsible for these contributions.

6.6 Appendix

Dielectric Constants

Table 6.1: Dielectric constants extracted from fitting long-range PMFs to Coulomb potential. From MD, extracting the dielectric constant from the PMF above 1D is not reliable due to the small oscillations in the PMF arising from packing effects. Other parameters are $\sigma = 3\,\text{Å}$, $T = 300\,\text{K}$, $q_1 = -q_2 = e$, $v = 30\,\text{Å}^3$.

Dipole Moment (D)	ε_r (DSCFT)	ε_r (MD)
0.00	1.00	1.00
0.25	1.21	1.32
0.40	1.54	2.25
0.50	1.84	2.54
0.75	2.89	4.55
1.00	4.37	9.62
1.50	8.57	–
1.85	12.52	–
2.00	14.46	–

Comparison of PMFs for DSCFT and MD Simulations

Here, we provide a direct comparison of the PMFs computed using ABF with the Stockmayer fluid model and the modified DSCFT theory. For low and moderate dipole moments, we find remarkable agreement between the curves, with deviations becoming large at high dipole moments. Despite the disagreement, we do note that the mean-field theory can still predict a maximum in the PMF just beyond $r = 1\sigma$.

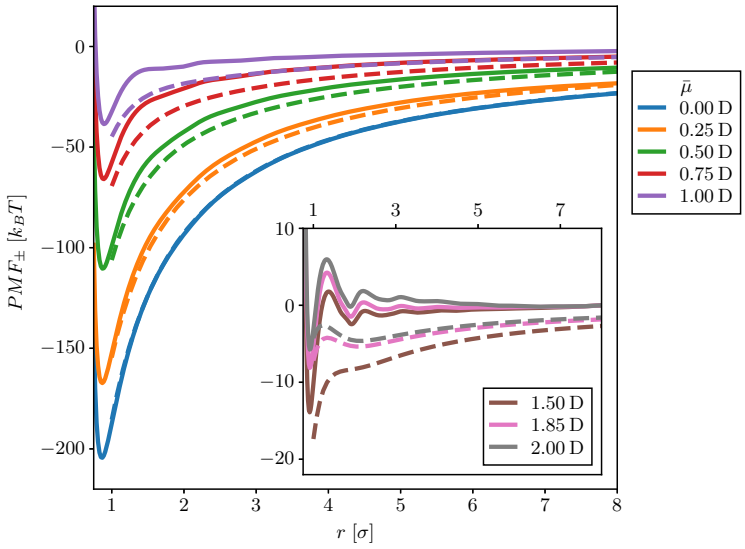

Figure 6.9: PMFs for various dipole moments with $\sigma = 3\,\text{Å}$, $T = 300\,\text{K}$, $q_1 = -q_2 = e$ and $\nu = 30\,\text{Å}^3$. The solid and dashed lines are results from MD and DSCFT, respectively. The inset zooms in on higher dipole moments to highlight the strong oscillations.

Additional Plots of Entropy versus Energy Contributions

Here, we give additional PMFs and their corresponding enthalpic and entropic contributions. The PMFs computed from MD simulation are smooth, but the energy and entropy are noisy. This is a result of the large energy fluctuations combined with the small magnitude of the PMF as the dipole increases. Note that for high dipole moments (and therefore high dielectric constants), both MD simulation and theory predict that the energy increases upon association. In other words, when ion-dipole interactions are very strong, freeing dipoles increases the energy, but also significantly increases the entropy. Thus, association can still be favorable even though the internal energy increases.

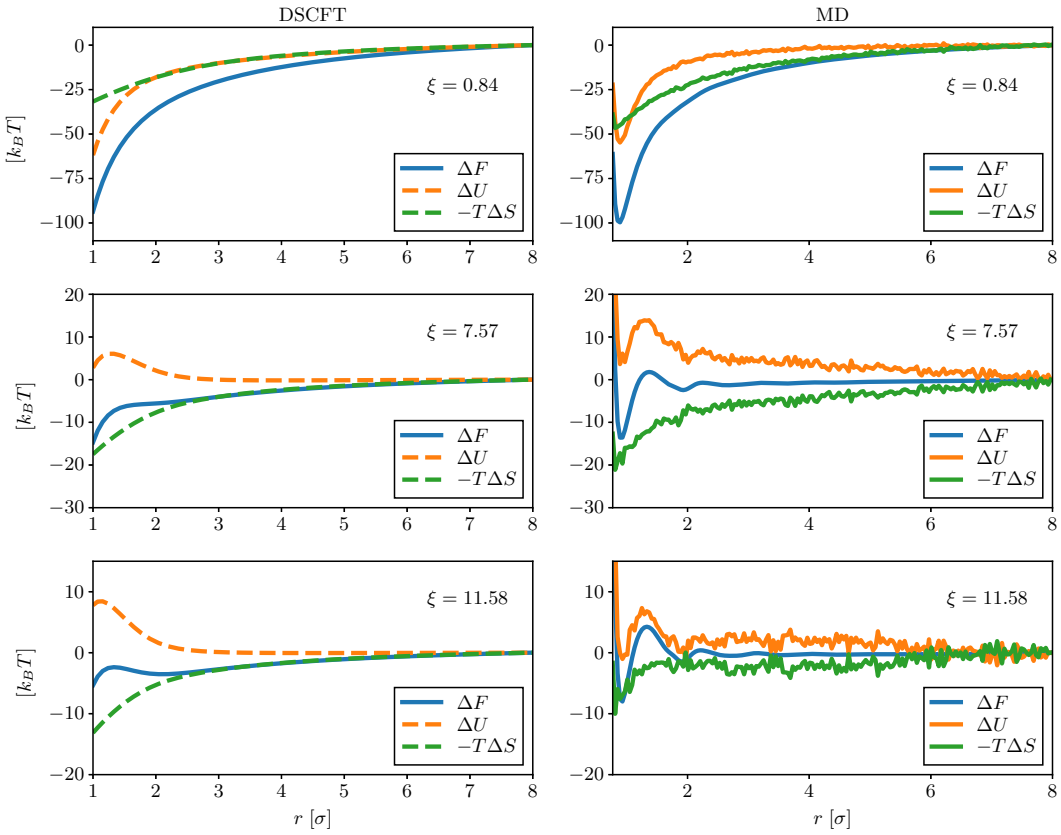

Figure 6.10: PMFs decomposed into their energetic and entropic contributions for $\sigma = 3$ Å, $T = 300$ K, $q_1 = -q_2 = e$, $v = 30$ Å^3 and various $\xi = \frac{\beta\tilde{\mu}^2}{3v\varepsilon_0}$. The PMFs on the left are calculated via DSCFT and on the right via MD.

Simulation Details for Fixed Ion Separation

To analyze the solvent orientations around two ions at a given separation, we use a slightly different simulation routine from that for calculating the PMFs. For a fixed ion separation, the ion position does not update with each timestep. To accomplish this, the thermostat is only applied to the solvent particles. Each simulation consists of 4000 solvent particles and two ions of opposite charge with parameters described in the main text. The simulation box size is $15\sigma \times 15\sigma \times 19.69\sigma$ with the longest dimension in the direction of the ion separation. Each system was equilibrated for 5×10^6 timesteps ($\delta t = 0.005\tau$) and production of 10^7 timesteps. To calculate $|\langle \boldsymbol{\mu}(\mathbf{r}) \rangle|$, space is discretized into voxels in which x-,y-,and z-components of the dipole moment are sampled and averaged every 500 timesteps during the production run.

Example Plots of Dielectric Function from DSCFT

Within the DSCFT theory, the spatially varying dielectric function is a natural output. It is computed as $\epsilon_r(\mathbf{r}) = 1 + \chi_{\text{or}}(\mathbf{r}) + \chi_{\text{el}}$. The orientational and electronic susceptibility are both functions of the local electric field. As expected, we find that the dielectric function is 1 inside the ions since no solvent (and therefore no dipoles) can penetrate the ions. Near the ion radius, the dielectric function smoothly increases up to the bulk value, which is identical to the Debye dielectric constant ($\epsilon_r = 1 + \xi$) since DSCFT is a mean-field theory.

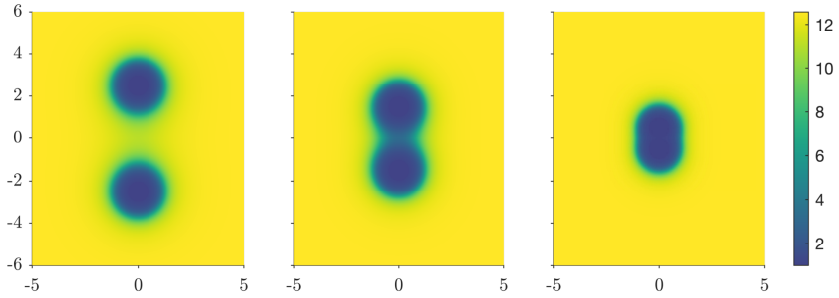

Figure 6.11: Dielectric function, $\varepsilon_r(\mathbf{r})$ at the midplane of the ions, calculated from DSCFT. Spatial positions are in units of σ. The solvent has the gas-phase dipole moment of water, $\bar{\mu} = 1.85\,\text{D}$. The ions are at separations of $r = 5\sigma$, 3σ and 1σ going from left to right. Both ions have size $\sigma = 3\,\text{Å}$ and charges $q_1 = -q_2 = e$.

Additional Plots of Normalized Excess Polarization

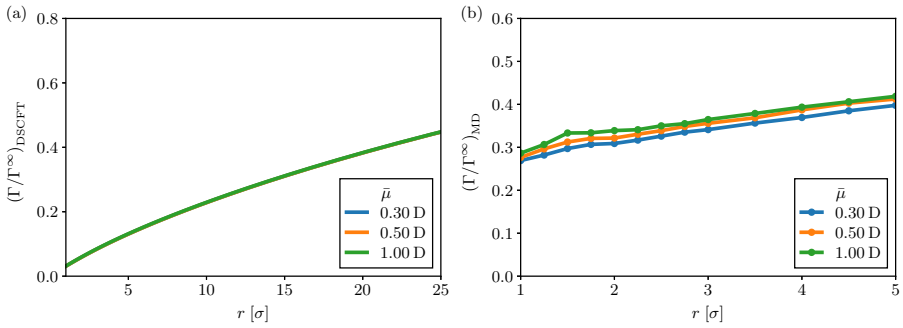

Figure 6.12: Normalized excess polarization versus the ion separation for various dipole moments $\bar{\mu}$ with $\sigma = 3\,\text{Å}$ and $q_1 = -q_2 = e$. Here, the excess polarization is normalized by the infinite separation excess polarization for each dipole moment. Calculations were done using (a) DSCFT and (b) simulation. We note that when normalized in this way the curves collapse together for DSCFT.

References

(1) Varner, S.; Balzer, C.; Wang, Z.-G. Entropic Origin of Ionic Interactions in Polar Solvents. *The Journal of Physical Chemistry B* **2023**, *127*, 4328–4337, DOI: 10.1021/acs.jpcb.3c00588.

(2) Roux, B.; Simonson, T. Implicit solvent models. *Biophysical Chemistry* **1999**, *78*, 1–20, DOI: 10.1016/S0301-4622(98)00226-9.

(3) Ponder, J. W.; Case, D. A. Force fields for protein simulations. *Advances in Protein Chemistry* **2003**, *66*, ed. by Daggett, V., 27–85.

(4) Ferrara, P.; Apostolakis, J.; Caflisch, A. Evaluation of a fast implicit solvent model for molecular dynamics simulations. *Proteins: Structure, Function, and Bioinformatics* **2002**, *46*, 24–33, DOI: 10.1002/prot.10001.

(5) Götz, A. W.; Williamson, M. J.; Xu, D., et al. Routine Microsecond Molecular Dynamics Simulations with AMBER on GPUs. 1. Generalized Born. *Journal of Chemical Theory and Computation* **2012**, *8*, 1542–1555, DOI: 10.1021/ct200909j.

(6) Anandakrishnan, R.; Drozdetski, A.; Walker, R. C.; Onufriev, A. V. Speed of Conformational Change: Comparing Explicit and Implicit Solvent Molecular Dynamics Simulations. *Biophysical Journal* **2015**, *108*, 1153–1164, DOI: 10.1016/j.bpj.2014.12.047.

(7) Connolly, M. L. Solvent-Accessible Surfaces of Proteins and Nucleic Acids. *Science* **1983**, *221*, 709–713, DOI: 10.1126/science.6879170.

(8) Richmond, T. J. Solvent accessible surface area and excluded volume in proteins: Analytical equations for overlapping spheres and implications for the hydrophobic effect. *Journal of Molecular Biology* **1984**, *178*, 63–89, DOI: 10.1016/0022-2836(84)90231-6.

(9) Mongan, J.; Case, D. A.; McCammon, J. A. Constant pH molecular dynamics in generalized Born implicit solvent. *Journal of Computational Chemistry* **2004**, *25*, 2038–2048, DOI: 10.1002/jcc.20139.

(10) Feig, M.; Onufriev, A.; Lee, M. S., et al. Performance comparison of generalized born and Poisson methods in the calculation of electrostatic solvation energies for protein structures. *Journal of Computational Chemistry* **2004**, *25*, 265–284, DOI: 10.1002/jcc.10378.

(11) Baker, N. A. Improving implicit solvent simulations: a Poisson-centric view. *Current Opinion in Structural Biology* **2005**, *15*, 137–143, DOI: 10.1016/j.sbi.2005.02.001.

(12) Chen, J.; Brooks, C. L.; Khandogin, J. Recent advances in implicit solvent-based methods for biomolecular simulations. *Current Opinion in Structural Biology* **2008**, *18*, 140–148, DOI: 10.1016/j.sbi.2008.01.003.

(13) Kleinjung, J.; Fraternali, F. Design and application of implicit solvent models in biomolecular simulations. *Current Opinion in Structural Biology* **2014**, *25*, 126–134, DOI: 10.1016/j.sbi.2014.04.003.

(14) Onufriev, A. V.; Case, D. A. Generalized Born Implicit Solvent Models for Biomolecules. *Annual Review of Biophysics* **2019**, *48*, 275–296, DOI: 10.1146/annurev-biophys-052118-115325.

(15) Griffiths, D. J., *Introduction to Electrodynamics*, 4th edition; Cambridge University Press: Cambridge, United Kingdom ; New York, NY, 2017; 620 pp.

(16) Fröhlich, H., *Theory of Dielectrics: Dielectric Constant and Dielectric Loss*; Oxford University: 1958; book.

(17) Muthukumar, M., *Physics of Charged Macromolecules: Synthetic and Biological Systems*; Cambridge University Press: Cambridge, 2023.

(18) Bucur, C. B.; Sui, Z.; Schlenoff, J. B. Ideal Mixing in Polyelectrolyte Complexes and Multilayers: Entropy Driven Assembly. *Journal of the American Chemical Society* **2006**, *128*, 13690–13691, DOI: 10.1021/ja064532c.

(19) Priftis, D.; Laugel, N.; Tirrell, M. Thermodynamic Characterization of Polypeptide Complex Coacervation. *Langmuir* **2012**, *28*, 15947–15957, DOI: 10.1021/la302729r.

(20) Priftis, D.; Megley, K.; Laugel, N.; Tirrell, M. Complex coacervation of poly(ethylene-imine)/polypeptide aqueous solutions: Thermodynamic and rheological characterization. *Journal of Colloid and Interface Science* **2013**, *398*, 39–50, DOI: 10.1016/j.jcis.2013.01.055.

(21) Fu, J.; Schlenoff, J. B. Driving Forces for Oppositely Charged Polyion Association in Aqueous Solutions: Enthalpic, Entropic, but Not Electrostatic. *Journal of the American Chemical Society* **2016**, *138*, 980–990, DOI: 10.1021/jacs.5b11878.

(22) Elder, R. M.; Emrick, T.; Jayaraman, A. Understanding the Effect of Polylysine Architecture on DNA Binding Using Molecular Dynamics Simulations. *Biomacromolecules* **2011**, *12*, 3870–3879, DOI: 10.1021/bm201113y.

(23) Rathee, V. S.; Sidky, H.; Sikora, B. J.; Whitmer, J. K. Role of Associative Charging in the Entropy–Energy Balance of Polyelectrolyte Complexes. *Journal of the American Chemical Society* **2018**, *140*, 15319–15328, DOI: 10.1021/jacs.8b08649.

(24) Singh, A. N.; Yethiraj, A. Driving Force for the Complexation of Charged Polypeptides. *The Journal of Physical Chemistry B* **2020**, *124*, 1285–1292, DOI: 10.1021/acs.jpcb.9b09553.

(25) Singh, A. N.; Yethiraj, A. Liquid–Liquid Phase Separation As the Second Step of Complex Coacervation. *The Journal of Physical Chemistry B* **2021**, *125*, 3023–3031, DOI: 10.1021/acs.jpcb.0c07349.

(26) Chen, S.; Wang, Z.-G. Driving force and pathway in polyelectrolyte complex coacervation. *Proceedings of the National Academy of Sciences* **2022**, *119*, e2209975119, DOI: 10.1073/pnas.2209975119.

(27) Shi, Y.; Beck, T. Deconstructing Free Energies in the Law of Matching Water Affinities. *The Journal of Physical Chemistry B* **2017**, *121*, 2189–2201, DOI: 10.1021/acs.jpcb.7b00104.

(28) Pettitt, B. M.; Rossky, P. J. Alkali halides in water: Ion–solvent correlations and ion–ion potentials of mean force at infinite dilution. *The Journal of Chemical Physics* **1986**, *84*, 5836–5844, DOI: 10.1063/1.449894.

(29) Debye, P. Some Results of a Kinetic Theory of Insulators. *Physik Z* **1912**, *13*.

(30) Onsager, L. Electric Moments of Molecules in Liquids. *Journal of the American Chemical Society* **1936**, *58*, 1486–1493, DOI: 10.1021/ja01299a050.

(31) Davies, R. O.; Scaife, B. K. Onsager's Theory of the Dielectric Constant of Polar Liquids. *The Journal of Chemical Physics* **1954**, *22*, 148–149, DOI: 10.1063/1.1739832.

(32) Lumry, R.; Rajender, S. Enthalpy–entropy compensation phenomena in water solutions of proteins and small molecules: A ubiquitous properly of water. *Biopolymers* **1970**, *9*, 1125–1227, DOI: 10.1002/bip.1970.360091002.

(33) Grunwald, E.; Steel, C. Solvent Reorganization and Thermodynamic Enthalpy-Entropy Compensation. *Journal of the American Chemical Society* **1995**, *117*, 5687–5692, DOI: 10.1021/ja00126a009.

(34) Bulo, R. E.; Donadio, D.; Laio, A., et al. "Site Binding" of Ca2+ Ions to Polyacrylates in Water: A Molecular Dynamics Study of Coiling and Aggregation. *Macromolecules* **2007**, *40*, 3437–3442, DOI: 10.1021/ma062467l.

(35) Shock, C. J.; Stevens, M. J.; Frischknecht, A. L.; Nakamura, I. Solvation Energy of Ions in a Stockmayer Fluid. *The Journal of Physical Chemistry B* **2020**, *124*, 4598–4604, DOI: 10.1021/acs.jpcb.0c00769.

(36) Weeks, J. D.; Chandler, D.; Andersen, H. C. Role of Repulsive Forces in Determining the Equilibrium Structure of Simple Liquids. *The Journal of Chemical Physics* **1971**, *54*, 5237–5247, DOI: 10.1063/1.1674820.

(37) Darve, E.; Rodríguez-Gómez, D.; Pohorille, A. Adaptive biasing force method for scalar and vector free energy calculations. *The Journal of Chemical Physics* **2008**, *128*, 144120, DOI: 10.1063/1.2829861.

(38) Hénin, J.; Fiorin, G.; Chipot, C.; Klein, M. L. Exploring Multidimensional Free Energy Landscapes Using Time-Dependent Biases on Collective Variables. *Journal of Chemical Theory and Computation* **2010**, *6*, 35–47, DOI: 10.1021/ct9004432.

(39) Brown, W. M.; Wang, P.; Plimpton, S. J.; Tharrington, A. N. Implementing molecular dynamics on hybrid high performance computers – short range forces. *Computer Physics Communications* **2011**, *182*, 898–911, DOI: 10.1016/j.cpc.2010.12.021.

(40) Brown, W. M.; Kohlmeyer, A.; Plimpton, S. J.; Tharrington, A. N. Implementing molecular dynamics on hybrid high performance computers – Particle–particle particle-mesh. *Computer Physics Communications* **2012**, *183*, 449–459, DOI: 10.1016/j.cpc.2011.10.012.

(41) Fiorin, G.; Klein, M. L.; Hénin, J. Using collective variables to drive molecular dynamics simulations. *Molecular Physics* **2013**, *111*, 3345–3362, DOI: 10.1080/00268976.2013.813594.

(42) Thompson, A. P.; Aktulga, H. M.; Berger, R., et al. LAMMPS - a flexible simulation tool for particle-based materials modeling at the atomic, meso, and continuum scales. *Computer Physics Communications* **2022**, *271*, 108171, DOI: 10.1016/j.cpc.2021.108171.

(43) Stukowski, A. Visualization and analysis of atomistic simulation data with OVITO-the Open Visualization Tool. *Modelling and Simulation in Materials Science and Engineering* **2010**, *18*, 015012, DOI: 10.1088/0965-0393/18/1/015012.

(44) Levy, A.; Andelman, D.; Orland, H. Dielectric Constant of Ionic Solutions: A Field-Theory Approach. *Physical Review Letters* **2012**, *108*, 227801, DOI: 10.1103/PhysRevLett.108.227801.

(45) Levy, A.; Andelman, D.; Orland, H. Dipolar Poisson-Boltzmann approach to ionic solutions: A mean field and loop expansion analysis. *The Journal of Chemical Physics* **2013**, *139*, 164909, DOI: 10.1063/1.4826103.

(46) Martin, J. M.; Li, W.; Delaney, K. T.; Fredrickson, G. H. Statistical field theory description of inhomogeneous polarizable soft matter. *The Journal of Chemical Physics* **2016**, *145*, 154104, DOI: 10.1063/1.4964680.

(47) Grzetic, D. J.; Delaney, K. T.; Fredrickson, G. H. Contrasting Dielectric Properties of Electrolyte Solutions with Polar and Polarizable Solvents. *Physical Review Letters* **2019**, *122*, 128007, DOI: 10.1103/PhysRevLett.122.128007.

(48) Zhuang, B.; Wang, Z.-G. Statistical field theory for polar fluids. *The Journal of Chemical Physics* **2018**, *149*, 124108, DOI: 10.1063/1.5046511.

(49) Nakamura, I.; Shi, A.-C.; Wang, Z.-G. Ion Solvation in Liquid Mixtures: Effects of Solvent Reorganization. *Physical Review Letters* **2012**, *109*, 257802, DOI: 10.1103/PhysRevLett.109.257802.

(50) Zhuang, B.; Wang, Z.-G. A molecularly based theory for electron transfer reorganization energy. *The Journal of Chemical Physics* **2015**, *143*, 224502, DOI: 10.1063/1.4936586.

(51) Zhuang, B.; Wang, Z.-G. Molecular-Based Theory for Electron-Transfer Reorganization Energy in Solvent Mixtures. *The Journal of Physical Chemistry B* **2016**, *120*, 6373–6382, DOI: 10.1021/acs.jpcb.6b03295.

(52) Levesque, D.; Weis, J. J.; Patey, G. N. The potential of mean force for an infinitely dilute ionic solution. *Physics Letters A* **1978**, *66*, 115–118, DOI: 10.1016/0375-9601(78)90012-9.

(53) Patey, G. N.; Carnie, S. L. Theoretical results for aqueous electrolytes. Ion–ion potentials of mean force and the solute-dependent dielectric constant. *The Journal of Chemical Physics* **1983**, *78*, 5183–5190, DOI: 10.1063/1.445388.

(54) Hirata, F.; Levy, R. M. Ionic association in methanol and related solvents: an extended RISM analysis. *The Journal of Physical Chemistry* **1987**, *91*, 4788–4795, DOI: 10.1021/j100302a028.

(55) Outhwaite, C. W. The potential of mean force between two ions in a dipolar solvent. *Molecular Physics* **2006**, DOI: 10.1080/00268977700101041.

(56) Sides, S. W.; Kim, B. J.; Kramer, E. J.; Fredrickson, G. H. Hybrid Particle-Field Simulations of Polymer Nanocomposites. *Physical Review Letters* **2006**, *96*, 250601, DOI: 10.1103/PhysRevLett.96.250601.

(57) Koski, J.; Chao, H.; Riggleman, R. A. Field theoretic simulations of polymer nanocomposites. *The Journal of Chemical Physics* **2013**, *139*, 244911, DOI: 10.1063/1.4853755.

(58) Chao, H.; Hagberg, B. A.; Riggleman, R. A. The distribution of homogeneously grafted nanoparticles in polymer thin films and blends. *Soft Matter* **2014**, *10*, 8083–8094, DOI: 10.1039/C4SM01188K.

(59) Fredrickson, G. H., *The equilibrium theory of inhomogeneous polymers*; International series of monographs on physics 134; Clarendon Press ; Oxford University Press: Oxford : New York, 2006; 437 pp.

(60) Wang, D.; Zhao, R.; Weeks, J. D.; Tiwary, P. Influence of Long-Range Forces on the Transition States and Dynamics of NaCl Ion-Pair Dissociation in Water. *The Journal of Physical Chemistry B* **2022**, *126*, 545–551, DOI: 10.1021/acs.jpcb.1c09454.

(61) Pollock, E. L.; Alder, B. J. Static dielectric properties of Stockmayer fluids. *Physica A: Statistical Mechanics and its Applications* **1980**, *102*, 1–21, DOI: 10.1016/0378-4371(80)90058-8.

(62) Ivanov, A. O.; Kuznetsova, O. B. Magnetic properties of dense ferrofluids: An influence of interparticle correlations. *Physical Review E* **2001**, *64*, 041405, DOI: 10.1103/PhysRevE.64.041405.

(63) Johnson, L. E.; Barnes, R.; Draxler, T. W.; Eichinger, B. E.; Robinson, B. H. Dielectric Constants of Simple Liquids: Stockmayer and Ellipsoidal Fluids. *The Journal of Physical Chemistry B* **2010**, *114*, 8431–8440, DOI: 10.1021/jp1010605.

(64) Kohns, M.; Marx, J.; Langenbach, K. Critical assessment of perturbation theories for the relative permittivity of dipolar model fluids. *Chemical Engineering Science* **2021**, *245*, 116875, DOI: 10.1016/j.ces.2021.116875.

(65) Zhuang, B.; Ramanauskaite, G.; Koa, Z. Y.; Wang, Z.-G. Like dissolves like: A first-principles theory for predicting liquid miscibility and mixture dielectric constant. *Science Advances* **2021**, *7*, eabe7275, DOI: 10.1126/sciadv.abe7275.

(66) Duan, X.; Nakamura, I. A new lattice Monte Carlo simulation for dielectric saturation in ion-containing liquids. *Soft Matter* **2015**, *11*, 3566–3571, DOI: 10.1039/C5SM00336A.

(67) Gavrilov, A. A.; Kramarenko, E. Y. Two contributions to the dielectric response of polar liquids. *The Journal of Chemical Physics* **2021**, *154*, 116101, DOI: 10.1063/5.0038440.

(68) Zhang, J.; Zhang, H.; Wu, T.; Wang, Q.; van der Spoel, D. Comparison of Implicit and Explicit Solvent Models for the Calculation of Solvation Free Energy in Organic Solvents. *Journal of Chemical Theory and Computation* **2017**, *13*, 1034–1043, DOI: 10.1021/acs.jctc.7b00169.

(69) Li, X.; Liu, C.; Van der Bruggen, B. Polyelectrolytes self-assembly: versatile membrane fabrication strategy. *Journal of Materials Chemistry A* **2020**, *8*, 20870–20896, DOI: 10.1039/D0TA07154D.

(70) Froimchuk, E.; Carey, S. T.; Edwards, C.; Jewell, C. M. Self-Assembly as a Molecular Strategy to Improve Immunotherapy. *Accounts of Chemical Research* **2020**, *53*, 2534–2545, DOI: 10.1021/acs.accounts.0c00438.

(71) Dergham, M.; Lin, S.; Geng, J. Supramolecular Self-Assembly in Living Cells. *Angewandte Chemie International Edition* **2022**, *61*, e202114267, DOI: 10.1002/anie.202114267.

(72) Krieger, A.; Zika, A.; Gröhn, F. Functional Nano-Objects by Electrostatic Self-Assembly: Structure, Switching, and Photocatalysis. *Frontiers in Chemistry* **2022**, *9*.

(73) Dragan, A. I.; Read, C. M.; Crane-Robinson, C. Enthalpy–entropy compensation: the role of solvation. *European Biophysics Journal* **2017**, *46*, 301–308, DOI: 10.1007/s00249-016-1182-6.

(74) Chen, Y.; Krämer, A.; Charron, N. E., et al. Machine learning implicit solvation for molecular dynamics. *The Journal of Chemical Physics* **2021**, *155*, 084101, DOI: 10.1063/5.0059915.

Chapter 7

INTERFACIAL BEHAVIOR OF ASYMMETRIC POLAR FLUIDS

We investigate the properties of the liquid–vapor interface in the shifted Stockmayer fluid using molecular dynamics simulations in the canonical ensemble. We study the role of the dipole moment strength and the degree of asymmetry on equilibrium interfacial characteristics, including density profiles, polar order, nematic order, interfacial polarization, electric field, and electrostatic potential. In addition, we compute angular distribution functions across the interface to gain insight into how the dipole shift affects the molecular orientation. We find that the shift significantly effects angular distribution functions by altering the polar order while leaving the nematic order relatively unaffected, in comparison to the reference symmetric Stockmayer fluid. We find that these results are consistently explained using an image-dipole construction that has been previously applied to symmetric Stockmayer fluids but has never been extended to the shifted model. We find remarkable agreement between the simple theory and the simulations in the qualitative shape of the distribution functions for both the liquid and vapor phases in proximity to the interface. Unexpectedly, the spontaneous polarization at the interface, and therefore the generated electric field, changes sign as the dipole moment strength increases. This also leads to an inversion of the sign of the potential difference across the interface.

This chapter includes content from our previously published article:

Varner, S.; Walker, P. J.; Venkatachalam, A.; Zhuang, B.; Wang, Z.-G. Stockmayer Fluid with a Shifted Dipole: Interfacial Behavior, 2025, DOI: 10.48550/arXiv.2509.05523

I am very thankful for analysis code provided by Dr. Benjamin Ye that was crucial for efficiently reading in LAMMPS trajectories containing dipole moments.

7.1 Introduction

It has been well documented that reaction rates can increase by several orders of magnitude in systems with confined volumes and large interfacial area, such as microemulsions [2–10]. Interfaces between water and other phases, including air and oil, are known to promote certain reactions through a process often referred

to as “on-water” catalysis [4]. This phenomenon is especially important in atmospheric chemistry, where abundant microdroplets can catalyze many reactions of atmospheric relevance [11–13]. Despite their significance, the molecular mechanisms responsible for this unique form of catalysis remain elusive and actively debated [14]. Explanations for the enhanced reactivity at water interfaces include evaporation-induced reactant enrichment [15], pH changes [16], partial solvation environments [3, 17], spatially varying dielectric properties [18], and orientational changes near the interface driven by entropic or enthalpic effects [19].

Perhaps the most compelling physical phenomenon that has been thought to drive interfacial chemistry is the presence of a strong electric field. Namely, if water (or another polar solvent) shows a preferential orientation at the interface, then an electric field will be spontaneously generated that can potentially stretch reactive bonds and lower the activation barrier [20–22]. In fact, enzymes catalyze reactions in a similar manner, by orienting reactant molecules such that reactive bonds align with strong directional electric fields inside the active site [20, 23–29]. In the case of the air–water interface, vibrational sum frequency generation (vSFG) measurements have revealed that water preferentially orients with a "dangling" O-H bond at the surface [30–33], supported underneath by a 2-dimensional hydrogen bond network [34, 35]. These dangling O-H bonds can serve as probes for the local electric field. The Stark shifts measured in Infrared Photodissociation (IRPD) spectroscopy have revealed a significant electric field at the air–water interface [36]. Recently the electric field at an air-oil interface was quantified via Stimulated Raman excited flourescence (SREF) microscopy, where a magnitude of 10MV/cm was reported. This is also in agreement with electric fields recently computed from ReaxFF/C-GeM molecular dynamics (MD) simulations [37], while ab initio calculations predicted much stronger fields on the order of hundreds of MV/cm [38]. Nevertheless, these results all indicate the presence of electric fields strong enough to lower activation barriers or drive bond breaking.

For good reason, most studies of interfacial electric fields have focused on air–water and oil–water systems because of their atmospheric and biological relevance. Water has many distinctive features, including high polarity, autoionization, and a strong hydrogen bonding network [39–41]. The combination of these effects makes it difficult to determine the true origin of the strong electric fields observed at the water interface. In addition, results obtained specifically for water cannot be easily applied to other liquids that do not share its special bulk properties. To better identify

the general physical factors that can generate interfacial polarization, coarse-grained models are especially useful.

The Stockmayer fluid[42, 43] (SF) is by far the most studied model for general polar fluids. In this model, molecules are represented as Lennard-Jones spheres with a point dipole located at the center. A large body of work has explored the properties of the SF model and its connections to real fluids. Research has examined ion solvation energy and dynamics [44–46], dielectric properties [47–49], ferroelectric transitions [50–53], and phase equilibria [54–56]. The liquid–vapor interface of the SF model has also been the subject of extensive theoretical and simulation studies. These works show that spherical particles with permanent dipoles adopt preferential orientations across the interface that are largely determined by strong dipolar interactions. Classical density functional theory (cDFT) and integral equation theory predict that dipoles align parallel to the interface on the liquid side and perpendicular on the vapor side [57–59]. MD simulations of the SF model support the parallel orientation within the liquid but generally do not reproduce the perpendicular orientation in the vapor [56, 60–62]. However, because of the spherical symmetry of the molecules, the SF model cannot produce a net electric field at the interface (in the absence of a ferroelectric transition).

We hypothesize that introducing slight molecular asymmetry into the SF model is sufficient to break the symmetry at the interface and generate an electric field. In real molecules, the geometric structure does not always coincide with the charge distribution, which can shift the effective dipole toward one side of the molecule. The simplest way to capture this effect is with a spherical particle that carries a point dipole displaced by a distance d from its geometric center. This extension of the SF model is known as the shifted Stockmayer fluid (sSF) [63]. Although still highly coarse-grained, the sSF model is more realistic than the SF model, since nearly all real dipolar molecules have non-centered dipoles. The earliest use of the sSF model we found in the literature is by Kusaka et al., who applied it to study the sign effect in ion-induced water-droplet nucleation in the atmosphere [64]. Subsequently, the model received little attention until Langenbach introduced the Co-Oriented Fluid Functional Equation for Electrostatic interactions (COFFEE) in 2017 [63]. This perturbative approach enables accurate predictions of the properties of homogeneous liquids and vapors for both SF and sSF models at a fraction of the cost of molecular dynamics simulations, though it is restricted to certain dipole strengths and shifts. However, because it is formulated for homogeneous fluids,

COFFEE cannot be applied directly to interfacial properties such as density and electric field profiles. To complement and validate this theory, Marx, Kohns, and Langenbach have performed extensive MD and Monte Carlo simulations to characterize the liquid–vapor equilibrium and dielectric behavior of the SF and sSF models [54, 55, 65]. To the best of our knowledge, the properties of the liquid–vapor interface for the sSF model have yet to be studied.

In this study, we investigate whether a small shift of the dipole from the molecular center is sufficient to drive interfacial polarization and generate a measurable electric field. To address this question, we perform MD simulations of the liquid–vapor interface using the sSF model. Our analysis uncovers the mechanisms of orientational polarization at the interface and quantifies the spontaneously generated local electric field across a wide range of dipole strengths and shifts. To interpret these results, we employ a simple image dipole framework that clarifies the origin of the angular distribution functions in the liquid and vapor regions adjacent to the interface. We start by presenting the simulation setup and methodology for studying the interface in the next section.

7.2 Shifted Stockmayer Simulation Model

In this section, we outline the simulation setup and methodology for analyzing the properties of the liquid–vapor interface for the shifted Stockmayer fluid model.

Molecular Dynamics

To study the interfacial structure in asymmetric polar fluids, we utilize a modified version of the Stockmayer fluid (SF) model sometimes referred to as the *shifted* Stockmayer fluid (sSF) [63]. In this model, molecules are represented by hard spherical particles that contain a point-dipole. In the SF, the point dipole is located at the center of the hard sphere, whereas in the sSF the dipole can be shifted off the center. A schematic of a particle in the sSF model is provided in Figure 7.1.

The hard-sphere and van der Waals interactions are captured using the 12-6 Lennard-Jones (LJ) potential.

$$U_{\mathrm{LJ}}(r_{ij}) = \begin{cases} 4\epsilon \left[\left(\frac{\sigma}{r_{ij}}\right)^{12} - \left(\frac{\sigma}{r_{ij}}\right)^{6} \right] + S\,, & \text{if } r_{ij} \leq r_c \\ 0\,, & \text{if } r_{ij} > r_c. \end{cases} \tag{7.1}$$

Here, ϵ is the interaction strength, σ is the particle size, and $r_{ij} = ||\mathbf{r}_{ij}||$ is the distance between particles i and j. We utilize the truncated and shifted LJ potential

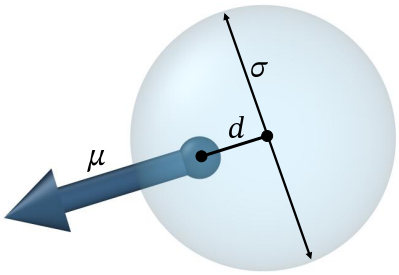

Figure 7.1: Schematic of shifted Stockmayer particle where σ is the particle diameter, d is the distance between the particle center and point dipole, and μ is the permanent dipole strength.

with a cutoff of $r_c = 2.5\sigma$ to decrease the computational cost while still allowing for a liquid–vapor split. S then provides the shift necessary such that $U_{\mathrm{LJ}}(r_c) = 0$. We note that this choice is inconsequential since we only require the van der Waals interaction to naturally create the interface within our simulation and not to provide any quantitative description or comparison to previous simulations or real fluids. Also note that the original work by Langenbach and co-workers used the full LJ potential. As such, quantitative differences are to be expected. The dipole–dipole interaction potential is given by,

$$U_{\mathrm{dipole}}(\boldsymbol{\mu}_i, \boldsymbol{\mu}_j, \mathbf{r}_{ij}) = \frac{\boldsymbol{\mu}_i \cdot \boldsymbol{\mu}_j}{r_{ij}^3} - \frac{(\boldsymbol{\mu}_i \cdot \mathbf{r}_{ij})(\boldsymbol{\mu}_j \cdot \mathbf{r}_{ij})}{r_{ij}^5}, \tag{7.2}$$

where $\boldsymbol{\mu}_i$ is the dipole moment vector of particle i, and $\mathbf{r}_{ij}$ is the displacement vector between dipoles i and j [66]. To represent the sSF model, we separate the LJ and dipole potential between an LJ (real) and dipole (ghost) particle. The location of the dipole particle is offset by a distance d from the center of the LJ particle. Thus, the location of the dipole particle can be written with respect to the LJ particle coordinate according to $\mathbf{r}_i' = \mathbf{r}_i + \hat{\boldsymbol{\mu}}_i d$. Note that this also requires that the dipole moment will always be pointing away from the center of the LJ particle, parallel to the bond vector between the two particles. As such, the LJ+dipole molecule must be rigid, with no internal translation or rotation. To enforce this constraint within our MD simulations, we utilize the rigid small-molecule NVT integrator that is freely available in LAMMPS [67]. To compute the long-ranged dipole–dipole interactions, we utilize the particle-particle particle-mesh (PPPM) solver [68, 69]. We adjust the real-space cutoff for each simulation independently to maximize the efficiency. The cutoff is typically between $8 - 10\sigma$.

To generate a natural interface, we employ a strategy commonly used for studying

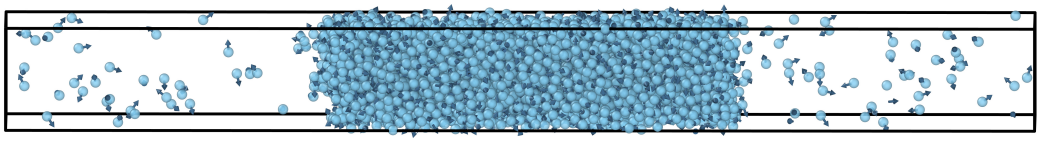

Figure 7.2: Snapshot of liquid–vapor equilibrium simulation using the sSF model. Blue spheres represent the Lennard–Jones particles and yellow arrows represent the point dipoles which are interior to the Lennard-Jones particles. Visualizations are made in OVITO [70].

liquid–vapor equilibrium. We simulate 3000 molecules total (i.e., 3000 LJ particles and 3000 dipoles) in a box of dimensions $L_x, L_y, L_z = 10\sigma, 10\sigma, 100\sigma$. The extended z-dimension allows for a liquid slab located in the center of the box that is approximately $40 - 50\sigma$ in length, with vapor on either side. This style of system setup has been widely used for studying properties of liquid–vapor and liquid-liquid interfaces with both classical and ab-initio MD simulations [32, 33, 38, 71–84], and has also been used to study the liquid–vapor equilibrium of the regular Stockmayer fluid [56, 60–62, 85, 86]. We provide an example snapshot from our slab simulations in Figure 7.2. We assign a mass of $m = 1$ to the LJ particle and $m = 0.001$ to the dipole particle. In addition, we turn off all LJ interactions involving the point dipole particles. Unless otherwise stated, we set $k_B = 1$, $T = 1$, $\sigma = 1$, and $\epsilon = 1$. Within a given simulation, all dipole particles have the same dipole moment magnitude, $\mu = \|\boldsymbol{\mu}_i\|$. We use the `rigid/nvt/small` integrator in LAMMPS with a timestep of 0.005τ and a damping parameter of 0.5τ, where $\tau = \sqrt{m\sigma^2/\epsilon}$ [67].

We create a randomized initial configuration using Packmol [87]. Then, we create the liquid slab in the center of the simulation box by running a short simulation with a dragging force applied in the z-direction that is antisymmetric about $z = L_z/2$. Once the liquid slab is stabilized, we turn off the dragging force and allow the liquid–vapor equilibrium to develop for 5×10^4 timesteps. Following the equilibration run, we perform a production run for 4×10^6 timesteps, where we output the particle coordinates and dipole orientations every 100 timesteps for analysis.

Finally, during analysis we use the instantaneous interface [88] position to shift the particle coordinates, as described in the following section. We believe this method is more robust than zeroing the system center of mass, as the presence of more vapor particles on one side of the liquid than the other can significantly affect the interface location. All trajectory analysis was performed using custom analysis modules implemented in the open-source MDCraft software [89].

Instantaneous Interface

Our main focus of this work is to analyze the interfacial properties of the sSF. Thus, it behooves us to utilize a rigorous definition of the interface, which can undulate and drift throughout the course of our simulations. By computing the location of the interface at each simulation frame, we can shift the coordinates during analysis to maintain a consistent frame for computing spatially varying profiles. We define the location of the interface according to the *instantaneous interface*, as defined by Willard and Chandler [88, 90]. Specifically, we center Gaussians of form $f(r) = (2\pi\eta^2)^{-3/2} e^{-r^2/2\eta^2}$ at the location of each *LJ* particle. We sum all of the Gaussians, accounting for periodic boundary conditions, to generate a continuous three-dimensional density field. We then define the *left* and *right* interfaces by computing the two density iso-surfaces $z_l(x, y)$ and $z_r(x, y)$, respectively. The target density is chosen to be exactly halfway between that of the liquid and the vapor, as determined from the computed density field. To obtain a scalar definition of the location of the two interfaces, we compute their averages via integration using $\bar{z}_l = (L_x L_y)^{-1} \int dx \int dy \; z_l(x, y)$ and $\bar{z}_r = (L_x L_y)^{-1} \int dx \int dy \; z_r(x, y)$. We provide example visualizations of the instantaneous interface for a single frame in Figures 7.3 and 7.4.

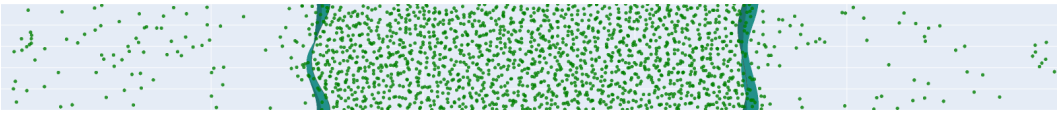

Figure 7.3: Example of instantaneous interfaces computed using the method of Willard and Chandler [88].

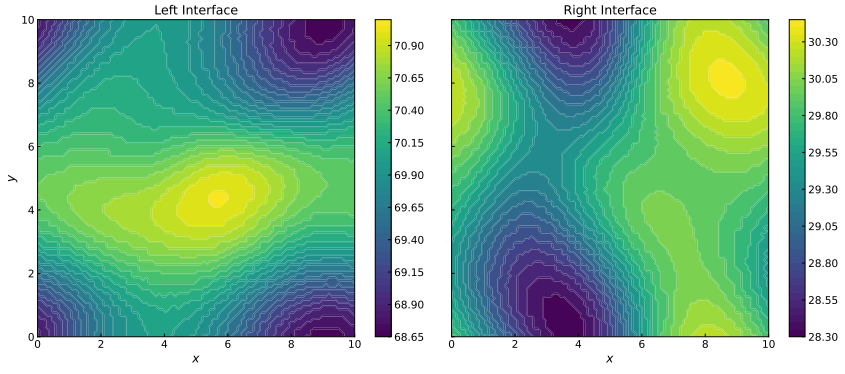

Figure 7.4: 2d contour plots of the left and right interfaces from Figure 7.3.

7.3 Extension of Dipolar Field Theory

In addition to molecular dynamics simulations, we develop a mean-field theory for a shifted dipolar fluid that is an extension of the dipolar self-consistent field theory (DSCFT) presented in the previous chapter. Here we study the simplest possible system containing an inhomogeneous density of asymmetric polar molecules. We represent the molecules as spheres with point dipoles that are offset from the molecule center. The orientation of the dipole is rigid with respect to the molecule frame, such that the dipole rotates with the molecule, but not independently. Also for simplicity, we impose density profiles characteristic of VLE, rather than including non-electrostatic interactions, since our main objective is to analyze the polarization in response to a density gradient, regardless of how the density gradient is generated.

Canonical Partition Function

The molecules are represented as point dipoles that are shifted or offset from the molecular center. Thus, the intstaneous polarization of a single molecule is given by the following,

$$\hat{\mathbf{P}}_i(\mathbf{r}) = \boldsymbol{\mu}_i \delta(\mathbf{r} - (\mathbf{r}_i + d\hat{\boldsymbol{\mu}}_i)) \tag{7.3}$$

where $\boldsymbol{\mu}_i$ is the dipole moment of molecule i, $\hat{\boldsymbol{\mu}}_i$ is the unit vector of the dipole moment, $\mathbf{r}_i$ is the position of the center of molecule i, and d is the dipole offset. The total instantaneous polarization is the sum of all the molecular dipoles,

$$\hat{\mathbf{P}}(\mathbf{r}) = \sum_{i=1}^{N} \hat{\mathbf{P}}_i(\mathbf{r}) = \sum_{i=1}^{N} \boldsymbol{\mu}_i \delta(\mathbf{r} - (\mathbf{r}_i + d\hat{\boldsymbol{\mu}}_i)) \tag{7.4}$$

and the microscopic number density is,

$$\hat{\rho}(\mathbf{r}) = \sum_{i=1}^{N} \delta(\mathbf{r} - \mathbf{r}_i) \ . \tag{7.5}$$

The dipoles interact via the typical dipolar interaction potential, which gives rise to the following potential energy,

$$\beta U(\mathbf{r}^N, \hat{\boldsymbol{\mu}}^N) = \frac{1}{2} \int d\mathbf{r} \int d\mathbf{r}' \hat{\mathbf{P}}(\mathbf{r}) \mathbf{T}(\mathbf{r} - \mathbf{r}') \hat{\mathbf{P}}(\mathbf{r}') \tag{7.6}$$

with the interaction kernel given by

$$\begin{aligned} \mathbf{T}(\mathbf{r} - \mathbf{r}') &= -\nabla\nabla \frac{\beta}{4\pi\epsilon_0 |\mathbf{r} - \mathbf{r}'|} \\ &= H(|\mathbf{r} - \mathbf{r}'| - \eta) \frac{\beta}{4\pi\epsilon_0 |\mathbf{r} - \mathbf{r}'|^3} \left[\mathbf{I} - \frac{3(\mathbf{r} - \mathbf{r}')(\mathbf{r} - \mathbf{r}')}{|\mathbf{r} - \mathbf{r}'|^2} \right] + \frac{\beta}{3\epsilon_0} \mathbf{I} \delta(\mathbf{r} - \mathbf{r}') \end{aligned} \tag{7.7}$$

Rather than include non-electrostatic interactions, we instead impose an artificial density profile $\rho(\mathbf{r})$, that is characteristic of a vapor-liquid interface.

$$\delta[\hat{\rho}(\mathbf{r}) - \rho(\mathbf{r})] = \int \mathcal{D}w \exp\left\{ i \int d\mathbf{r} w(\mathbf{r})[\hat{\rho}(\mathbf{r}) - \rho(\mathbf{r})] \right\} \tag{7.8}$$

The full canonical partition function is thus,

$$Z(N) = \frac{1}{N!} \int \mathcal{D}w \left(\prod_{i=1}^{N} \frac{1}{4\pi v} \int d\mathbf{r}_i \int d\hat{\boldsymbol{\mu}}_i \right) \exp\left\{ -\frac{1}{2} \int d\mathbf{r} \int d\mathbf{r}' \hat{\mathbf{P}}(\mathbf{r}) \mathbf{T}(\mathbf{r}-\mathbf{r}') \hat{\mathbf{P}}(\mathbf{r}') \right.$$
$$\left. + i \int d\mathbf{r} w(\mathbf{r})[\hat{\rho}(\mathbf{r}) - \rho(\mathbf{r})] \right\} \tag{7.9}$$

Normally at this stage, we would perform the Hubbard-Stratonovich transformation to decouple the quadratic interactions via introduction of a fluctuating field. The dipolar interaction kernel, $\mathbf{T}$, however, does not have a functional inverse, and thus the HS transformation cannot be performed. Instead, we introduce a coarse-grained polarization density, $\mathbf{P}(\mathbf{r})$ that we couple to a fluctuating field, $\mathbf{G}(\mathbf{r})$, using a delta functional identity transform.

$$1 = \int \mathcal{D}\mathbf{P} \delta\left[\hat{\mathbf{P}} - \mathbf{P}\right] = \int \mathcal{D}\mathbf{P} \int \mathcal{D}\mathbf{G} \exp\left\{ i \int d\mathbf{r} \mathbf{G}(\mathbf{r}) \cdot \left[\hat{\mathbf{P}}(\mathbf{r}) - \mathbf{P}(\mathbf{r})\right] \right\} \tag{7.10}$$

Thus, the canonical partition function can now be written as,

$$Z(N) = \int \mathcal{D}w \int \mathcal{D}\mathbf{P} \int \mathcal{D}\mathbf{G} \exp\left\{ -\frac{1}{2} \int d\mathbf{r} \int d\mathbf{r}' \mathbf{P}(\mathbf{r}) \mathbf{T}(\mathbf{r}-\mathbf{r}') \mathbf{P}(\mathbf{r}') \right.$$
$$\left. - i \int d\mathbf{r} w(\mathbf{r}) \rho(\mathbf{r}) - i \int d\mathbf{r} \mathbf{G} \cdot \mathbf{P} \right\} \frac{1}{N!} \left(\prod_{i=1}^{N} \frac{1}{4\pi v} \int d\mathbf{r}_i \int d\hat{\boldsymbol{\mu}}_i \right) \times$$
$$\times \exp\left\{ i \int d\mathbf{r} w(\mathbf{r}) \hat{\rho}(\mathbf{r}) + i \int d\mathbf{r} \mathbf{G} \cdot \hat{\mathbf{P}} \right\} \tag{7.11}$$

To simplify this expression, we can group all of the terms that depend on particle coordinates and orientations into the single particle partition function, $Q[w, \mathbf{G}]$,

$$Q[w, \mathbf{G}] = \frac{1}{4\pi v} \int d\mathbf{r} \int d\hat{\boldsymbol{\mu}} \exp\left\{ i w(\mathbf{r}) + i \int d\mathbf{r}' \mathbf{G}(\mathbf{r}') \cdot \mu \hat{\boldsymbol{\mu}} \delta(\mathbf{r}' - (\mathbf{r} + d\hat{\boldsymbol{\mu}})) \right\}$$
$$= \frac{1}{4\pi v} \int d\mathbf{r} \int d\hat{\boldsymbol{\mu}} \exp\left\{ i w(\mathbf{r}) + i \mathbf{G}(\mathbf{r} + d\hat{\boldsymbol{\mu}}) \cdot \hat{\boldsymbol{\mu}} \mu \right\} \tag{7.12}$$

To simplify this expression, we can assume that $\mathbf{G}$ is slowly varying, and the offset d is small, such the following Taylor expansion can be used.

$$\mathbf{G}(\mathbf{r} + d\hat{\boldsymbol{\mu}}) \approx \mathbf{G}(\mathbf{r}) + d \nabla \mathbf{G}(\mathbf{r}) \cdot \hat{\boldsymbol{\mu}} \tag{7.13}$$

The partition function is then,

$$\begin{aligned} Q[w,\mathbf{G}] &= \frac{1}{4\pi v}\int d\mathbf{r}\int d\hat{\boldsymbol{\mu}}\exp\{iw + i\mathbf{G}\cdot\hat{\boldsymbol{\mu}}\mu + id\mu\hat{\boldsymbol{\mu}}\cdot\nabla\mathbf{G}\cdot\hat{\boldsymbol{\mu}}\} \\ &= \frac{1}{4\pi v}\int d\mathbf{r}e^{iw(\mathbf{r})}\int d\hat{\boldsymbol{\mu}}\exp\{i\mathbf{G}\cdot\hat{\boldsymbol{\mu}}\mu + id\mu\hat{\boldsymbol{\mu}}\cdot\nabla\mathbf{G}\cdot\hat{\boldsymbol{\mu}}\} \\ &= \frac{1}{4\pi v}\int d\mathbf{r}e^{iw(\mathbf{r})}\int d\hat{\boldsymbol{\mu}}\exp\{\mathbf{A}\cdot\hat{\boldsymbol{\mu}} + \hat{\boldsymbol{\mu}}\cdot\mathbf{B}\cdot\hat{\boldsymbol{\mu}}\} \end{aligned} \tag{7.14}$$

where $\mathbf{A} = i\mu\mathbf{G}$ and $\mathbf{B} = id\mu\nabla\mathbf{G}$. If we assume that $\mathbf{G}$ only varies in the z dimension, then we can greatly simplify the integral over the dipole orientation,

$$\begin{aligned} q[\mathbf{G},\nabla\mathbf{G}] &= 2\pi\int_0^\pi \sin\theta d\theta e^{A_z\cos\theta + B_{zz}\cos^2\theta} = 2\pi\int_{-1}^{1} dx e^{ax+bx^2} \\ &= \frac{\pi^{3/2}e^{-a^2/4b}}{b^{1/2}}\left[\operatorname{erfi}\left(\frac{a+2b}{2b^{1/2}}\right) - \operatorname{erfi}\left(\frac{a-2b}{2b^{1/2}}\right)\right] \end{aligned} \tag{7.15}$$

Thus, the single particle partition function is equal to

$$Q[w,\mathbf{G}] = \frac{1}{4\pi v}\int d\mathbf{r}e^{iw(\mathbf{r})}q[\mathbf{G},\nabla\mathbf{G}] \tag{7.16}$$

The full partition function can then be simply written as

$$\begin{aligned} Z(N) = \int \mathcal{D}w\int \mathcal{D}\mathbf{P}\int \mathcal{D}\mathbf{G}\exp\Bigg\{-\frac{1}{2}\int d\mathbf{r}\int d\mathbf{r}'\mathbf{P}(\mathbf{r})\mathbf{T}(\mathbf{r}-\mathbf{r}')\mathbf{P}(\mathbf{r}') \\ - i\int d\mathbf{r}w(\mathbf{r})\rho(\mathbf{r}) - i\int d\mathbf{r}\mathbf{G}\cdot\mathbf{P} + N\ln Q[w,\mathbf{G}] - \ln N!\Bigg\} \end{aligned} \tag{7.17}$$

More simply put, we have

$$Z(N) = \int \mathcal{D}w\int \mathcal{D}\mathbf{P}\int \mathcal{D}\mathbf{G}e^{-\beta H[w,\mathbf{G},\mathbf{P}]} \tag{7.18}$$

where the Hamiltonian is given by,

$$\begin{aligned} \beta H[w,\mathbf{G},\mathbf{P}] = \frac{1}{2}\int d\mathbf{r}\int d\mathbf{r}'\mathbf{P}(\mathbf{r})\mathbf{T}(\mathbf{r}-\mathbf{r}')\mathbf{P}(\mathbf{r}') + i\int d\mathbf{r}w(\mathbf{r})\rho(\mathbf{r}) \\ + i\int d\mathbf{r}\mathbf{G}\cdot\mathbf{P} - N\ln Q[w,\mathbf{G}] + \ln N! \end{aligned} \tag{7.19}$$

Saddle-Point Equations

We can determine the equilibrium configuration by finding the saddle-point of the Hamiltonian, which yields the maximal contribution to the partition function. The saddle-point approximation gives an approximate free energy, $\beta F = -\ln Z \approx$

βH^*, where H^* is the saddle-point Hamiltonian. We can find the saddle-point by extremizing the Hamiltonian (free energy) with respect to all of the fluctuating fields. Note that at the saddle-point, the Hamiltonian is real-valued, which means that w and $\mathbf{G}$ are purely imaginary. Thus, for simplicity, we will make the following replacements in all equations: $iw = \omega$ and $i\mathbf{G} = \mathbf{U}$.

$$\beta H[\omega, \mathbf{U}, \mathbf{P}] = \frac{1}{2}\int d\mathbf{r}\int d\mathbf{r}'\mathbf{P}(\mathbf{r})\mathbf{T}(\mathbf{r}-\mathbf{r}')\mathbf{P}(\mathbf{r}') + \int d\mathbf{r}\omega(\mathbf{r})\rho(\mathbf{r}) + \int d\mathbf{r}\mathbf{U}\cdot\mathbf{P} - N\ln Q[\omega, \mathbf{U}] + \ln N! \quad (7.20)$$

Extremizing the Hamiltonian with respect to $\mathbf{P}$ yields,

$$\frac{\delta\beta H}{\delta\mathbf{P}} = \mathbf{U} + \int d\mathbf{r}'\mathbf{T}(\mathbf{r}-\mathbf{r}')\mathbf{P}(\mathbf{r}') = 0 \quad (7.21)$$

Extremizing with respect to ω yields,

$$\frac{\delta\beta H}{\delta\omega} = \rho(\mathbf{r}) - \frac{N}{Q}\frac{\delta Q}{\delta\omega} = \rho(\mathbf{r}) - \frac{N}{4\pi v Q}e^{\omega(\mathbf{r})}q[\mathbf{U}, \nabla\mathbf{U}] = 0 \quad (7.22)$$

and lastly, we can extremize with respect to $\mathbf{U}$,

$$\frac{\delta\beta H}{\delta\mathbf{U}} = \mathbf{P} - \frac{N}{Q}\frac{\delta Q}{\delta\mathbf{U}} = 0 \quad (7.23)$$

where we have

$$\begin{aligned}
\frac{\delta Q}{\delta \mathbf{U}} &= \frac{1}{4\pi v}\int d\mathbf{r}''\int d\hat{\boldsymbol{\mu}}\mu\hat{\boldsymbol{\mu}}\delta(\mathbf{r}-(\mathbf{r}''+d\hat{\boldsymbol{\mu}}))e^{\int d\mathbf{r}'\mu\hat{\boldsymbol{\mu}}\cdot\mathbf{U}(\mathbf{r}')\delta(\mathbf{r}'-(\mathbf{r}''+d\hat{\boldsymbol{\mu}}))+\omega(\mathbf{r}'')} \\
&= \frac{\mu}{4\pi v}\int d\hat{\boldsymbol{\mu}}\hat{\boldsymbol{\mu}}e^{\mu\hat{\boldsymbol{\mu}}\cdot\mathbf{U}(\mathbf{r})+\omega(\mathbf{r}-d\hat{\boldsymbol{\mu}})} \\
&\approx \frac{\mu}{4\pi v}\int d\hat{\boldsymbol{\mu}}\hat{\boldsymbol{\mu}}e^{\mu\hat{\boldsymbol{\mu}}\cdot\mathbf{U}(\mathbf{r})+\omega(\mathbf{r})-\nabla\omega\cdot\hat{\boldsymbol{\mu}}d} \\
&= \frac{\mu}{4\pi v}e^{\omega(\mathbf{r})}\int d\hat{\boldsymbol{\mu}}\hat{\boldsymbol{\mu}}e^{[\mu\mathbf{U}(\mathbf{r})-d\nabla\omega]\cdot\hat{\boldsymbol{\mu}}} \\
&= \frac{\mu}{4\pi v}e^{\omega(\mathbf{r})}\int_0^{\pi} d\theta\sin\theta e^{|\mu\mathbf{U}(\mathbf{r})-d\nabla\omega|\cos\theta}\int_0^{2\pi} d\phi\begin{bmatrix}\sin\theta\cos\phi\\ \sin\theta\sin\phi\\ \cos\theta\end{bmatrix} \\
&= \frac{\mu}{2v}e^{\omega(\mathbf{r})}\int_{-1}^{1} dx e^{|\mathbf{J}(\mathbf{r})|x}\begin{bmatrix}0\\0\\x\end{bmatrix} \\
&= \frac{\mu}{v}e^{\omega(\mathbf{r})}\begin{bmatrix}0\\0\\ \frac{|\mathbf{J}|\cosh|\mathbf{J}|-\sinh|\mathbf{J}|}{|\mathbf{J}|^2}\end{bmatrix} \\
&= \frac{\mu}{v}e^{\omega(\mathbf{r})}\frac{|\mathbf{J}|\cosh|\mathbf{J}|-\sinh|\mathbf{J}|}{|\mathbf{J}|^3}\mathbf{J}
\end{aligned} \tag{7.24}$$

where $\mathbf{J}(\mathbf{r}) = \mu\mathbf{U}(\mathbf{r}) - d\nabla\omega$. In the above analysis, we rotated the coordinate axis to be parallel with $\mathbf{J}$, and then after the integration, we rotated it back. Later, we will reduce the system to variation in a singular dimension, and so $\mathbf{J}$ will ultimately only have a single component. Finally, we have

$$\frac{\delta\beta H}{\delta\mathbf{U}} = \mathbf{P} - \frac{N\mu}{vQ}e^{\omega(\mathbf{r})}\frac{|\mathbf{J}|\cosh|\mathbf{J}|-\sinh|\mathbf{J}|}{|\mathbf{J}|^3}\mathbf{J} = 0 \tag{7.25}$$

Thus, the final set of self-consistent saddle-point equations is:

$$\mathbf{U}(\mathbf{r}) = -\int d\mathbf{r}'\mathbf{T}(\mathbf{r}-\mathbf{r}')\mathbf{P}(\mathbf{r}') \tag{7.26}$$

$$\rho(\mathbf{r}) = \frac{N}{4\pi vQ}e^{\omega(\mathbf{r})}q[\mathbf{U},\nabla\mathbf{U}] \tag{7.27}$$

$$\mathbf{P} = \frac{N\mu}{vQ}e^{\omega(\mathbf{r})}\frac{|\mathbf{J}|\cosh|\mathbf{J}| - \sinh|\mathbf{J}|}{|\mathbf{J}|^3}\mathbf{J} \tag{7.28}$$

$$\mathbf{J}(\mathbf{r}) = \mu\mathbf{U}(\mathbf{r}) - d\nabla\omega \tag{7.29}$$

$$Q[\omega,\mathbf{U}] = \frac{1}{4\pi v}\int d\mathbf{r}e^{\omega(\mathbf{r})}q[\mathbf{U},\nabla\mathbf{U}] \tag{7.30}$$

$$q[\mathbf{U},\nabla\mathbf{U}] = \frac{\pi^{3/2}e^{-a^2/4b}}{b^{1/2}}\left[\mathrm{erfi}\left(\frac{a+2b}{2b^{1/2}}\right) - \mathrm{erfi}\left(\frac{a-2b}{2b^{1/2}}\right)\right] \tag{7.31}$$

$$a = \mu U_z \tag{7.32}$$

$$b = d\mu\frac{\partial U_z}{\partial z} \tag{7.33}$$

Dipole Interaction Integral

Everything is mostly straightforward from this point, except for evaluation of the first equation in the box above.

$$\begin{aligned}\mathbf{U}(\mathbf{r}) &= -\int d\mathbf{r}'\mathbf{T}(\mathbf{r}-\mathbf{r}')\mathbf{P}(\mathbf{r}') \\ &= -\int d\mathbf{r}'\Bigg\{H(|\mathbf{r}-\mathbf{r}'|-\eta)\frac{\beta}{4\pi\epsilon_0|\mathbf{r}-\mathbf{r}'|^3}\left[\mathbf{I} - \frac{3(\mathbf{r}-\mathbf{r}')(\mathbf{r}-\mathbf{r}')}{|\mathbf{r}-\mathbf{r}'|^2}\right] \\ &\quad + \frac{\beta}{3\epsilon_0}\mathbf{I}\delta(\mathbf{r}-\mathbf{r}')\Bigg\}\mathbf{P}(\mathbf{r}')\end{aligned} \tag{7.34}$$

We will assume that $\mathbf{P} = (0, 0, P_z(z))$, and we will integrate each term separately in cylindrical coordinates.

$$\begin{aligned}I_1(z) &= \int d\mathbf{r}'H(|\mathbf{r}-\mathbf{r}'|-\eta)\frac{\beta}{4\pi\epsilon_0|\mathbf{r}-\mathbf{r}'|^3}\mathbf{I}\mathbf{P} \\ &= \int d\mathbf{r}'H(|\mathbf{r}-\mathbf{r}'|-\eta)\frac{\beta}{4\pi\epsilon_0|\mathbf{r}-\mathbf{r}'|^3}\begin{bmatrix}1&0&0\\0&1&0\\0&0&1\end{bmatrix}\begin{bmatrix}0\\0\\P_z(z')\end{bmatrix}\end{aligned} \tag{7.35}$$

$$
\begin{aligned}
I_{1,z}(z) &= \frac{\beta}{4\pi\epsilon_0}\int d\mathbf{r}' H(|\mathbf{r}-\mathbf{r}'|-\eta)\frac{1}{|\mathbf{r}-\mathbf{r}'|^3}P_z(z') \\
&= \frac{\beta}{4\pi\epsilon_0}\int_0^{2\pi} d\theta \int_{-L}^{L} dz' P_z(z') \int_0^{\infty} drr \frac{H\left[(r^2+(z-z')^2)^{1/2}-\eta\right]}{(r^2+(z-z')^2)^{3/2}} \\
&= \frac{\beta}{2\epsilon_0}\int_{-L}^{L} dz' P_z(z') \int_{|z-z'|}^{\infty} du \frac{H\left[u-\eta\right]}{u^2}
\end{aligned} \tag{7.36}
$$

This integral has to be evaluated piecewise, based on whether $|z-z'| < \eta$ or $|z-z'| > \eta$.

$$
\int_{|z-z'|}^{\infty} du \frac{H\left[u-\eta\right]}{u^2} = \begin{cases} |z-z'|^{-1} & \text{if} \quad |z-z'| \geq \eta, \\ \eta^{-1} & \text{if} \quad |z-z'| < \eta \end{cases} \tag{7.37}
$$

Finishing the integral over z' we get the following,

$$
\begin{aligned}
I_{1,z}(z) &= \frac{\beta}{2\epsilon_0}\int_{|z-z'|<\eta} dz' \frac{P_z(z')}{\eta} + \frac{\beta}{2\epsilon_0}\int_{|z-z'|\geq\eta} dz' \frac{P_z(z')}{|z-z'|} \\
&= \frac{\beta}{\epsilon_0}\left\langle P_z(z)\right\rangle_{|z-z'|<\eta} + \frac{\beta}{2\epsilon_0}\int_{|z-z'|\geq\eta} dz' \frac{P_z(z')}{|z-z'|}
\end{aligned} \tag{7.38}
$$

Once we are done evaluating all of the components, then we can take the limit as $\eta \to 0$. The second term in the integral can be evaluated in a similar manner, however, we first have to enumerate $(\mathbf{r}-\mathbf{r}')(\mathbf{r}-\mathbf{r}')$,

$$
(\mathbf{r}-\mathbf{r}')(\mathbf{r}-\mathbf{r}') = \begin{bmatrix} (x-x')^2 & (x-x')(y-y') & (x-x')(z-z') \\ (y-y')(x-x') & (y-y')^2 & (y-y')(z-z') \\ (z-z')(x-x') & (z-z')(y-y') & (z-z')^2 \end{bmatrix} \tag{7.39}
$$

With this we can compute the product, $(\mathbf{r}-\mathbf{r}')(\mathbf{r}-\mathbf{r}')\mathbf{P}(\mathbf{r}')$,

$$
\begin{aligned}
(\mathbf{r}-\mathbf{r}')(\mathbf{r}-\mathbf{r}')\mathbf{P}(\mathbf{r}') &= \begin{bmatrix} (x-x')^2 & (x-x')(y-y') & (x-x')(z-z') \\ (y-y')(x-x') & (y-y')^2 & (y-y')(z-z') \\ (z-z')(x-x') & (z-z')(y-y') & (z-z')^2 \end{bmatrix} \begin{bmatrix} 0 \\ 0 \\ P_z(z') \end{bmatrix} \\
&= \begin{bmatrix} (x-x')(z-z')P_z(z') \\ (y-y')(z-z')P_z(z') \\ (z-z')^2 P_z(z') \end{bmatrix}
\end{aligned} \tag{7.40}
$$

Thus, the integral can be written as,

$$
\begin{aligned}
I_{2,z}(z) &= \frac{3\beta}{4\pi\epsilon_0}\int_0^{2\pi} d\theta \int_{-L}^{L} dz' (z-z')^2 P_z(z') \int_0^{\infty} drr \frac{H[(r^2+(z-z')^2)^{1/2}-\eta]}{(r^2+(z-z')^2)^{5/2}} \\
&= \frac{3\beta}{2\epsilon_0} d\theta \int_{-L}^{L} dz' (z-z')^2 P_z(z') \int_{|z-z'|}^{\infty} du \frac{H[u-\eta]}{u^4}
\end{aligned} \tag{7.41}
$$

Once again, the integral over u must be evaluated piecewise,

$$\int_{|z-z'|}^{\infty} du \frac{H\left[u-\eta\right]}{u^4} = \begin{cases} |z-z'|^{-3}/3 & \text{if} \quad |z-z'| \geq \eta, \\ \eta^{-3}/3 & \text{if} \quad |z-z'| < \eta \end{cases} \tag{7.42}$$

Finishing the integral over z' we get the following,

$$I_{2,z}(z) = \frac{\beta}{2\epsilon_0} \int_{|z-z'|<\eta} dz' \frac{(z-z')^2}{\eta^3} P_z(z') + \frac{\beta}{2\epsilon_0} \int_{|z-z'|\geq\eta} \frac{P_z(z')}{|z-z'|} \tag{7.43}$$

Let's see what we have so far,

$$\begin{aligned} I_{1,z} - I_{2,z} &= \frac{\beta}{2\epsilon_0} \int_{|z-z'|<\eta} dz' \frac{P_z(z')}{\eta} + \frac{\beta}{2\epsilon_0} \int_{|z-z'|\geq\eta} dz' \frac{P_z(z')}{|z-z'|} \\ &\quad - \frac{\beta}{2\epsilon_0} \int_{|z-z'|<\eta} dz' \frac{(z-z')^2}{\eta^3} P_z(z') - \frac{\beta}{2\epsilon_0} \int_{|z-z'|\geq\eta} \frac{P_z(z')}{|z-z'|} \\ &= \frac{\beta}{2\epsilon_0} \int_{|z-z'|<\eta} dz' \frac{P_z(z')}{\eta} - \frac{\beta}{2\epsilon_0} \int_{|z-z'|<\eta} dz' \frac{(z-z')^2}{\eta^3} P_z(z') \end{aligned} \tag{7.44}$$

Note that this is well-defined for $\eta \to 0$. We can find this limit but Taylor expanding $P_z(z')$ around z, since $|z-z'| < \eta$ where η is very small (going to 0).

$$\lim_{\eta\to 0} [I_{1,z}(z) - I_{2,z}(z)] = \frac{\beta}{2\epsilon_0} \left[2P_z(z) - \frac{2}{3} P_z(z) \right] = \frac{2}{3} \frac{\beta}{\epsilon_0} P_z(z) \tag{7.45}$$

The final integral in Equation (7.34) is simple to evaluate,

$$I_{3,z}(z) = \frac{\beta}{3\epsilon_0} \int d\mathbf{r}' \delta(\mathbf{r}-\mathbf{r}') \begin{bmatrix} 1 & 0 & 0 \\ 0 & 1 & 0 \\ 0 & 0 & 1 \end{bmatrix} \begin{bmatrix} 0 \\ 0 \\ P_z(z') \end{bmatrix} = \frac{1}{3} \frac{\beta}{\epsilon_0} P_z(z) \tag{7.46}$$

Putting everything together, we finally obtain,

$$\boxed{\mathbf{U}(\mathbf{r}) = U_z(z) = -\frac{\beta}{\epsilon_0} P_z(z)} \tag{7.47}$$

Now we should address the x and y components that appeared in the evaluation of I_2,

$$\begin{aligned} I_{2,x} &= \frac{3\beta}{4\pi\epsilon_0} \int_{-\infty}^{\infty} dy' \int_{-L}^{L} dz' (z-z') P_z(z') \int_{-\infty}^{\infty} dx' \frac{(x-x') H[|\mathbf{r}-\mathbf{r}'| - \eta]}{|\mathbf{r}-\mathbf{r}'|^5} \\ &= 0 \end{aligned} \tag{7.48}$$

and similarly, $I_{2,y} = 0$.

Nondimensionalization

From this point, we only consider variation in the z coordinate, thus all vector quantities will be replaced with scalars corresponding tot their z component. We will find it convenient to define the following nondimensional quantities,

$$x \equiv \frac{z}{\sigma}, \quad \delta = \frac{d}{\sigma}, \quad u \equiv \mu U, \quad p \equiv \frac{v}{\mu} P, \quad \xi \equiv \frac{\beta \mu^2}{\epsilon_0 v}, \quad \phi \equiv \rho v \tag{7.49}$$

where we choose $\sigma^3 = v$ with σ being the particle size. The nondimensional set of equations reduced to 1 dimension is thus,

$$u(x) = -\xi p(x) \tag{7.50}$$

$$\phi(x) = \frac{N}{4\pi Q} e^{\omega(x)} q[u, u_x] = \frac{N}{A} \frac{e^{\omega(x)} q[u, u_x]}{\int dx e^{\omega(x)} q[u, u_x]} \tag{7.51}$$

$$p(x) = \frac{4\pi N}{A} e^{\omega(x)} \frac{|J| \cosh |J| - \sinh |J|}{|J|^3 \int dx e^{\omega(x)} q[u, u_x]} J \tag{7.52}$$

$$J(x) = u - \delta \omega_x \tag{7.53}$$

$$Q[\omega, u] = \frac{A}{4\pi} \int dx e^{\omega(x)} q[u, u_x] \tag{7.54}$$

$$q[u, u_x] = \frac{\pi^{3/2} e^{-u^2/4\delta u_x}}{\sqrt{\delta u_x}} \left[\operatorname{erfi}\left(\frac{u + 2\delta u_x}{2\sqrt{\delta u_x}} \right) - \operatorname{erfi}\left(\frac{u - 2\delta u_x}{2\sqrt{\delta u_x}} \right) \right] \tag{7.55}$$

7.4 Results and Discussion

The following results are all collected from molecular dynamics simulations of the sSF model. Results from shifted-DSCFT are presented in a later section. Here, we provide a detailed analysis of the density and electrostatic profiles at the liquid–vapor interface for a variety of conditions. In general, we span from weak to strong dipole moments, $\mu \in 1.0 - 2.0$, and small to large offsets, $d \in 0.0 - 0.25$, and study the effects on the liquid density and interfacial polarization. For some additional context, we mention briefly here how water maps onto the parameters of this model. Namely, choosing $\sigma = 2.75\,\text{Å}$, $\mu_0 = 1.8\,\text{D}$, and $T = 300\,\text{K}$ yields a reduced dipole moment of 1.94. Modeling the water very roughly as a spherical molecule, we can compute the effective dipole shift as the distance between the center of geometry and the center of charge as approximately 0.10 Å(or 0.036σ). Other molecules, such as refrigerants, typically have much large dipole shifts, reaching up to 0.2σ.

We rely on angular distribution functions to provide a detailed molecular picture and explanation of the observed interfacial polarization.

Density Profiles

We first compute the density profiles across the liquid–vapor interface using Equation (7.56) given as,

$$\rho(z) = \frac{1}{L_x L_y} \sum_{i=1}^{N} \delta(z - z_i)\,, \tag{7.56}$$

where $\delta(x)$ is the Dirac delta function. In practice, the coordinates are binned into narrow windows instead of using an exact delta function. Density profiles at various dipole strengths are provided in Figure 7.5. As expected, Figures 7.5b and c show that the density increases and the interface becomes sharper as μ increases. Note that this effect is not unique to shifted dipoles and occurs for any value of d.

The effects of μ and d on the coexistence liquid density are further summarized in Figure 7.5c. Here, we see that the liquid density increases as d increases for a given value of μ. We attribute the increase in density to a strengthening of dipolar interactions, as the introduction of a shift deepens the potential energy minimum in the sSF potential, thus allowing the particles to pack more closely. When $\mu > 1.8$, increasing d first results in a decrease in density, followed by an increase in density that follows the same trend as weaker dipole moments. This non-monotonic behavior is caused by the presence of a ferroelectric transition, which has been reported for dipolar hard spheres at high density [50–53, 91]. When $d = 0$, the dipoles prefer to align head to tail to minimize their energy. When μ is low, this preference is not strong enough to overcome thermal fluctuations and cause any spontaneous orientation in the liquid. However, when the dipole moment becomes strong enough, the dipoles spontaneously align, much like the spontaneous magnetization observed in ferromagnetic materials. This ferroelectric transition also causes the liquid to contract, resulting in an increased liquid density. As d increases, the perfect head-to-tail configuration of dipoles becomes less favorable relative to a slightly rotated configuration, and the ferroelectric transition is disrupted. A similar effect was also observed by Johnson et al. in their study of dipolar spheroids, where the ferroelectric transition was suppressed for both oblate and prolate spheroidal particles [91].

Since the shift places the dipoles closer to the particle surface, the optimal configuration for two dipoles is different than the regular Stockmayer potential. The dipole–dipole interaction energy is determined by both the distance and relative angle of the two dipoles. At large dipole shifts, the energy can become lower than the perfect head-to-tail configuration by rotating one of the particles slightly. This puts the dipoles closer together while sacrificing a small amount of attraction due

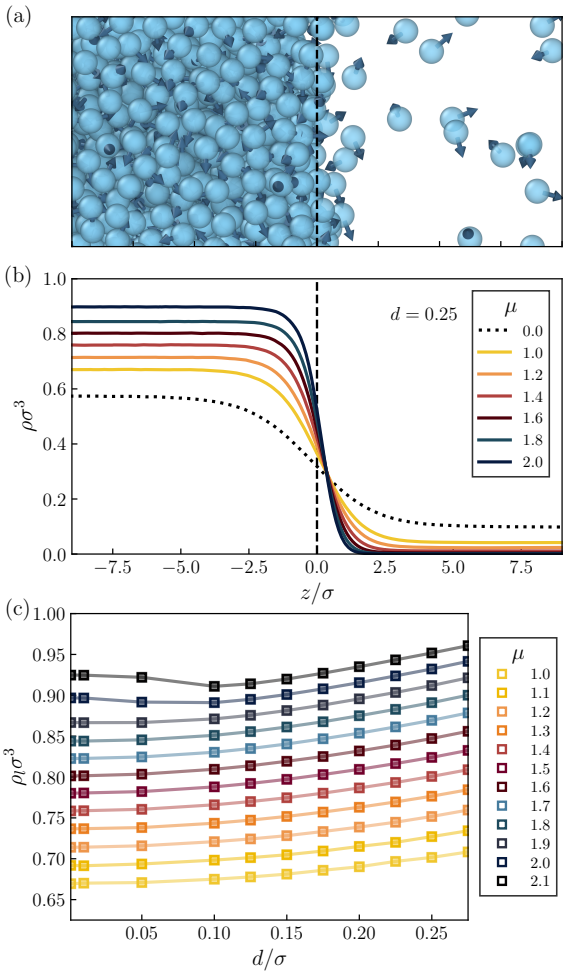

Figure 7.5: Interfacial density profiles for various μ and d. The interface is located between a bulk region of liquid on the left and a bulk region of vapor on the right. (a) Simulation snapshot with the average of the instantaneous interface plotted as a dashed line. (b) Density profiles with $d = 0.25\sigma$ and $T = 1$ for various values of μ, with the dotted line representing the reference LJ fluid with no dipoles. (c) Coexistence liquid densities at $T = 1$ for various values of μ and d.

to the non-optimal angle. The net effect is a lower overall energy due to the dipole interaction. Thus, at small but finite d, the ferroelectric transition is diminished but not fully suppressed, resulting in a decreasing density. At some value of d, the ferroelectric transition is suppressed completely, and further increasing d results in an increased density for the same reasons described in the low μ case. A more detailed description of the liquid structure and angular distribution functions is provided in our companion study on the bulk equilibrium properties of the sSF model (Venkatachalam et al. 2025).

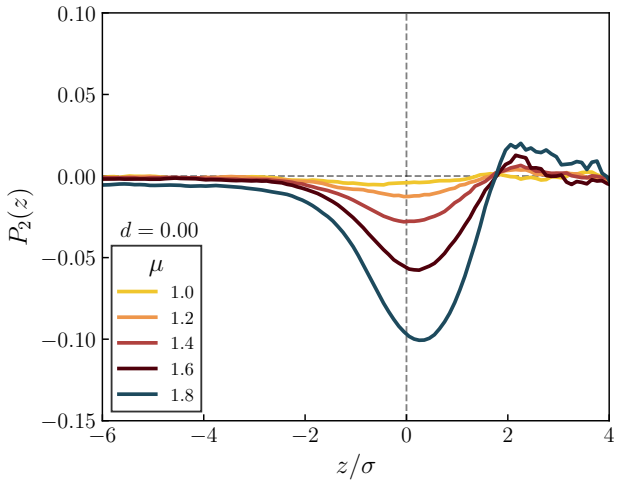

Figure 7.6: Nematic order profiles with interface surface normal as reference director. Profiles are plotted for no shift ($d = 0$) for various values of dipole moment μ. Note that $P_2(z) < 0$ indicates alignment parallel to the interface (perpendicular to the normal vector). The dashed lines are provided to guide the eye.

Nematic and Polar Order

A regular Stockmayer fluid with no dipole shift will necessarily have zero polar order throughout the fluid due to symmetry (assuming no ferroelectric transition occurs). The lack of polar order means that there can be no interfacial polarization and therefore no electric field or potential difference between the two phases. Despite the lack of polar order, we can still make an interesting observation about the nematic order at the interface for the regular SF model. Specifically, we take the unit normal of the interface to be a reference director, and we compute the relevant component of the nematic order parameter via the 2nd Legendre polynomial of orientation as

$$P_2(z) = \frac{1}{2}\left[3\left\langle \cos^2\theta \right\rangle(z) - 1\right], \tag{7.57}$$

where θ is the angle between a given dipole and the normal vector of the interface. The average $\langle \cdots \rangle(z)$ is computed within a narrow window around z. In words, $P_2(z)$ is a measure of how aligned the dipoles are with the surface normal as a function of distance from the interface. There are 3 interesting cases: (1) $P_2 = -1/2$ if all dipoles are perpendicular to the surface normal, (2) $P_2 = 1$ if all dipoles are parallel or antiparallel to the surface normal, (3) $P_2 = 0$ if the dipoles are randomly oriented with respect to the surface normal. In subsequent discussion, we refer to P_2 as the nematic order for simplicity, but it should be understood that it is only a component of the nematic order with an assumed nematic director parallel to the surface normal. This quantity has been used in several previous theoretical and simulation studies

of Stockmayer fluids at interfaces [56, 60, 62, 86, 92–94].

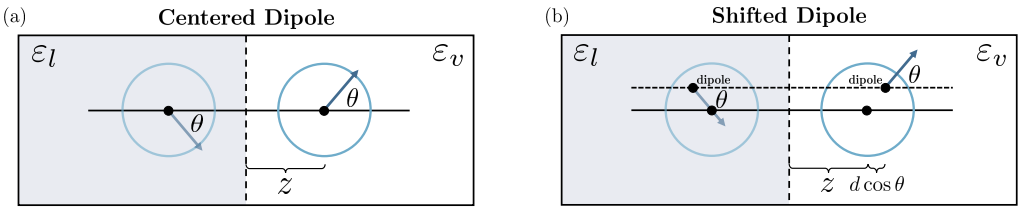

Figure 7.7: Image dipole construction at a liquid–vapor interface of the (a) Stockmayer fluid and (b) shifted Stockmayer fluid.

We plot the nematic order profile for the case of no dipole shift in Figure 7.6. It is clear from $P_2(z) < 0$ that there is a preference for the dipoles to lie in the interfacial plane, even with perfectly symmetric spherical molecules. This can be understood by considering image dipole interactions generated at the interface [14, 58, 94, 95]. Assuming that the interface can be approximated by a discontinuous jump between two homogeneous phases with disparate dielectric constants, molecules near the interface will experience interactions with an image dipole on the opposite side that has the same polar angle but is rotated azimuthally by π. This scenario is depicted in Figure 7.7a. The resulting interaction energy for a particle near the interface is

$$U(z,\theta) = \frac{\mu^2}{16}\frac{\epsilon_\alpha - \epsilon_\beta}{\epsilon_\alpha(\epsilon_\alpha + \epsilon_\beta)}\frac{1+\cos^2\theta}{z^3}, \tag{7.58}$$

where ϵ_α is the static dielectric constant of the host phase, ϵ_β is the dielectric constant of the coexisting phase, θ is the polar angle relative to the surface normal, and z is the distance from the interface. Note that the net sign of the interaction depends on whether the dipole is within the high dielectric or low dielectric medium. We can use Equation (7.58) to understand the orientational behavior of molecules on both the liquid and vapor sides of the interface. As we will later show, this analysis can also be used to predict the shape of the angular probability distributions, even in the presence of a dipole shift.

For a molecule in the liquid ($\epsilon_\alpha > \epsilon_\beta$), the energy in Equation (7.58) is minimized when $\theta = \pi/2$, indicating that the molecules will, on average, prefer to lie parallel to the interface. Alternatively, for a molecule in the vapor ($\epsilon_\alpha < \epsilon_\beta$), the energy is minimized when $\theta = 0$ and π, and the molecule will prefer to point perpendicular to the interface. Several studies using classical density functional theory (cDFT) and liquid state theory (LST) have predicted an S-shaped $P_2(z)$ profile across the liquid–vapor interface, where molecules on the liquid side are parallel to the interface and

molecules on the vapor side are perpendicular [57–59, 92]. On the other hand, several molecular dynamics simulation studies predicted only a parallel orientation ($P_2 < 0$) on both sides of the Gibbs dividing surface (GDS) [56, 60–62]. To the best of our knowledge, this disagreement between theory and simulation has still not been resolved. The two main hypotheses for the disagreement are (1) that the theoretical frameworks are unable to fully describe the essential physics of the density and dipole correlations, and (2) that the profiles computed from simulation carry too much statistical uncertainty, particularly in the dilute vapor phase.

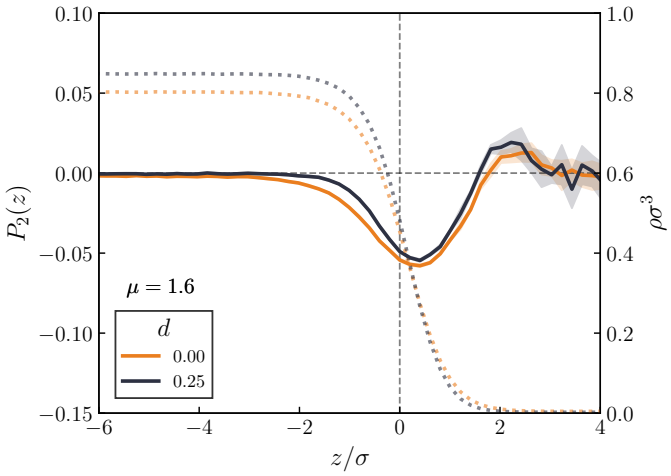

Figure 7.8: Nematic order profile (solid lines) from extended simulations for $\mu = 1.6$ and $d = 0$, 0.25. The shaded areas represent 95% confidence intervals computed from block averaging, and the dotted lines are the corresponding density profiles.

The simulation results in Figure 7.6 agree with previous MD simulations of Stockmayer fluids in that $P_2(z)$ is negative across the interface, with the minimum located near the GDS. In contrast to previous works, our simulations seem to produce a pronounced peak within the vapor region when the dipole moment is high ($\mu \geq 1.6$). However, significant noise once again makes the interpretation difficult. To verify this behavior with statistical certainty, we conducted simulations with $\mu = 1.6$ and $d = 0$, 0.25 for 10^7 timesteps. We saved every 100th frame for analysis, resulting in a total of 10^5 frames. Treating the two interfaces as independent, we were able to double the amount of data and obtained the profile of the nematic order using a total of 2×10^5 frames. We broke the data into 10 blocks of 2×10^4 frames each and used the standard error of the mean to estimate the uncertainty in the profiles. The resulting nematic order parameter profiles with 95% confidence intervals are plotted in Figure 7.8. These show a statistically significant peak within the vapor phase, which agrees qualitatively with the predictions of cDFT and LST, as well as

the image dipole result based on Equation (7.58). However, we note that cDFT and LST predict that the transition from negative to positive $P_2(z)$ occurs at the GDS, whereas our calculations show that $P_2(z)$ does not become positive until around 2σ outside the GDS.

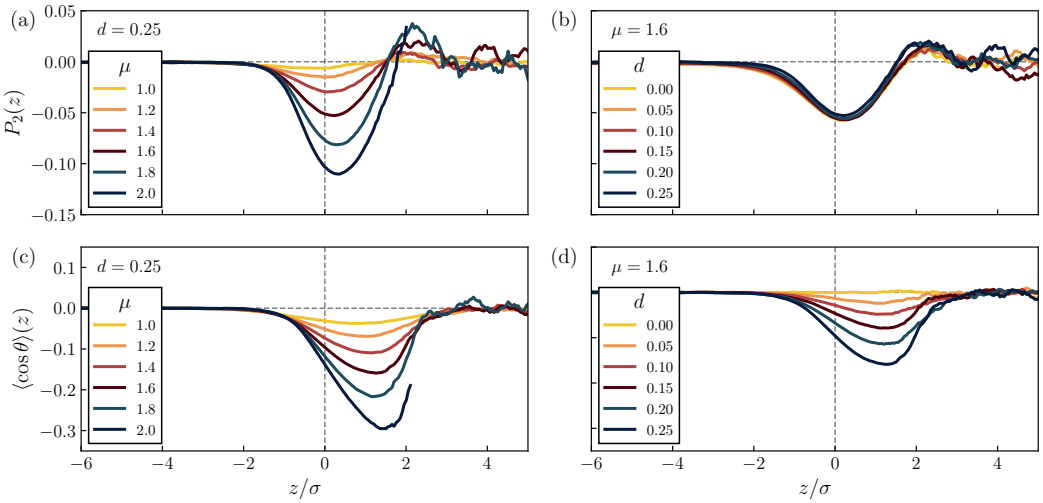

Figure 7.9: Spatially varying nematic ((a) and (b)) and polar ((c) and (d)) order parameters with respect to surface normal vector. (a)+(c) Profiles for a shift of $d = 0.25$ for various values of dipole moment μ. (b)+(d) Profiles for a dipole moment of $\mu = 1.6$ for various values of shift d. We omit averages computed from less than 100 data points due to significant statistical uncertainty. Note that $m(z) < 0$ and $m(z) > 0$ indicate dipoles pointing towards the liquid and vapor, respectively. The dashed lines are provided to guide the eye.

Introducing a shift to the dipole has little effect on the spatially varying nematic order parameter, which we plot in Figure 7.9b. We can modify Equation (7.58) to include the dipole shift, which results in

$$U(z,\theta) = \frac{\mu^2}{16}\frac{\epsilon_\alpha - \epsilon_\beta}{\epsilon_\alpha(\epsilon_\alpha + \epsilon_\beta)}\frac{1+\cos^2\theta}{(z + d\cos\theta)^3}\,, \tag{7.59}$$

where d is the dipole shift. The shift effectively couples the dipole angle with the distance of the dipole from the interface. This scenario is depicted in Figure 7.7b. Dipoles pointing towards the interface will have stronger interactions with their images than those that are pointing away. Note that the effect of the shift diminishes as z grows larger than $d\cos\theta$ and the energy approaches that of Equation (7.58). The asymmetry introduced by the shift leads to a preferential orientation of the dipoles at the interface, which is most easily seen through the polar order profile and the shape of the angular distribution functions in the interfacial region.

Similar to $P_2(z)$, we define the spatially varying polar order parameter $m(z)$ in Equation (7.60). We use the coordinates of the LJ particles to determine the positions and the dipole vectors for the orientations.

$$m(z) = \langle \cos\theta \rangle(z) = \langle \hat{\mu}_z \rangle(z) \,. \tag{7.60}$$

Again, θ is the angle between the dipole and the surface normal which is the unit vector in the z-direction, and theaverage $\langle \dots \rangle(z)$ is computed within a narrow window around z. In words, $m(z)$ is a measure of the average orientation of the molecules, specifically in the z-direction. A value of $m(z) = 0$ means that the molecules have no *net* preference to point towards the liquid or vapor, while $m(z) < 0$ and $m(z) > 0$ indicate preferences to orient towards the liquid and vapor regions, respectively. Note that $m(z) = 0$ with $P_2(z) \neq 0$ is achieved by having a non-uniform distribution on $\cos\theta$ that is still symmetric about $\theta = \pi/2$, which is exactly the case for the regular Stockmayer fluid.

We plot the spatially varying polar order for a dipole shift of $d = 0.25$ in Figure 7.9c. A shift in the dipole induces an orientational order normal to the interface across a wide range of dipole moments. The strength of the ordering increases with dipole moment as the electrostatic interactions become stronger and a denser solvation environment becomes more favorable. In Figure 7.9d, we show that the orientational order also becomes more pronounced as the dipole shift increases for a fixed dipole moment. These observations are also consistent with the image dipole construction of Equation (7.59). Namely, a finite d skews the minimum of the energy due to image dipole interactions for molecules in both the liquid and vapor phases. In both cases, the molecules will show a preference to point towards the liquid phase when $d > 0$, resulting in a purely negative $m(z)$ across the interface.

Together, Figures 7.9a and 7.9c paint an almost complete picture of the molecular orientations across the liquid–vapor interface for the sSF model. The liquid features $P_2(z) < 0$ and $m(z) < 0$, indicating that molecules are largely oriented in the plane of the interface, with a slight preference to point towards the liquid. On the other hand, the vapor features $P_2(z) > 0$ and $m(z) < 0$, indicating that molecules are largely oriented perpendicular to the interface, also with a preference to point towards the liquid.

Providing further quantitative insights, we plot the probability distribution of $\cos\theta$ within the interfacial region in Figure 7.10. We denote these as *angular distribution functions*. The interfacial region is chosen as $-0.5 < z < 2.0$ based on the profiles

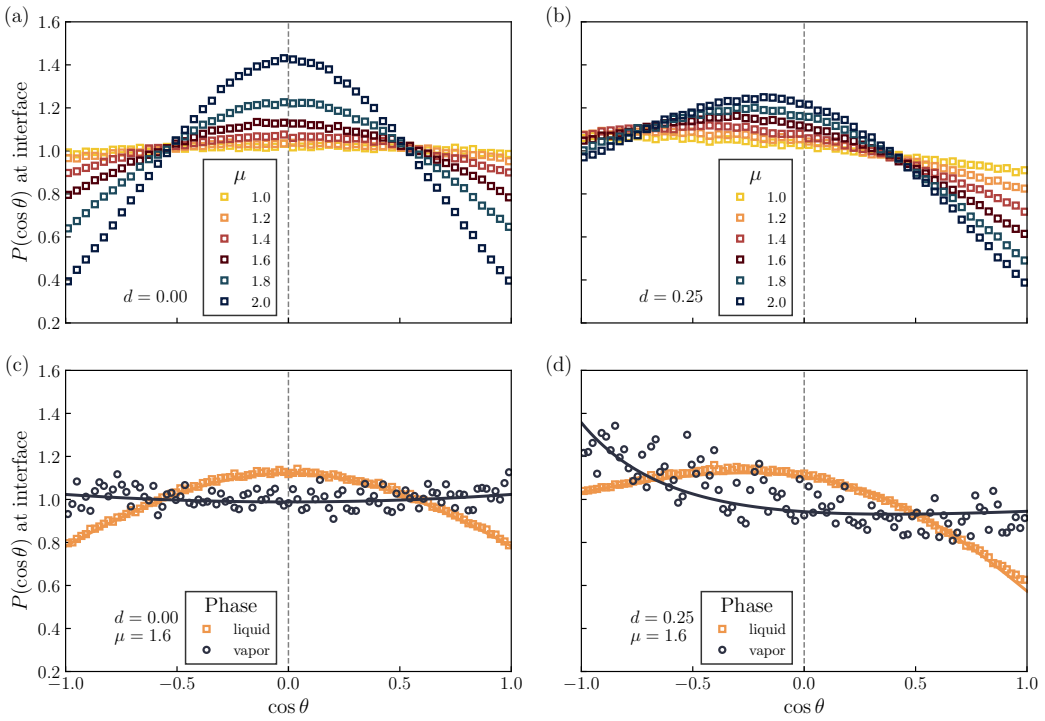

Figure 7.10: Angular distribution functions in the interfacial region for various dipole moments μ and dipole offsets d. Distributions in (a) and (b) are extracted from the entire interfacial region within $-0.5 < z < 2.0$. Distributions in (c) and (d) are broken into separate regions for the liquid and vapor phases. Symbols represent MD data and curves represent fits to Equations (7.58) and (7.59) for (c) and (d) respectively. The distributions are normalized and then multiplied by a constant factor of 2. Recall that $\cos\theta < 0$ and $\cos\theta > 0$ correspond to molecules pointing towards the liquid and vapor, respectively.

in Figure 7.9. The distributions in Figure 7.10a show that, for the SF, the preference to lie in the interfacial plane becomes stronger with increasing dipole moment, indicated by the sharpening of the peak around $\cos\theta = 0$. The picture becomes more complicated when the dipole is shifted off-center, as shown for $d = 0.25$ in Figure 7.10b. For weak dipole moments, the distribution becomes skewed towards -1. As the dipole moment increases, the skew increases, and a prominent peak appears within $-1 < \cos\theta < 0$. The shape of this distribution explains how molecules with high μ and high d have significantly negative $P_2(z)$ and $m(z)$ near the interface. The negative skew in the distributions supports the conclusion that the molecules prefer to point towards the liquid. Due to the way we constructed our molecules, this also implies that the molecules are positioning their point-dipoles closer to the liquid phase than the vapor phase. This orientation allows for the dipoles to interact more strongly with dipoles just below the surface layer, providing

some additional solvation from liquid-phase particles.

As mentioned previously, Equations (7.58) and (7.59) can be used to make predictions about the angular distributions on the liquid and vapor sides of the interface. Figures 7.10c and 7.10d show remarkable qualitative agreement between the MD simulations and the theoretical predictions. The lines were computed through a fitting procedure where the parameters of the distribution (i.e., ε, μ, d, z, etc.) were varied to minimize residuals. The open symbols were computed by splitting the interfacial region into a *liquid side* and a *vapor side*, and accumulating dipole orientations in the two separate regions. While the liquid–vapor interface itself is diffuse, we choose to define the transition from liquid to vapor at $z \approx 2\sigma$ based on the location where $P_2(z)$ crosses from negative to positive in Figures 7.6, 7.8, and 7.9. We do this to remain in line with the predictions of the image-dipole method which predicts that P_2 is negative in the liquid and positive in the vapor. We don't expect quantitative agreement as we have a diffuse interface and significant dipole correlation effects that are completely ignored by treating dipoles as independent particles immersed in a homogeneous medium with a dielectric discontinuity. Amazingly, the qualitative behavior can still be captured for both the liquid and vapor, whether or not there is a dipole offset.

Interfacial Electric Field and Potential

The primary objective of this work is to determine if molecular asymmetry in polar fluids is sufficient to induce a significant interfacial electric field. To this end, we discuss in the following section the electric properties of the interface including the electric field and the electrostatic potential profile. To compute the spatially varying electric field, we start from the differential form of Gauss's Law,

$$\varepsilon_0 \nabla \cdot \mathbf{E} = -\nabla \cdot \mathbf{P} + \rho_f \,, \tag{7.61}$$

where ε_0 is the vacuum permittivity, $\mathbf{E}$ is the electric field, $\mathbf{P}$ is the polarization density, and ρ_f is the *free* charge. In our case, no free ions are present such that $\rho_f = 0$. In addition, the system is infinitely vast in the dimensions parallel to the interface, implying that $\mathbf{E}_{||}$, $\mathbf{P}_{||}$, and their derivatives are identically 0 in the absence of a bulk ferroelectric transition. Thus, Equation (7.61) reduces to the simple relation $\varepsilon_0 E_z(z) = -P_z(z)$, where E_z and P_z are scalar fields for the z-component of each quantity, which both vanish deep within the homogeneous vapor and liquid phases. This relation implies that the electric field points in the opposite direction of the polarization. Importantly, this provides a straightforward way to compute E_z

from MD simulation, since P_z is easily computed with Equation (7.62) given below,

$$P_z(z) = \frac{1}{L_z L_y} \sum_{i=1}^{N} \delta(z - z_i)\mu_z^i \,, \tag{7.62}$$

where μ_z^i is the z-component of the dipole moment of molecule i, and z_i refers to the position of the dipole particle (not the LJ particle). In practice, dipoles are binned within a small region around z and accumulated over the course of a long simulation run. The electrostatic potential profile, $\psi(z)$, is then computed from the electric field or the polarization by recognizing that $E_z(z) = -\partial_z \psi(z)$, which yields the following integral equation

$$\psi(z) - \psi_0 = -\int_{z_v}^{z} E_z(t)dt = \frac{1}{\varepsilon_0}\int_{z_v}^{z} P_z(t)dt \,, \tag{7.63}$$

where ψ_0 is the reference potential, taken to be deep within the vapor region.

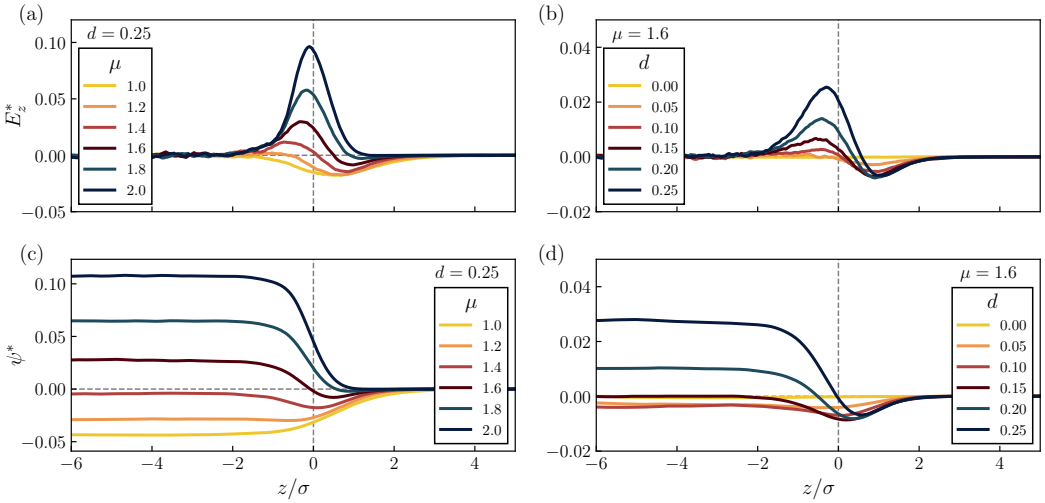

Figure 7.11: Spatially varying electric field ((a) and (b)) and electrostatic potential ((c) and (d)). (a)+(c) Profiles for a shift of $d = 0.25$ for various values of dipole moment μ. (b)+(d) Profiles for a dipole moment of $\mu = 1.6$ for various values of shift d. The dashed lines are provided to guide the eye. The liquid phase is located at $z < 0$ and the vapor phase at $z > 0$.

We plot the reduced electric field, E_z^*, and the corresponding reduced electrostatic potential, ψ^*, in Figure 7.11. As expected, the electric field vanishes in the bulk phases and is finite at the interface. This interfacial field arises solely from the asymmetry of the polar molecules and the resulting polar order. Unexpectedly, the interfacial electric field E_z^* can change sign. With increasing dipole moment strength, the electric field switches from negative to positive. This trend is also

reflected in the electrostatic potential shown in Figures 7.11c where, for weak dipole moments, ψ^* increases across the interface. For strong dipole moments, ψ^* decreases. Figure Although we do not yet have a definitive physical explanation for this sign inversion, its existence is plausible given the complex interplay among liquid and vapor densities, interfacial width, dipole strength, and dipole shift. Here we provide one possible logical interpretation of this anomalous behavior.

The distribution functions in Figure 7.10b show that increasing the dipole strength at a fixed, large shift enhances the tendency of interfacial molecules to orient up the density gradient toward the liquid phase ($-0.5 < \cos\theta < 0$). At sufficiently strong dipole moments, this preference becomes strong enough to produce a negative polarization and, correspondingly, a positive electric field (blue curves in Figure 7.11a and 7.11c). Thus, molecules with both a significant dipole shift and a strong dipole moment tend to generate polarization aligned with the density gradient.

By contrast, molecules with weak dipole moments exhibit a relatively flat angular distribution near the interface, which has two consequences. First, the weak preference for pointing toward the liquid is insufficient to generate appreciable negative polarization (positive electric field) at the weakest dipole moments studied. Molecules oriented toward the liquid point up the density gradient, placing their dipoles in a dense region where the polarization is averaged out by the random orientations of surrounding molecules. Molecules oriented toward the vapor point down the gradient, positioning their dipoles in a low-density region with few neighboring molecules. The combined effect is a net polarization of opposite sign to the density gradient (yellow/orange curves in Figures 7.11a and 7.11c).

The behavior of the electric field and electrostatic potential for various d at fixed $\mu = 1.6$ are given in Figures 7.11b and Figure 7.11d, respectively. The curves for $d = 0$ confirm that the regular Stockmayer fluid produces no electric field at the interface and therefore no potential difference between the two phases. In general, the dipole strength sets the shape of the electric field at the the interface, while the dipole shift sets the magnitude. For example, at fixed $d = 0.25$, the electric field goes from purely negative, to S-shaped, to purely positive as μ increases from 1.0 to 2.0. On the other hand, at fixed $\mu = 1.6$, the shape remains S-shaped as d increases while the positive peak on the liquid side of the interface increases in height. We provide further examples of this general observation for different regimes of d and μ in the Appendix.

To quantify the strength of the interfacial electric field, we can substitute the proper-

ties of a real fluid. For water we have $\sigma = 2.75$ Å, $\mu_0 = 1.8$ D, and $\epsilon = k_B T$, which yields a reduced dipole moment of $\mu = 1.94$. Thus, the simulations at $\mu = 2.0$ can be reasonably interpreted within the context of the air–water interface. For $\mu = 2.0$ and $d = 0.25$, the reduced electric field at the interface is $E_z^* \approx 0.10$ (Figure 7.11a), which corresponds to $E_z \approx 16$ MV/cm for the water properties listed above. This electric field is a reasonable order of magnitude for an air–water interface and agrees well with previous experiments [96], and molecular dynamics simulation using the ReaxFF/C-GeM forcefield [37]. Any specific quantitative agreement should be interpreted cautiously since the sSF model is a simplified picture that ignores effects from electronic polarization, mean inner potential, hydrogen bonding, and steric effects of nonspherical molecules. We make this comparison simply to show that the magnitude of the interfacial electric field can reach experimentally relevant values.

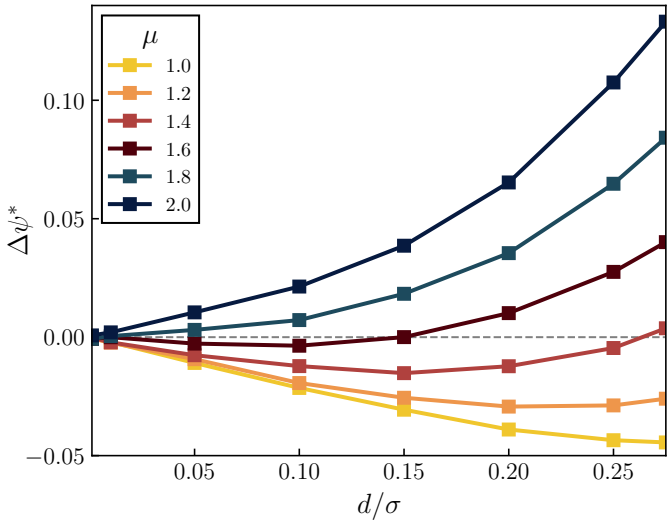

Figure 7.12: The potential difference between the bulk regions of vapor and liquid for various μ and d. $d = 0$ corresponds to the regular Stockmayer fluid, which has no polarization and therefore no potential difference. $\Delta\psi^* = \psi_l^* - \psi_v^*$.

The potential difference between the two phases across all combinations of μ and d is given in Figure 7.12. The sSF model exhibits highly nontrivial behavior in the potential difference across the range of parameters studied here. For weak dipole moments, the dipole shift leads to a potential drop across the interface when going from the liquid to the vapor. However, strong dipole moments lead to a positive potential difference. These two contrasting behaviors can be understood based on the previous discussion. Of particular interest are the intermediate dipole moments

and shifts where, due to the competing dipole orientations in the liquid and vapor regions, for a given dipole moment ($\mu = 1.6$ for example), increasing the dipole shift can cause an inversion in the sign of $\Delta\psi^*$. However, the point where $\Delta\psi^* \approx 0$ does not necessitate that $\psi^*(z) = 0$. As shown in Figure 7.11d, ψ^* exhibits a minimum for $\mu = 1.6$ and $d = 0.15$ despite having $\Delta\psi^* = 0$. While we are not aware if any real molecule corresponds to such parameters, this minimum in ψ^* and corresponding S-shaped electric field could provide preferential localization for chemical reactions at liquid–vapor interfaces, even between atoms with similar partial charges. In addition, the sign inversion of $\Delta\psi$ implies that asymmetry alone could lead to the adsorption of differently charged ions for differing μ and d. We leave the exploration of electrolyte systems for a future study.

These results confirm that molecular asymmetry is a crucial factor in controlling interfacial electrostatic properties, and can even contribute a significant electric field in the absence of any other effects.

7.5 Conclusions

In this study, we conducted molecular dynamics simulations of the shifted Stockmayer fluid model to study the interfacial properties of asymmetric polar fluids. We systematically varied both the dipole shift, d, and the dipole moment, μ, to observe the effect of the molecular properties on the equilibrium interfacial profiles. Specifically, we reported profiles for the density, nematic order (2nd Legendre polynomial of orientation), polar order, electric field, and electrostatic potential. The density of the liquid phase was enhanced by the presence of a dipole shift, which we attributed to the strengthened electrostatic interactions between dipoles that lie closer to the surface of the spherical particles. For strong dipole moments, and therefore high liquid densities, we encountered a ferroelectric transition known to occur in the Stockmayer fluid model. Interestingly, a moderate shift in the dipole completely destroyed the ordering in the ferroelectric transition as a result of the most favorable conformation changing from the typical end-aligned (parallel). A more detailed study of the bulk liquid equilibrium properties is currently in preparation (Venkatachalam et al. 2025).

We found that the presence of even a small shift in the dipole could lead to significant interfacial polarization. In line with previous MD simulations, we found that the molecules at the Gibbs dividing surface prefer to lie parallel to the interface ($P_2 < 0$). In contrast to previous simulations, but in agreement with theoretical pre-

dictions from classical density functional theory, our simulations revealed that vapor molecules just outside the interface have a preference to point perpendicular to the interface ($P_2 > 0$) for sufficiently strong dipole moments. To make simple analytical predictions for the angular distribution functions in proximity to the interface, we utilized the energy due to image dipole interactions. We extended the traditional image dipole interaction to include the effect of a dipole shift and found excellent agreement between the theoretical predictions and the distributions collected from MD simulations. We found that the regular Stockmayer fluid produces $P_2(z) < 0$ in the liquid, $P_2(z) > 0$ in the vapor, and $m(z) = 0$ everywhere. On the other hand, the angular distribution functions of a shifted Stockmayer fluid are skewed towards the liquid ($\cos\theta < 0$). While $P_2(z)$ does not significantly change, $m(z)$ is consistently negative, indicating a preference for the molecules to point towards the liquid.

We computed the polarization density, electric field, and the electrostatic potential difference between the two phases. The sign of the electric field displayed an inversion as the strength of the dipole moment was increased with a constant dipole shift. Namely, the electric field had the same sign as the density gradient for weak dipole moments and the opposite sign for strong dipole moments. At parameters consistent with those of water, we found that the interfacial electric field was roughly 16 MV/cm. We note that this agrees in both sign and magnitude with experimental observations and quantum mechanical MD simulations of water. The quantitative agreement is surprising and should not be read into since the shifted Stockmayer fluid is a minimal model that ignores many unique aspects of real fluids such as the mean inner potential, geometric asymmetry, polarization, and hydrogen bonding.

With this work, we have shown that slight molecular asymmetry in the Stockmayer fluid leads to rich interfacial behavior, including significant interfacial polarization. In the modern discussion of how interfacial electric fields catalyze reactions, this work provides context for a potentially important effect that is likely to be present to some extent in all polar fluids. In future studies we will explore the role of dipole shift on the bulk and interfacial properties of electrolyte solutions.

7.6 Appendix

Electric Fields and Electrostatic Potentials

Here we provide additional plots of the electric field and electrostatic potential for the full range of simulation parameters tested.

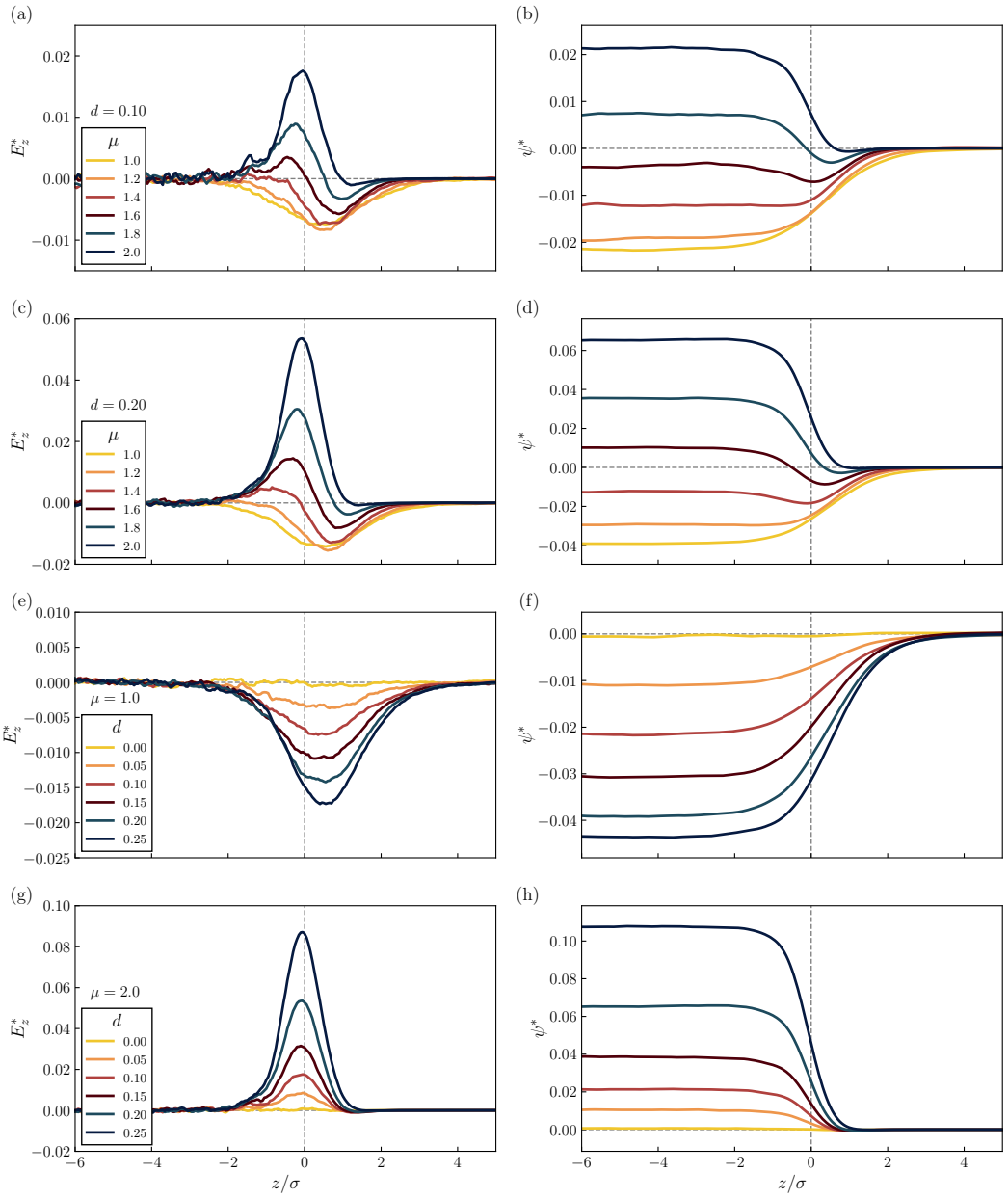

Figure 7.13: Electric field and electrostatic potential for various combinations of μ and d.

References

(1) Varner, S.; Walker, P. J.; Venkatachalam, A.; Zhuang, B.; Wang, Z.-G. Stockmayer Fluid with a Shifted Dipole: Interfacial Behavior, 2025, DOI: 10.48550/arXiv.2509.05523.

(2) Yan, X.; Bain, R. M.; Cooks, R. G. Organic Reactions in Microdroplets: Reaction Acceleration Revealed by Mass Spectrometry. *Angewandte Chemie International Edition* **2016**, *55*, 12960–12972, DOI: 10.1002/anie.201602270.

(3) Wei, Z.; Li, Y.; Cooks, R. G.; Yan, X. Accelerated Reaction Kinetics in Microdroplets: Overview and Recent Developments. *Annual Review of Physical Chemistry* **2020**, *71*, 31–51, DOI: 10.1146/annurev-physchem-121319-110654.

(4) Narayan, S.; Muldoon, J.; Finn, M. G., et al. "On Water": Unique Reactivity of Organic Compounds in Aqueous Suspension. *Angewandte Chemie International Edition* **2005**, *44*, 3275–3279, DOI: 10.1002/anie.200462883.

(5) Serrano-Luginbühl, S.; Ruiz-Mirazo, K.; Ostaszewski, R.; Gallou, F.; Walde, P. Soft and dispersed interface-rich aqueous systems that promote and guide chemical reactions. *Nature Reviews Chemistry* **2018**, *2*, 306–327, DOI: 10.1038/s41570-018-0042-6.

(6) Jordan, C. J. C.; Lowe, E. A.; Verlet, J. R. R. Photooxidation of the Phenolate Anion is Accelerated at the Water/Air Interface. *Journal of the American Chemical Society* **2022**, *144*, 14012–14015, DOI: 10.1021/jacs.2c04935.

(7) Chen, H.; Wang, R.; Xu, J., et al. Spontaneous Reduction by One Electron on Water Microdroplets Facilitates Direct Carboxylation with CO2. *Journal of the American Chemical Society* **2023**, *145*, 2647–2652, DOI: 10.1021/jacs.2c12731.

(8) Liu, T.; Abbatt, J. P. D. Oxidation of sulfur dioxide by nitrogen dioxide accelerated at the interface of deliquesced aerosol particles. *Nature Chemistry* **2021**, *13*, 1173–1177, DOI: 10.1038/s41557-021-00777-0.

(9) Wan, Z.; Fang, Y.; Liu, Z.; Francisco, J. S.; Zhu, C. Mechanistic Insights into the Reactive Uptake of Chlorine Nitrate at the Air–Water Interface. *Journal of the American Chemical Society* **2023**, *145*, 944–952, DOI: 10.1021/jacs.2c09837.

(10) Rossignol, S.; Tinel, L.; Bianco, A., et al. Atmospheric photochemistry at a fatty acid–coated air-water interface. *Science* **2016**, *353*, 699–702, DOI: 10.1126/science.aaf3617.

(11) Xia, D.; Chen, J.; Xie, H.-B.; Zhong, J.; Francisco, J. S. Counterintuitive Oxidation of Alcohols at Air–Water Interfaces. *Journal of the American Chemical Society* **2023**, *145*, 4791–4799, DOI: 10.1021/jacs.2c13661.

(12) Liang, Q.; Zhu, C.; Yang, J. Water Charge Transfer Accelerates Criegee Intermediate Reaction with H2O– Radical Anion at the Aqueous Interface. *Journal of the American Chemical Society* **2023**, *145*, 10159–10166, DOI: 10.1021/jacs.3c00734.

(13) George, C.; Ammann, M.; D'Anna, B.; Donaldson, D. J.; Nizkorodov, S. A. Heterogeneous Photochemistry in the Atmosphere. *Chemical Reviews* **2015**, *115*, 4218–4258, DOI: 10.1021/cr500648z.

(14) Ruiz-Lopez, M. F.; Francisco, J. S.; Martins-Costa, M. T. C.; Anglada, J. M. Molecular reactions at aqueous interfaces. *Nature Reviews Chemistry* **2020**, *4*, 459–475, DOI: 10.1038/s41570-020-0203-2.

(15) Yan, X.; Augusti, R.; Li, X.; Cooks, R. G. Chemical Reactivity Assessment Using Reactive Paper Spray Ionization Mass Spectrometry: The Katritzky Reaction. *ChemPlusChem* **2013**, *78*, 1142–1148, DOI: 10.1002/cplu.201300172.

(16) Girod, M.; Moyano, E.; Campbell, D. I.; Cooks, R. G. Accelerated bimolecular reactions in microdroplets studied by desorption electrospray ionization mass spectrometry. *Chemical Science* **2011**, *2*, 501–510, DOI: 10.1039/C0SC00416B.

(17) Pestana, L. R.; Hao, H.; Head-Gordon, T. Diels–Alder Reactions in Water Are Determined by Microsolvation. *Nano Letters* **2020**, *20*, 606–611, DOI: 10.1021/acs.nanolett.9b04369.

(18) Matyushov, D. V. Electrostatic solvation and mobility in uniform and non-uniform electric fields: From simple ions to proteins. *Biomicrofluidics* **2019**, *13*, 064106, DOI: 10.1063/1.5124390.

(19) Muñoz-Santiburcio, D.; Marx, D. Confinement-Controlled Aqueous Chemistry within Nanometric Slit Pores. *Chemical Reviews* **2021**, *121*, 6293–6320, DOI: 10.1021/acs.chemrev.0c01292.

(20) Welborn, V. V.; Ruiz Pestana, L.; Head-Gordon, T. Computational optimization of electric fields for better catalysis design. *Nature Catalysis* **2018**, *1*, 649–655, DOI: 10.1038/s41929-018-0109-2.

(21) Ashton, M.; Mishra, A.; Neugebauer, J.; Freysoldt, C. Ab initio Description of Bond Breaking in Large Electric Fields. *Physical Review Letters* **2020**, *124*, 176801, DOI: 10.1103/PhysRevLett.124.176801.

(22) Shaik, S.; Danovich, D.; Joy, J.; Wang, Z.; Stuyver, T. Electric-Field Mediated Chemistry: Uncovering and Exploiting the Potential of (Oriented) Electric Fields to Exert Chemical Catalysis and Reaction Control. *Journal of the American Chemical Society* **2020**, *142*, 12551–12562, DOI: 10.1021/jacs.0c05128.

(23) Bím, D.; Alexandrova, A. N. Local Electric Fields As a Natural Switch of Heme-Iron Protein Reactivity. *ACS Catalysis* **2021**, *11*, 6534–6546, DOI: 10.1021/acscatal.1c00687.

(24) Eberhart, M. E.; Wilson, T. R.; Jones, T. E.; Alexandrova, A. N. Electric fields imbue enzyme reactivity by aligning active site fragment orbitals. *Proceedings of the National Academy of Sciences* **2024**, *121*, e2411976121, DOI: 10.1073/pnas.2411976121.

(25) Aragonès, A. C.; Haworth, N. L.; Darwish, N., et al. Electrostatic catalysis of a Diels–Alder reaction. *Nature* **2016**, *531*, 88–91, DOI: 10.1038/nature16989.

(26) Shaik, S.; Mandal, D.; Ramanan, R. Oriented electric fields as future smart reagents in chemistry. *Nature Chemistry* **2016**, *8*, 1091–1098, DOI: 10.1038/nchem.2651.

(27) Stuyver, T.; Danovich, D.; Joy, J.; Shaik, S. External electric field effects on chemical structure and reactivity. *WIREs Computational Molecular Science* **2020**, *10*, e1438, DOI: 10.1002/wcms.1438.

(28) Zheng, C.; Mao, Y.; Kozuch, J., et al. A two-directional vibrational probe reveals different electric field orientations in solution and an enzyme active site. *Nature Chemistry* **2022**, *14*, 891–897, DOI: 10.1038/s41557-022-00937-w.

(29) Welborn, V. V.; Head-Gordon, T. Fluctuations of Electric Fields in the Active Site of the Enzyme Ketosteroid Isomerase. *Journal of the American Chemical Society* **2019**, *141*, 12487–12492, DOI: 10.1021/jacs.9b05323.

(30) Morita, A.; Hynes, J. T. A theoretical analysis of the sum frequency generation spectrum of the water surface. *Chemical Physics* **2000**, *258*, 371–390, DOI: 10.1016/S0301-0104(00)00127-0.

(31) Du, Q.; Superfine, R.; Freysz, E.; Shen, Y. R. Vibrational spectroscopy of water at the vapor/water interface. *Physical Review Letters* **1993**, *70*, 2313–2316, DOI: 10.1103/PhysRevLett.70.2313.

(32) Medders, G. R.; Paesani, F. Dissecting the Molecular Structure of the Air/Water Interface from Quantum Simulations of the Sum-Frequency Generation Spectrum. *Journal of the American Chemical Society* **2016**, *138*, 3912–3919, DOI: 10.1021/jacs.6b00893.

(33) Moberg, D. R.; Straight, S. C.; Paesani, F. Temperature Dependence of the Air/Water Interface Revealed by Polarization Sensitive Sum-Frequency Generation Spectroscopy. *The Journal of Physical Chemistry B* **2018**, *122*, 4356–4365, DOI: 10.1021/acs.jpcb.8b01726.

(34) Pezzotti, S.; Galimberti, D. R.; Gaigeot, M.-P. 2D H-Bond Network as the Topmost Skin to the Air–Water Interface. *The Journal of Physical Chemistry Letters* **2017**, *8*, 3133–3141, DOI: 10.1021/acs.jpclett.7b01257.

(35) Pezzotti, S.; Serva, A.; Gaigeot, M.-P. 2D-HB-Network at the air-water interface: A structural and dynamical characterization by means of ab initio and classical molecular dynamics simulations. *The Journal of Chemical Physics* **2018**, *148*, 174701, DOI: 10.1063/1.5018096.

(36) Cooper, R. J.; O'Brien, J. T.; Chang, T. M.; Williams, E. R. Structural and electrostatic effects at the surfaces of size- and charge-selected aqueous nanodrops. *Chemical Science* **2017**, *8*, 5201–5213, DOI: 10.1039/C7SC00481H.

(37) Hao, H.; Leven, I.; Head-Gordon, T. Can electric fields drive chemistry for an aqueous microdroplet? *Nature Communications* **2022**, *13*, 280, DOI: 10.1038/s41467-021-27941-x.

(38) Kathmann, S. M.; Kuo, I.-F. W.; Mundy, C. J.; Schenter, G. K. Understanding the Surface Potential of Water. *The Journal of Physical Chemistry B* **2011**, *115*, 4369–4377, DOI: 10.1021/jp1116036.

(39) Stillinger, F. H. Water Revisited. *Science* **1980**, *209*, 451–457, DOI: 10.1126/science.209.4455.451.

(40) Franks, F., *Water: A Matrix of Life*; Royal Society of Chemistry: 2000; 248 pp.

(41) Ball, P., *Life's Matrix: A Biography of Water*; University of California Press: 2001; 444 pp.

(42) Stockmayer, W. H. Second Virial Coefficients of Polar Gas Mixtures. *The Journal of Chemical Physics* **1941**, *9*, 863–870, DOI: 10.1063/1.1750858.

(43) Stockmayer, W. H. Second Virial Coefficients of Polar Gases. *The Journal of Chemical Physics* **1941**, *9*, 398–402, DOI: 10.1063/1.1750922.

(44) Shock, C. J.; Stevens, M. J.; Frischknecht, A. L.; Nakamura, I. Solvation Energy of Ions in a Stockmayer Fluid. *The Journal of Physical Chemistry B* **2020**, *124*, 4598–4604, DOI: 10.1021/acs.jpcb.0c00769.

(45) Bagchi, B.; Jana, B. Solvation dynamics in dipolar liquids. *Chemical Society Reviews* **2010**, *39*, 1936–1954, DOI: 10.1039/B902048A.

(46) Perera, L.; Berkowitz, M. L. Dynamics of ion solvation in a Stockmayer fluid. *The Journal of Chemical Physics* **1992**, *96*, 3092–3101, DOI: 10.1063/1.461954.

(47) Adams, D.; Adams, E. Static dielectric properties of the Stockmayer fluid from computer simulation. *Molecular Physics* **1981**, *42*, 907–926, DOI: 10.1080/00268978100100701.

(48) Pollock, E. L.; Alder, B. J. Static dielectric properties of Stockmayer fluids. *Physica A: Statistical Mechanics and its Applications* **1980**, *102*, 1–21, DOI: 10.1016/0378-4371(80)90058-8.

(49) Shock, C. J.; Stevens, M. J.; Frischknecht, A. L.; Nakamura, I. Molecular dynamics simulations of the dielectric constants of salt-free and salt-doped polar solvents. *The Journal of Chemical Physics* **2023**, *159*, 134507, DOI: 10.1063/5.0165481.

(50) Groh, B.; Dietrich, S. Ferroelectric phase in Stockmayer fluids. *Physical Review E* **1994**, *50*, 3814–3833, DOI: 10.1103/PhysRevE.50.3814.

(51) Weis, J. J.; Levesque, D. Ferroelectric phases of dipolar hard spheres. *Physical Review E* **1993**, *48*, 3728–3740, DOI: 10.1103/PhysRevE.48.3728.

(52) Pounds, M. A.; Madden, P. A. Are dipolar liquids ferroelectric? Simulation studies. *The Journal of Chemical Physics* **2007**, *126*, 104506, DOI: 10.1063/1.2672734.

(53) Bartke, J.; Hentschke, R. Dielectric properties and the ferroelectric transition of the Stockmayer-fluid via computer simulation. *Molecular Physics* **2006**, *104*, 3057–3068, DOI: 10.1080/00268970600961990.

(54) Marx, J.; Kohns, M.; Langenbach, K. Phase Equilibria in Mixtures of Differently Polar Fluids: Molecular Simulation and Perturbation Theory. *Chemie Ingenieur Technik* **2022**, *94*, 1345–1345, DOI: 10.1002/cite.202255007.

(55) Marx, J.; Kohns, M.; Langenbach, K. Vapor-liquid equilibria of binary mixtures containing Stockmayer-type model fluids from Monte-Carlo simulations. *Fluid Phase Equilibria* **2023**, *568*, 113742, DOI: 10.1016/j.fluid.2023.113742.

(56) Moore, S. G.; Stevens, M. J.; Grest, G. S. Liquid-vapor interface of the Stockmayer fluid in a uniform external field. *Physical Review E* **2015**, *91*, 022309, DOI: 10.1103/PhysRevE.91.022309.

(57) Frodl, P.; Dietrich, S. Bulk and interfacial properties of polar and molecular fluids. *Physical Review A* **1992**, *45*, 7330–7354, DOI: 10.1103/PhysRevA.45.7330.

(58) Frodl, P.; Dietrich, S. Thermal and structural properties of the liquid-vapor interface in dipolar fluids. *Physical Review E* **1993**, *48*, 3741–3759, DOI: 10.1103/PhysRevE.48.3741.

(59) Iatsevitch, S.; Forstmann, F. Structure of fluid interfaces: an integral equation study. *Molecular Physics* **2000**, *98*, 1309–1322, DOI: 10.1080/002689700413569.

(60) Mecke, M.; Fischer, J.; Winkelmann, J. Molecular dynamics simulation of the liquid–vapor interface of dipolar fluids under different electrostatic boundary conditions. *The Journal of Chemical Physics* **2001**, *114*, 5842–5852, DOI: 10.1063/1.1349177.

(61) Enders, S.; Kahl, H.; Mecke, M.; Winkelmann, J. Molecular dynamics simulation of the liquid–vapor interface: I. The orientational profile of 2-center Lennard–Jones and of Stockmayer fluid molecules. *Journal of Molecular Liquids* **2004**, *115*, 29–39, DOI: 10.1016/j.molliq.2003.12.020.

(62) Eggebrecht, J.; Thompson, S. M.; Gubbins, K. E. The liquid–vapor interface of simple polar fluids. II. Computer simulation. *The Journal of Chemical Physics* **1987**, *86*, 2299–2308, DOI: 10.1063/1.452128.

(63) Langenbach, K. Co-Oriented Fluid Functional Equation for Electrostatic interactions (COFFEE). *Chemical Engineering Science* **2017**, *174*, 40–55, DOI: 10.1016/j.ces.2017.08.025.

(64) Kusaka, I.; Wang, Z.-G.; Seinfeld, J. H. Ion-induced nucleation: A density functional approach. *The Journal of Chemical Physics* **1995**, *102*, 913–924, DOI: 10.1063/1.469158.

(65) Kohns, M.; Marx, J.; Langenbach, K. Relative Permittivity of Stockmayer-Type Model Fluids from MD Simulations and COFFEE. *Journal of Chemical & Engineering Data* **2020**, *65*, 5891–5896, DOI: 10.1021/acs.jced.0c00769.

(66) Allen, M. P.; Tildesley, D. J., *Computer Simulation of Liquids*; Oxford University Press: 2017.

(67) Kamberaj, H.; Low, R. J.; Neal, M. P. Time reversible and symplectic integrators for molecular dynamics simulations of rigid molecules. *The Journal of Chemical Physics* **2005**, *122*, 224114, DOI: 10.1063/1.1906216.

(68) Toukmaji, A.; Sagui, C.; Board, J.; Darden, T. Efficient particle-mesh Ewald based approach to fixed and induced dipolar interactions. *The Journal of Chemical Physics* **2000**, *113*, 10913–10927, DOI: 10.1063/1.1324708.

(69) Cerdà, J. J.; Ballenegger, V.; Lenz, O.; Holm, C. P3M algorithm for dipolar interactions. *The Journal of Chemical Physics* **2008**, *129*, 234104, DOI: 10.1063/1.3000389.

(70) Stukowski, A. Visualization and analysis of atomistic simulation data with OVITO-the Open Visualization Tool. *Modelling and Simulation in Materials Science and Engineering* **2010**, *18*, 015012, DOI: 10.1088/0965-0393/18/1/015012.

(71) Jungwirth, P.; Tobias, D. J. Specific Ion Effects at the Air/Water Interface. *Chemical Reviews* **2006**, *106*, 1259–1281, DOI: 10.1021/cr0403741.

(72) Matsumoto, M.; Kataoka, Y. Study on liquid–vapor interface of water. I. Simulational results of thermodynamic properties and orientational structure. *The Journal of Chemical Physics* **1988**, *88*, 3233–3245, DOI: 10.1063/1.453919.

(73) Matsumoto, M.; Kataoka, Y. Molecular orientation near liquid–vapor interface of methanol: Simulational study. *The Journal of Chemical Physics* **1989**, *90*, 2398–2407, DOI: 10.1063/1.455982.

(74) Cendagorta, J. R.; Ichiye, T. The Surface Potential of the Water–Vapor Interface from Classical Simulations. *The Journal of Physical Chemistry B* **2015**, *119*, 9114–9122, DOI: 10.1021/jp508878v.

(75) Yeh, Y. L.; Zhang, C.; Held, H., et al. Structure of the acetone liquid/vapor interface. *The Journal of Chemical Physics* **2001**, *114*, 1837–1843, DOI: 10.1063/1.1333761.

(76) Martins-Costa, M. T. C.; Ruiz-López, M. F. Electrostatics and Chemical Reactivity at the Air–Water Interface. *Journal of the American Chemical Society* **2023**, *145*, 1400–1406, DOI: 10.1021/jacs.2c12089.

(77) Kuo, I.-F. W.; Mundy, C. J. An ab Initio Molecular Dynamics Study of the Aqueous Liquid-Vapor Interface. *Science* **2004**, *303*, 658–660, DOI: 10.1126/science.1092787.

(78) Tobias, D. J.; Stern, A. C.; Baer, M. D.; Levin, Y.; Mundy, C. J. Simulation and Theory of Ions at Atmospherically Relevant Aqueous Liquid-Air Interfaces. *Annual Review of Physical Chemistry* **2013**, *64*, 339–359, DOI: 10.1146/annurev-physchem-040412-110049.

(79) Kathmann, S. M.; Kuo, I.-F. W.; Mundy, C. J. Electronic Effects on the Surface Potential at the Vapor-Liquid Interface of Water. *Journal of the American Chemical Society* **2008**, *130*, 16556–16561, DOI: 10.1021/ja802851w.

(80) Mundy, C. J.; Kuo, I.-F. W.; Tuckerman, M. E.; Lee, H.-S.; Tobias, D. J. Hydroxide anion at the air–water interface. *Chemical Physics Letters* **2009**, *481*, 2–8, DOI: 10.1016/j.cplett.2009.09.003.

(81) Dodia, M.; Ohto, T.; Imoto, S.; Nagata, Y. Structure and Dynamics of Water at the Water–Air Interface Using First-Principles Molecular Dynamics Simulations. II. NonLocal vs Empirical van der Waals Corrections. *Journal of Chemical Theory and Computation* **2019**, *15*, 3836–3843, DOI: 10.1021/acs.jctc.9b00253.

(82) Horváth, L.; Beu, T.; Manghi, M.; Palmeri, J. The vapor-liquid interface potential of (multi)polar fluids and its influence on ion solvation. *The Journal of Chemical Physics* **2013**, *138*, 154702, DOI: 10.1063/1.4799938.

(83) Mecke, M.; Winkelmann, J.; Fischer, J. Molecular dynamics simulation of the liquid–vapor interface: The Lennard-Jones fluid. *The Journal of Chemical Physics* **1997**, *107*, 9264–9270, DOI: 10.1063/1.475217.

(84) Taylor, R. S.; Dang, L. X.; Garrett, B. C. Molecular Dynamics Simulations of the Liquid/Vapor Interface of SPC/E Water. *The Journal of Physical Chemistry* **1996**, *100*, 11720–11725, DOI: 10.1021/jp960615b.

(85) Samin, S.; Tsori, Y.; Holm, C. Vapor-liquid coexistence of the Stockmayer fluid in nonuniform external fields. *Physical Review E* **2013**, *87*, 052128, DOI: 10.1103/PhysRevE.87.052128.

(86) Paul, S.; Chandra, A. Liquid-Vapor Interfaces of Simple Electrolyte Solutions: Molecular Dynamics Results for Ions in Stockmayer Fluids. *The Journal of Physical Chemistry B* **2003**, *107*, 12705–12712, DOI: 10.1021/jp0302820.

(87) Martínez, L.; Andrade, R.; Birgin, E. G.; Martínez, J. M. PACKMOL: A package for building initial configurations for molecular dynamics simulations. *Journal of Computational Chemistry* **2009**, *30*, 2157–2164, DOI: https://doi.org/10.1002/jcc.21224.

(88) Willard, A. P.; Chandler, D. Instantaneous Liquid Interfaces. *The Journal of Physical Chemistry B* **2010**, *114*, 1954–1958, DOI: 10.1021/jp909219k.

(89) Ye, B. B.; Walker, P. J.; Wang, Z.-G. MDCraft: A Python assistant for performing andanalyzing molecular dynamics simulations of soft matter systems. *Journal of Open Source Software* **2024**, *9*, 7013, DOI: 10.21105/joss.07013.

(90) Tarazona, P.; Chacón, E.; Bresme, F. Intrinsic profiles and the structure of liquid surfaces. *Journal of Physics: Condensed Matter* **2012**, *24*, 284123, DOI: 10.1088/0953-8984/24/28/284123.

(91) Johnson, L. E.; Benight, S. J.; Barnes, R.; Robinson, B. H. Dielectric and Phase Behavior of Dipolar Spheroids. *The Journal of Physical Chemistry B* **2015**, *119*, 5240–5250, DOI: 10.1021/acs.jpcb.5b00009.

(92) Eggebrecht, J.; Gubbins, K. E.; Thompson, S. M. The liquid–vapor interface of simple polar fluids. I. Integral equation and perturbation theories. *The Journal of Chemical Physics* **1987**, *86*, 2286–2298, DOI: 10.1063/1.452127.

(93) Teixeira, P. I.; Gama, M. M. T. D. Density-functional theory for the interfacial properties of a dipolar fluid. *Journal of Physics: Condensed Matter* **1991**, *3*, 111–125, DOI: 10.1088/0953-8984/3/1/009.

(94) Teixeira, P. I. C.; Gama, M. M. T. d. Orientation and association at the liquid–vapour interface of dipolar fluids. *Journal of Physics: Condensed Matter* **2002**, *14*, 12159, DOI: 10.1088/0953-8984/14/46/319.

(95) Martins-Costa, M. T. C.; Ruiz-Lopez, M. F. Solvation effects on electronic polarization and reactivity indices at the air–water interface: insights from a theoretical study of cyanophenols. *Theoretical Chemistry Accounts* **2015**, *134*, 17, DOI: 10.1007/s00214-014-1609-z.

(96) Xiong, H.; Lee, J. K.; Zare, R. N.; Min, W. Strong Electric Field Observed at the Interface of Aqueous Microdroplets. *The Journal of Physical Chemistry Letters* **2020**, *11*, 7423–7428, DOI: 10.1021/acs.jpclett.0c02061.